3-DIMENSIONAL NUMERICAL AND EXPERIMENTAL STUDIES TO MODEL ARTIFICIAL HEART VALVES HEMODYNAMICS

KUAN YEE HAN

(B.Eng.(Hons.), NUS)

A THESIS SUBMITTED

FOR THE DEGREE OF

DOCTOR OF PHILOSOPHY (Ph.D)

DEPARTMENT OF BIOMEDICAL ENGINEERING

NATIONAL UNIVERSITY OF SINGAPORE

2014

DECLARATION

I hereby declare that the thesis is my original work and it has been written by me in its entirety. I have duly acknowledged all the sources of information which have been used in the thesis.

This thesis has also not been submitted for any degree in any university previously.

Kuan Yee Han

August 2014

ACKNOWLEDGEMENT

What a hell of a ride! It has been a long roller coaster ride since 2010 embarking on this journey of self-discovery. Throughout the entire roller coaster experience, there were many twists and turns. Sometimes I went past sharp corners at top speed when inspirations came. That was when lots of momentum started and I do not mind going back to the Biofluid Mechanics Research Laboratory to work on my research. Sometimes, the wait was a bit too long when I hit a stumbling block till I dreaded to look at the computer screen. What were wrong with the codes?! And then came “Eureka!”. At the end of the day, the experiences and the people were part of this roller coaster experience. I survived. I have learned many lessons, lessons about the impact that you can make in the world of research, friendship, people, new experiences and being the master of your own time. And these experiences and lessons were crafted deep in my heart and shaped who I am today. I must say, it has been a wonderful four years of roller coaster ride with the people around me. My friends always asked me, why I pursued Ph.D. My reply was always that I enjoyed the people and the little things beside my research work. These were the main motivator to keep me going in this lonely journey. Now the last lesson to complete this Ph.D is to work on this thesis. Writing this dissertation wasn’t easy but I am glad that I made it through with the personal support from numerous people.

I would like to thank my supervisors Dr Leo Hwa Liang and Dr Nguyen Vinh-Tan for the continuous support and guidance throughout my years in the research. Thank you Dr Leo for the trust and faith that you have in me, for the friendship, understanding and making available all the resources for me. Thank you Dr Vinh-Tan for guiding me to debug the codes whenever the errors appeared on the Linux station. Without both of you, I would have lost my way in both the Computational Fluid Dynamics and heart valves world. I would also like to thank my laboratory friends: Foad, George, Yee Wei, Boyang, Munirah, Sean, Sianglin, my former students Po-Yu and Jia Loon. I would like to personally thank Foad for the constant guidance, source of knowledge especially with the PIV, and help in reviewing my manuscripts. Thank you George for the companionship and numerous times we spent together on our mini adventures. Thank you Yee Wei for the support in the lab

and for helping me during my TA role. I am really thankful to have colleagues who were willing to share their time, which made my journey so exciting.

I would like to thank my family members for the unwavering support and love all these years. You all were always there for me throughout my years of highs and lows. Thank you “Papa” and “Mama” for the continuous support and allowing me to pursue my post-graduate studies. You will get to attend my graduation ceremony this time. Thank you to my sisters, Da Jie, Er Jie, Pei Xuan and Pei Huang for the constant support and listening to me whining. Words cannot express my gratitude to all of you for every time that you were there to listen and encourage. I would also like to thank my girlfriend, Geraldine, for her patience and support. Thank you for your words of encouragements and care just spending time with me. The last two years of the roller coasters have been memorable with you around. I also like to thank Uncle Teoh, Uncle Choh Kee and Uncle Francis for their support and Twinkle for her unconditional love and burst of the maltipoo energy.

To my colleagues and partner in crime at the Tembusu College, thank you Kelvin for being a big brother to me all these years. I enjoyed all the fun we have so far in working with students. Thank you Sara, Junhong, Frank, and many others in Tembusu for making my journey more manageable in forgetting the struggle of the lonely journey. Thank you also my friends in NUSSU for the many years of friendship (Jeremy, Feng Fu, Jason, Jia Mein, Nur, Ser Xing, Ria, EK, YSL, etc), my NOC mates (Wenhan, Patrick, Zwee, Gary, Donald, etc), and my Team Advent Access friends (Ruey, James and Yan Ling) and many more.

Though some of these people may not be involved in my research directly, without them, my life, as a post-graduate student would not have been so enriching. No words of thanks can express my gratitude, including those I forgot to mention here. Thank you very much for the support and trust! Perhaps the journey wasn’t that lonely after all. ☺

Yee Han
April 2014

TABLE OF CONTENTS

LIST OF TABLES

LIST OF FIGURES

LIST OF SYMBOLS AND ABBREVIATIONS

f	Aperture number
h	Height (m)
L, l	Length (m)
μ	Dynamic viscosity (kg m^{-1} s^{-1})
ν	Kinematic viscosity (m^2 s^{-1})
ρ	Density (kg m^{-3})
p	Pressure (mm Hg)
Δp	Pressure Gradient (mm Hg)
T, t	Time (s)
u	Instantaneous axial velocity (m s^{-1})
τ	Reynolds shear stress (dynes cm^{-2}, 10 x Nm^{-2})
$\dot{\gamma}$	Shear rate (s^{-1})
D	Diameter (m)
Q	Volumetric flow rate (m^3 s^{-1})
r	Radial distance (m)
V	Volume (m^3)
Γ	Boundary surface (m^2)
S	Face Area (m^2)
$\mathcal{M}$	Mesh
θ	Angle of leaflet position (rad or degrees)
I	Moment of Inertia (kg m^2)
M	Moment (kg m^2 s^{-2})
ζ	Damping coefficient (kg s^{-1})
ε	Convergence (s^{-2})

ALE	Arbitrary Lagrangian Eulerian
ATS	Advancing The Standard
AV	Atrioventricular
BMHV	Bileaflet Mechanical Heart Valve
bpm	Beats per minute
CCD	Charged-Coupled Device
CFD	Computational Fluid Dynamics
CFL	Courant-Friedrichs-Lewy

CO	Cardiac output
DES	Detached Eddy Simulation
DNS	Direct Numerical Simulation
EOA	Effective orifice area (m^2)
FEM	Finite Element Method
FIDAP	Fluid Dynamic Analysis Program
FSI	Fluid-Structure Interaction
FV	Finite Volume
GCL	Geometric Conservation Law
GOA	Geometric orifice area (m^2)
HITS	High Intensity Transient Signals
HR	Heart rate
LA	Left atrium
LDV	Laser Doppler Velocimetry
LES	Large Eddy Simulations
LV	Left ventricle
NaI	Sodium Iodide
Nd:YAG	Neodymium-doped yttrium aluminium garnet
NS	Navier-Stokes
OpenFOAM	Open Field Operation And Manipulation
PCU	Polycarbonate urethane
PFV	Pivot flow visualization
PISO	Pressure Implicit with Splitting of Operator
PIV	Particle Image Velocimetry
RA	Right atrium
RANS	Reynolds Averaged Navier-Stokes
Re	Reynolds number
RV	Right ventricle
SA	Spalart-Allmaras
SJM	St Jude Medical
SNR	Signal-to-noise ratio
SV	Stroke Volume
TMHV	Trileaflet Mechanical Heart Valve

Abstract

The characterization of the artificial heart valve flow fields is a crucial step to improve heart valve engineering. With the advancement of Computational Fluid Dynamics, the study of complex hemodynamics in details such as stagnation, recirculation zones and shear stresses can be performed on artificial heart valve models. The objective of this study is (1) to develop a prescribed motion code to study the flow through a bileaflet mechanical heart valve with prescribed motions in body fitted grid framework using arbitrary Lagrangian Eulerien (ALE) method (2) To study the effect of sinus and downstream geometry on the flow fields in the hinge region and the effect of implantation angles on the downstream flow field of bileaflet mechanical heart valve (3) To study the flow hemodynamic through a trileaflet mechanical heart valve design and compare it with that of a bileaflet mechanical heart valve and (4) To develop the Fluid-Structure Interaction of a rigid mechanical heart valve using solid body motion

The 3-dimensional numerical simulation to study the hemodynamic performance of a bileaflet mechanical heart valve was performed using OpenFOAM, and was validated experimentally for both laminar and pulsatile flows with prescribed motion. The influence of the flow fields in the hinge regions by different aortic sinus shape, the downstream aortic arch geometry and the location of the hinge recess were investigated. Regions of high wall shear stress which cause platelet activation were highlighted in the study. Differences in the flow field contours of the four hinges were observed even though the leakage flow rate through the hinges had minimal variation. Nevertheless, the hinge should be simulated with a three-sinus aortic root geometry and curved downstream aortic arch since this geometry resembled that of native human model.

The effects of implantation angles of bileaflet mechanical heart valves on the sinus region and downstream flow profiles were also investigated. The simulation results showed that the flow profile through valve implanted at anatomically correct position at angle 0° has more distributed flow and lower velocity gradient. The implantation angle affected the flow recirculation region

in the sinus chambers and the downstream flow. Subsequently, comparisons between the flow of bileaflet and trileaflet mechanical heart valves were made, followed by the effect of implantation angles of trileaflet mechanical heart valves on the downstream flow profiles. The implantation angles of trileaflet mechanical heart valves did not affect the downstream flow field much as compared to the bileaflet mechanical heart valves. The hemodynamics showed that the placement of bileaflet mechanical heart valve models in an anatomical correct position is important to minimize the high velocity gradients in the downstream aorta.

Finally, the continuous and full interaction between the blood flow and the valve leaflets, using Fluid-Structure Interaction to investigate the flow through a bileaflet mechanical heart valve was considered and compared with the prescribed and experimental results. The FSI model was able to capture accurately flow structures at early systole when the leaflets were in motion. The prescribed leaflet motions were not able to replicate the important flow parameters during the valve motion.

This research aims to provide a more accurate representation to study the hemodynamic parameters of artificial heart valves. The current study should be conducted in the pre-clinical evaluation phase for all new artificial heart valve design and downstream aorta geometry due to the importance of hemodynamic flow fields observed. The numerical study may potentially determine the clinical performance of the valve.

CHAPTER 1: BACKGROUND

In this chapter, an overview of the human heart physiology, the diseases associated with heart valves and the existing treatments are provided. Specifically, the different types of artificial heart valves and the complications with these valves are presented. Following that, the different types of hemodynamic assessments of artificial heart valves are described. Finally, different types of studies (*in vitro*, *in vivo* and computational fluid dynamics) conducted to assess the artificial heart valves performances are shown.

In the last 50 years, different types of artificial prosthetic heart valve have been implanted to replace defective heart valves. Since the first heart valve replacement in the 1960s, mechanical heart valve remains the most frequently used largely due to its durability among all prosthetic heart valves implanted. Of all the mechanical heart valves, bileaflet mechanical heart valve (BMHV) is regularly used. Despite mechanical valve being able to function well, patients require life-long anti-coagulation therapy after heart valve replacement. As early as 1970, it was shown that patients with the first generation mechanical heart valve suffered from decreased half-life of platelet destruction (Harker and Slichter 1970). Additionally, complications such as hemolysis, chronic platelet activation and initiation of thrombus formation associated with mechanical heart valve implantation have resulted in ischemic attacks and strokes (Bourguignon *et al.,* 2011, Yin *et al.,* 2004, Sacks 2002). Besides material properties and contact activation, hemodynamics performance and shear stress are believed to be the main causes for the complications (Shahriari *et al.,* 2012, Dumont *et al.,* 2007). Taking hemolysis as an example; as blood passes through the BMHV, valve leaflet act as obstruction to the flow of blood, which causes velocity jet through the valve orifices. The velocity jet results in elevated shear stress, leading to hemolysis and platelet activation.

In vitro and in vivo testing of different valves prototypes have been conducted. In the valve design process, virtual valve prototypes are computer-designed and tested in the early stage. Computational fluid dynamics (CFD) simulation emerged as a potentially useful tool to predict the

hemodynamic performance of these heart valves. Most early works of CFD used 2-dimensional simulations or symmetrical 3-dimensional models due to limited computational power. 2-dimensional and 3-dimensional simulations provide insights into the flow pattern near peak systole Reynolds Number. However, in order to have a better understanding, the continuous and full interaction between the valve leaflets and the blood flow should be considered, which will be helpful in getting insight of the hemodynamics in the areas where it is difficult to capture experimentally.

1.1 Anatomy and physiology of human heart valves

The human heart is a four-chambered muscular pump that provides the circulation of blood in both the systemic and pulmonary circulatory systems as shown in Figure 1-1. The dynamics of blood flow and intrachamber pressures are different on each side of the heart. The left atrium receives oxygenated blood from pulmonary vein and pumps the blood to aorta via left ventricle. Right atrium on the other hand, receives deoxygenated blood from inferior and superior vena cava. The deoxygenated blood is pumped to pulmonary artery via right ventricle. The four cardiac valves function to maintain unidirectional blood flow through the chambers of the heart. These valves are of two types; the atrioventricular (AV) and semilunar valves. AV valves separate the atria from the ventricles while semilunar valves separate the pulmonary artery and the aorta from their corresponding ventricles. The opening and closing of the valves in a synchronized manner is in response to the pressure and volume changes within the cardiac chambers and vessels (Price and Wilson 2003).

The AV valves leaflets are delicate but durable. The tricuspid valve contains three cusps, or leaflets and is located between the right atrium (RA) and right ventricle (RV). The mitral valve that separates the left atrium (LA) and left ventricle (LV) is a bicuspid valve with two leaflets. Both semilunar valves; the aortic valve and pulmonic valve, are similar in configuration and prevent backflow from the aorta or pulmonary artery into the ventricles during ventricular relaxation. These four valves ensure the one-way flow of the blood circulation in human by opening and closing in a synchronized manner.

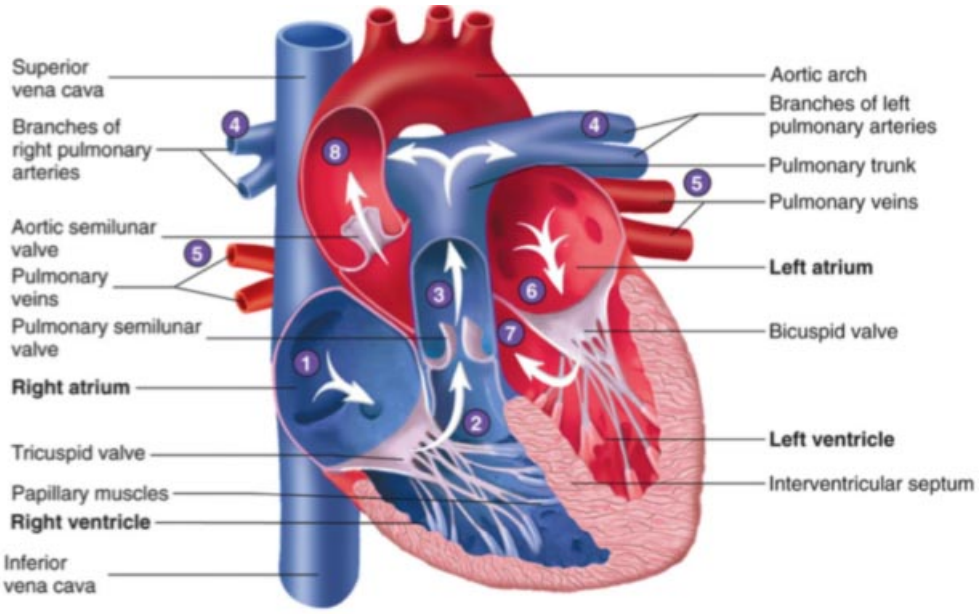

Figure 1-1: Anatomy of human heart (Mc-Graw Hill, 2014)

1.2 The cardiac cycle

The cardiac cycle describes the sequence of ventricular contraction and emptying (systole), and ventricular relaxation and filling (diastole). During each heartbeat, there is a sequence of events collectively known as the cardiac cycle that lasts approximately 0.86s. This corresponds to about 70 beats per minute (bpm) for a healthy person. There are two major stages in a single cardiac cycle; the ventricular diastole and the ventricular systole.

The cycle begins with the “late diastole” of the heart. Both semilunar valves are closed and both atrioventricular valves are open. The entire heart is in a relaxed state and blood flows down a pressure gradient from the vena cava and pulmonary veins into the right and left atria respectively and subsequently into the right and left ventricles. The ventricular pressure rises as more blood flows into the ventricles. The flow rate of atrial blood entering the ventricles decreases as the ventricular pressure reaches the level of the atrial pressure. The diminishing pressure gradient no longer allows blood to flow passively into the ventricles. This is when atrial systole occurs. The isotonic contraction of both atria increases the atrial pressure, forcing the remaining blood into the ventricles through the atrioventricular valves. As the ventricular pressure exceeds the atrial pressure, the atrioventricular valves close to prevent backflow of blood into the atria. Ventricular systole follows,

with the contraction of both ventricles. The atrioventricular and semilunar valves are all close and the ventricular pressure increases without a change in ventricular volume. This is also referred to as the “isovolumetric ventricular contraction” (Klabunde, 2011).

Eventually, the semilunar valves open as ventricular pressure exceeds the pressure in the aorta or pulmonary arteries. Blood is ejected from the ventricles. This is the “ventricular ejection” phase with isotonic contraction of the ventricular muscles, where the aortic velocity is about 1 to 1.4ms^{-1}, while ventricular and aortic pressures increase to 120mmHg. Once blood has been forced out of the ventricles, ventricular pressure decreases sharply. The semilunar valves immediately close to prevent backflow of blood from the aorta or pulmonary arteries. As the atrioventricular valves remain close, no blood flows into the ventricles as they relax – “isovolumetric ventricular relaxation”. The cardiac cycle ends with complete cardiac diastole where both atria and ventricles relax (Laberge 2002). At this phase, blood enters the left and right atria passively from pulmonary veins and vena cava respectively and the cycle repeats. Figure 1-2 shows the pressure change in left atrium, left ventricle and aorta at different phase of cardiac cycle. Typically, an adult male pumps blood at an average flow rate of 5 liters per minute. The heart beats about 100,000 times and pumps about 7500 liters of blood every day. In a life span of about 70 years, an average human heart beats more than 2.5 billion times (American Heart Association 2012a).

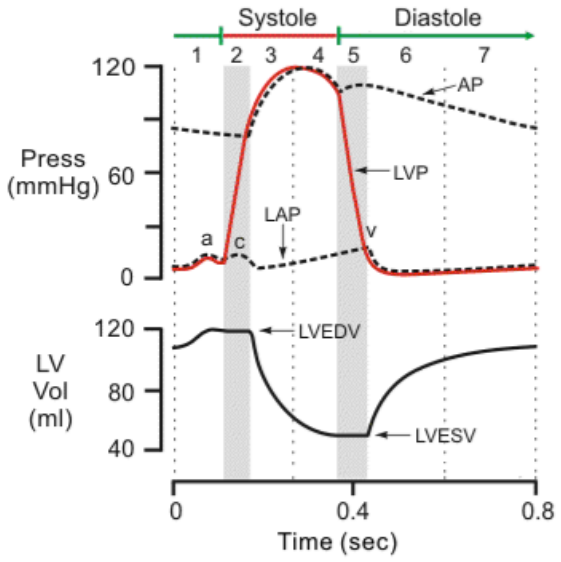

Figure 1-2: Cardiac cycle illustrating the pressure changes in the heart during systole and diastole (Klabunde, 2011)

1.3 The heart valves

The heart has two distinct sides and four chambers for blood circulation. There are four valves located within these chambers and their roles are critical to ensure the proper flow of blood through the heart. When the valves function normally, they act as one-way valves by allowing blood to flow either from one chamber to another or allowing blood to flow out of the heart and preventing it from flowing backwards.

1.3.1 Semilunar Valves

The semilunar valves (Figure 1-3) are composed of three delicate half-moon shape leaflets attached to the fibrous ring located at the base of the aorta (aortic valve) and pulmonary artery (pulmonic valve). They have no cords but consist of flaps of tissue or cusps at the exit from the chamber. The rising of ventricular systolic pressure forces the aortic and pulmonic valve leaflets open. The individual cusp has a margin that is attached to the wall of the aorta or pulmonary artery and another free margin. The cusps are positioned such that a portion of their free margin overlaps the adjacent cusp. This is to prevent backflow of blood into the ventricles throughout the remainder of diastole (Price and Wilson 2003).

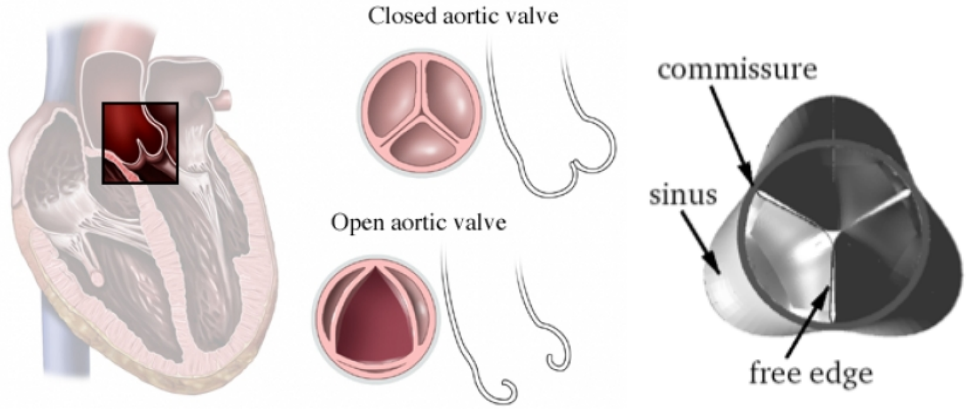

Figure 1-3: Semilunar valves (Carson-DeWitt, 2014, Price and Wilson, 2003)

1.3.2 Atrioventricular valves

The atrioventricular valves (Figure 1-4) are located between the atria and the ventricles. The right AV valve (tricuspid valve) has three leaflets while the left AV valve (mitral valve) has two leaflets; a larger anteromedial leaflet and a smaller posterior leaflet. These two valves are connected by fibrous cords (chordae tendineae) to the papillary muscles in the chamber walls. During

diastole, the leaflets passively open into ventricles and form a funnel like shape. During systole, the leaflets spread out like an open parachute and are pushed upward by rising intraventricular pressure. The contraction of the papillary muscles during systole applies tension to the chordae tendineae which helps to prevent the leaflets from flipping upward into the atria (Price and Wilson 2003).

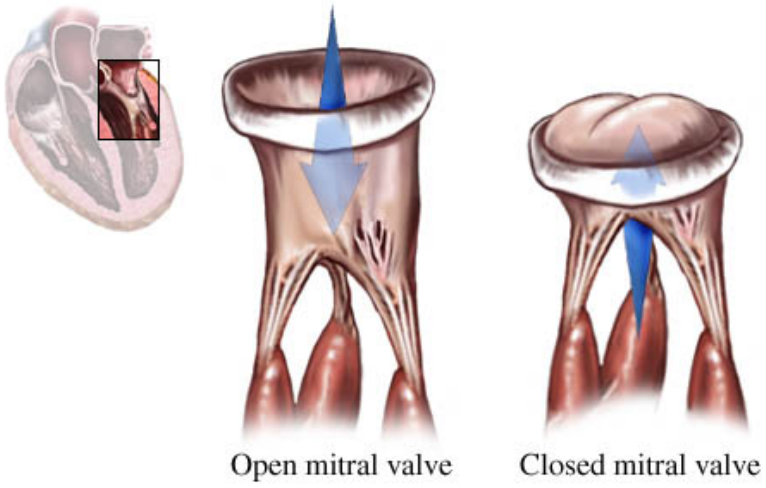

Figure 1-4: Atrioventricular valve (WebMD, 2014)

1.4 Characteristics of Human Blood

The properties of blood are important for experimental and numerical studies because they will affect the behavior of heart and valves. Human blood is a liquid tissue comprising of plasma (55%) and cells (45%), or corpuscles. The various types of corpuscles include the red blood cells, or erythrocytes (99%), platelets, or thrombocytes (0.6-1.0%), and the white blood cells, or leukocytes (0.2%) (Fung, 1984). The red blood cells are bi-concave discs with a flattened center of about 6 – 8 μ m in diameter. Platelets are smaller disc-shaped, 2 -3 μ m in diameter. White blood cells have irregular shapes and typically about twice the size of red blood cells. Plasma is a liquid intercellular material made up of 99% water by weight, 7% plasma proteins, 1% other organic substances and 1% inorganic substances.

Blood is a two-phase non-Newtonian flow medium and its fluidity is measured over a range of shear rates, resulting in a viscosity curve for a blood sample. Figure 1-5 shows the shear-thinning behavior of normal human blood (Baskurt and Meiselman 2003).

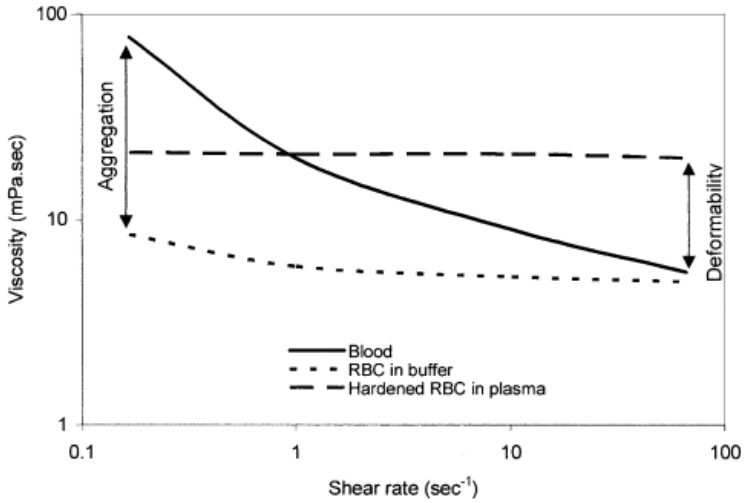

Figure 1-5: Shear rate-viscosity curves for normal blood, blood in protein-free buffer (no aggregation) and chemically hardened blood in plasma (no deformation) (Baskurt and Meiselman 2003)

At low shear rates ($\gamma < 10s^{-1}$), the apparent viscosity is high due to the aggregation of red blood cells. Increased in shear rates will deform the red blood cells and eventually decrease the viscosity (Dupire *et al.,* 2012, Chien, 1975, Merrill, 1969, Rand *et al.,* 1964). Blood viscosity was observed to decrease in tubes with small diameters (< 500 μ m) but since heart valves have much bigger diameter, this effect will not be discussed further (Fahraeus and Lindqvist 1931). In most literature of blood flow in large arteries and heart valves, blood is usually modeled as a Newtonian fluid with constant viscosity value and high shear rate limit viscosity of blood ($\mu = \mu_\infty$) (Nguyen *et al.,* 2012, Borazjani and Sotiropoulos 2010, Govindarajan *et al.,* 2010, Simon *et al.,* 2010, Leo *et al.,* 2006, Ge *et al.,* 2005, De Hart *et al.,* 2003). Non-Newtonian character of the blood is only important when analyzing the shear stress flow characteristics at low speeds. Carreau model is commonly used to model the shear rate dependent viscosity of blood (Morbiducci *et al.,* 2011, Banerjee *et al.,* 2008, Gijsen, 1999a, Gijsen, 1999b, Yasuda and Cohen, 1981, Carreau, 1972).

$$\mu = \mu_\infty + (\mu_0 - \mu_\infty)[1 + (\lambda\dot{\gamma})^2]^{\frac{n-1}{2}} \qquad (1.1)$$

where the viscosity at high shear rate μ_∞ equals the value for the Newtonian model (i.e. 0.0035 Pa.s) while the value at zero shear is $\mu_0 = 0.056$ Pa.s. Also, λ=3.313s, n=0.3568 and $\dot{\gamma}$=shear rate in s^{-1}. (Johnston *et al.,* 2004, Cho and Kensey, 1991).

Other models used for modeling of the non-Newtonian behavior of blood in the low shear rate region are Walburn-Schneck model and power-law model. At large flow speeds in aorta, the differences between the different models are reduced, especially for models such as the Carreau model that limit the change in viscosity at large strains (Siebert and Fodor, 2009).

1.4.1 Platelet Activation and Blood Coagulation

Platelet has been regarded as the pre-eminent cell involved in both physiologic hemostasis and pathologic thrombosis. Platelet activation and blood coagulation are complementary, mutually dependent process in hemostasis and thrombosis. The mechanical force that is most relevant to platelet-mediated hemostasis and thrombosis is shear stress. Fluid shear stress is the force per unit area generated by flow of a viscous liquid (Obi *et al.,* 2009, Kroll *et al.,* 1996). 1 dynes/cm^2 is equal to 0.1Pa. Shear stress is defined as "the force per unit area between laminae" and blood flow can be described as an "infinite number of infinitesimal laminae sliding across one another, each lamina suffering some frictional interaction with its neighbors." (Bird *et al.,* 1960). Exposures to high shear stresses lasting a few milliseconds were known to cause platelet activation (Sheriff *et al.,* 2010, Wurzinger *et al.,* 1985). Since the blood is approximately to behave as a Newtonian fluid in a relatively high flow environment of the arterial circuit, shear stress (τ) in a tubular chamber with radius *r* and flow direction *z* can be represented by

$$\tau = -\mu \frac{dv_z}{dr} \tag{1.2}$$

where $\frac{dv_z}{dr}$ is the local velocity gradient (shear rate) and dynamic viscosity μ is the proportionality constant.

In Figure 1-6, it is shown that blood flow in a tubular chamber generates a parabolic velocity flow profile, with shear rate $\frac{dv_z}{dr}$ is designated as τ. As a result, minimum velocity and maximum shear located at vessel wall, while maximum velocity and minimum shear at the center of the blood flow stream. The difference in the velocity between the laminae of flowing blood generated the shearing forces.

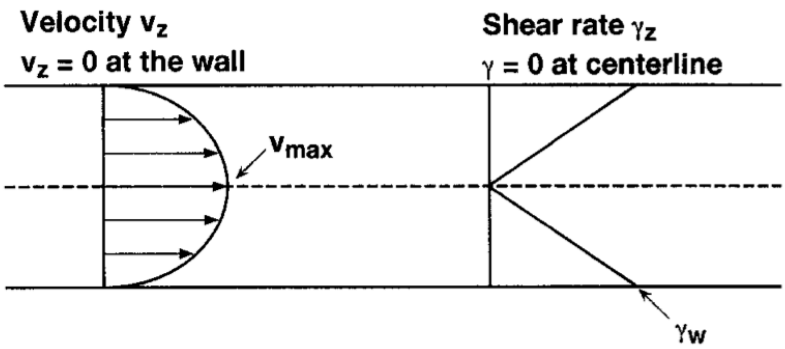

Figure 1-6: Parabolic flow velocity profile of blood in a tubular chamber, with the difference in shear rate (Kroll *et al.,* 1996)

Wall shear stress of Newtonian fluids in a tubular chamber can be calculated as a function of volumetric flow rate as follows:

$$\tau_w = \frac{4\mu Q}{\pi r^3} \quad (1.3)$$

where μ is dynamic viscosity, Q is the volumetric flow rate and r is radial distance of the tubular chamber. The shear forces *in vivo* based on this formula can be found in Table 1-1.

Table 1-1: Typical Ranges of Wall Shear Rates and Wall Shear Stresses, with viscosity is 3.8 x 10^{-6} m^2s^{-1} (Kroll *et al.,* 1996)

Blood Vessel	**Wall Shear Rate (s^{-1})**	**Wall Shear Stress (dynes/cm^2)**
Large arteries	300 – 800	11.4 – 30.4
Arterioles	500 – 1,600	19.0 – 60.8
Veins	20 – 200	0.76 – 7.6
Stenotic Vessels	800 – 10,000	30.4 - 380

An *in vitro* study found that the maximum shear stress for human blood for platelet activation to occur was 300 dynes/cm^2 (Lu *et al.,* 2013). The expressions of proteins, which influence the aggregation of platelets, have been shown to be controlled by physiological shear. Blood elements in turbulent flow were found to encounter higher shear and rate of collision with the wall of the chambers. This led to prolonged contact with the surface. As a result of turbulent flow, the higher collision rate between activated and/or damaged blood elements caused by flow eddies and recirculation flow formed near the wall chambers (Tokarev *et al.,* 2011, Smith *et al.,* 1972).

1.5 Heart valve diseases

Valvular diseases cause abnormalities in blood flow across the cardiac valves. In normal valves, the two key characteristics are unimpeded flow and unidirectional flow. The valves open when the chamber upstream to the valve exceeds the pressure in the chamber or vessel downstream of the valve. It closes when pressure downstream of the valve exceeds pressure in the upstream chamber. When a valve is not working, it is due to several causes. Regurgitation happens when the valve leaflets fail to close properly which allow backward flow (also known as insufficiency and incompetence). Such condition causes the heart to pump harder and become less efficient over time. Stenosis occurs when the valve orifice becomes restricted, allowing only a small amount of blood through the valve due to the resistance to forward flow (Price and Wilson, 2003). There are several causes of heart valve diseases, such as (American Heart Association, 2012b, Cebi and Bozkurt, 2004, Goldsmith *et al.,* 2002):

- Rheumatic fever – This heart disease is caused by one or more attacks of rheumatic fever, which is an inflammatory condition that damages the heart, particularly the heart valves. The damage is caused by an autoimmune response which may result in the weakening of heart muscle, damaging the sac enclosing the heart or scarring of valves. Sometimes, the valves are scarred badly that they do not open or close normally.
- Congenital valve disease - Inborn defects of connective tissue and malformed leaflets or have leaflets that are not attached correctly.
- Ischemic heart disease – The narrowing of the coronary arteries cause heart ailments and reduce the blood supply to the heart.
- Infective endocarditis – The inner lining of the heart muscle and heart valves (endocardium) is infected by bacteria, viruses, fungi or other infectious agents.
- Atherosclerosis – Dysfunction or rupture of the papillary muscles as a result of thicken and stiffening of arteries walls due to plaques.
- Other causes – Heart valve diseases may be a result of other heart disease such as cardiomyopathy (heart muscle disease), heart attack, connective tissue diseases, aortic aneurysms and high blood pressure.

Generally, both the mitral and aortic valves on the left heart have a higher failure rate compared to the valves on the right heart. The mitral and aortic valves experience blood pressure variations of 0 – 120 mmHg and 80 – 120 mmHg respectively. Meanwhile, the blood pressure variation on the right chambers of the heart is typically less than 40 mmHg.

1.5.1 Type of heart valve diseases

There are several types of valvular diseases (Curtin and Griffin, 2008, American Heart Association, 2012b, Vahanian, 2012); mitral stenosis, mitral valve prolapse, mitral regurgitation, aortic stenosis, aortic regurgitation, tricuspid valve disease, pulmonic valve disease and compound valvular disease.

- Mitral stenosis – The mitral valve orifice is narrowed that results in impedance of filling of the left ventricle during diastole. This build-up of pressure gradient across the valve during diastole causes an increase in left atrial and pulmonary venous pressures. It is usually caused by rheumatic heart disease.
- Mitral valve prolapse – A common condition that causes the leaflets of the mitral valve to flip back into the left atrium during the heart's contraction. The tissues of the valve become stretchy and abnormal, causing the valve to leak.
- Mitral regurgitation – During systole, the blood leaks from the left ventricle into the left atrium. This disease is usually caused by various mechanisms related to structural or functional abnormalities of the mitral apparatus, adjacent myocardium, or both. During each heartbeat, the volume in the left ventricle is overloaded due to the significant mitral regurgitation as it has to take into account the stroke volume. To compensate for this, the left ventricle dilates and becomes hyper dynamic.
- Aortic stenosis – The aortic valve opening narrows and restricts the blood flow from the left ventricle to the aorta. This affects the pressure in the left ventricle, as the ventricle must work harder to pump blood through the narrow valve opening into the aorta. The thickened wall allows less room for an adequate amount of blood to be supplied to the body.

- Aortic regurgitation – During each diastole, the aortic valve leaks back into the left ventricle, resulting in an increase in volume and pressure of blood. The wall of the ventricle then thickens and becomes less effective. Eventually, the heart may fail.
- Other types of heart valve diesases: tricuspid and pulmonary stenosis and regurgitation.

1.6 Treatment

1.6.1 Medication Therapy

The clinical progression of mitral valve disease is gradual and prolonged. However, the major function of drugs administered in valve disorder is to reduce the severity of symptoms and to prevent further complications. The medical therapy is not able to cure severe valve diseases. Such medication therapy consists of (Price and Wilson, 2003):

- Diuretics – To lower the salt and fluid levels in the body and to reduce intra and extravascular volumes. It is also used to reduce congestion and swelling by decreasing the volume of blood that needs to be pumped.
- Digoxin – To reduce the ventricular response to atrial fibrillation or to increase contractile force in the presence of mitral regurgitation
- Anti-dysrhythmics – To maintain a regular heartbeat and prevent the occurrence of atrial fibrillation.
- Vasodilators – To dilate venules and peripheral arterioles, to reduce afterload by decreasing regurgitant flow and increasing forward blood flow. This therapy is used to treat congestive heart failure associated with heart valve disease (typically valve insufficiency).
- Anticoagulants – To prevent formation of blood clots especially when systemic embolization becomes a threat.

1.6.2 Balloon valvuloplasty

This technique, also known as catheter balloon valvotomy, is used increasingly as an alternative to surgical repair. Balloon valvuloplasty is a non-surgical procedure, performed in which a long balloon catheter with a small-deflated balloon is inserted through the skin into the blood vessels in the groin and guided into the chambers of the heart. A tiny hole is created in

the septum to provide an opening to access the left atrium. The balloon is inflated, which stretches the valve open to relieve some valvular obstructions. However, this technique will not cure valve diseases (Vahanian, 2012, Dumont, 2005).

1.6.3 Surgical Repair

Techniques of repairing deformities of the mitral valve have been improved tremendously in recent years. Mitral valve repair is generally performed to treat mitral regurgitation and mitral stenosis to remove calcium deposits and repair leaflets so that they close normally. Repair of the valve can involve lengthening and shortening the chordae tendineae or repositioning of the chordae. A prosthetic ring is inserted to the valve annulus to stabilize and repair the valve orifice to support an enlarged annulus. Calcification and cusp retraction appear to be the main adverse factors for repair procedures (Vahanian, 2012). Surgical repair is associated with steep learning curve and resulted in higher complication rates than desired.

1.6.4 Valve Replacement Surgery

Valve replacement is recommended when the valve is severely damaged or when aortic regurgitation and calcific aortic stenosis is observed (Vahanian, 2012). Existing commercial prosthetic heart valve designs can be classified into two groups: mechanical heart valves and bioprosthetic, or tissue valves. The latter is made from a combination of synthetic materials or chemically treated animal tissue mainly porcine in origin, whereas the former is manufactured entirely from synthetic materials. There are several essential requirements of an artificial heart valve design (Ghanbari *et al.,* 2009):

- The valve must fit well into the host anatomy.
- Minimum resistance to the forward flow by the valve leaflets and open at a minimum trans-valvular-pressure difference.
- Minimize thrombogenicity and damage to blood cells.
- Guarantee appropriate sealing of the leaflets in the closed position to minimize backward flow.
- Low peak stress on the valve components during cardiac cycle to ensure durability and minimal changes to the geometric features.

1.8 Types of Artificial Heart Valves

1.8.1 Mechanical Heart Valves

In the 1960s, Dr. Charles Hufnagel performed one of the earliest successful mechanical heart valve surgeries where six of the eight patients who received a caged ball heart valve survived the operation (Hufnagel *et al.*, 1966). Lots of progress has been made in the last 50 years in the development of mechanical heart valves to improve its performance in reducing hemolysis and thromboembolic complications. Different types of mechanical heart valves designs are shown in Figure 1-7.

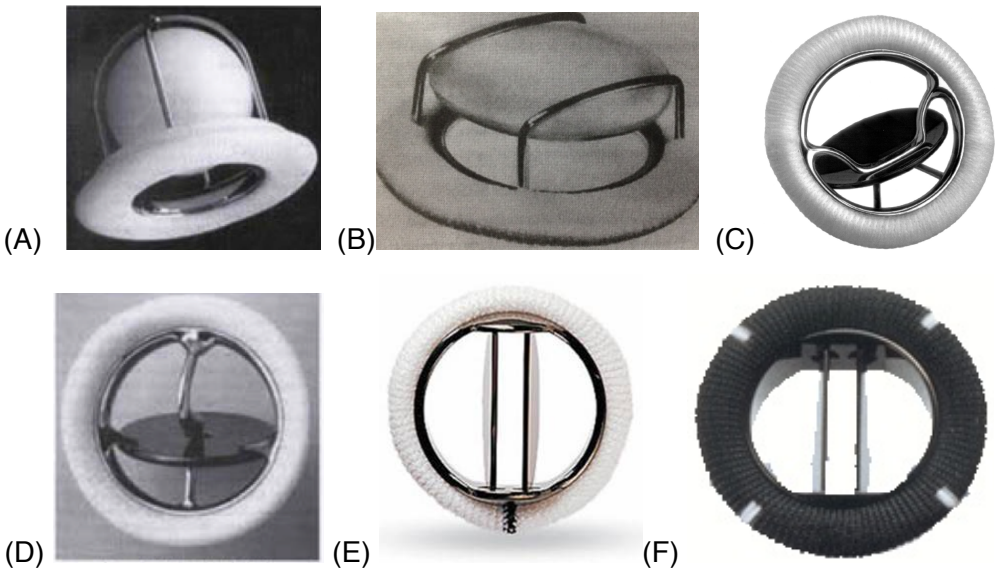

Figure 1-7: Types of mechanical heart valves (A) Starr-Edwards Caged ball valve, (B) caged disc heart valve, (C) Björk-Shiley tilting disc valve, (D) Medtronic Hall tilting-disc (single-leaflet) valve, (E) St Jude Medical (SJM) bileaflet valve, and (F) CarboMedics bileaflet valve (Matthews, 2011, Chandran *et al.,* 2012)

The materials used in these valves are made from pyrolytically coated carbon disc, which is attached to a polyester sewing cuff. The most commonly used heart valve today is the bileaflet mechanical heart valve. This design overcomes two major drawbacks of the earlier designs such as the high profile configurations and excessive occlude-induced turbulence in the flow through and distal to the valve (Chandran *et al.,* 2012). BMHV would be the focus in this study. Existing bileaflet models include St Jude Medical (SJM) Valve, CarboMedics Valve and ATS Open Pivot Valve. Figure 1-8 shows the typical structure of a BMHV, which consists of two approximately semi-circular, hinged, pyrolytic carbon occluders leaflets.

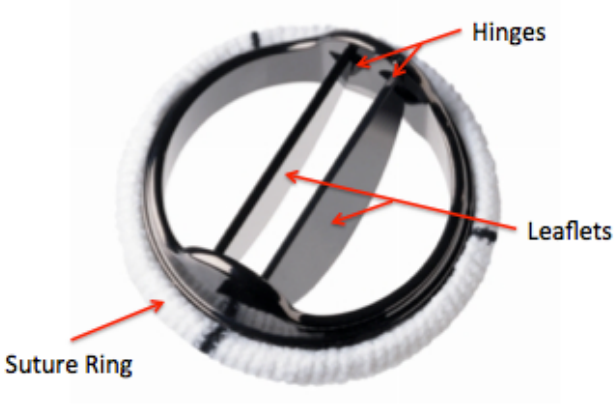

Figure 1-8: Structure of Bileaflet Mechanical Heart Valve (Pick, 2014)

This design allows the leaflets to pivot within the hinge made in the valve orifice housing. The leaflets open to an angle of 70° - 85° in fully open position, and provide minimal disturbance to the flow. The CarboMedics Valve is made of pyrolite that is durable and thromboresistance. Its two leaflets are radiopaque, semicircular, and open to a maximum angle of 78°. The SJM valve has increased internal orifice area compared to CarboMedics Valve available for flow, which offers an improved bulk flow hemodynamics. The ATS Open Pivot valve is different in the pivot design compared to SJM valve by inverting the pivot mechanism, which expose the pivot to bulk forward flow. Typical bileaflet valve designs comprise of an extension of leaflet fitting into a housing recess where the tendency of thrombus occurrence is high.

One major drawback associated with the implantation of mechanical heart valves is the need for daily chronic anti-coagulation therapy to reduce the risk of thrombosis and thromboembolic complications. Patients with such therapies are exposed to an increased risk of bleeding, infection, and/or autoimmune response (Walker and Yoganathan, 1992). Blood flow through mechanical prostheses can lead to high turbulent stresses that may damage and/or activate blood elements and initiate platelet aggregation. Platelet aggregation can lead to thrombus formation with disastrous consequences for the patient. Thrombi may even detach from the valve and become lodged in a downstream blood vessel, thus reducing or even cutting off the blood supply to vital tissues. Moreover, the hemodynamics of mechanical heart valve differs significantly from that of natural healthy heart valve.

1.8.2 Trileaflet Mechanical Heart valves

The prosthetic trileaflet mechanical heart valves strive to combine the best features of tissue and mechanical valves, which focus on improving the flow characteristics of tissue valves and increase the durability of mechanical valves. Trileaflet mechanical heart valves (TMHVs) are similar to natural ones in which the trileaflet design ensures central blood flow with a decreased in disturbance of blood due to the steady movements of the leaflets. The valve closure will also be similar to the native valves where the vorticity at the aortic root sinus will push the aortic valve leaflets in during diastole. The fan-shaped leaflets are curved to form a circular central orifice and maximize the EOA as can be seen in Figure 1-9. There are three small projections with smooth round sockets on both sides that serve as the leaflet hinges on the annulus ring. Triflo mechanical heart valve (Triflo Medical, Inc) is an experimental trileaflet prosthesis with three leaflets, nozzle-shaped and streamlined configuration valve orifice. The leaflet configuration provides a soft and early closure mechanism which is similar to the native aortic valve. The features of the valve include minimal regurgitation, low tendency for cavitation and streamlined design which minimizes flow separation. However, more extensive studies are required to study the long-term implantation of trileaflet mechanical heart valves in patients.

(A) 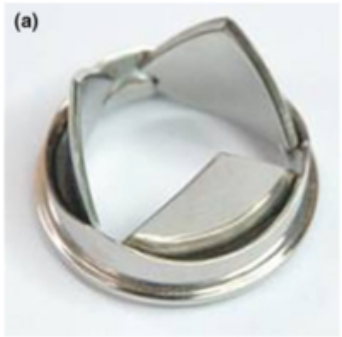

(B) 

Figure 1-9: (A) Trileaflet mechanical heart valves studied by Li and Lu (2012) and (B) Triflo Medical mechanical heart valve

1.8.3 Tissue Valves

An alternative to mechanical valves is using tissue valves that utilize the concept of a trileaflet configuration with one central orifice that mimics the design of the native valve. These valves have a lower potential for blood element damage than their mechanical counterparts. Porcine (manufactured from pig aortic valves) and bovine (manufactured from cow aortic valves)

valves are non-thrombogenic but are less durable compared to mechanical heart valves. The valve tissue is chemically stabilized and a frame made from synthetic materials supports the valve structure. Nevertheless, the mechanical properties of tissue valves appear to have limited durability, and they are prone to calcification due to the immune response (Manji *et al.,* 2014). Often, implanted tissue valves do not last for more than fifteen years, and reoperation is necessary. These valves tend to be recommended for elderly patients or when anti-coagulation is not to be used. An example of a tissue valve is shown in Figure 1-10.

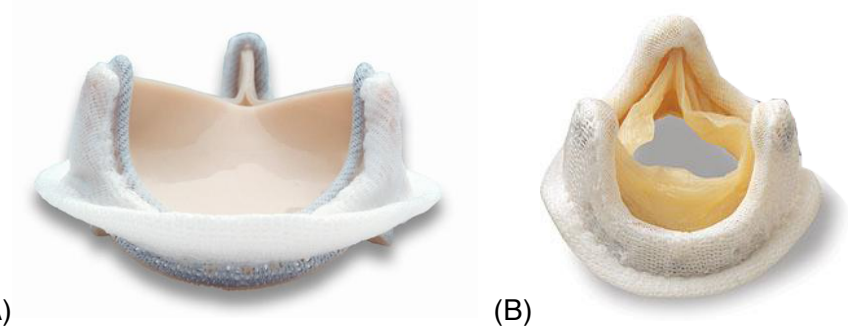

(A) (B)

Figure 1-10: Tissue valve by (A) Perimount Aortic Valve, (B) Mosaic Tissue Valve (Kardon, 2010)

1.8.4 Transcatheter Valves

The first percutaneous transcatheter aortic valve was implanted into the human in 2002 (Cribier *et al.,* 2002). Transcatheter heart valve (THV) replacement is performed on heavily symptomatic patients who are unable to undergo open-heart surgery. THVs leaflets are of animal origins sutured within a crimpable metallic stent frame (Narayan and Sharma, 2012). Usually, these stents may be coated with a layer of expanded polyfluoroethylene (ePTFE) to minimize paravalvular (Lozonschi *et al.,* 2008). The native heart valve is not removed but is pushed to the walls of the heart by the artificial valve. So far, several designs have been created and implanted into animal studies as shown in Figure 1-11. The design by Boudjemline *et al.,* (2005) consists of bovine jugular venous valve mounted on the central part of a 2-discs nitinol stent. Meanwhile Bai *et al.,* (2010) developed a similar valve but used the porcine pericardial leaflets instead. The double-edge design of its nitinol stent functioned as an anchorage without the use of traumatic hooks.

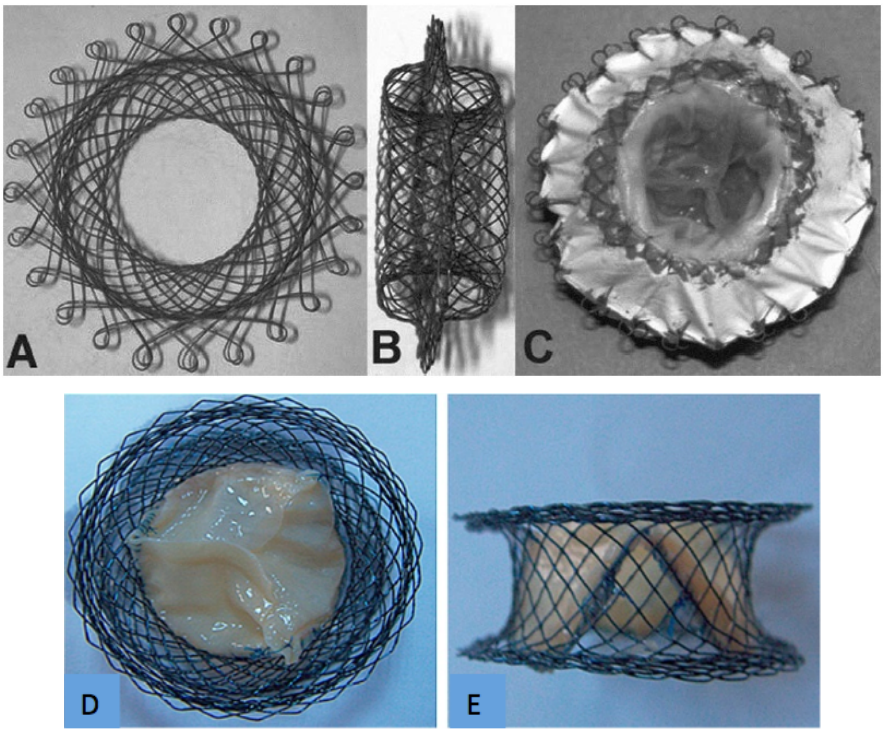

Figure 1-11: Top (A) and lateral (B) view without the PTFE coating and leaflets, (C) Valve with PTFE coating and bovine jugular venous valve sutured onto the central tubular section by Boudjemline *et al.,* (2005), (D) and (E) Transcatheter tricuspid valve by Bai *et al.,* (2010)

1.8.5 Polymeric Heart Valves

There are attempts to develop leaflet valves from man-made materials such as block-copolymers or modified polyurethanes. The polyurethane (PU) trileaflet polymeric heart valve has been researched as an alternative to prosthetic heart valve (Hyde *et al.,* 1999). The design is based on the natural aortic valve and is appealing from a hemodynamic perspective. Although the polymeric heart valve design is still in a developmental stage, preliminary studies have shown good forward flow hemodynamic properties, which is equivalent to that of a tissue heart valve and promise better durability comparable to that of a mechanical heart valve (Kidane *et al.,* 2009, Gallocher *et al.,* 2006, Daebritz *et al.,* 2004). However, other animal trials using polymeric valves have reported problems mainly related to thrombus formation occurring along the stent region of the valve and tearing of the leaflets (Wheatley, 2001). In addition, results of long term *in vivo* evaluations have suggested that calcification could be a limiting factor to long-term function of polymeric valves. The leaflets and basal attachments, such as the commissural region of the polymer valves, have been shown to undergo extrinsic calcification associated with surface micro thrombi that appear to be

independent of structural defects, suggesting that the flow characteristics inside the polymeric valve may be a contributor to the observed blood clots. An example of polymeric heart valves made from polycarbonatuerethane (PCU) is shown in Figure 1-12.

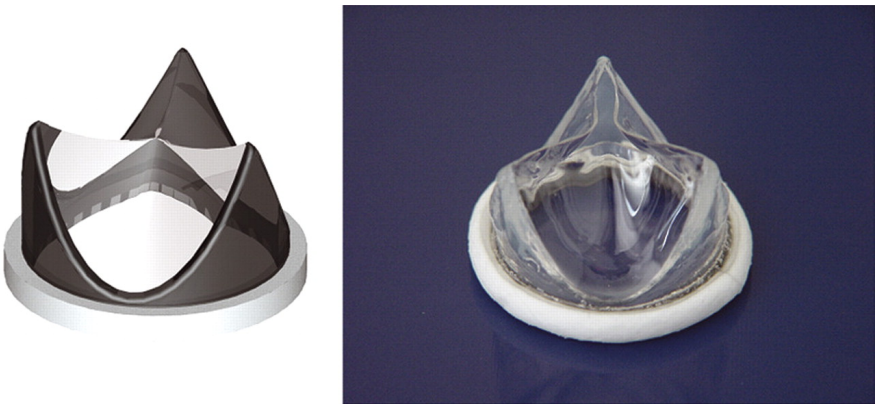

Figure 1-12: The ADIAM® PCU valve for aortic position (Daebritz et al., 2004)

1.9 Complications with Artificial Heart Valves

There is no ideal heart valve currently available in the market. These artificial heart valves are still exposed to risks of thrombosis and thromboembolism, pannus tissue overgrowth, infection, anti-coagulant related hemorrhage, and valve failure due to material fatigue or chemical change (Whitlock *et al.,* 2012, Starr *et al.,* 2002, Yoganathan, 2000, Korossis *et al.,* 2000,).

1.9.1 Valve Thrombosis

Valve thrombosis occurring in patients with hemodynamic instabilities will decrease the disc movement and reduce the orifice area by encapsulating the valve. In most cases, the thrombus formation prevents the valve from opening or closing properly, leading to stenosis and flow regurgitation. In Figure 1-13, the bilateral thrombus were found at the hinge mechanism area that has led to both leaflets to be fixed in the slightly open position in a SJM valve while a massive thrombus fills the valve pockets on the outflow area of the tissue valve, leading to prosthetic valvular stenosis.

(A) 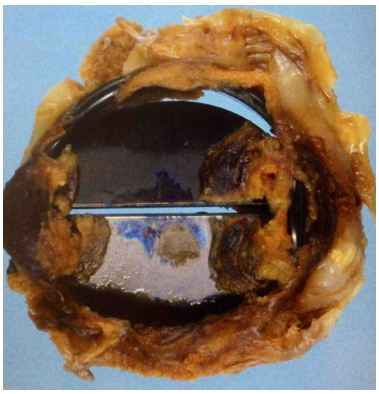 (B) 

Figure 1-13: Thrombus formation on (A) SJM bileaflet valve,
(B) Tissue porcine valve (Rose 2008)

1.9.2 Structural Failure

The risk of embolization increases when implanted with artificial heart valves. Fracture embolization of a mechanical valve is uncommon since the valve is durable and semi-permanent. However, if it fails, it is potentially fatal and will lead to acute severe valve regurgitation and subsequently heart failure. Nevertheless, leaflet fracture embolization, which relates to mechanical failure, may occur due to the structural fragilities. A case of fatal Edward-Duromedics mechanical mitral valve leaflet fracture embolization implanted 20 years ago was reported in Korea (Lee *et al.,* 2011). The patient suffered from severe acute heart failure and shock. Only one leaflet remained as seen in Figure 1-14 and the patient died due to low cardiac output and cardiogenic shock. Another unique example of mechanical heart valve failure was the Björk-Shiley convexoconcave valve, which was implanted in approximately 86,000 patients between 1978 and 1986. The design resulted in an unanticipated increase in stress which led to outflow strut fracture and disc migration (Blot *et al.,* 2005).

Figure 1-14: Damaged 31mm Edwards-Duromedics mechanical valve showing the remaining leaflet (Lee *et al.,* 2011)

Structural failure for tissue heart valves occurs usually within 10 – 15 years. When the valves fail, it is usually due to a rupture or tear in one or more of the valve leaflets and/or the calcification of the leaflets. The failure of tissue valves is particularly high in patients below 40 years old. In a case reported in Japan, a patient was admitted with acute high failure. She had been diagnosed as having severe mitral stenosis and had undergone valve replacement with a 27mm Carpentier-Edwards mitral pericardial valve. The cause of the severe mitral regurgitation was found to be a tear in one of the leaflets of the tissue valve, as seen in Figure 1-15. Calcification was also observed on the leaflets (Ito *et al.,* 2011).

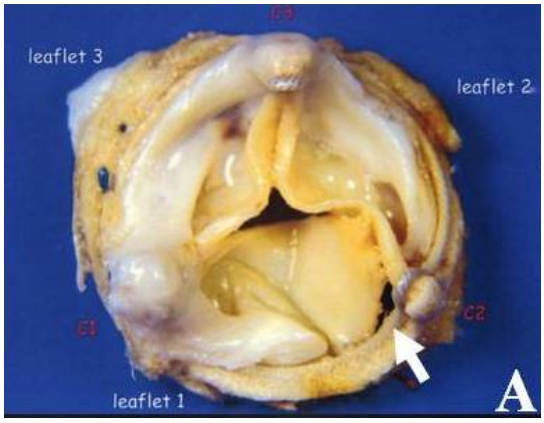

Figure 1-15: A view showing a tear in leaflet 1 (Ito *et al.,* 2011)

1.9.3 Regurgitation

Tissue valves may cause a small amount of regurgitation due to incomplete closing of the leaflets. A patient was reported to have hemolysis and transient prosthetic valve regurgitation occurred in the early stage after valve replacement with a Carpentier-Edwards pericardial bioprosthetic (Sezai *et al.,* 2005). On the other hand, paravalvular regurgitation is an uncommon but important complication resulting from valve replacement surgery. The reported incidence ranges from 18–48% of patients with a mitral or aortic prosthesis. Generally, the leaks are mild and do not progress beyond a two- to five-year follow-up (Rallidis *et al.,* 1999, O'Rourke *et al.,* 2001). Patients with mild to moderate paravalvular leakage may have a mild hemolytic anemia while in serious cases; patients may have severe anemia or heart failure. Such cases should be treated with surgical procedures or valve replacements.

1.9.4 Calcification

Calcification remains a major cause of clinical failure when deposits of calcium phosphates or other calcium-containing compounds form on cardiovascular devices. The causes of heart valve calcification are due to host factors, mechanical effects, and fixation conditions. Calcium phosphates deposit and occur more frequent at regions of stress concentrations in cusps (Vyavahare *et al.,* 1997). The hemodynamic function of the polymeric heart valves will be affected when high calcium phosphates deposit on the valve surface. This often leads to valve obstruction and subsequently stiffening of leaflet cusps (Otto, 2002). Studies have shown that higher tendency of calcification occurs at the commissural region of the valve leaflets. This is mainly due to the high deformations and strains that occur in this region due to the valve movements (Corden *et al.,* 1995). In addition, the abnormal flow patterns due to elevated shear stresses may induce leaflet calcification and tear in polymeric and tissue valves (Dasi *et al.,* 2009). Figure 1-16 shows the calcification of a Hancock porcine aortic valve prosthesis which produced severe mitral stenosis.

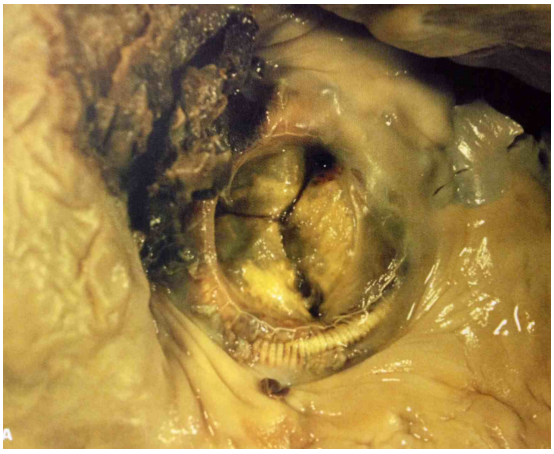

Figure 1-16: Calcification of a Hancock porcine valve (Rose, 2008)

With all these problems associated with existing artificial heart valves, it is difficult to create replacement valve with same anatomical and functional characteristics of a native valve. Nevertheless, polymeric valves can be designed in any shape and with different types of materials. There have been major factors such as long term biocompatibility issues and material degradation, which limit the success of polymeric heart valves. Even though there are no polymeric heart valves currently available in the market, polymeric materials are increasingly researched in heart valves development

because of their wide variety of functions. Modifications of materials would result in substantial improvement in the long-term biostability and biocompatibility. Improving the valve design can reduce the stresses in the leaflets. There have been improvement works to reproduce the behavior of native valves such as the long-term performance and durability (Kuan *et al., 2*011).

1.10 *In vitro* Study of Valve Performance

In vitro studies are conducted to determine the performance of artificial heart valves. Many of these valves have been tested *in vitro* under pulsatile flow conditions for the hydrodynamic functions.

In vitro studies have shown that a centralized flow with a relatively flat profile comparable to that of tissue and native heart valves was generated by polymeric heart valves. The flow patterns of four different trileaflet polyurethane heart valves were compared to the Hancock porcine heart valve and Ionescu-Shiley pericardial valve by measuring the down-stream velocity distributions using Laser Doppler Anemometry or also known as Laser Doppler Velocimetry (LDV) (Herold *et al.,* 1987). It was observed that the velocity distributions at peak systole were very similar between the polyurethane valve and Hancock prosthesis. Both flow fields could be characterized as a triangular jet-flow, with the recirculation areas located near the right aortic wall downstream of the stent post and in the opposite sinus cavity. However, flat plug type flow was observed for the Ionescu-Shiley valve. The flow was positive with recirculation in the aortic sinus cavity and one small transient recirculating vortex near the right aortic wall. Overall, the flat flow profile of polyurethane valves was similar to those of the native and tissue valves with vortex formation observed behind the leaflets in the sinus cavity.

D'Souza *et al.,* (2003) characterized the turbulence and velocity waveforms distal to several trileaflet polymeric heart valves with varying degrees of stenosis. They observed that the orientation and shape of the spatial velocity profile in a polyurethane heart valve depicted the effect of the constriction

caused by the valve leaflet in a similar manner to that observed in tissue valves.

In another study, the flow dynamics of two polyurethane valves were investigated; one with leaflets bound to the edge of the supporting stents (PU-I) and the other with leaflets mounted outside the stents (PU-II) (Chandran *et al.,* 1989). The PU-II valves had larger inlet EOA diameter with a smaller tissue annulus diameter, which provided more unobstructed area for blood flow. Such valve design was also found to reduce the maximum turbulent shear stresses distal to the valves, which appeared more advantageous. Furthermore, the turbulent shear stress in the PU-II valve was half that in the PU-I valve showing that the increase in orifice diameter can help reduce the turbulent shear stresses and corresponding damage to blood elements. When compared to tissue valves, polymeric valves have larger turbulent shear stresses. The orifice diameters in polymer valves are usually smaller than those in tissue valves, and as a result, polyurethane valves have larger observed velocity magnitudes and larger velocity gradients than the tissue valves.

There were studies which have shown that the trileaflet design was more efficient than double or quadruple arrangements (Cheeta and Llyod 1980, Jansen *et al.,* 1991, Leat and Fisher 1995, Mackay *et al* 1996), and that the maximal stresses in these trileaflet configurations were found near the commissural attachment, which was consistent with other synthetic and tissue valves (Leat and Fisher 1995). Corden and team calculated the bending stresses and strains at the free leaflet edge by measuring the curvature and the study showed that the highest curvatures occurred at the commissural regions when the valves were fully open (Corden *et al.,* 1995).

There are several flow visualization techniques used to measure the flow profiles of *in vitro* studies of artificial heart valves. One flow visualization technique includes the hydrogen bubble techniques which is based on the electrolysis of water. Hydrogen bubbles are formed at the cathode and oxygen bubbles are formed on the anode when electrodes are inserted in the fluid and a voltage is applied to the electrodes. All kinds of flow streak lines

and time can be obtained by isolating some parts of the electrodes and by varying the voltage level. Another technique is through photochemical reaction where a visible tracer (dye) is produced in the fluid by focusing a laser to produce a dye along a line in a fluid. Typically, the fluid should not be disturbed at all (Post and van Walsum, 1993).

Laser Doppler Velocimetry uses the Doppler shift in a laser beam to measure the velocity in fluid flows. Two beams of monochromatic and coherent laser light intersect in the flow field of the fluid to be measured. Usually, the two beams are obtained by splitting a single beam. This ensures the coherence between the two beams. Particles in the fluid will reflect light, which is then collected by a photo detector. One disadvantage of LDV is that the sensors are range-dependent and have to be calibrated precisely. LDV only allows measurement of velocity only at a particular point

The most commonly used flow visualization technique is Particle Image Velocimetry (PIV). It is a technique to provide instantaneous velocity vector measurements and related properties in a cross-section of a fluid flow. The fluid is seeded with sufficiently small tracer particles, which are assumed to follow the flow dynamics. The flow is illuminated with a sheet of double-pulsed laser and the movement of particles between the pulses is measured. The most commonly used laser sources is the pulsed Neodyme-YAG (Nd:YAG) laser, doubled in frequency at 532nm. The pulse duration Δt is usually 5-10ns, and repetition rate is on the order of 10Hz. The laser energy used in PIV typically can reach 400 mJ/pulse. The PIV systems are made of two independent laser cavities. However the laser sheets illuminate the exact same area by superimposing the laser beams in the near and far-fields. A camera is used to capture the images, typically digital image recording via a Charge-Coupled Device (CCD) sensor, which converts photons to an electric charge based on the photoelectric effect. The CCD sensor consists of many individual sensors that are arranged in a rectangular array, with size of about $10\times10\,\mu$m (Brossard *et al.,* 2009). The captured motion of the seeding particles will be used to calculate speed and the velocity field of the flow. PIV can produce two or three dimensional vector fields. The individual particles

within an image can be identified with PIV. Figure 1-17 shows the concept of PIV.

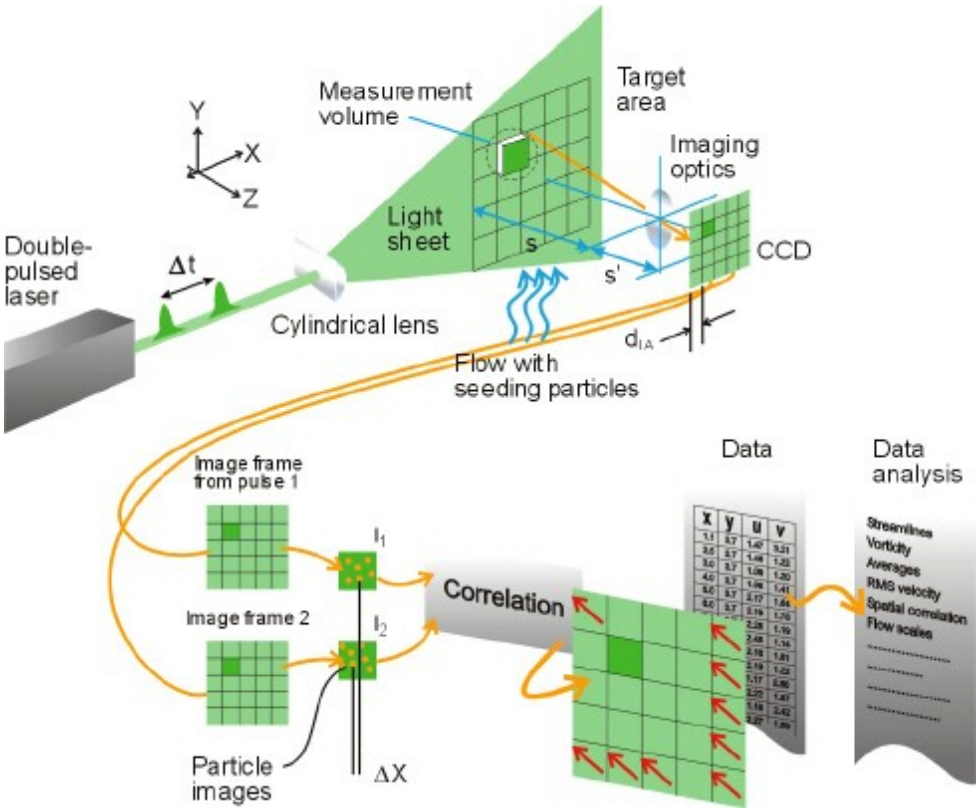

Figure 1-17: PIV system (Dantec Dynamics, 2011)

Leo and colleagues performed LDV and PIV studies of three Aortech polymeric heart valves investigating the effect of commissural design and leaflet thickness on the hemodynamic performance of the heart valves (Leo 2005). These studies indicated that leaflet thickness and commissural design could influence the thrombogenic potential of tri-leaflet polymeric valves. The studies, as seen in Figure 1-18, identified the following regions of high shear stress and high velocity flow in the three polymeric heart valves: 1) the leakage jet inside the valve during diastole; 2) the trailing edge of the valve; 3) the vortex ring surrounding the forward jet during the acceleration phase; 4) the edge of the central orifice jet, which extended from the inside of the valve into the distal part of the flow chamber; and 5) the distal region of the flow chamber where turbulence mixing occurred during systole.

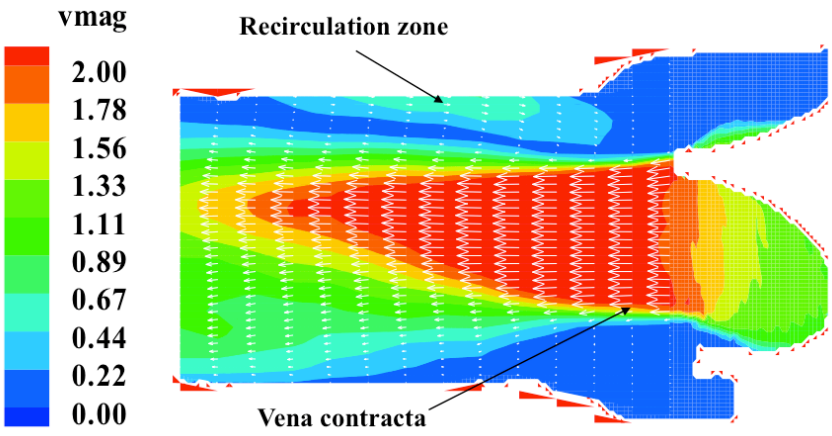

Figure 1-18: Velocity fields at the center plane of an Aortech polymeric heart valve during peak systole. Velocity central orifice jet of 2.3ms^{-1} was observed issuing from the valve orifice with flow separation occurring at the trailing edge of the leaflet. Plug flow profile was evident at the immediate downstream of leaflet trailing edge and became more parabolic at the distal end of the flow chamber (Leo, 2005)

Using flow visualization, several studies have demonstrated that trileaflet tissue valves produced jet-type flow fields like those observed in the polymeric heart valves (Woo *et al.,* 1983, Yoganathan *et al.,* 1983, Yoganathan *et al.,* 1986). Under the same CO, valves with larger orifice sizes tend to have reattachment points closer to the trailing edge of the valve leaflet. Reattachment of the orifice jet occurred at different downstream locations in the upper and lower parts of the flow chamber. This observation was attributed to the asymmetric nature of the central orifice jet.

Table 1-2 compares the Reynolds shear stress values and peak velocities of previous valve studies and the polymeric valve experiments in the study by Leo (2005). The peak Reynolds shear stress levels at downstream of all the valves during systole was found to be between 1,000 – 2,900 dynes/cm^2. In the study, typically, elevated Reynolds shear stress levels were observed along the edge of the central orifice jet and spread out over to a wider area further downstream from the valve as the energy of the central jet becomes dissipated. Reynolds shear stress in excess of 200 dynes/cm^2 were producd by all the aortic valves during the majority portion of systole. Therefore, it was obvious that the elevated Reynolds shear stress levels could potentially lead to sub-lethal and/or lethal damage to the blood elements (Leo, 2005).

Table 1-2: Comparison of the velocity magnitudes and Reynolds shear stresses from different trileaflet valve designs (Leo 2005)

	Effective annular orifice diameter (mm)	*Maximum phase averaged velocity during systole (ms^{-1})*	Maximum phase averaged shear stress during systole ($dynes/cm^2$)
Carpentier-Edwards 2625 porcine valve (27 mm)	23.0	3.3	4,500
Hancock modified orifice porcine valve (25 mm)	21.8	3.0	2,900
Ionescu-Shiley pericardial valve (27 mm)	23.4	2.3	2,500
Carpentier-Edwards 2650 porcine valve (27 mm)	25.0	2.0	2,000
Hancock II porcine valve (27 mm)	24.0	2.6	2,500
Hancock pericardial valve (27 mm)	23.3	1.8	2,100
Ionescu-Shiley low profile pericardial valve (27 mm)	23.0	2.2	2,400
Carpentier-Edwards pericardial valve (27 mm)	25.7	1.8	1,000
Abiomed (21 mm)	18.6	3.7	4,500
Abiomed (25 mm)	22.8	2.2	2,200
Aortech prototype A (23 mm)	23.0	2.8	8,347
Aortech prototype B (23 mm)	23.0	2.5	1,725
Aortech prototype C (23 mm)	23.0	2.3	1,327

1.11 *In vivo* Valve Performance on Animal Models

Pre-clinical assessment for artificial heart valves includes *in vivo* testing in animal models. Animal models are good at evaluating anti-calcification strategies in polymeric heart valves. Typical animal studies involve both subdermal (rat) and circulatory (sheep or calf) implants. Sheep is widely use

to investigate thromboembolic complications as it is generally less thrombogenic than humans. Meanwhile, in an extreme calcification model, a growing calf model is used as it is more thrombogenic than sheep, due to the extreme hemodynamic workload and fast growth (Schoen *et al.,* 1992).

In animal studies performed in the 1950s, polyurethane trileaflet valves were implanted in dogs. However, most dogs only survived for a few hours post operation (Akutsu *et al.,* 1959). Years later, a study on calves were conducted by comparing various polyurethane valves with two Ionescus-Shirley bovine pericardial valves. The study demonstrated that polyurethane valves have similar advantages to tissue valves in term of thrombus formation (Herold *et al.,* 1987). However, all explanted valves were calcified and thrombosed, which was likely due to the severe hemodynamic and surface alterations by the calcium deposits on the upstream and downstream sides of the leaflets.

Polyurethane valves were assessed *in vivo* in a growing sheep model and showed good comparison with tissue valves and other mechanical valves (Wheatley *et al.,* 2000). The hemodynamic performance was better than the tissue valves and lower thrombogenicity when compared to mechanical valves. The team found that high intensity transient signals (HITS) were less frequent in either the porcine or the polyurethane valve groups than the mechanical valve group. There was also a relationship between the HITS count and platelet aggregation in the valves, suggesting that these phenomenons were related and that changes in valve factors, such as reduction in flow orifice area, that tend to increase valve thrombogenicity could also increase the number of HITS. However, three of the eight valves showed serious thrombosis, which highlighted a concern as sheep are less thrombogenic than humans.

In a research conducted by Daebritz *et al.* (2003), PCU valve prostheses meant for mitral position showed great durability and hemodynamic performance *in vivo* when implanted in a growing calf model for 22 weeks. When implanted correctly, the valve showed minimal degradation of material and pathological findings showed that animals with PCU valves did clinically better than those with Perimount and Mosaic commercial valves. Minor

thrombus deposits were observed at the commissural regions of the SPU valves, but the tissue valves showed moderate to severe thickening and deformation of the leaflets. One tissue valve in the mitral position was completely covered by a huge thrombus.

The ideal artificial heart valve which has both the blood compatibility and flow hemodynamics of a tissue heart valve prosthesis, and the durability of a mechanical prosthesis, does not exist. In the recent years, studies have focused on the trileaflet mechanical heart valve which has several key design features, such as minimal flow disturbance and flow stagnation around the hinge region, central flow and durability. In a study by Sato *et al.,* (2003), the blood compatibility of a 29mm Triflo MHV in the mitral position of eight calves was evaluated for 5 months without any post-operative anticoagulation and exhibited excellent results. Another study by Gallegos *et al.,* (2006) also showed the equivalent safety levels and performance of Triflo MHV compared to the standard SJM BMHV when implanted in the aortic and mitral positions. The valve was implanted in 26 sheep and allocated to 150- and 365-day survival cohort. The Triflo valve appeared to emulate the hemodynamic properties of the native tissue valve compared to the traditional bileaflet design. However, more studies have to be performed to evaluate the long term outcome on the effectiveness of TMHV.

Both *in vitro* and *in vivo* experiments are expensive to setup. Most of the setups vary from one another and difficult when results are compared. *In vitro* testing allows valve to undergo tests to characterize its performances in the following hemodynamics performances: steady flow pressure gradient, dynamic function visualization and energy loss, static competence and dynamic regurgitation (Herold *et al.,* 1987). However, the disadvantage of *in vitro* experimental studies is that it can be challenging to match the physiological conditions and many assumptions are made. For *in vivo* testing, Herold *et al.* (1997) also conducted in vivo testing by implanting the valves in 35 animals over 3 ½ years. Such long period of testing is expensive and not desirable if the valve is still in the design refinement phases.

With the advancement of computational power, much attention has been given to CFD as a potentially promising alternative to investigate the hemodynamics within the heart valves. There are various flow characteristics that are of concern when accessing the hemodynamic performance of heart valves such as high shear stress, cavitations, stagnation point and high separation flow. The application of computational model enhances the development of improved artificial valves by significantly reducing the number of experiments required and giving insight in system responses that cannot or hard to be obtained experimentally.

1.12 Computational Fluid Dynamics of Heart Valves

A detailed description on the CFD analysis will be presented in Chapter 3. A numerical study was performed by Ge *et al.,* (2005), where full 3-dimensional flows over BMHV were investigated at different Reynolds numbers. The study simulated two flow conditions through aortic position at Re=750 corresponding to the flow at unsteady laminar regime, and Re=6000 corresponding to the flow near peak-systole which is fully turbulent. For turbulent flows, the unsteady Reynolds Averaged Navier-Stokes (URANS) and detached eddy simulation (DES) models were employed. The study shows triple-jet structure and the switching of central orifice jet from horizontal axis to vertical axis. However, pulsatile effects and leaflet motions were not considered. Figure 1-19 shows the axis switching of central orifice jet.

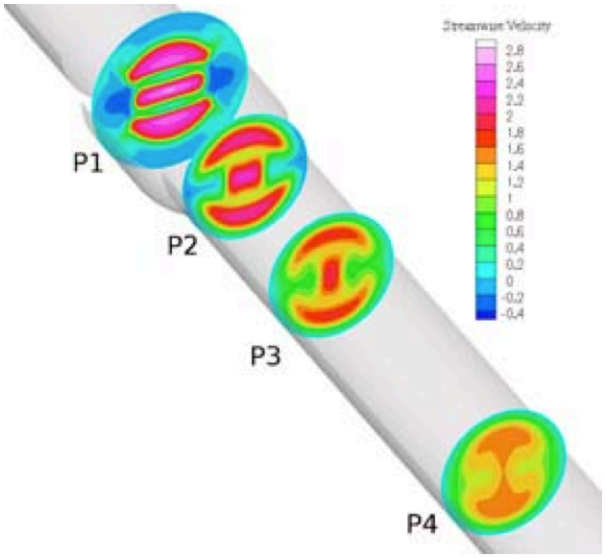

Figure 1-19: Plan view of streamwise velocity contours showing the axis switching of central orifice (Ge et al., 2005)

There are several challenges in CFD simulations such as the complex geometry, leaflet motion and flow unsteadiness. Studies have been done to investigate the wall shear stresses in the clearance region with the leaflets in closed position (Lee and Chandran, 1995, Reif, 1991). Nevertheless, the effect of leaflet motion was neglected. Bluestein et al., (1994) performed a simulation of the motion of leaflets for the last few degrees of motion during valve closure. Another study was conducted using a prescribed valve motion in a simplified flow domain (Aluri and Chandran, 2001). It was reported that the simulation with leaflet motion was simplified by restricting it to a 2-dimensional model. Lai *et al.,* (2002) also used a 2-dimensional model with a prescribed motion of the leaflets obtained from experimental data.

In 1994, Bluestein *et al.,* studied the squeeze flow phenomenon at the closing phase of BMHV. Cavitation is a phenomenon that occurs when "local pressure in the flow field falls below the vapor pressure of the field", resulting in "small vapor bubbles formation". Usually, these bubbles last for only microseconds before they are destroyed when entering high-pressure region. The violent collapse process, also known as implosion induces erosion to the surface and rupture of blood cells. Several factors contribute to mechanical heart valve cavitation, including regurgitant leak flow between valve leaflet and valve body, reduced pressure in accelerating flow, negative pressure generated at downstream surface of the leaflet when the valve suddenly closes and the squeeze flow pattern during valve closure. A laminar fluid flow of velocity magnitude as high as 14.17ms^{-1} was observed in the simulation, when the fluid squeezed through closing of BMHV (Bluestein *et al.,* 1994). The study suggested that cavitation could cause damage to the formed elements of blood and increased the risk of thromboembolic complications.

Yin *et al.,* (2004) conducted experiments *in vitro* to quantify platelet activation induced by flow through monoleaflet (Björk-Shiley) and bileaflet (CarboMedics) valves. Also, flow patterns that may induce platelet activation were predicted using CFD simulations. The study employed 2-dimensional simulation of Non-Newtonian flow with valve 15° off the flow axis. The simulation focused at the moment when the leaflet was in the fully open position during flow deceleration following peak systole when shed vortices

started to appear. This study was able to show the difference in the shear stresses between the bileaflet and monoleaflet valves. However, it did not consider the contribution of other cardiac cycle flow phases, such as, leaflet closure, regurgitant flow during diastole, and effects of flow in the valve hinge region. Figure 1-20 shows shed vortices developed in the valve area after peak systole.

Despite numerous advantages, there were still drawbacks associated with the BMHVs, which include platelet activation, thromboembolic complications and hemolysis. These complications were often associated with non-physiological high fluid shear stresses imposed on the blood elements through the BMHVs, particularly in the hinge recesses about which the leaflets pivot (Ellis *et al.,* 1996, Ellis *et al.,* 2000, Lu *et al.,* 2001).

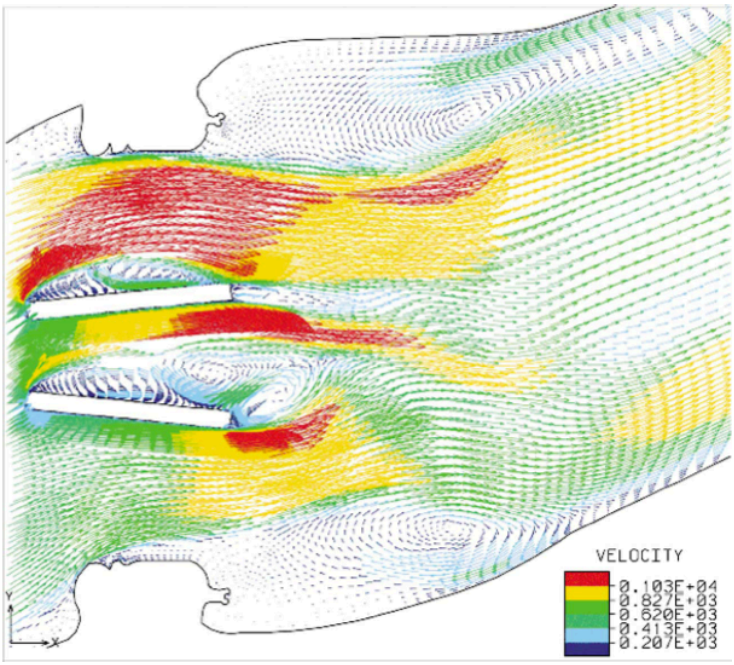

Figure 1-20: Shed vortices developed in the valve area after peak systole (Yin et al., 2004)

Many *in vitro* studies have been conducted to characterize the flow field inside the hinge regions in order to better understand the relationship between the thromboembolic complications and hinge designs (Ellis *et al.,* 2000, Kelly *et al.,* 1999, Leo *et al.,* 2002). Many of these studies mainly captured 2-dimensional velocity fields at selected locations within the hinge recess (Elllis *et al.,* 1996, Saxena *et al.,* 2003, Simon *et al.,* 2004). One major challenge faced by the experimental studies is the limited optical access to

the small hinge regions, which is made worse by the moving leaflet and opacity of the actual BMHV implants. Therefore, in recent years CFD has emerged as a potentially promising alternative to investigate the hinge microflow field.

An earlier CFD study conducted by Wang *et al.,* (2001) on a protruded hinge design was conducted on fixed and fully open leaflets under steady flow. Small vortices were observed behind the protruded stopper and reverse flow was evident inside the hinge socket. In another computational simulation, the hinge flow field of a 25mm ATS valve placed under aortic flow condition was studied (Kelly *et al.,* 1999). Here, the authors assumed a simplified sinusoidal pulse wave and modeled only the forward flow phase. In recent years, more complex 3-dimensional hinge simulation studies were conducted: Simon *et al.,* (2010) studied the microflow field characteristics of one hinge of a SJM valve at the aorta position in a straight pipe with an axisymmetric expansion sinus region while Yun *et al.,* (2012) studied the blood damage in the hinge area during diastolic phase in a straight pipe. The study observed high reverse flow and elevated wall shear stress in the hinge regions. In the survey of past hinge microflow studies, it was observed that most studies focused on one hinge recess, which was based on the assumption of flow symmetry across the valve. However, this assumption may mask the actual variations in hinge microflow fields at the different location of a BMHV.

All mechanical heart valve designs encounter leakage flow upon the valve closure. The space between the leaflets and the valve housing is to ensure the leaflets can freely open or close with minimal pressure difference across the valve. However, this free space inadvertently becomes regions of high leakage flow when the valve closes. Experimental studies have shown that the BMHV hinge regions were prone to high Reynolds shear stresses and have blood flow velocity exceeding $4ms^{-1}$. The observed high Reynolds shear stress may predispose the valve to higher incidence of hemolysis and platelet activation in the hinge regions.

Another area of interest is the angle of implantation of artificial heart valves. Usually, surgeons use as large an artificial heart valve as possible to fit into

the annulus. Tight suturing of the valve to the native human annulus may distort the surrounding tissues. One of the key issues that have not been studied extensively in earlier works is the impact of valve implantation orientation on the prostheses' performance on the sinus shape and downstream geometries. Often, the orientation of the implanted BMHVs is dependent on the discretion and skill of the surgeons. It has been found in earlier studies that both the valve type and implantation orientation affect the valve performance (Kleine *et al.,* 1998, Kleine *et al.,* 2002, Borazjani and Sotiropoulos, 2010). Studies have shown that there were differences in pressure drop across the valve and turbulent Reynolds stresses in an *in vitro* model when valves were implanted in different orientations (Travis *et al.,* 2002). Most of the valve models used in earlier CFD studies consisted of an axisymmetric sinus chamber in a straight pipe (Nguyen *et al.,* 2012, Simon *et al.,,* 2010, Dumont *et al.,* 2007, Ge *et al.,* 2005) or the Valsalva sinuses in a straight downstream pipe (Nobili *et al.,* 2008). These earlier simulations setup may not be physiological relevant as compared to a curved aortic arch downstream.

Results of the numerical study conducted by Hong and Kim (2011) showed that the rotation angle of BMHV increased the degree of asymmetry in the blood flow. In their study, the valves were placed at three different rotation angles of 0°, 15° and 30°. The flow recirculation regions were different among different sinuses, leading to asymmetrical blood flow near the heart valve leaflets. An *in vivo* study conducted by Kleine *et al.,* (2002) demonstrated that the turbulences downstream of both Medtronic and SJM valves changed significantly with rotation, although they found that Reynolds stresses downstream in the supravalvular aorta were less susceptible to change in SJM valve orientations (Kleine *et al.,* 1998). Another numerical study conducted by Borazjani and Sotiropoulos (2010) which used three implantation angles (0°, 45° and 90°) found that the valve orientation did not have a significant effect on the hemodynamic stresses experienced by blood elements. In their simulations, the leaflets model was simplified and the hinge mechanism connecting the leaflets and the valve housing was neglected. Nevertheless, limited studies have been conducted to look at the impact on

the downstream flow of different sinus geometry and downstream anatomy due to different valve orientation.

In the numerical study of TMHV, Kaufmann *et al.,* (2011) simulated a flow through a Triflo MHV and analyzed the pressure and shear stress rates for each leaflet position to investigate the thrombus formation. The mesh consisted of approximately 900,000 tetrahedral elements and only 1/6 of the geometry was simulated, which was the smallest symmetrical element. One complete cycle of the valve was simulated and performed using ANSYS CFX 11.0. Li and Lu (2012) used a new trileaflet valve design and simulated the flow using Fluent 6.3 and compared with the SJM BMHV. The mesh of the trileaflet valve was about 540,000 elements and simulated using k-ω turbulence model. The flow in the TMHV was mainly central compared to obstructions in the BMHV. However, the turbulence model and boundary conditions were simplified to ideal conditions. Esquivel *et al.,* (2003) also simulated the flow through and found similarities, with the central flow through a TMHV account for 86–95% of the total flow. Limited simulations were performed to understand the flow profile in the downstream regions of TMHV and compared with BMHV.

1.12.1 Turbulence Modeling in CFD

When the flow reaches a certain Reynolds number, the flow goes from being laminar to turbulent. Turbulence is a three dimensional and highly transient continuum phenomenon in which fluid irregular motions are described in a continuously wide range of scale, from the smallest turbulence eddies (or eddies of turbulence) defined by Kolmogorov scales to the largest eddies characterized by the particular flow and these eddies carry most of the turbulent kinetic energy. The Reynolds number for most of pulsatile cardiovascular flows ranges from 0 to around 10^4 based on vessels geometric configuration. The pulsatile fluid flow downstream of mechanical heart valves transforms from laminar to turbulent over the cardiac cycle.

The scale distribution of the large coherent “noisy” eddies agrees very well with the phenomenological predictions of Kolmogorov, which assumes that the turbulent energy content of isotropic (invariant under rotation) turbulence

is dependent only on the rate of energy dissipation, at which the smallest scales of turbulence convert motion into heat and the wave number, *k*, (proportional to the inverse of the eddy length scale). This implies that provided the length scale at which the turbulence energy is injected into the system is sufficiently far removed from that at which the energy dissipates into heat, the character of the turbulence will be independent of both the large forcing scales and molecular viscosity.

Depending on the level of resolution of turbulence scales, various methodologies for modeling turbulence can be employed. Among those, Direct Numerical Simulation (DNS), Large Eddy Simulation (LES) and Reynolds Averaged Navier-Stokes (RANS) approaches have gained much attention and exploration over the last few decades. DNS appears to be the most desirable solution to a turbulent flow problem. However, it is also more computationally intensive. LES is less complex and RANS is the least complex.

In the DNS approach, the fully nonlinear solutions of the NS equations are computed directly by discretization and numerical algorithms. DNS will fully resolve the flow by attempting to solve all scales of motions in the fluid, from the largest coherent structures to the smallest dissipating eddies, without any averaging and smoothing of the solution field. This captures the important flow structures in the process of transition as well as turbulence. However, the difficulty in using DNS is that the turbulence contains wide range of vortices with equal physical importance. When the Reynolds numbers increase, the size ratio of the largest to the smallest vortices increases. Modi (1999) found it difficult to perform the DNS of turbulent flow with a higher Reynolds number.

In the LES approach, large scales are resolved on a given computational mesh, using the same spatial discretization method for flow variables. Compared to DNS, the LES approach is able to provide a more detailed description of turbulent flows. However, the requirements on mesh resolution and time-step size put very high demands on the computer resources; thus, rendering it a more computational intensive method.

LES has shown good accuracy in calculation of traditionally difficult turbulent flow cases, such as recirculation and unsteady flows. However, it is computationally costlier compared to conventional RANS approach. The way in which LES interacts with the wall boundaries has been identified as a major contributor to the problem. Villiers (2006) addressed the issue through the application of approximate wall treatments and improved mesh distribution.

LES does not resolve the full range of turbulent scales unlike DNS, but it captures a much larger range of scales than the Reynolds average equations. Large eddies contain most of the energy, do most of the transporting of conserved properties and vary most from case to case. In contrast, the smaller eddies are believed to be more universal (largely independent of the boundary conditions) and therefore easier to model. Since the contribution of the small-scale turbulence to the resolved flow field is small, the errors introduced by their modeling should also be small. In addition, the resolved scales carry much more information than the mean flow predicted by the RANS approach.

RANS approach approximates time-averaged solutions to the Navier-Stokes equations based on the properties of the flow turbulence was used to. In RANS turbulence modeling, all of the unsteadiness in the flow is averaged out and regarded as part of the turbulence. The instantaneous flow field is divided into a time-averaged part and a fluctuating part, expressed in terms of mean quantities. Although known as a less detailed turbulence simulation method, RANS solutions show reasonable resolutions to turbulent flows, especially for relatively large Reynolds numbers. In addition, the method is the least expensive of all the turbulence modeling methods where the total arithmetic is independent of Reynolds number while it is in the order of Re^2 and Re^3 for LES and direct numerical simulations, respectively.

Numerical simulations of turbulent flows have a key disadvantage in engineering applications, which is their inability to guarantee accuracy in all conditions unless validated. As such, the development of a cost effective and accurate simulation method is the key focus of research in CFD. The flow at

physiologic conditions takes place in complex geometries with compliant walls, undergoes transition to turbulence, and is dominated by the pulsatile flow effects.

1.12.2 Verification of Numerical and Experimental Results

Validation of numerical and experimental results is a very important step forward to gain confidence in the results of the numerical simulations. King *et al.,* (1997) compared and analyzed flow through a BMHV using experimental and numerical methods. Laser Doppler Velocimetry (LDV) experiments were performed and compared with CFD simulation based on FIDAP, a commercially available finite element code. The study showed a fair agreement between numerically predicted and experimental results. Ge et al., (2005) validated their studies by measuring the flow velocities using the Particle Image Velocimetry (PIV) technique. The flow was seeded with silver coated glass spheres and was illuminated by a YAG double cavity laser, which double pulsed at a rate of 15Hz. The team was able to validate the simulation results at laminar and turbulent flow as shown in Figure 1-21. The black line denotes numerical simulations while the circle denotes experimental measurements.

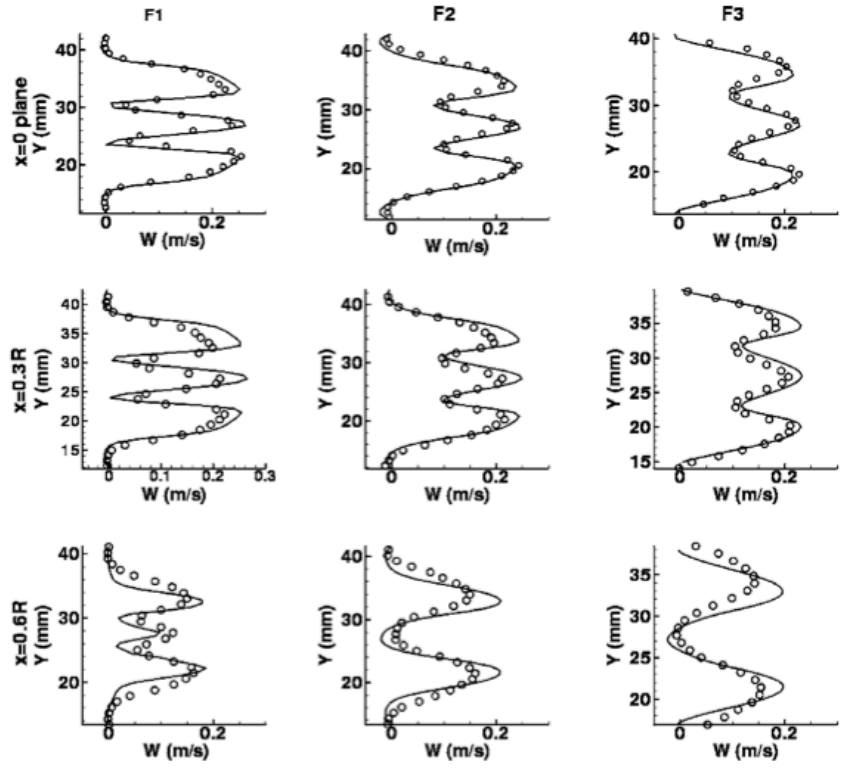

Figure 1-21: Velocity profile comparison between simulation and experimental (Ge *et al.,* 2005)

Shu *et al.,* (2003) also conducted a velocity validation between CFD simulations with pivot flow visualization (PFV). The study comprised of three different techniques to overcome limitation of each technique: PFV, CFD simulation and LDV. The technique used enabled pivot flow structure detection, such as “vena contractas, flow recirculation zones, small vortices, continuous-flow washing and absence of persistent flow stasis”. Vena contractas is the jet flow contraction at opening of heart valve. These detections agree with other journal paper findings on flow through BMHV. The only difference was probably be continuous-flow washing, which was observed only in Medtronic ADVANTAGE heart valve and absent in SJM heart valve. The measured and computed velocities resembled each other closely in terms of velocity magnitudes and profile shapes. Figure 1-22 shows the comparison between CFD simulated and LDV experimental velocities value.

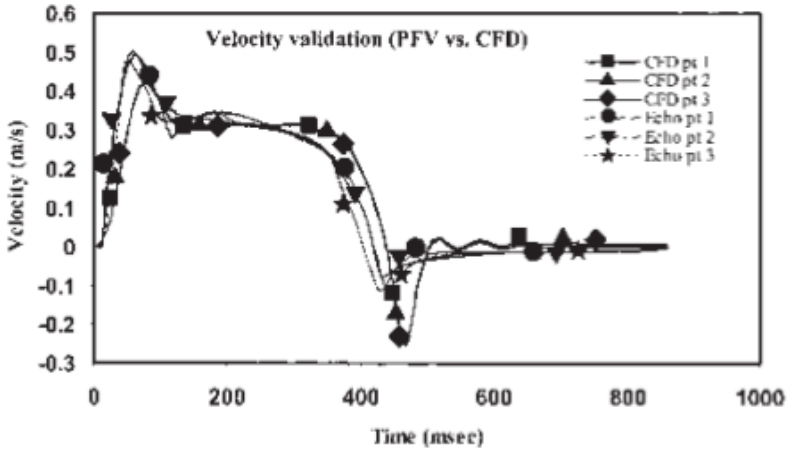

Figure 1-22: Velocity Validation with PFV and CFD in a cardiac cycle (Shu *et al.,* 2003)

Other analyses and validations of simulation results have been performed using PIV to understand the flow in the vicinity of BMHV. Lim *et al.,* (2001) performed a 2-dimensional PIV to map the velocity flow fields and Reynolds shear stresses in the immediate downstream of a porcine bioprosthetic heart valve. The data from these experimental studies will be very important in comparing the results from numerical simulations. Manning *et al.,* (2003) analyzed the regurgitant flow field of the SJM BMHV using PIV under physiological pulsatile flow conditions.

1.12.3 Fluid-Structure Interaction

The numerical simulation techniques in valve modeling focus on the valve structure rather than the Fluid-Structure Interaction (FSI). The complex interaction between the blood, the valve leaflets and heart wall plays an important role in response of the system to its physiological loading.

Several studies have been conducted on computational modeling of the recirculation region and the wall shear stresses in the clearance region (Lee and Chandran 1995). Often, these studies neglect the interaction between the leaflet motion and the flow field. There are also other studies which coupled the fluid flow with the leaflet motion using a prescribed valve motion from the fully open to fully closed position (Lai *et al.,* 2002). This simplified flow domain helps to avoid the complex problem of the leaflet-fluid interaction during systole and diastole. However, it does not address the actual movement of the heart leaflets in physiological conditions. As such, it is important to have an accurate simulation of the heart valve by developing a validated FSI algorithm for the prediction of the leaflet motion resulting from the fluid stresses acting on the leaflet. Some of the recent work focused on moving leaflets and pulsatile flow. Many attempts have been reported to develop a FSI algorithm for mechanical heart valve function. However, such studies were restricted to 2-dimensional analyses (Cheng *et al.,* 2003). A complete 2-dimensional FSI algorithm for the ATS Open Pivot heart valve was attempted by Dumont (2005) using ANSYS Fluent Inc. However, further experimental measurements are needed to validate the agreement between the measured and calculated 2-dimensional flow field around the moving valve leaflet.

FSI is the interaction of a deformable structure with the surrounding fluid flow. Generally, two main approaches are used in the simulation of FSI problems: (1) Monolithic approach where the equations governing the flow and the displacement of the structure are solved simultaneously, with a single solver, (2) Partitioned approach where the equations governing the flow and the displacement of the structure are solved separately, with two distinct solvers. In the monolithic approach, a code developed for this particular combination of physical problems is required. In the partitioned approach, software modularity is preserved as the existing flow solver and structural solver are

coupled. Besides that, the solution of the flow equations and the structural equations are facilitated by the partitioned approach with different and possibly more efficient techniques. These have been developed for either flow equations or structural equations. Meanwhile, a stable and accurate coupling algorithm required in partitioned simulations should be developed. A strong coupling algorithm for the simulation of BMHV was presented by Annerel *et al.,* (2011) to study the wall shear stresses on the valve leaflet surfaces which was able to predict the leaflet gangular accelerations.

3-dimensional FSI models are computationally expensive and have been restricted to study native or prosthetic heart valves placed in simplified domains, such as in straight axisymmetric aortic lumens (Griffith 2013). Dumont *et al.,* (2007) have demonstrated that the hemodynamics of BMHV is dependent on the geometric design parameters of the valve. Their FSI algorithm is based on the dynamic mesh model of the commercial CFD software package FLUENT (Fluent, Inc). Using an implicit coupling procedure, flow profiles through SJM Regent Valve and ATS Open Pivot Valve were investigated and the shear stress on the leaflets and platelets were then measured as shown in Figure 1-23.

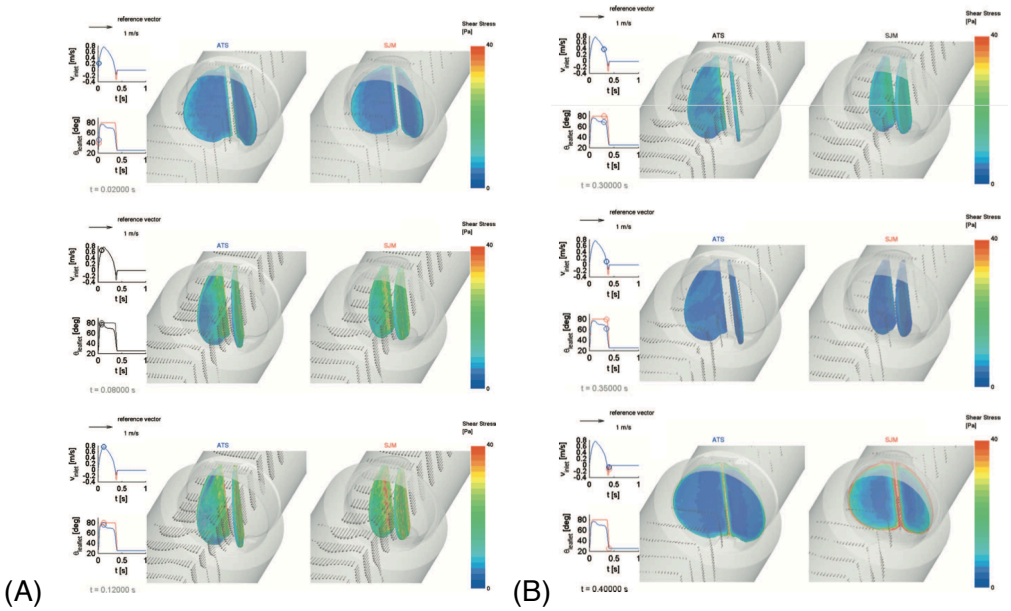

Figure 1-23: Flow field and wall shear stress during (A) Opening of the valves [ATS (left panel)], [SJM (right panel)], (B) Closing of the valves [ATS (left panel)], [SJM (right panel)] (Dumont *et al.,* 2007)

The numerical results were able to show that the designs of the SJM and ATS valves, which differ mostly in their hinge mechanism, had led to different potential for platelet activation, especially at the regurgitation phase. However, they may have underestimated the shear stress levels in the leakage jets, and accordingly the platelet stress accumulation values due to the difference in the estimated clearance gaps in the constructed model.

There are two main methods suitable to handle the full FSI problem, which involves the compliant aortic/left ventricle walls and moving valve leaflets. They are moving grid methods and fixed grid methods.

In the moving grid method, the computational grid is fitted to and deforms with the moving boundary, using the arbitrary Lagrangian Eulerian (ALE) method. This method has been used to simulate the flow through mechanical heart valves (Cheng *et al.,* 2004). Nevertheless, at all times, the mesh must conform to the moving boundary and constantly deform according to the motion of the boundary. It can be quite challenging to update the mesh in every time-step, especially for such a complicated problem. The difficulties with ALE methods involve large structural displacements (in this case the movement of the valve leaflets). The mesh quality needs to be maintained at every time-step but it is possible to simulate the flow using ALE approach. Furthermore, the 3D FSI simulation carried out had a grid of about 200,000 nodes to discretize the flow domain. The study used a quadrant symmetry assumption which only focused on one quarter of the valve for simulation. van Loon *et al.,* (2005) have also performed a 3D FSI simulation of a tissue valve with symmetry assumption.

Dumont (2005) studied the Fluid-Structure Interaction with highly flexible bodies using strong coupling of a commercial CFD solver (Fluent Inc) with an in-house coded structural solver using the moving grid method. He studied the opening and closing of a 2-dimensional model of a flexible aortic valve leaflet during the complete cardiac cycle as seen in Figure 1-24, using an implicit iteration scheme. The dynamic mesh approach used ALE formulation of the NS equations to simulate the flow in which shape of the domain

changes with time due to the movement of the domain boundaries. The shear stress on the leaflets was calculated accordingly.

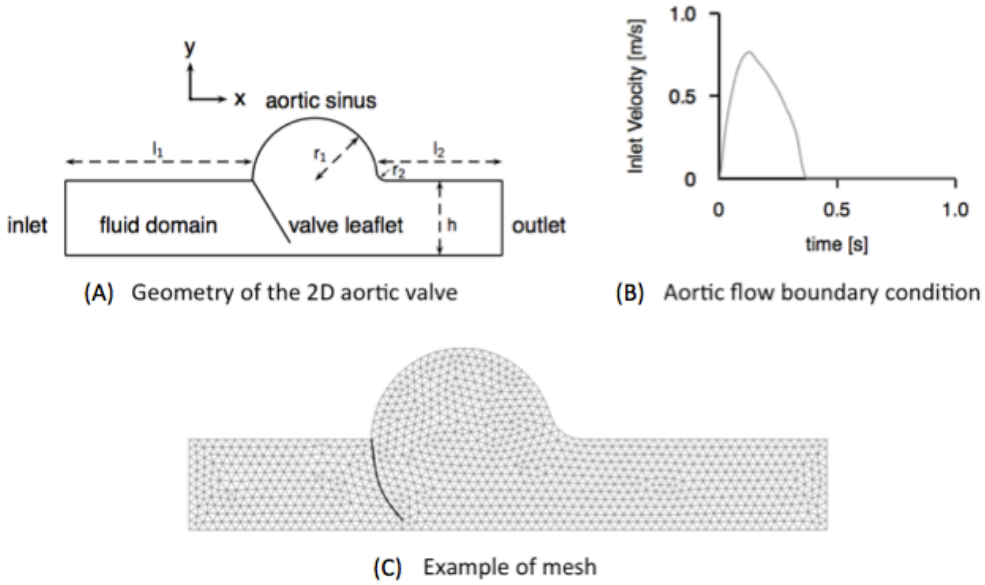

Figure 1-24: 2-dimensional Flexible Aortic Valve model (A) Geometry of the 2-dimensional aortic valve (B) Aortic flow boundary condition (C) Example of mesh (Dumont 2005)

Fixed grid method has been increasingly popular due to their capability in simulating FSI problems which involve large structural displacements (De Hart *et al.,* 2003, Dasi *et al.,* 2007, Tai *et al.,* 2007, Borazjani *et al.,* 2008). The entire fluid domain is discretized with a single, fixed, and non-boundary conforming grid system. Usually, a Cartesian mesh is used as the fixed background mesh. Meanwhile, the structural domain is further discretized with a separate grid, which can move inside the fluid domain freely. In order to move the immersed body in the fluid, body forces are calculated and added to the governing equations of the fluid motion. As such, the presence of a no-slip boundary at the location of the solid/fluid interface can be felt by the surrounding flow. An example of the fixed grid method used by De Hart is shown in Figure 1-25 to analyze the Fluid-Structure Interaction of the aortic valve in 3-dimensional.

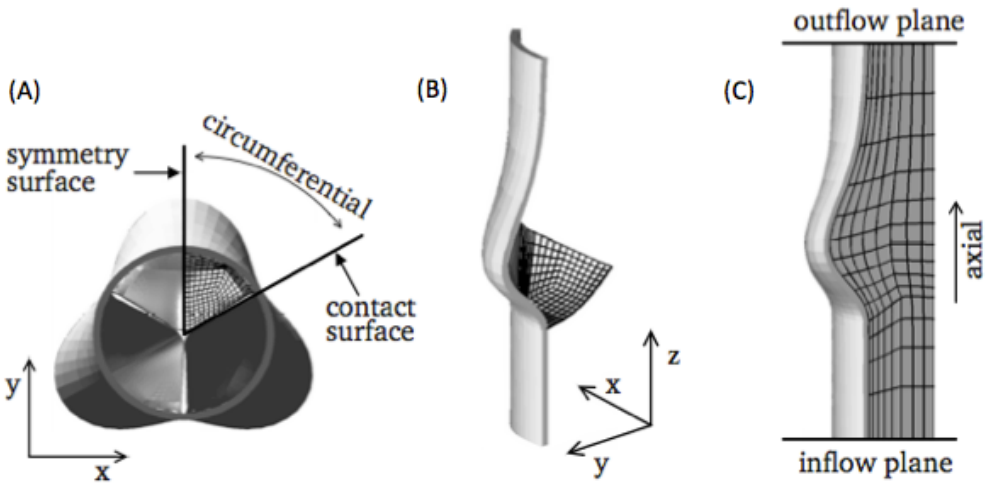

Figure 1-25: 3-dimensional FEM model of the stented aortic valve (A) part of the valve used for the computation, (B) Structure mesh, and (C) fluid mesh (De Hart *et al.,* 2003)

Peskin's pioneering work in immersed boundary method is the earliest work in applying a fixed grid method to simulate heart valve flow (Peskin 1972). The presence of the immersed deformable solid boundary on the surrounding fluid grid nodes was accounted for by adding a body force in the Navier–Stokes equations. The body force was then distributed on all nodes of the fixed background grid through a discrete delta function that has the effect to diffuse the solid boundary over several fluid grid nodes in the vicinity of the boundary. To obtain accurate results, such methods usually require an increased in grid resolution in the vicinity of the boundary. A practical approach to simulate FSI problems is to partition the domain into two separate fluid and structure domains. Such approach can be implemented in either a loosely coupled or strongly coupled domain. For loosely coupled domain, the boundary conditions at the interface are obtained from the domain solutions from the previous time level (explicit in time). For strongly coupled domain, the boundary conditions are obtained from the domain solutions from the current time level (implicit in time). This is achieved by performing several sub-iterations at every time-step, until the FSI equations have converged within a desired tolerance. There is a need to capture the hemodynamics of the heart valves more accurately near the interface, such as the wall shear stresses in particular, when analyzing the effects of flow in the heart.

Borazjani *et al.,* (2008) developed a Curvilinear Immersed Boundary (CURVIB) method where the moving boundary was immersed in a domain that can be discretized efficiently with a curvilinear body-fitted mesh. However, the difficulty faced was that the loose coupling algorithm was unstable and difficult to converge during the valve opening phase.

Major progress has been made in the past few years to perform numerical simulations of BMHV flows at physiological conditions. The simulations are able to provide sufficiently high resolution to investigate the link between valve fluid mechanics and thromboembolic complications. A major computational challenge is to develop a computational model with physiological conditions and anatomically more accurate model that can look into the flow hemodynamics in the microscopic regions of BMHV designs, such as the hinge recess. Such phenomenon can induce shear stresses that may damage red blood cells and lead to platelet activation. The numerical simulation acted as a tool for thromboembolic potential characterization to observe the physical viscous stresses experienced by the blood elements and the capability to refine the analysis to a level of spatial details that would be hard to achieve experimentally. The research will contribute to the use of an ALE method with moving mesh technique using an open source software OpenFOAM by the validation study performed for both laminar and pulsatile flow. Also through this contribution, the understanding of the effect of anatomical model and the implantation angles of both bileaflet and trileaflet mechanical heart valve on the hinge and downstream aorta flowfields can further be advanced. The computational model from this research will also look into the optimization of valve implantation angle that analyses the flow dynamics of the mechanical heart valves. This may potentially determine the clinical performance of the valve.

CHAPTER 2: HYPOTHESIS AND PROJECT AIMS

This chapter focuses on the hypothesis and project aims of the research. A code based on open source codes was developed and used for the simulations.

Hypothesis:

In this study, a computational method using OpenFOAM software package is proposed to incorporate leaflet motions by simulating the flow dynamics in a BMHV model. By constructing an ALE based fluid structure interaction model using solid body motion technique to investigate the flow hemodynamics, the valve movement in the aortic root was applied successfully. Specifically, a code based on open source codes have been developed and tailored to incorporate the leaflet motion by simulating the flow dynamics in a BMHV model. This method is hypothesized to be a more accurate approach for investigations of a heart valve simulation in a cardiac cycle. The numerical method once validated experimentally, will be able investigate the valve hemodynamics and predict important parameters such as regions of recirculation and wall shear stress loading on the valve leaflets. The effect of implantation angles on the downstream flow field as well as the influence of the sinus and downstream geometry on the hinge flow fields will be investigated. This computational model can be used as a research tool to understand the hemodynamics of existing and new artificial heart valves. This current investigation forms part of a continuing study of heart valve engineering. The broader objective of this study is to provide an improved quantitative and qualitative understanding of the functionality and potential thrombogenicity of BMHVs beyond that available from previous studies. The current study helps to push forward our effort to develop a computational framework, which can support decision-making for clinicians. The results of this work will also provide new insight into the roles the subtle design features have on the potential for blood damage.

Project Aim 1: To develop a prescribed motion code to study the flow through a bileaflet mechanical heart valve with prescribed motions in body fitted grid framework using ALE techniques

This aim of the study is to allow us to simulate deformable moving bodies in a 3-dimensional simulation. To accomplish this, the flow through a BMHV in a prescribed motion will be studied. The robustness of the developed open source code will be tested with various turbulence models (k-epsilon, Spalart-Allmaras and LES) and the motion of the leaflets. Simulations of flows over fixed valve leaflets will be performed and validated with experiments. The leaflet motion will also be prescribed from a fully open position to full closure, corresponding to the velocity wave profile of a typical cardiac cycle. By comparing the simulation results with the experimental data, the pulsatile flow model can be validated for the entire phase of the cardiac cycle. The experimental data will be obtained from the *in vitro* studies, using Particle Image Velocimetry (PIV).

Project Aim 2a: To study the effect of sinus and downstream geometry on the flow fields in the hinge region and the effect of implantation angles on the downstream flow field of bileaflet mechanical heart valve

The aim of this study is to provide a detailed 3-dimensional flow features in the hinge region of a BMHV with two different aortic sinus shapes and downstream geometries. This study constitutes the first attempt to evaluate the flow fields of all four hinges in a single BMHV. The results of this work will provide insights into impact of different aortic sinus shape, the aortic arch geometry and the location of the hinge recess on hinge microflow fields during systolic and diastolic phase. In order to accurately capture the impact of valve's orientation on its downstream flow profile, the study quantifies the flow through the valve placed in different sinus and aortic arch models. The study will compare the downstream flow fields of two different sinus geometry and two different downstream aortic arch geometry as a result of different valve orientations (0°, 30°, 60° and 90°) during peak systole. The result of this work will provide insights into the impact of different valve orientation on the flow fields of aortic sinus and aortic arch.

Project Aim 2b: To study the flow hemodynamic through a trileaflet mechanical heart valve design and compare it with that of a bileaflet mechanical heart valve

The aim of this study is to provide a detailed 3-dimensional flow simulation in a trileaflet mechanical heart valve placed in a downstream curved aorta. The study will evalute the flow fields through a trileaflet mechanical heart valve and compare it with that of the BMHV to predict important parameters such as regions of recirculation and wall shear stress loading on the valve leaflets and aorta wall. This study will compare the downstream flow fields of different trileaflet valve orientations (0°, 30°, 60° and 90°) during peak systole. The result of this work will provide insights into the impact of different valve orientation on the flow fields of aortic sinus and aortic arch for trileaflet mechanical heart valve.

Project Aim 3: To develop the Fluid-Structure Interaction of a rigid mechanical heart valve using solid body motion

It has become increasingly important for simulations of coupled problems in engineering. When modeling the aortic valve, the interaction between the blood and the valve determines the valve movement and the valvular hemodynamics. Nevertheless, only a few studies have focused on the opening and closing behavior during systole. For this Project Aim, the FSI for the mechanical heart valve using solid body motions will be performed. In order to predict the numerical behavior of the coupling procedure more accurately, a complete model of the BMHV configuration has to be considered, including the hinge mechanism. A grid and time-step independence study will be conducted to demonstrate the robustness of the FSI algorithm. The algorithm will be developed in OpenFOAM framework with a customized solver. The simulated data (pressure and velocity fields) will be used to calculate and characterize the valve hemodynamic performance. The results will be compared with the prescribed leaflet movements simulation of the pulsatile flow and experimental results.

CHAPTER 3: NUMERICAL METHODS

This chapter is organized to provide the description on numerical tools, parameters and methods used in the study.

3.1 Simulation Tools

Various CFD tools have been developed and used by researchers in heart valves flow simulation. Some of the common CFD tools include FIDAP CFD package by Yin *et al.,* (2004), Bluestein *et al.,* (1994), Ge *et al.,* (2005) and King *et al.,* (1997). CFD-ACE+ version 6.4 and FEMSTRESS used by Choi *et al.,* (2003), ANSYS used by Ghaeb *et al.,* (2009) and FLUENT used by Dumont *et al.,* (2007), and Li and Lu (2012). Su *et al.,* (2014) also used ANSYS FLUENT to conduct simulations. FlowVision HPC 3.08 was used by Marom *et al., (*2013) to manage the coupling of the FSI codes. Simon *et al*., (2010) sued the Generalized Minimal Residual Method (GMRES) solver coupled by immersed boundary approach proposed by Glimanov and Sotiropoulos (2005).

As for creating mesh for simulation, Gambit is used by Dumont *et al.,* (2007), Li and Lu (2012), and Yin *et al.,* (2004). Another type of mesh generator created by Marom *et al.,* (2013) using TrueGrid (XYZ Scientific Applications).

The improvement and development of open source codes have certainly invited much needed comparison of their performances with commercial ones. In particular, there are several aspects, which differentiate between the open source and commercial codes:

- Ease of use
- Portability
- Pre and post-processing of input and output data respectively
- Accuracy of simulations
- Simulation speed and scalability
- Additional priorities in handling industrial needs
- Availability and applicability of physical models

CFD analysis consists of mainly three different stages; pre-processing, solver and post-processing as shown in Figure 3-1. The pre-processing involves the creation of model, generation of surface meshes and the setup of boundary conditions for computer modeling.

Mesh generation is an important step to ensure accurate results. The correct mesh density and mesh continuity are needed to efficiently capture the boundary layer effects and compute the results. The solver involves the use of various physical models to perform simulation. The initialization phase, time-step and convergence criteria for the solver is performed before it solves the transport equations. In the post-processing, the simulation results are interpreted and visualized. Various analysis such as the velocity vectors, graphs, flow rate and streamlines can be analyzed.

Since the pioneering work of 2-dimensional simulations by Peskin, the CFD study of flows in BMHV has achieved a considerable progress towards understanding of hemodynamics and the issues associated with artificial heart valves failure (Peskin 1972, Peskin 1982). King *et al.,* (1997) investigated the effect of opening angles on the time-dependent flow through a BMHV using a quarter valve symmetric model. The assumption of a symmetric flow failed to show other secondary flow features such as interaction on the edges of the jets and spiraling vortices shed downstream of the valve. The differences observed between experimental and CFD simulations demonstrate that a 3-dimensional model is required for a better accuracy.

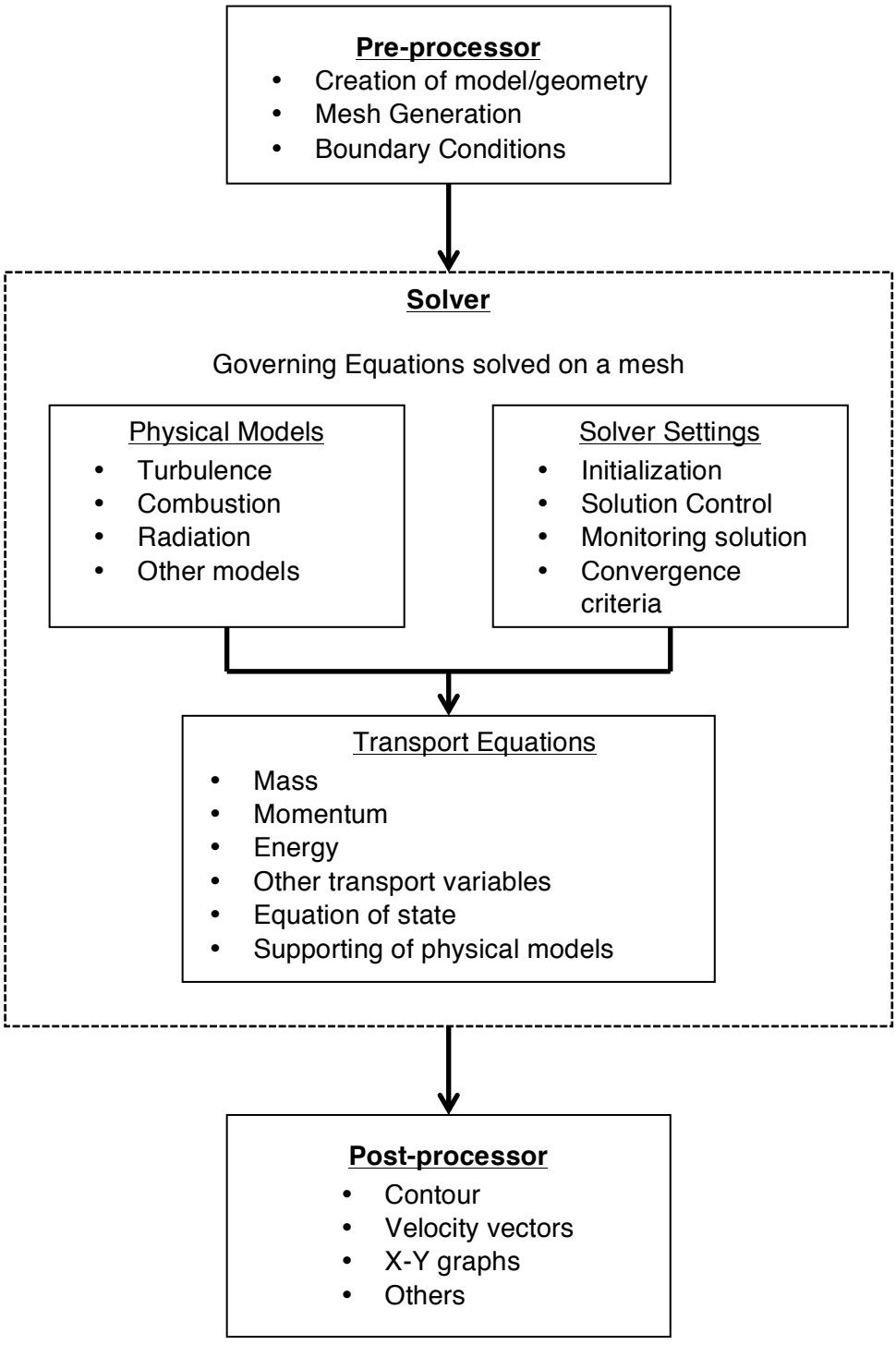

Figure 3-1: The flow diagram of a CFD analysis

3.1.1 Pre-processing: GAMBIT (Fluent, Inc)

OpenFOAM has built-in mesh generating software such as **blockMesh** and **snappyHexMesh** functions. **blockMesh** generates block-structured hexahedral meshes that are converted into arbitrary unstructured format of

OpenFOAM; but this requires tremendous effort for complex geometries. Compared to **blockMesh**, **snappyHexMesh** does not require as much work, although it still requires lots of parameters to refine the various local mesh shapes and boundary layer cells. Even though OpenFOAM has this built-in mesh generating capability, the heart valve structure is too complicated to be generated using OpenFOAM mesh functions. Therefore, a different mesh creating software is essential to allow control over mesh generation and easy integration to other software. GAMBIT (Fluent, Inc) suits the requirement perfectly as drawings from other software such as SolidWorks could be imported and meshed accordingly. The GAMBIT preprocessor was introduced into the Fluent CFD package in 1998 but has not been developed further in the recent years. GAMBIT provides a single graphic user interface (GUI) for geometry creation, mesh generation and mesh quality diagnostic. It has advanced meshing-techniques using mapped quad/hexahedral, unstructured triangle/tetrahedral as well as hybrid meshing. Mesh created by GAMBIT could be further defined, for instance by size-function. Size-function enables users to specify the mesh spacing at different regions and boundaries, allowing the user to have a finer mesh in the region of interest and a coarser mesh in regions further away. In this research, GAMBIT was utilized in specifying the boundary types, defining the solution domain, and generating suitable computational domain by accessing the mesh quality. With this in mind, a fine mesh can be created immediately downstream of the valve leaflets to better capture the velocity jet structure, as well as the gap between the leaflet ears and the valve housing at the hinge regions. The conversion of mesh from GAMBIT .msh file to OpenFOAM compatible file can be performed using the command **fluentMeshToFoam** with the appropriate scale.

3.1.2 Simulation: OpenFOAM

The intention for this research is to develop a FSI model using OpenFOAM, which is an open source, C++ toolbox for the numerical solution of the continuum mechanics problems including CFD program. OpenFOAM provides flexibility towards model development and numerical simulation to the user, even though assistance is still required from other open source and/or commercial tools for pre-/post-processing. OpenFOAM is an open

platform and offers immediate access and freedom to customize and extend its existing computational fluid dynamics capabilities for users. OpenFOAM has been well utilized by many research institutions and industries (ESI Group, ICON, Silicon Graphic International (SGI) Corp, Australia National Computational Infrastructure, Imperial College London, Delft University of Technology) for the flexibility of fine-tuning the code to suit their specific needs. OpenCFD became a wholly owned subsidiary of the ESI Group in 2012, following acquisition from SGI Corp (who had acquired OpenCFD in 2011). For this study, the source code is accessible and all the required tools to build a customized application. The OpenFOAM library functions make it simple to create a solver. There are many advantages to OpenFOAM, such as:

- User-friendly syntax for partial differential equations
- Source code accessible at both top solver and bottom library level
- Freely available and well validated quality code
- Ease of interface with commercial pre-processor software
- Unstructured polyhedral grid capabilities
- Wide range of models and applications ready to use
- High scalability, extendibility and parallelization of applications written using OpenFOAM high-level syntax
- Commercial training and support provided by the developers
- Free and open source software under the GNU General Public License

Nevertheless, the disadvantages associated with OpenFOAM are as follows:

- Absence of an integrated graphic user interface (stand-alone Open source and proprietary options are available)
- The learning curve is steep as the user guide does not provide sufficient details
- Difficult for new users due to the lack of maintained documentation

The OpenFOAM versions used in the studies are OpenFOAM-1.5-dev and OpenFOAM-1.6-ext. There are several main solvers from OpenFOAM which are used in this study. For Project Aim 1, the code used is the modified **icoFoam**, which solves the incompressible laminar NS equations using

pressure implicit with splitting of operator (PISO) algorithm. The code is provided in Appendix A. The code in this solver requires an initial condition and boundary conditions, and is inherently transient. The **icoFoam** code can take the non-orthogonality of the mesh into account with successive non-orthogonality iterations. The user input can control the number of PISO corrections and non-orthogonality corrections. The modified **icoFoam** contains a variable time-step, which limits the maximum time-step (maxDeltaT). In simulations, the Courant-Friedrichs-Lewy (CFL) condition is important to ensure stability while solving the partial differential equations by the method of finite differences. The need for CFL condition arises in the numerical analysis of implicit time integration schemes, when used for numerical solution.

$$C = \frac{u\Delta t}{\Delta x} \leq C_{max} \tag{3.1}$$

where C is the dimensionless number known as the Courant number, with u is the velocity, Δt is the time-step, and Δx is the length interval.

The value of C_{max} changes with the method used to solve the discretized equation with implicit solvers, which are typically less sensitive to numerical instability. As such, larger values of C_{max} may be tolerated. The Courant number is an important parameter to control the time-step in transient simulations, which affects the stability and computational cost.

The next solver used is a modified **turbFoam**, which solves incompressible, turbulent flow with adjustable time-step. The code is provided in Appendix A. There are several methods and models to simulate turbulence in OpenFOAM, which are highlighted below (OpenFOAM 2012):

- Reynolds-Average Navier-Stokes: The governing equations are solved in ensemble-average form and include appropriate models for the effect of turbulence. Several incompressible RANS models are used in OpenFOAM such as the standard k-epsilon, k-omega, and Spalart-Allmaras (SA).
- Large eddy simulation (LES): The governing equations resolve the large turbulent structures in the flow, while the effect of the sub-grid scales is modeled.

- Detached eddy simulation (DES): The hybrid method between RANS and LES method whereby RANS approach is used on near-wall regions and LES approach is used on the bulk flow.

For LES modeling, **pisoFoam** can be modified to include moving mesh features.

Another solver used in OpenFOAM is **icoMMeshTrackFoam** and **turbMMeshTrackFoam** solver, which solves incompressible NS equation of a deformable mesh in a prescribed motion and will be used for Project Aims 1, 2a and 2b. To simulate the turbulent flow, both the **icoMMeshTrackFoam** and **turbMMeshTrackFoam** were modified based on the governing equation used in **icoFoam** and **turbFoam**. This solver uses a mesquite mesh quality improvement toolkit (Brewer *et al.,* 2003). These two codes are provided in Appendix A.

To conduct the FSI simulation for Project Aim 3, another solver has to be used, **pimpleDyMFoam**, when performing the simulations. It is important to ensure the convergence of the sub-iteration process when working on such FSI problems (Maus 2009). These solvers are useful for flow computation when valve is on the transition from open to closed position or vice versa. Flow condition can be simulated as the heart valve moves. The codes are provided in Appendix A.

3.1.3 Post-processing: ParaView (Kitware)

After OpenFOAM carries out the simulation, only velocity and pressure at each node is stored. This numbers are not easy to analyze or view. Thus, a post- processing is required to translate the simulation data into a more user-friendly form, such as a contour or vector plot. ParaView is an open-source, multi-platform data analysis and visualization application, and is designed to harness the power of distributed memory-computing resources. ParaView is an application framework and turnkey application. It is possible to quickly build visualizations to analyze data using qualitative and quantitative techniques, as well as with data exploration done interactively in 3-dimensional or programmatically using ParaView's batch processing

capabilities. Besides that, the ParaView code base is designed so that all of its components can be reused to quickly develop vertical applications. This flexibility allows ParaView developers to quickly develop applications that have specific functionality for a specific problem domain (Kitware 2014). In ParaView, various parameters such as velocity, pressure or shear stress can be shown as a plot, allowing user to see the distribution of these parameters on the mesh. Besides, ParaView can show how these parameters change as a function of time similar to an animation. Flow profile, pressure profile and wall shear stress distribution of valve *in vivo* can be simulated and analyzed.

3.2 Problem Statement

To handle the movement of the heart valves, an ALE technique was used to discretize the system. The moving mesh velocity, $\boldsymbol{u_S}$ at the interface must be equal to the boundary velocity, $\boldsymbol{u_\Gamma}$, for the prescribed movement of fixed boundaries. The movement of the boundaries cause the computational mesh to deform and unable to preserve its quality. As such, a moving mesh solver is necessary to deform the mesh and move the internal points in order to maintain the quality of the mesh and avoid solution degeneration due to mesh validity. A six degree of freedom (DOF) solid body motion approach in OpenFOAM was used to address this issue. The method was applied for simulation of pulsatile flows over BMHV with prescribed leaflet motions in the cardiac cycle and simulated for two cycles. In all the models, the flow was assumed to be continuous from the inlet to outlet and the valve leaflets were rotated along the Y-axis along the hinges. The finite volume method was used in the simulation.

3.3 Hemodynamic Assessment of Artificial Heart Valves

The heart valve performance depends mainly on the principles of flow fluid mechanics passing through it. Several hemodynamic parameters typically used in evaluation are transvalvular pressure gradients (ΔP), effective orifice area (EOA), Regurgitation, Flow Patterns and Shear Stress, and Cardiac Output (CO). These parameters help the design and evaluation of artificial heart valves. In this study, the flow patterns, shear stresses and cardiac output will be used as an assessment for the hemodynamic performances.

3.3.1 Transvalvular Pressure Gradients

An ideal way to quantify aortic stenosis is through transvalvular pressure gradients, which are flow-dependent and measurement of the pressure drop ($\Delta\rho$) across an artificial heart valve (Vahanian, 2012). This can affect the pressure within the left ventricle and is related to the energy lost due to the valves' presence. In natural valves, the pressure drops can be measured with invasively performed catheterization, where catheters are passed through the valves. This however cannot be performed through an artificial heart valve and has to be measured using continuous wave Doppler ultrasound velocimetry. The simplified Bernoulli equation is derived based on the assumptions that the flow through the stenosis is laminar with negligible viscous effects. Under mean conditions, it is shown:

$$P_1 - P_2 = \frac{1}{2}\rho(u_2^2 - u_1^2) \tag{3.2}$$

where P_1 and u_1 is the upstream location pressure and velocity and P_2 and u_2 is the downstream location pressure and velocity near the orifice. If the velocity downstream of the valve is much higher than the upstream velocity ($v_2 >> v_1$), such that u_1 can be neglected, then a simplified Bernoulli equation can be obtained:

$$\Delta P = 4u_2^2 \tag{3.3}$$

where ΔP is in (mmHg) and u_2 is in ms^{-1}.

3.3.2 Effective Orifice Area (EOA)

The convergence of streamlines blood flow through an opening of the valve (orifice) forms the flow passage, where high velocities, turbulence, shear stress and associated high-pressure drops are avoided. EOA is a standard measure of the clinical assessment on the effectiveness of valve opening during the forward flow phase (Dasi *et al.,* 2009). The flow through the valve is usually narrower compared to the geometric orifice area (GOA), as seen in Figure 3-2. A small EOA is usually linked with a higher net blood pressure loss across the valve.

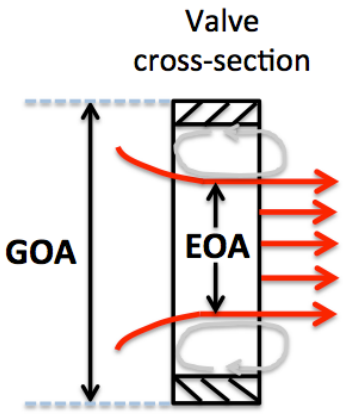

Figure 3-2: Comparison of the flow through the effective orifice area (EOA) and geometric orifice area (GOA)

Using the Gorlin relation, EOA is computed from measured flow and pressure drop and is based on the principle of conservation of energy:

$$EOA(cm^2) = \frac{Q_{rms}}{51.6\sqrt{\Delta\bar{p}}} \quad (3.4)$$

where Q_{rms} is the root mean square systolic/diastolic flow rate (cm^3s^{-1}) and $\Delta\bar{p}$ is the mean systolic/diastolic pressure drop (mmHg).

3.3.3 Regurgitation

Regurgitation is the reversed flow observed through the 'one-way' valve, and corresponds to the closing volume during valve closure and leakage volume after closure, as can be seen in Figure 3-3.

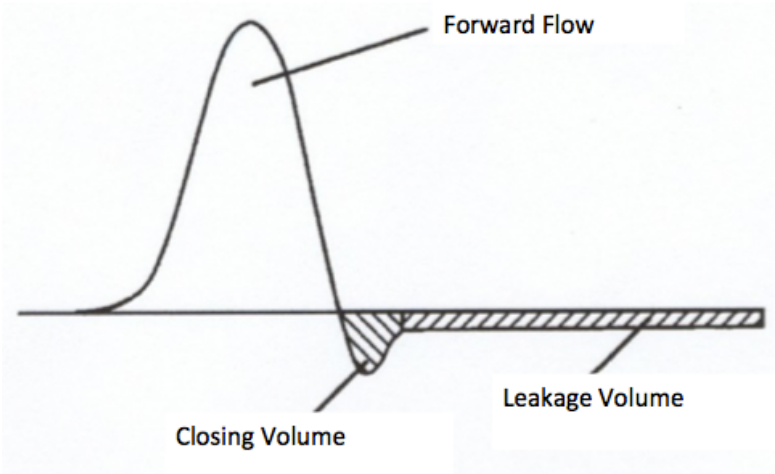

Figure 3-3: The forward flow, closing and leakage volume across artificial heart valve (Yoganathan 2000)

The percentage of regurgitation of the total stroke volume (SV) is calculated as follows:

$$\%\, reg = \frac{V_{reg}}{(V_{reg}+SV)} \tag{3.5}$$

where V_{reg} is the total volume of regurgitation due to V_{close}, regurgitation during closing and V_{leak}, regurgitation during leakage. The overall tendency for regurgitation is more prevalent in mechanical heart valves compared to tissue valves.

3.3.4 Flow Patterns and Shear Stress

The analysis of the blood flow patterns can determine the efficacy of the cardiovascular system. Non-physiological flow patterns can be detrimental and damage blood elements, often lead to thrombus formation. Recirculation regions are vortical areas where the concentration of coagulation inducing proteins and activated platelets can be found. These regions have high shear rates, and may cause stagnation points when platelets are directed toward a vessel wall in a fluid path. The speed of flow in the vessels influences the platelet collision frequency. As a result, higher platelet aggregation in recirculation region and adhesion to vessel walls are observed. Laminar or turbulent flow are often observed in a circulatory system and can be quantified by Reynolds number.

$$Re = \rho \frac{u\, D}{\mu} \tag{3.6}$$

where ρ is the density of the fluid (kgm^{-3}), u is the velocity of the flow (ms^{-1}), D is the diameter of the vessel (m) and μ is the dynamic viscosity of the fluid (Pa.s). Generally, a fluid flow is laminar for Re < 2000. Transition flow occurs between laminar and turbulent flow at 2000 < Re < 4000. At higher Reynolds number Re > 4000, fluid flow becomes turbulent. At peak flow in an aortic valve, the average Reynolds number is 4500 (Stalder *et al.,* 2011).

Blood flowing through a vessel will exert a physical force on the vessel wall. The tangential force is known as shear stress, which is the frictional force exerted by the flowing blood at the endothelial surface of the wall, as seen in Figure 3-4.

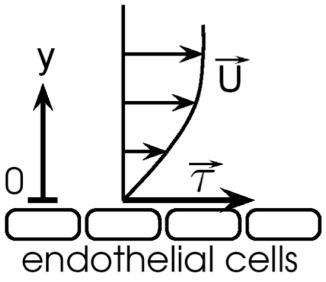

Figure 3-4: Shear stress (τ) is the frictional force exerted by the flowing blood on the endothelial surface of the vessel wall (Dumont, 2005)

The shear stress on the wall is usually known as wall shear stress, whereas the normal stress or pressure is perpendicular to the wall. The laminar flow shear stress is as follows:

$$\vec{\tau}_{laminar} = \mu \cdot \frac{\partial \vec{U}}{\partial y} = \mu \cdot \dot{\gamma} \text{ (N/m}^2\text{)} \quad (3.7)$$

where μ is the dynamic viscosity of the fluid, $\vec{U}$ is the velocity vector and $\dot{\gamma}$ is the shear rate. Meanwhile, the resistance to flow is increased by turbulent flow in the blood system, which leads to higher pressure gradients. The turbulent shear stress is as follows:

$$\vec{\tau}_{turbulent} = \mu \cdot \frac{\partial \vec{U}}{\partial y} - \rho\overline{u'v'} \quad (3.8)$$

where *u'* and *v'* are the turbulent fluctuations of the velocities *u* and *v* respectively. High shear stresses in the blood have shown to activate platelet, leading to thrombosis formation and risk of embolism (Kroll *et al.,* 1996).

3.3.5 Cardiac Output (CO)

The performance of the valve often depends on the blood flow through the valve. One of the important parameters used in valve performance evaluation is the total flow rate. In each cardiac cycle, the stroke volume (SV) of blood is pumped from the heart. The amount of cardiac cycles or beats per minute refers to the body heart rate (HR). The CO is the total volume of blood pumped by the ventricles per minute, which is usually 4-6 liters/min at rest and up to 20-35 liters/min during exercise.

$$\text{CO} = \text{SV} \times \text{HR} \quad (3.9)$$

3.4 Finite Volume Method

This section has been published in an earlier work (Nguyen *et al.,* 2012). In this study, flows were modeled for an incompressible viscous fluid and

governed by incompressible NS equations. The governing equations were then discretized using the finite volume method where a finite set of discrete equations was constructed on unstructured hybrid grids to approximate the NS equations. The construction was performed by a cell-centered FV approach where the FV discretization was based on the integral form of the governing equation over a polyhedral control volume. To handle movement of heart valves, the ALE formulation was used to discretize the system. ALE method was used to test the robustness of the moving mesh solver in OpenFOAM. The solver also allows simulation of the movement of the valve leaflets. A dynamic moving mesh approach was adopted to deform and regenerate the mesh, following the moving boundaries. The resulting numerical scheme was able to solve for flow through moving heart valves.

A second order Crank-Nicholson implicit time discretization with adjustable time-step at CFL number = 1 was used. A dynamic moving mesh approach was adopted to deform and regenerate the mesh following the moving boundaries. The resulting numerical scheme was able to solve for flows over moving heart valves. To understand the flow regimes in a cardiac cycle, CFD simulations was performed to investigate flow through the BMHV at aortic area under the pulsatile conditions of velocity and pressure deduced from a typical human cardiac cycle.

3.4.1 Governing Equations

For blood flow through heart valves, the governing equations are the 3-dimensional unsteady incompressible continuity and Navier-Stokes (NS) equations (Sotiropoulos *et al.,* 2009):

$$\frac{\partial u_i}{\partial x_i} = 0 \tag{3.10}$$

$$\frac{du_i}{dt} = \frac{\partial p}{\partial x_i} + \frac{1}{Re}\frac{\partial^2 u_i}{\partial x_j \partial x_j} \tag{3.11}$$

where u_i are the Cartesian velocity components, *p is* the pressure divided by the density *ρ*, *a*nd *Re is* the Reynolds number of the flow based on a characteristic length and velocity scale. *d/dt* is the material derivative defined as:

$$\frac{d}{dt}(\cdot) = \frac{\partial}{\partial t}(\cdot) + u_j \frac{\partial}{\partial x_j}(\cdot) \tag{3.12}$$

Blood is assumed to be Newtonian even though there are small regions of the flow domain (areas at the valve hinges and jet leakage during valve closure) in which non-Newtonian effects could be important. According to Sotiropoulos *et al.*, (2009), Equation 3.11 needs to be solved in a domain defined by the aortic lumen and the left ventricle within which the leaflets are immersed. The motion of the left ventricle, which creates the physiologic pulse that drives the blood flow through the aorta, will be replaced by a physiologic inflow waveform.

In the study by Dumont et al., (2007), blood was assumed to be laminar, incompressible and Newtonian with a density of 1050kgm^{-3} and viscosity of 4×10^{-3}kgm^{-1}s^{-1}. The blood flow followed a prescribed velocity waveform, with a systole lasting 0.4s and diastole 0.6s. Inlet velocity had a spatial trapezoidal distribution, which later developed into a parabolic velocity profile. Figure 3-5 shows the inlet velocity-time pattern and trapezoidal spatial inlet profile.

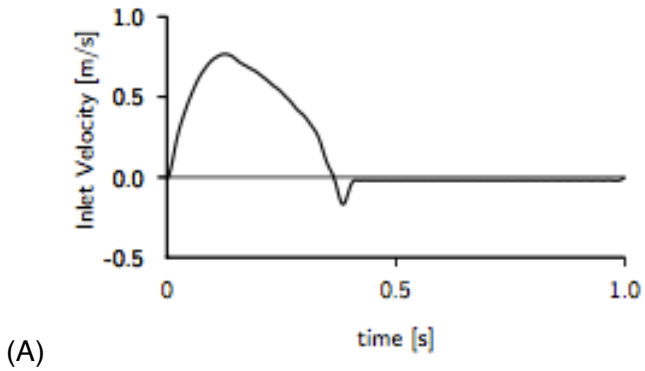

(A)

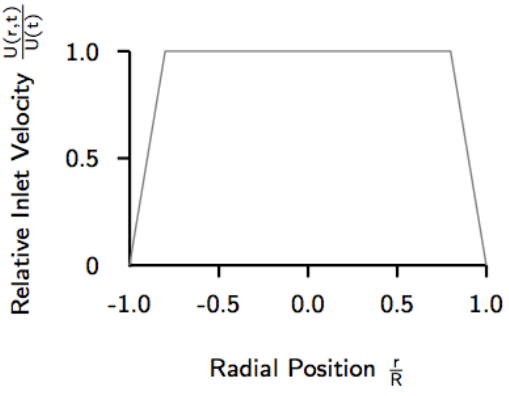

(B)

Figure 3-5: Inlet aortic velocity-time pattern and spatial profile, (A) inlet aortic velocity-time pattern, (B) Trapezoidal spatial inlet velocity profile (Dumont *et al.,* 2007)

In the study by Choi *et al.,* (2003), the pressure boundary condition followed the pressure waveforms measured in vitro as shown in Figure 3-6. Blood was

also modeled as Newtonian fluid with density of 1000kgm^{-3} and dynamic viscosity 3.5×10^{-3}kgm^{-1}s^{-1}. Leaflet opening angle varied between 25° and 85° where opening angle was computed at each time-step.

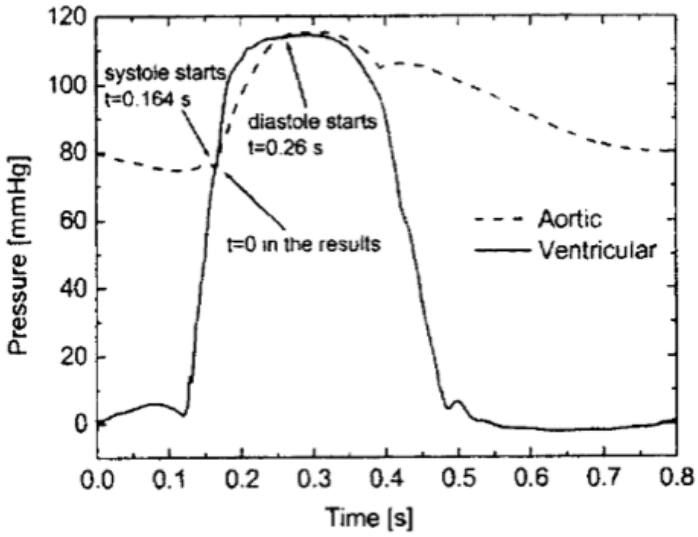

Figure 3-6: Pressure waveform at simulation boundaries (Choi *et al.,* 2003)

In this research, considering incompressible viscous flows over a domain Ω, the governing incompressible NS equations and boundary condition that express the conservation of mass and momentum are written as follows:

$$\nabla \cdot \boldsymbol{u} = 0 \quad \text{in } \Omega, \tag{3.13}$$

$$\frac{\partial \rho \boldsymbol{u}}{\partial t} + \boldsymbol{u} \cdot \nabla \rho \boldsymbol{u} = -\nabla p + \nabla \cdot (\mu \nabla \boldsymbol{u}) + \boldsymbol{f} \quad \text{in } \Omega, \tag{3.14}$$

$$\boldsymbol{u}(t=0) = \boldsymbol{u_0} \quad \text{in } \Omega. \tag{3.15}$$

In these equations, velocity vector is denoted by $\boldsymbol{u}$, ρ is the density, p is the pressure and μ is the dynamic viscosity of the fluid. The blood is considered as Newtonian fluid of density ρ=1050kgm^{-3} and kinematic viscosity of v=3.81x10^{-6}m^{2}s^{-1}. $\boldsymbol{f}$ is the body force and the total fluid stress tensor including pressure and viscous force can be expressed as:

$$\sigma = \boldsymbol{\tau} - p\boldsymbol{I}, \quad \boldsymbol{\tau} = \mu(\nabla \boldsymbol{u} + \nabla \boldsymbol{u}^T) \tag{3.16}$$

where τ is the viscous stress. The flow is characterized by Reynolds number,

$$Re = \frac{U_{ref} L_{ref}}{v} \tag{3.17}$$

where U_{ref} and L_{ref} are the reference velocity and length scale. The equations are closed with boundary conditions imposed on the boundary of the domain $\Gamma=\delta\Omega$ as:

$$\boldsymbol{u} = \overline{\boldsymbol{u}} \ \ in\ \Gamma_D, \tag{3.18}$$

$$\boldsymbol{\sigma}.\boldsymbol{n} = \overline{\boldsymbol{t}} \ \ in\ \Gamma_N, \tag{3.19}$$

where $\Gamma = \Gamma_N \cup \Gamma_D$. Γ_N denotes a boundary where Neumann conditions are applied in the form of prescribed tractions ($\bar{\boldsymbol{t}}$) and Γ_D corresponds to a Dirichlet boundary on which the velocity is imposed (Nguyen et al., 2012).

3.4.2 Finite Volume Discretization

Finite volume method is based on the integral form of the governing equations over the arbitrary moving domain Ω bounded by closed surface Γ as follows:

$$\oint_{\Gamma} \boldsymbol{n} \cdot \boldsymbol{u} dS = 0 \tag{3.20}$$

$$\frac{\partial}{\partial t}\int_{\Omega} \rho \boldsymbol{u} dV + \oint_{\Gamma} \boldsymbol{n} \cdot \rho(\boldsymbol{u} - \boldsymbol{u}_S)\boldsymbol{u} dS = \oint_{\Gamma} \boldsymbol{n} \cdot (\mu \nabla \boldsymbol{u}) dS - \int_{\Omega} \nabla p dV + \int_{\Omega} \nabla \boldsymbol{f} dV \tag{3.21}$$

In the above expression, $\boldsymbol{n}$ is the outward normal vector to the bounding surface Γ and $\boldsymbol{u}_S$ is the moving velocity of the surface. As the boundary moves, the geometric conservation law (GCL) (Ferziger and Peric 1999) defines the conservation of space with respect to the change in volume and boundary velocity

$$\frac{\partial}{\partial t}\int_{\Omega} dV - \oint_{\Gamma} \boldsymbol{n} \cdot \boldsymbol{u}_S dS = 0 \tag{3.22}$$

The computational domain is then subdivided into a set of non-overlapping polyhedral elements or control volumes. Figure 3-7 shows a sample control volume at point P and its notations of faces and neighboring cells. The FV discretization transforms surface and volume integrals into a sum of face and control volume integrals and approximates them to second order accuracy. The FV discretization of momentum equation (3.21) for every moving control volume V_P is written as:

$$\frac{\partial}{\partial t}\rho \boldsymbol{u}_P V_P + \sum_f (F - F_S)\boldsymbol{u}_f = \sum_f \mu_f \boldsymbol{n}_f \cdot (\nabla \boldsymbol{u})_f S_f + (\nabla p)_P V_P \tag{3.23}$$

where the subscript P denotes volume values, f represents face values, V_P is the cell volume and S_f is the face area. In this expression F is the face fluid flux $F = \rho_f(\boldsymbol{n}_f \cdot \boldsymbol{u}_f)S_{\boldsymbol{f}}$ and F_S is the face moving volume flux satisfying the GCL condition (3.22).

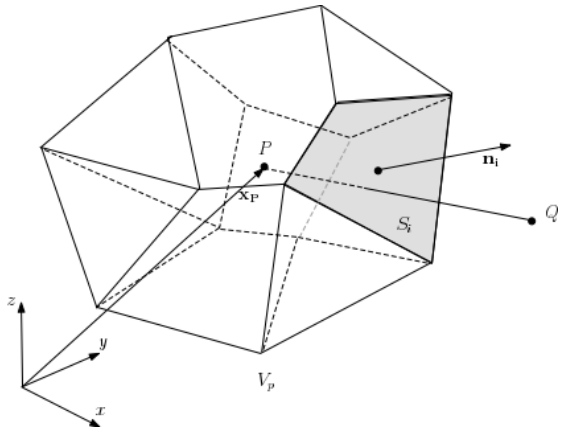

Figure 3-7: Illustration of polyhedral control volume V_P around point P located at the centroid of the cell. The control volume is bounded by convex polygons or faces S_i with the face unit normal vector n_i. Each face S_i is only shared between two adjacent cells P and Q

In the discrete form, equation (3.22) is expressed as

$$\frac{V_P^{(t+\Delta t)} - V_P^t}{\Delta t} - \sum_f F_S = 0 \tag{3.24}$$

Thus the moving volume flux F_S is consistently computed as the volume swept by the face *f* in motion during the current time-step rather than from the mesh velocity $\boldsymbol{u}_S$. The spatial and temporal discretizations have been implemented and well tested in the open source package OpenFOAM (Weller *et al.,* 1998).

3.5 Simulation parameters

3.5.1 Geometric Model

Different valve geometries were used in the various studies. There were four general geometries modeled as follows: (i) a simplified axisymmetric sinus in a straight downstream pipe (simple-straight), (ii) a simplified axisymmetric sinus in a downstream curved aortic arch (simple-arch), (iii) a three-sinus aortic root model in a straight downstream pipe (three-sinus straight) and (iv) a three-sinus aortic root model in a simplified downstream curved aortic arch (three-sinus arch), as shown in Figure 3-8. The different heart valve designs were inserted in the each geometric model. The computational fluid domain of each of the four cases; namely simple-straight, three-sinus straight, simple-arch and three-sinus arch was subdivided into an unstructured mesh of ranging from approximately 3.6×10^6 tetrahedral elements.

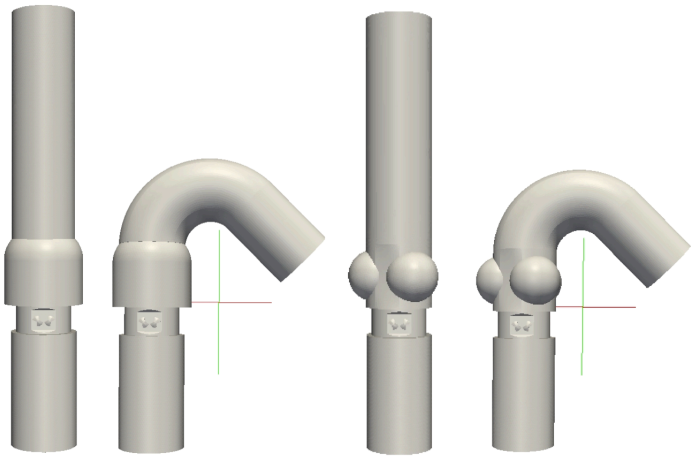

Figure 3-8: Different geometric models used in the simulation studies consist of simple-straight, simple-arch, three-sinus straight, and three-sinus arch

Figure 3-9 shows one of the meshes created for the heart valve model simulation using Gambit and viewed in ParaView. Mesh is drawn based on the geometry of the valve holder with SJM Bileaflet Mechanical Heart Valve. The centerline of the aorta followed the curvature of the normal diameters for the thoracic aorta of adults obtained by helical computed tomography (Hager et al 2002). To minimize the computational time, the normal model under steady-state was selected for grid independence test. Models with $2.5x10^6$, $3.6x10^6$, $4.5x10^6$ and $5.6x10^6$ elements were simulated, and the one with $3.6x10^6$ elements was chosen based on the critern that the relative difference between the maximum velocity with respect to the one with $5.6x10^6$ elements was less than 0.5%.

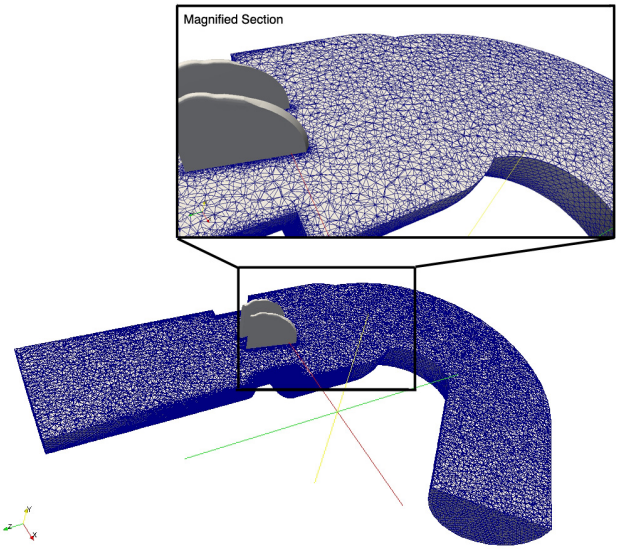

Figure 3-9: Computational grid of the 3-dimensional mechanical heart valve in a simplified aorta with curved downstream and magnified grid section

3.5.2 Valve Models

The GAMBIT preprocessor was utilized to create the mesh for heart valve simulation. For mechanical valve, the 29mm ATS Open Pivot Heart Valve and 29mm SJM Masters Series were used. The ATS valve was drawn without hinge while the SJM was drawn with hinge. The other valve that was drawn in Gambit is the trileaflet mechanical heart valve which is based on Li and Lu (2012). GAMBIT allows the freedom to define the size function, the cell gaps and the growth rate. The mesh between the hinge and the hinge holder was set to 10 cells per gap, while several different growth factors were adjusted to ensure that the mesh quality is maintained. The mesh element can be set as primarily hexahedral or tetrahedral. The three valves can be viewed in ParaView as shown in Figure 3-10. The 3-dimensional models of the mechanical heart valves were drawn based on the geometry of commercially available valves as accurate as possible as shown in Figure 3-11. It is assumed that the valve is in the maximum opening angle of 85°.

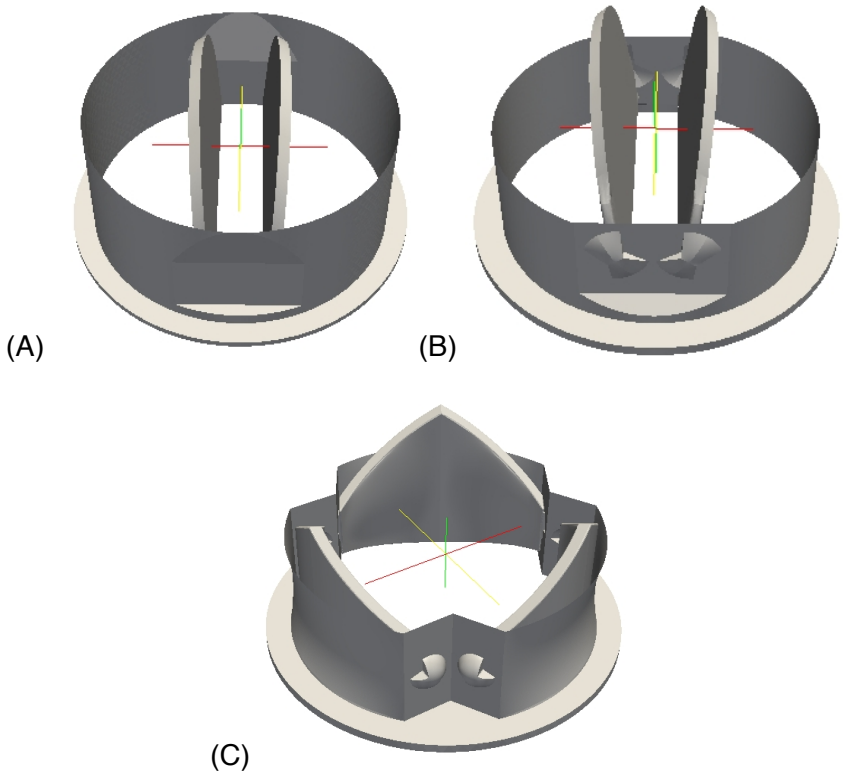

Figure 3-10: Heart Valve model as viewed in ParaView (A) ATS Open Pivot Bileaflet Heart Valve without hinge (B) SJM Masters Series Bileaflet Mechanical Heart Valve (C) Trileaflet Mechanical Heart Valve

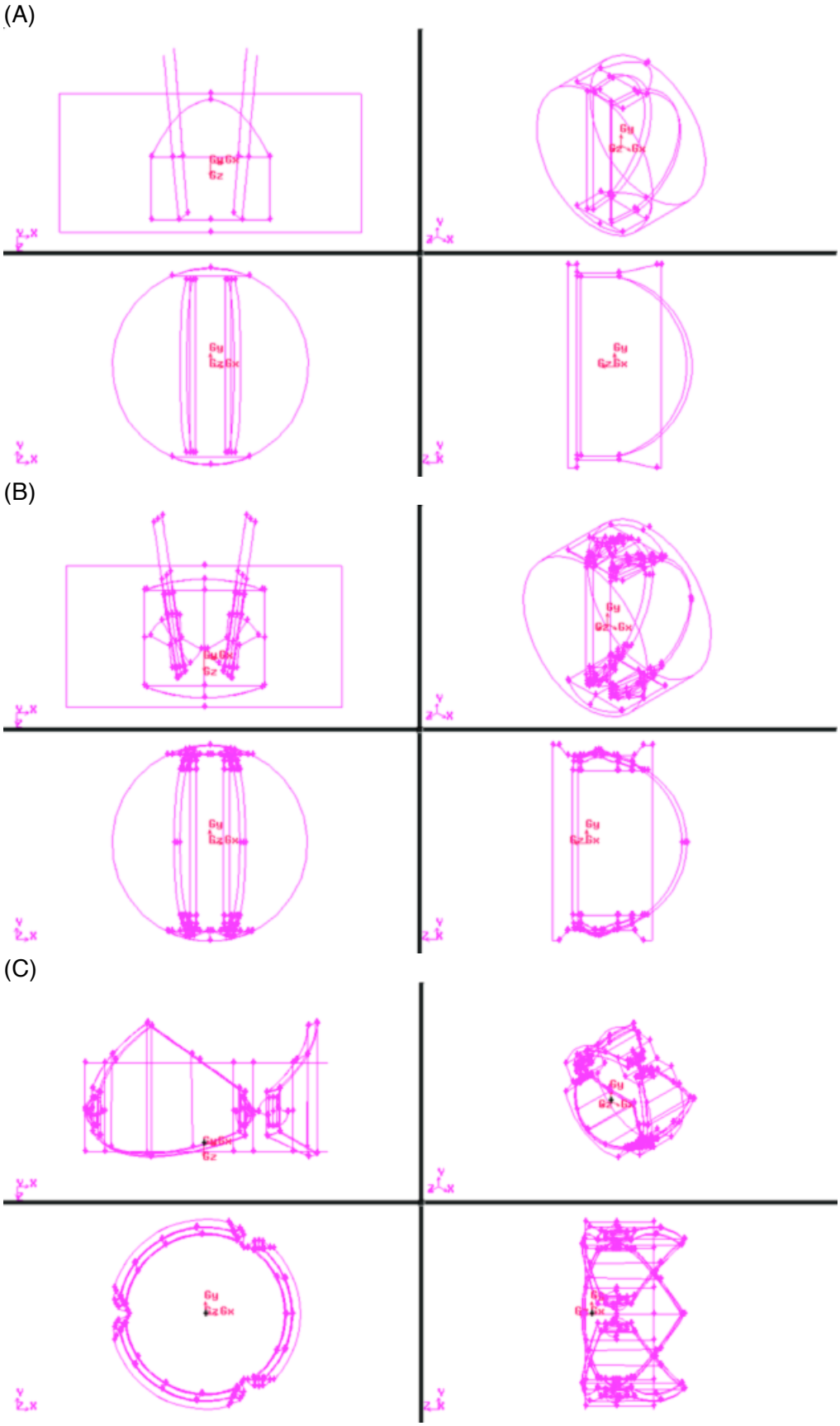

Figure 3-11: Heart Valve model as viewed in Gambit (A) ATS Open Pivot Bileaflet Heart Valve without hinge (B) SJM Masters Series Bileaflet Mechanical Heart Valve (C) Trileaflet Mechanical Heart Valve

3.5.3 Boundary Conditions

Generally, the Dirichlet and Neumann boundary conditions can be effectively implemented in the context of the current finite volume discretization. For a Dirichlet type of boundary conditions where a fixed value of dependent variables Φ_b is prescribed at the boundary, the value of the variable can be directly set as the boundary value $\Phi_f = \Phi_b$ while the gardient of the variable can be reconstructed as

$$\boldsymbol{S}_f \cdot (\nabla\phi)_f = |S_f| \frac{\phi_b - \phi_P}{|d|} \tag{3.25}$$

In this expression, ***d*** is the distance vector from a point on the surface to the control point P. As for Neumann type of boundary conditions, gradient of variables in normal direction to the boundaries are specified

$$g_b = \left(\frac{\boldsymbol{S}}{|\boldsymbol{S}|} \cdot \phi\right)_f \tag{3.26}$$

Thus the gradient of the variables at the face can be recovered directly as $\boldsymbol{S}_f \cdot (\nabla\phi)_f = |S|_f g_b$, while the value of the variable can be interpolated as

$$\phi_f = \phi_P + |\boldsymbol{d}|\, g_b \tag{3.27}$$

In the study, a fully developed parabolic velocity profile was generated based on the Hagen-Poiseuille equation. No slip boundary condition was assumed at the channel walls as well as at the valves wall. Parabolic laminar flow for the cylindrical tube was generated using a user defined velocity, Groovy Boundary Condition (**groovyBC**) as shown in Figure 3-12. The code is provided in Appendix A. Pulsatile flow mimics flow in an actual human heart through a BMHV in aortic position. To generate a user defined velocity profile, **timeVaryingUniformFixedValue** pressure inlet and velocity outlet were used.

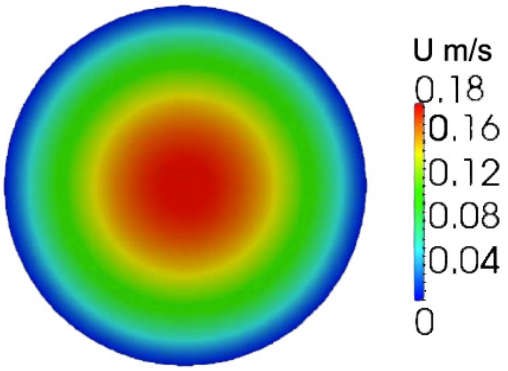

Figure 3-12: Parabolic flow using groovyBC

3.5.4 Full Cardiac Cycle Modeling

Typically, a cardiac cycle is divided into a systolic and diastolic time interval where the heart's atria and ventricles are working synchronously to pump the blood through the circulatory system. In order to investigate the errors of the initial configuration over multiple cardiac cycles, the BMHV was simulated over two cardiac cycles. Usually, simulation is done over at least three cardiac cycles. However, no significant difference was found between the first and second cardiac cycles. As such, results were presented for the second cycle.

The prescribed periodic condition started at fully open position of the valve, where ejecting velocity kept increasing from zero to a peak value of $1.35ms^{-1}$. The duration of the systole was 0.3s. During this period, aortic pressure also increased. The valve then moved from open to closed position in about 0.04s, while velocity dramatically dropped to zero until full closure of the valve leaflets. The valve remained at fully closed position during diastole for about 0.48s. Backflow occurred at the inlet when it opened again for about 0.04s due to a further decrease in aortic pressure. The whole cycle of about 0.86s was derived from a heart beat condition of a healthy person, which corresponds to about 70 bpm. The leaflets motion was set at a constant angular velocity of $1000degs^{-1}$ to correspond to the inlet velocity and for the valve to move from fully open to closed position.

The complete cardiac cycle of the flow which is divided into four main phases: valve fully opened, valve closing, valve fully closed and valve opening, is shown in Table 3-1.

Table 3-1: Duration for each flow phase

Heart Valve Phase	Duration (seconds)
Fully Opened	0.30
Closing	0.04
Fully Closed	0.48
Opening	0.04
Total	**0.86**

The flow has a periodic pressure and velocity arising from systematic pumping of the heart. In this study, inlet refers to the flow from left ventricle and has the pressure defined, whereas outlet refers to the aorta and has the velocity defined. Flow inlet does not have both the pressure and velocity fixed simultaneously because of the likelihood of simulation error occurrence.

The outlet velocity-time profile was obtained through regression and interpolation of several data points. As the velocity-time profile varies from an individual to another, most sources do not display every data points but a graph instead. However, regression and interpolation of several data points provides a reasonable estimate. Data points for velocity profile from the left ventricle were obtained from Lim *et al., (*2001). Using the data points, a Piecewise Cubic Interpolating Polynomial (PCHIP) interpolation method was adopted using MATLAB to create a list of data points with time-step of 0.0005s. The finalized velocity-time profile is as shown in Figure 3-13. In the study, flows over the BMHV were initialized with free stream initial conditions where velotiy and pressure were given.

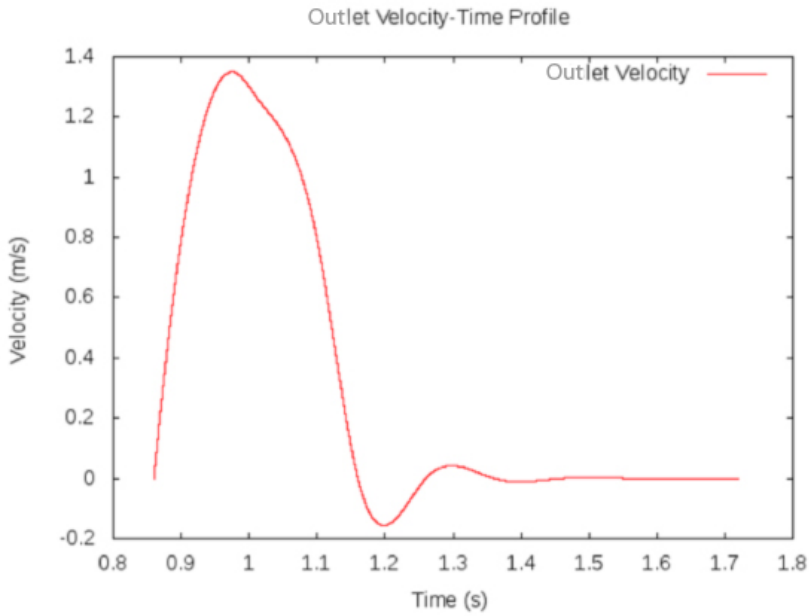

Figure 3-13: Outlet velocity-time profile

Pressure-time profile at the outlet is obtained with similar methods as velocity-time profile. Data points for aorta pressure-time profile were obtained from Nichols and O'Rourke (2005) and interpolated using MATLAB. The finalized pressure-time profile is as shown in Figure 3-14.

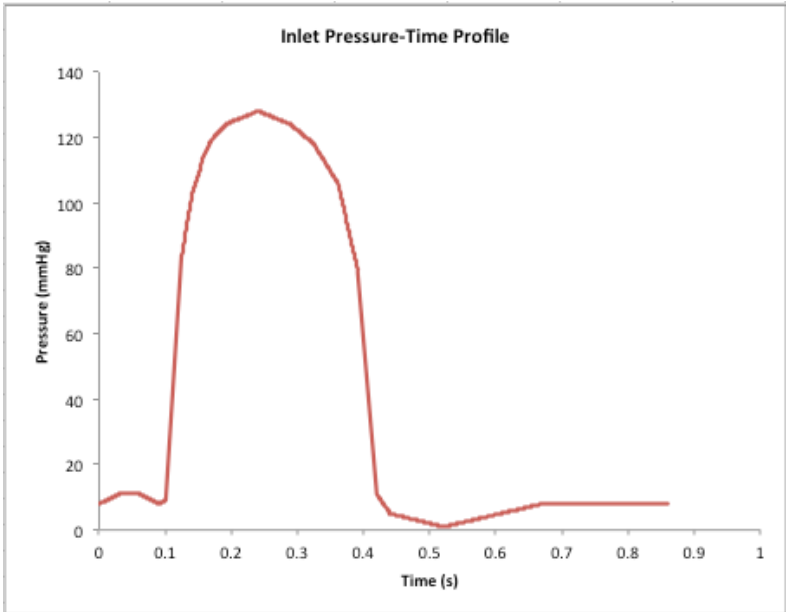

Figure 3-14: Inlet pressure-time profile

As the velocity-time and pressure-time profile were obtained from different sources, it is vital to ensure that these two graphs have valve movement timing synchronized. Rate of change of the left ventricle volume could represent the inlet velocity from the left ventricle. The no-slip boundary condition was assumed at the walls.

3.5.5 Wall Shear Stress

OpenFOAM uses **wallShearStress** command to calculate and write wall shear stress for the specified times when using RANS turbulence models. The code is provided in Appendix A. The wall shear stress, τ_w, is given by

$$\tau_w = \mu \left(\frac{\partial u}{\partial y}\right)_{y=0} \tag{3.28}$$

where μ is the dynamic viscosity, u is the flow velocity parallel to the wall and y is the distance to the wall. The unit of wall shear stress is Pascal (Pa) or $kgm^{-1}s^{-2}$.

3.6 Laminar Modeling for Steady Flow

For steady laminar flow simulation, a fully developed flow condition is required. The flow profile changes with position in the entrance region as shown in Figure 3-15. To minimize difficulty in predicting the flow profile at the instant when fluid arrives at BMHV, it would be optimum to ensure that the flow is fully developed upon reaching the valve in both experiment validations

and simulations. Three laminar flow cases were performed by simulations as well as experimentally for Reynolds numbers 350, 750, and 1,000. The mean velocity of the fluid can be related to Hagen-Poiseuille equation through the maximum velocity of the fluid.

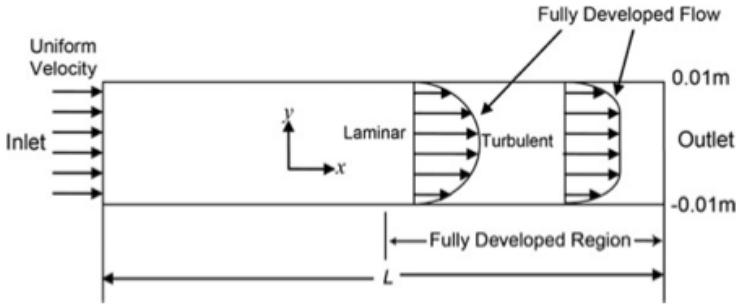

Figure 3-15: Change in velocity profile along entrance region (Tu *et al.,* 2013)

Table 3-2 shows the maximum velocity of fluid for each of the Reynolds number.

Table 3-2: Average and maximum velocity for Re=350, 750 and 1,000

Re	ρ (kgm^{-3})	D (m)	μ (kgm^{-1}s^{-1})	u (ms^{-1})	u_{max} (ms^{-1})
350	1050	0.028	4.0 x 10^{-3}	0.0476	0.0953
750	1050	0.028	4.0 x 10^{-3}	0.102	0.204
1000	1050	0.028	4.0 x 10^{-3}	0.136	0.272

3.7 Turbulence Modeling

Turbulence modeling contructs and uses a model to predict the effects of turbulence. It includes the additional algebraic or transport equations to augment the governing averaged equations (momentum, continuity and energy) to account for the turbulence fluxes and Reynolds stresses. The turbulence modeling in CFD was described earlier in section 1.12.1. The current study aims to develop a code, which can help the decision-making process for clinicians in the most effective way. The decision was to solve the RANS appended with a turbulence model. Since the large-scale features of the flow dynamics is the focus in this study, RANS provides a good balance between the results and the computational cost. In this work, RANS equations are solved with two most popular turbulence models, namely

Spalart-Allmaras and *k-epsilon*. In both models, the transport equation for turbulence kinetic energy is written as:

$$\frac{\partial k}{\partial t} + \overline{u_j}\frac{\partial k}{\partial x_j} = \tau_{ij}\frac{\partial \overline{u_i}}{\partial x_j} - \epsilon + \frac{\partial}{\partial x_j}\left[(\upsilon + \upsilon_t/\sigma_k)\frac{\partial k}{\partial x_j}\right] \tag{3.29}$$

The Reynolds Averaged for velocity can be written as

$$\boldsymbol{u}(\boldsymbol{x},t) = \overline{\boldsymbol{u}}(\boldsymbol{x},t) + \boldsymbol{u}'(\boldsymbol{x},t) \tag{3.30}$$

where ***u'(x,t)*** is the fluctuation about the average value ***ū(x,t).*** In these expressions,

$\epsilon = \upsilon\overline{\nabla u' : \nabla u'}$ is the dissipation of the kinetic energy, σ_k is the closure coefficient and ν_t is the turbulent or eddy viscosity which is determined by the appended turbulence model.

3.7.1 Spalart-Allmaras Model

In the SA model (Spalart 2000), kinematic eddy viscosity is modeled as

$$\upsilon_t = \tilde{\upsilon} f_{v1},\ f_{v1} = \frac{X^3}{X^3 + c_{v1}^3},\quad X = \frac{\tilde{\upsilon}}{\upsilon}, \tag{3.31}$$

where $\tilde{\upsilon}$ is the modified kinematic viscosity.

The transport equation for eddy viscosity is deduced from (4.19) as

$$\frac{\partial \tilde{\upsilon}}{\partial t} + \overline{u}_j\frac{\partial \tilde{\upsilon}}{\partial x_j} = c_{b1}\tilde{S}\tilde{\upsilon} - c_{w1}f_w\left(\frac{\tilde{\upsilon}}{d}\right)^2 + \frac{1}{\sigma_k}\frac{\partial}{\partial x_j}\left[(\upsilon + \widetilde{\upsilon})\frac{\partial \tilde{\upsilon}}{\partial x_j}\right] + \frac{c_{b2}}{\sigma_k}\frac{\partial \tilde{\upsilon}}{\partial x_j}\frac{\partial \tilde{\upsilon}}{\partial x_j}, \tag{3.32}$$

where *d* is the distance from the closest surface. The standard SA model includes eight closure coefficients:

$$c_{b1}=0.1335,\quad c_{b2}=0.622,\quad c_{v1}=7.1,\quad \sigma_k=2/3, \tag{3.33}$$

$$c_{w1} = \frac{c_{b1}}{\kappa^2} + \frac{(1+c_{b2})}{\sigma_k},\quad c_{w2}=0.3,\ c_{w3}=2,\quad \kappa=0.41 \tag{3.34}$$

There are many different forms of SA models whose details can be found in (Spalart 2000).

3.7.2 k-epsilon Model

In the k-epsilon model, the kinematic eddy viscosity is expressed as a function of the turbulent kinetic energy *k* and its dissipation rate ε as

$$\upsilon_t = C_\mu\frac{k^2}{\varepsilon} \tag{3.35}$$

The transport equation for the dissipation rate is written as follows

$$\frac{\partial \varepsilon}{\partial t} + \overline{u_j}\frac{\partial \varepsilon}{\partial x_j} = C_{\varepsilon 1}\frac{\varepsilon}{k}\tau_{ij}\frac{\partial \overline{u_i}}{\partial x_j} - C_{\varepsilon 2}\frac{\varepsilon^2}{k} + \frac{\partial}{\partial x_j}\left[(\upsilon + \frac{\upsilon_t}{\sigma_\varepsilon})\frac{\partial \varepsilon}{\partial x_j}\right] \tag{3.36}$$

The closure coefficients are:

$$C_{\varepsilon 1}=1.44,\ C_{\varepsilon 2}=1.92,\quad C_\mu=0.09,\quad \sigma_k=1.0,\quad \sigma_\varepsilon=1.3 \tag{3.37}$$

There are several other two-equation models that try to describe the turbulence including the RNG k–epsilon model (Yakhot and Orszag 1986) and the nonlinear k-epsilon Shih model (Shih et al., 1994). Many of them are based on the k–epsilon model described above; however, they are more complicated and contain more parameters than the standard k–epsilon model. All of these models including the above one-equation SA model are implemented in the OpenFOAM package.

3.8 Moving Mesh Technique using ALE

To handle the mesh movement in the simulation, the moving mesh technique using ALE is used, where the moving mesh velocity, $\boldsymbol{u_S}$, can be arbitrarily found such that the moving velocity at the interface is equal to the boundary velocity, $\boldsymbol{u_\Gamma}$, either prescribed for fixed boundaries or obtained from the structure response in applications of Fluid-Structure Interaction. Due to the movement of the boundaries, the computational mesh is deformed and possibly fails to preserve its quality. A moving mesh solver is necessary to deform the mesh and move the internal points in order to maintain the quality of the mesh and avoid solution degeneration due to mesh validity. In the context of ALE framework, one has to either regularize the grid moving velocity or decide to re-mesh after certain steps, which often leads to an increased computational cost and loss of accuracy and conservation. Deriving a robust and efficient scheme of constructing mesh velocity could help in reducing the effort of remeshing. This has motivated many different approaches for computing the grid velocity, including the velocity smoothing technique in which the mesh velocity is directly computed from the velocity of the moving boundaries in order to minimize the grid distortion, such as Laplacian smoothing with variable diffusivity approaches (Lohner and Yang 1996, Lomtev et al., 1999).

The Laplacian smoothing is able to distribute the nodes according to a certain distribution function. However, it is not directly related to a measure of element quality and may cause badly shaped elements during the process, especially for 3-dimensional unstructured grids. In parallel development, a mesh optimization-based smoothing approach (Brewer *et al.,* 2003), adopted in the work, is more attractive in maintaining the quality of the mesh for

moving boundary problems. Casting the mesh smoothing as an optimization problem, the method optimizes the mesh quality based on a particular quality metric and optimization criteria to ensure the quality of mesh. Given a distorted mesh $\mathcal{M}(v_i, e_j)$ of n vertices and k elements, the objective of the method is to distribute the mesh points such that the quality of the mesh is maximized. Mathematically, the mesh optimization problem can be formulated as follows:

$$\boldsymbol{x}=\arg\max \mathcal{F}=f(q_i(\boldsymbol{x})),\ \ \forall \boldsymbol{x}, i \in \mathcal{M} \tag{3.38}$$

where $q_i(\boldsymbol{x})$ is the element or vertex based quality metric of mesh entities and $f(q_i(\boldsymbol{x}))$ is the objective function. The objective functions operating on different quality metrics can be combined together to provide maximum flexibility in controlling the mesh quality. When the mesh is modified, conjugate gradient or feasible Newton optimization algorithms can be used to look for optimal positions. The method is proven to be capable of extensively providing an effective way to maintain and improve the mesh quality due to the movement of the domain boundaries. In situations of large deformations, vertices may undesirably deform too much; and upon exceeding the smoothing capability, mesh topology needs to be modified. In order to maintain the mesh quality, topology modification operations, including edge swapping, bisection and collapse as shown in Dai and Schmidt (2005), can be employed. Figure 3-16 shows the application of the approach for a simple problem of two cubes rotating with prescribed velocities using Mesquite Smoother in OpenFOAM.

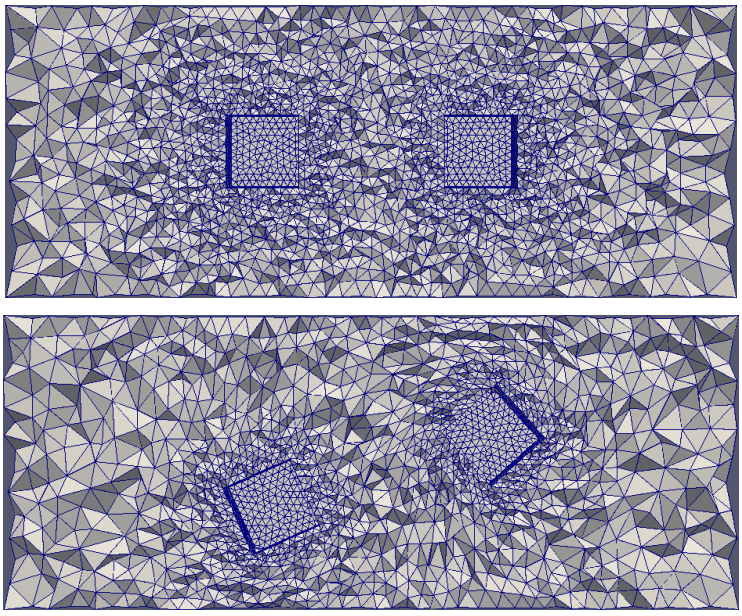

Figure 3-16: Moving mesh solver for motion of 2 cubes in a channel: Initial Mesh (top), deformed mesh conforming to the motion of the cubes (bottom)

Another type of mesh motion was used to solve the Laplace smoothing equation for a given mesh by the Finite Element Method. The mesh is rebuilt after a decomposition of all cells and faces (Kassiotis, 2008).

3.9 Fluid-Structure Interaction

The prescribed movement of the valve leaflets do not take into account the interaction of the fluid flow with respect to the leaflets. These interactions change the boundary conditions of the flow and rotate the leaflets based on the force generated from the fluid flow. As such, there is a need to consider fluid structure interaction in the study. The FSI phenomenon involves two domains; the fluid and the structure domains. Different types of boundary conditions couple the two domains. The first type of boundary condition is the force exerted on the immersed structure by the fluids. The fluid forces on the structures are interpolated for the structural nodes on the FSI interface after the computation of flow field. Subsequently, the movement of the structure will be applied. The other type of boundary condition is the velocity continuity at the fluid-structure interface. At the same location on the surface, the velocity of fluid is equal to that of the structure. This simply means that the structure movement follows the movement of its surrounding fluids. According to Xia *et al.,* (2009), the velocity continuity is enforced through the velocity extrapolations for the ghost nodes, thus representing the influence of the immersed structure on the fluid flow and providing a boundary condition for the computation of fluid flow.

The computation is to be performed with dynamic mesh model in the OpenFOAM using modified FSI solver package. The leaflet is assumed to be a rigid body in rotation around a fixed hinge axis. The equation of motion for the stiff valve leaflet is as follows (Dumont, 2005):

$$\ddot{\theta} + \zeta\dot{\theta} = {}^{M}/_{I} \tag{3.39}$$

with M as the moment resulting from the forces acting on the surface of the leaflet, I as the moment of inertia, θ as the angle that determines the position of the leaflet, and ζ is the damping coefficient which is often neglected due to the small value compared to the flow forces.

For the valve leaflet, the moment of inertia, *I,* with the rotational axis at the end of the leaflet is given by:

$$I = (1/3)ml^2 \tag{3.40}$$

with $m = \rho lt$, where *m is* the mass of the leaflet per unit length, ρ is the density of the leaflet, *t* is the thickness of the leaflet and *l* is the length of the leaflet.

In most FSI algorithms, the fluid and structure domains are coupled by these two boundary conditions. The process of FSI between the flow and leaflets is shown in Figure 3-17. There is a sub-iteration FSI cycle besides the time advancement cycle for the fluid. At the start, the variables $t, \Delta t, n, k, I, \theta, \dot{\theta}\ and\ \ddot{\theta}$ are initialized. The subsequent position of the leaflets is calculated.

$$\dot{\theta}_{n+1} = \dot{\theta}_n + \ddot{\theta}_{n+1} \cdot \Delta t \tag{3.41}$$

$$\theta_{n+1} = \theta_n + \dot{\theta}_{n+1} \cdot \Delta t \tag{3.42}$$

The indices *n* and *n+1* correspond to the time *t* and $t+\Delta t$. An iterative approach is used to obtain the new position θ_{n+1} at $t + \Delta t$. For each time-step, *k* iterations are performed in order to reach convergence of equation 3.39.

Using OpenFOAM package, the new position of $\theta_{n+1}^{k=0}$ is computed with the previous value of the angular acceleration $\ddot{\theta}_n$. Using equation 3.41 and 3.42, the angle of the leaflets can be established. The mesh is then adapted with the dynamic mesh model at $t+\Delta t$ based on the initial guess of the new position. Following that, OpenFOAM will solve the continuity and momentum equations of the flow. When the NS equations converge, $M_{n+1}^{k=0}$ is calculated based on equation 3.43.

$$\varepsilon > |M_{n+1}^{k} - I\ddot{\theta}_{n+1}^{k}| \tag{3.43}$$

After each sub-iteration, the convergence value is checked whether it is below the threshold, ε, at $500s^{-2}$ (Nobili *et al.,* 2008). This step will be repeated until convergence of equation 3.43 is achieved. The simulation ends when $t=T_{END}$.

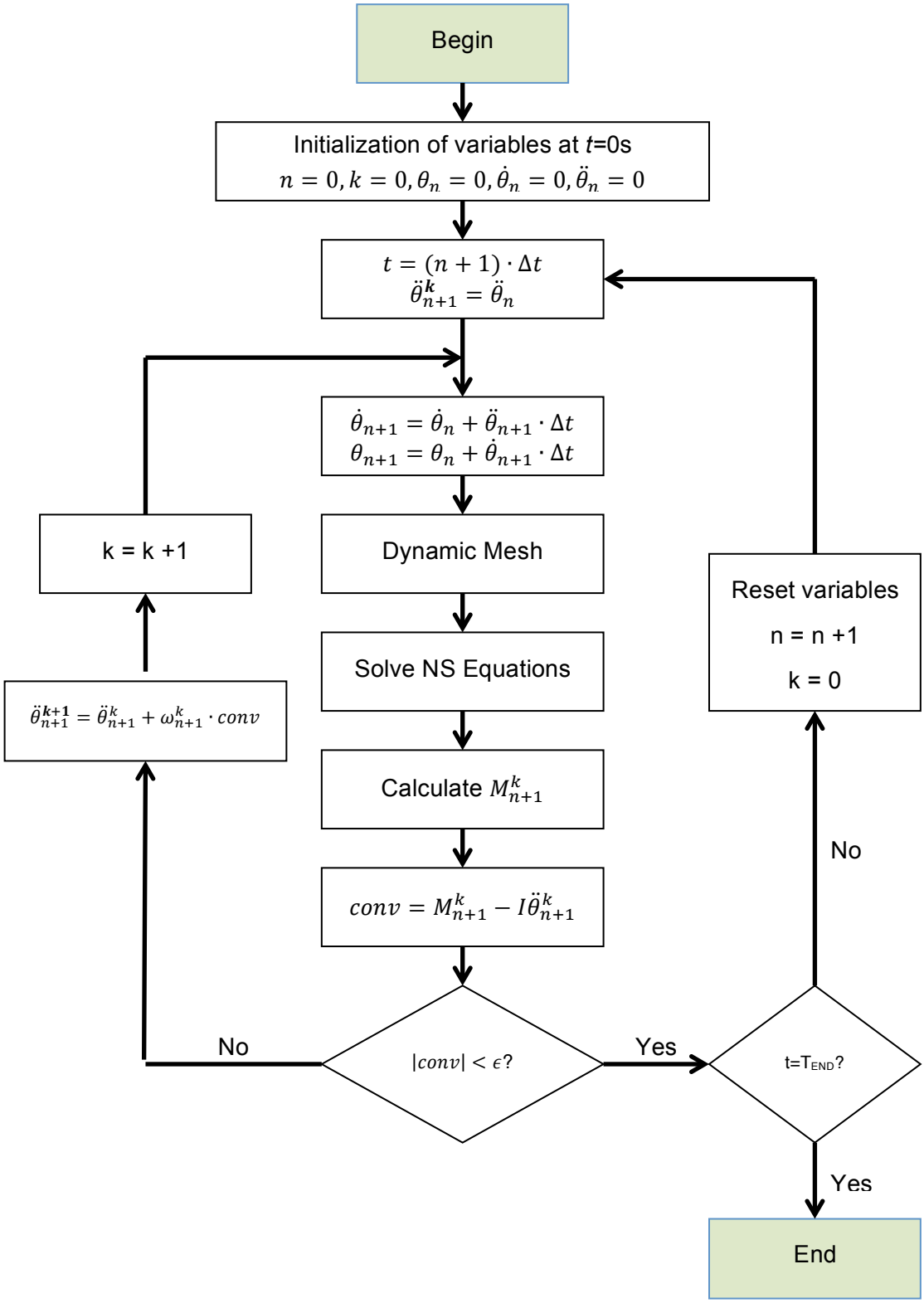

Figure 3-17: Fluid-Structure Interaction process between flow and leaflets

CHAPTER 4: EXPERIMENTAL SETUP AND PROCEDURES

This chapter is organized to give a description of each of the experimental procedures for the validation study of both laminar and pulsatile flow using the PIV setup. The laminar flow validation study is for Project Aim 1 while the pulsatile flow validation study is for Project Aim 1 and 3.

4.1 Bileaflet Heart Valve Prostheses

The important design feature of a BMHV is that the two leaflets are shaped as semicircular discs and held within the ring or valve annular housing by four hinges. The hinge mechanism allows a slight protrusion called the ear on either end of each leaflet mates with the recess of the hinge profile inside the valve annular housing. As such, blood may leak through the hinge when the valve is either closed or open due to the design of the hinge geometry. The two leaflets move independent of one another and open to allow unimpeded flow through both the central and lateral areas of the opening orifice. The leaflets open and close due to the forces exerted by the blood flow through the valve. Typically, at fully open position, the leaflets form an angle of between 77° and 90° with respect to the orifice ring plane. At fully closed position, the two leaflets meet while leaving a narrow opening of approximately 100 μm between the edges for leakage. The leakage flow through the narrow opening and hinges allow continuous flushing of all surfaces of the components and parts of the prosthesis during the cardiac cycle. The leaflets and valve housing are made of pyrolytic carbon, which is biocompatible with very high strength and wear resistance. Generally during implantation, the bileaflet prosthetic valves use a rigid sewing ring or cuff to help the attachment of the valve to the surrounding tissue. This sewing ring or cuff is made of non-thrombogenic Dacron cloth or polyester fabric, which helps to ensure the encapsulation of endothelialized tissue or pannus growth. It also prevents the tissue from interfering with the leaflets motion (Leo, 2005). Figure 4-1 shows a typical BMHV prosthesis.

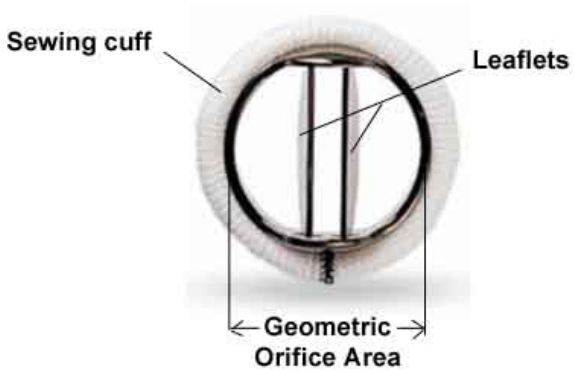

Figure 4-1: Picture of a typical bileaflet mechanical heart valve

4.1.1 ATS Open Pivot Bileaflet Heart Valve

The ATS Open Pivot Bileaflet Heart Valve is a low profile bileaflet consisting of pyrolytic carbon orifice ring and leaflets. The leaflets consist of pyrolytic carbon coated over a graphic substrate with 20% tungsten for radiopacity. The pivot guides are located in the inner circumference of the orifice ring and control the leaflet motion range. The pivot area does not have any recesses or cavities and the geometry comprises of spherical protrusions at four places on the orifice and arc-shaped notches at either end of each leaflet. The plane of each leaflet forms an angle of 85° with the orifice ring at fully open position, while at fully closed position, the plane of each leaflet forms an angle of 25° with the orifice ring plane. The 29mm ATS valve has an internal diameter of 24.8mm, which forms an EOA of 4.59cm^2. The valve-sewing cuff is made of double velour polyester fabric. It is mounted on the orifice using titanium stiffening ring and secured with two titanium lock rings and a lock wire (ATS Medical 2014). Figure 4-2 shows the ATS valve used in the experimental study.

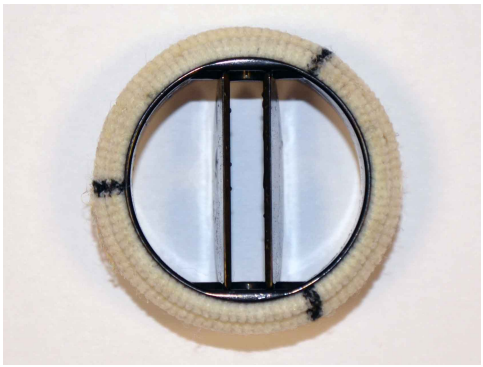

Figure 4-2: 29mm ATS Open Pivot Bileaflet Heart Valve

4.1.2 SJM Masters Series Bileaflet Mechanical Heart Valve

The SJM Masters Series Bileaflet Mechanical Heart Valve consists of pyrolytic carbon, which coats the graphite substrates of the leaflets and orifice ring. It offers exceptional biocompatibility, durability and increased thromboresistance. The valve housing has an extension upstream known as the pivot guard, which is designed to reduce exposure with subvalvular structures. This pivot guard reduces the working profile by allowing the leaflet to open and close entirely within the orifice ring. The SJM hinge is a butterfly-shaped recess. Projections on the leaflets within these hinge recesses, which are washed by blood during systole and diastole, minimize thrombogenesis. At fully closed position, the plane of each leaflet forms an angle of 35° with the orifice ring. At fully open position, the plane of each leaflet forms an angle of 85° which offers improved laminar flow and reduces turbulence. The sewing cuff is made of polyester polyethylene terephthalate (PET) or polytetrafluoroethylene (PTFE) and contains additional suture markets for more accurate placement; and it has controlled torque rotation mechanism that allows easy rotation and intraoperative adjustment (SJM 2014). Figure 4-3 shows the 29mm SJM Masters Series Bileaflet Mechanical Heart Valve used in the experimental study.

Figure 4-3: 29mm SJM Masters Series Bileaflet Mechanical Heart Valve

4.2 Valve Mounting Chambers and Setup

Figure 4-4 shows the clear valve chamber fabricated from a solid acrylic block which can be divided into two sections. The internal inlet diameter is 28mm. Section 1 is the upstream inlet section of the valve housing while section 2 consists of the simplified axisymmetric sinus chamber representing the human aortic root downstream of the valve housing. The valve used in the

experimental study is placed within a recess section and is held in place when the two blocks are fastened together by four bolts.

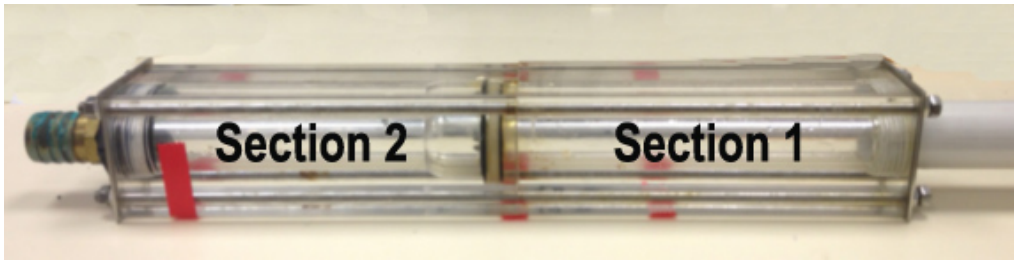

Figure 4-4: Acrylic valve holder for heart valve prostheses

The chamber was polished to allow optical access necessary to obtain the velocity measurement. The valve used in the study is placed in between additional gaskets and rapid prototyped valve extension holder to prevent fluid leakage as shown in Figure 4-5. The inlet and outlet of the model were connected to PVC piping and connected to the flow system. The 29mm ATS Open Pivot Bileaflet valve and 29mm SJM Masters Series valve were used in the experimental study.

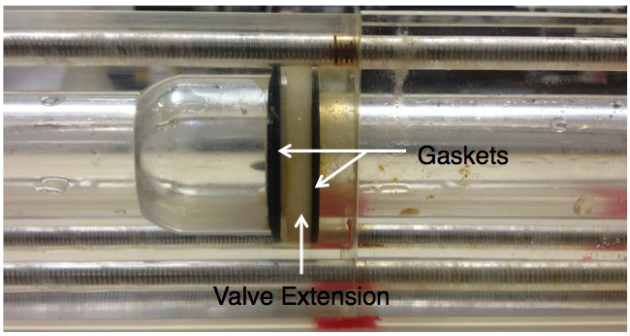

Figure 4-5: Gaskets and valve extension to secure the SJM valve

4.3 Steady Laminar Flow Loop Experimental Setup

Flow experiments were conducted with setups and operating conditions similar to the simulation runs. The mechanical heart valve used for the study was a 29mm ATS Medical Open Pivot Heart Valve. The valve was placed in a clear acrylic test section of length of at least 5D and 10D upstream and downstream, respectively (D is the diameter of the pipe inlet), to facilitate visualization and measurement of the flow. A steady flow water pump was used to provide constant fluid velocity. The flow setup was mainly comprised of sections of PVC tubing fitted together with rubber tubing and hose clamps. A plastic bucket was used as the fluid reservoir. The flow entering the test section had a fully developed profile matching that of the numerical

simulations, by passing the flow through a straight circular pipe of length 1.8m in the upstream of the valve as shown in Figure 4-6.

$$El = \frac{l_e}{D} \tag{4.1}$$

$$El_{laminar} = 0.06\,Re \tag{4.2}$$

where *El* is the Entrance Length Number, l_e is the entrance length to fully developed velocity and *D* is the tube diameter. Based on the steady laminar flow loop validation study of up to Reynolds number 1000, the minimum length for the velocity to become fully developed is 1.68m. As such the straight circular pipe of length 1.8m in the upstream is sufficient to achieve this fully developed velocity profile.

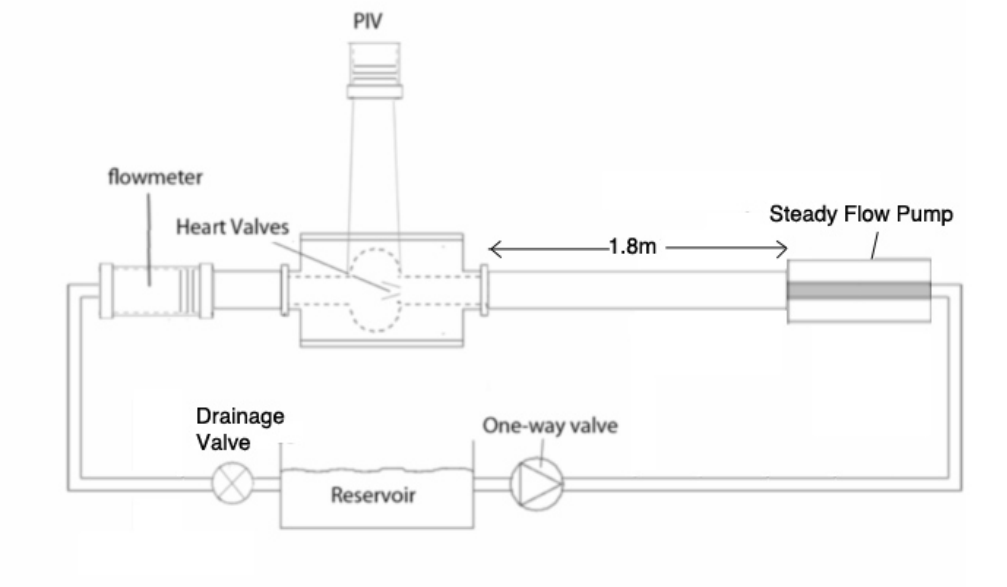

Figure 4-6: Steady flow experimental setup for bileaflet mechanical heart valve validation

4.4 Pulsatile Flow Loop Experimental Setup

In the validation study for a pulsatile flow of a BMHV for Project Aim 1, a modification to the steady laminar flow loop is required. Figure 4-7 shows the schematic diagram of the pulsatile loop used to investigate the flow field in the downstream of the 29mm SJM Masters Series Bileaflet Mechanical Heart Valve. The loop was used to simulate the physiological conditions corresponding to the left side of the human heart. The setup consists of the flow loop, and the pulse generation and delivery system. The pulse generation consisting of a high-precision piston pump (SuperPump AR, Vivitro Labs, Inc, Canada) was used to simulate the cardiac input flow. The piston pump is operated by the ViVitro ViViGen software application, which

allows new waveforms to be quickly created or modified by inserting the desired wave profile. The pump can control the power of each stroke and can be synchronized to activate the pulse (i.e. trigger signal) for velocity measurement at the particular timeframe of the cardiac cycle.

The flow loop comprised of the heart valve mounted in the acrylic chamber, a flow meter, a compliance chamber, a reservoir, and a one-way valve. PVC tubing and flexible rubber hose at joints connect the loop together. The compliance chamber placed downstream of the aortic valve was adjusted to achieve accurate flow waveform. The reservoir was a tower acrylic chamber.

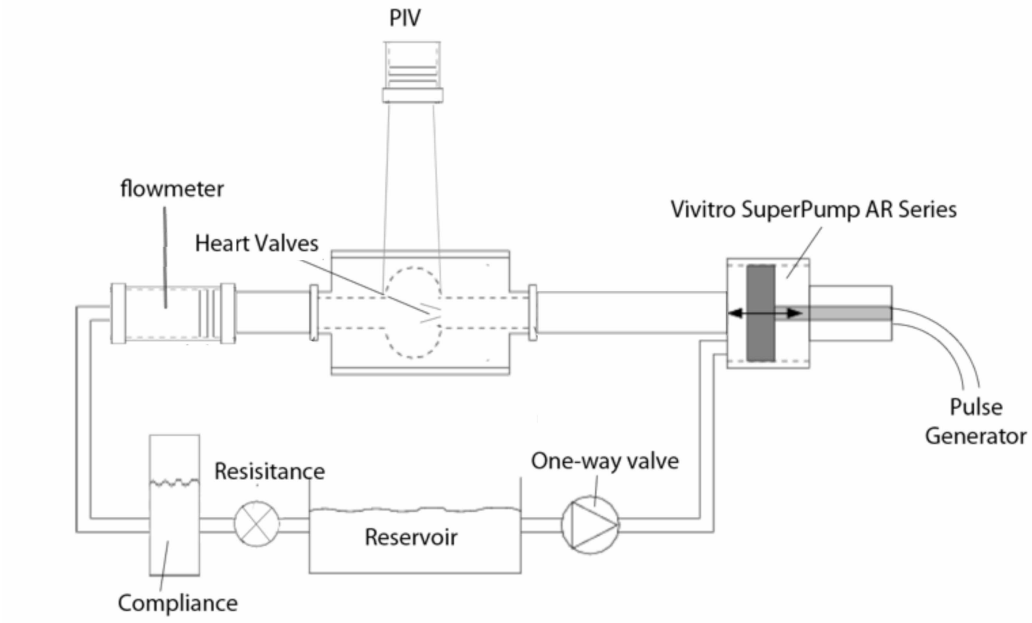

Figure 4-7: Schematic Diagram of Pulsatile Flow Loop Setup

A TTL signal (5V) was sent by the pump interface unit as the trigger to activate the laser pulse at specific time in order to record the required time frame of the flow profile.

The experiment setup for the pulsatile flow loop is shown in Figure 4-8.

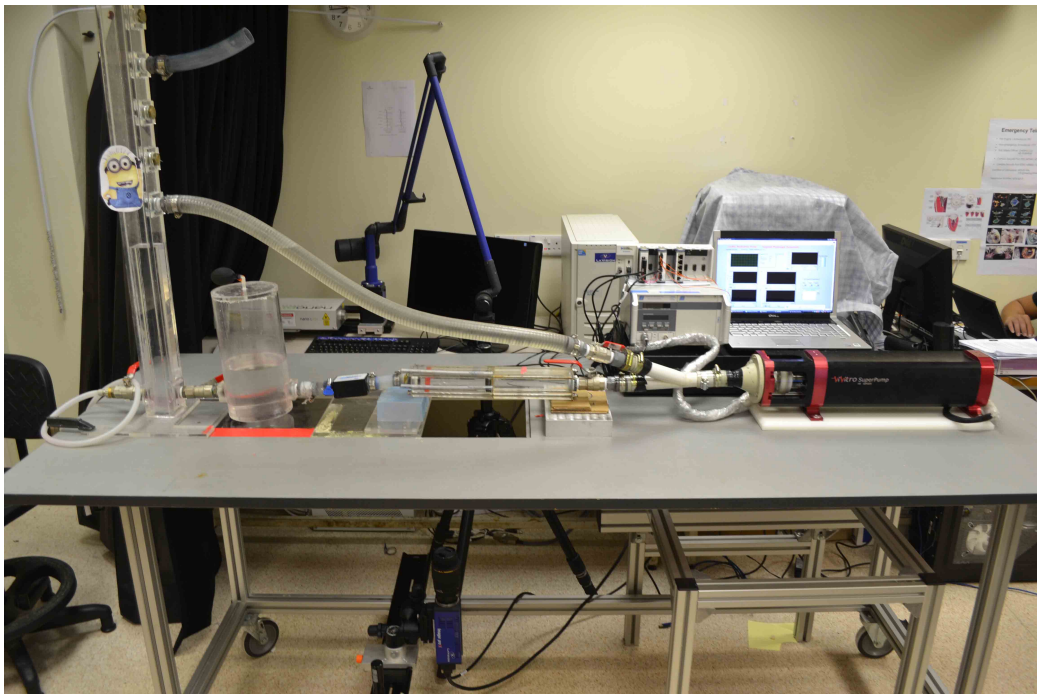

Figure 4-8: Pulsatile Flow Loop Experimental Setup

4.5 Working Medium and Seeding Particles

4.5.1 NaI/Glycerin/Deionized H_2O

The fluid used in the pulsatile experiments was composed of 59% saturated sodium iodide (NaI) solution, 40% glycerin and 1% deionized water by volume, which was transparent to allow the measurement of flow velocities using Particle Image Velocimetry (PIV) technique. The combined density and dynamic viscosity of the mixture matched the kinematic viscosity, ν, of blood at high shear rates which was between 3.5–4.0cSt or $3.5\text{x}10^{-6}$–$4.0\text{x}10^{-6}\text{m}^2\text{s}^{-1}$. With such fluid ratio, a kinematic viscosity $0.0038\text{kgm}^{-1}\text{s}^{-1}$ was similar to that of blood (0.0035–$0.004\text{kgm}^{-1}\text{s}^{-1}$). The refractive index of the fluid, (1.445) was tried to be as close as possible to that of the acrylic valve mounting chambers (1.49) in order to minimize the optical distortion of laser beams used in these studies. The viscosity of the working medium was determined by using a glass Cannon-Fenske routine viscometer (Viscometer Size 75, S695, Cannon Instruments Company, PA) and the refractive index was determined by means of a transparent liquid refractometer (Hand-held refractometer R5000, Atago, Japan).

Dynamic similarity was assumed between the fluid flow created by the prosthesis within the mounting chamber and the blood flow created by the

prosthesis within the human aorta by matching the kinematic viscosity of blood.The lifespan of saturated NaI solution had a lifespan of approximately 6–8 months depending on the experiments usage frequency because of the oxidation of the NaI constituent of the working fluid. The NaI turned dark brown after contact with atmosphere. The solution's viscosity and refractive index had to be corrected regularly due to evaporation of water in the solution.

4.5.2 Seeding Particles

PIV relies on scattering particles suspended in the flow to provide the velocity information for continuous fluid flow. To choose the optimal diameter for seeding particles, it is necessary to compromise between a quick response of the tracer particles in the fluid, requiring small diameters to follow fluid motion and not alter fluid flow properties, and a high signal-to-noise ratio (SNR) of the particle images, necessitating large diameters to be visible by the camera (Melling 1997).

Fluorescent polymer particles (FPP-RhB-10, Dantec Dynamics, Denmark) based on melamine resin were used in the PIV velocity measurement of steady laminar flow experiment. The size of the fluorescent particles is 1–20 μm in diameter and were delivered in suspension with the NaI/Glycerin/Deionized H_2O. These fluorescent particles were used to eliminate the laser glare off the polymeric valve surface. The laser light is absorbed by the particles at a wavelength of 532nm. Light is emitted at above 560nm. An orange lens filter (Quantaray, 60mm, Wolf Camera) mounted on the camera lens only allowed wavelengths of 560–600nm to pass, thus blocking the laser light that was reflected from the valve surface. For the pulsatile flow loop setup, Polyamide Seeding Particles with diameter 50 μm (PSP-50, Dantec Dynamics, Denmark) were used and added to the mixture of NaI/Glycerin/Deionized H_2O. An orange lens filter (La Vision VZ-Image Filter 532nm, 10nm) was mounted on the camera lens.

4.6 Equipment Measurement and Calibration

4.6.1 Flow Rate Measurement

The flow rate was measured using a calibrated Transonic Flow Probe (ME 25 PXN, Transonic System, Inc, USA). The voltage signal from the flow probe was received by flow output display (T402, Transonic System, Inc, USA). A laptop installed with LabView (National Instruments, USA) was also connected to measure the velocity profile.

4.6.2 Velocity Measurement

4.6.2.1 Particle Image Velocimetry

The system used for steady laminar flow experimental study was a 15Hz Q-switched, double cavity pulsed Nd:YAG laser (Minilase-III PIV system, New Wave Research, USA) with an energy of 150 mJ at a wavelength of 1064 nm, producing a light sheet which was adjusted to illuminate the seeding particles in the symmetry plane of the model. The particles' motion was recorded with a charge coupled device (CCD) camera (FlowSense, Dantec Dynamics, Denmark) with a spatial resolution of 1600×1200 pixels, and a Nikon lens (AF Micro Nikkor, 60/2.8) positioned normal to the laser sheet. All of these components were connected to a host computer, which controlled the measurement and post-processing using the DynamicStudio software (Version 2.20.18, Dantec Dynamics, Denmark).

The system used for pulsatile flow experimental study was a Nano PIV Pulsed Nd:YAG Lasers (Model Number: S35-15PIV – Class 4 Laser Product, Litron Lasers, England). The setup was a dual head high-energy laser system with output up to 300mJ at 1064nm, 4ns long pulses at up to 15Hz.

The CCD camera used was a LaVision camera (VC-Imager Pro X 2M, 1GB, CamLink, LaVision, Germany) with a spatial resolution of 1600×1200 pixels, and a Sigma Lens (100mm F2.8 EX Macro) was used to allow sequence of PIV data to be captured at freely adjustable intervals between image frames with similar intensities.

The correlation of the digital image pairs to calculate the velocity fields was performed using commercially available PIV software (DaVis 8.0.5, LaVision,

Germany). In the cross correlation program, each camera image was divided into rectangular regions, known as interrogation areas. In each interrogation area, the particle images captured during the first and second pulse of the laser light sheet were correlated to produce an average particle displacement vector. It was assumed that all particles move homogeneously between two laser pulses within one interrogation area. The vector map of average particle displacements was produced after the calculation for all interrogation areas were performed. These displacement vectors are divided by the known pulse separation time.

4.6.2.2 Important Considerations for PIV Experiments

Image Processing

The background intensities and image noise were removed by pre-processing of recorded image pairs. Non-fluid regions with zero pixel value intensity were masked to reduce bias error originating from wall reflections. The image pairs for steady flow were analyzed by a two-frame FFT adaptive multi-grid cross-correlation algorithm with the final interrogation areas of 32×32 pixels, overlapped by 50% on each side, to yield the local displacement vector for each interrogation area, using DynamicStudio software. The image pairs for pulsatile flow were analyzed by a two-frame FFT adaptive multi-grid cross-correlation with multi pass (decreasing size) iterations. The image pairs were overlapped by 50% on each side and with interrogation area of 128×128 pixels followed by 64×64 pixels using the LaVision Davis software.

Illumination

An important aspect of the PIV setup is sufficiently strong laser to illuminate the seeding particles in the flow. This enables scattered light to reach the CCD cameras. The interrogation area should be located where the light sheet is the thinnest so as to reduce the effect of out-of-plane particles. The control panel of the PIV setup allows adjustment of the laser gain.

Time delay between illumination pulses

The pulses must illuminate the displacement of particles between image pairs in order to have sufficient resolution yet short enough to prevent seeding particles with an out-of-plane velocity component from leaving the light sheet

between the pulses. For each image pair, there was a mix of both high and low velocity flows. As such, the time delay between the illumination pulses must be optimal to capture both types of flow. For steady laminar flow, the pulse separation time was set to values in the range of 100-500 μ s. Meanwhile, as the flow changes throughout the cardiac cycle and it was necessary to have a different time delay setting at each particular point of the cycle. The time delay ranged from 100-900 μ s.

Number of image pairs

The number of image pairs affects the accuracy of the calculated velocity components. The higher number of image pairs can improve the signal-to-noise ratio and lower the errors in the measured values. However, this would also mean longer time spent on data acquisition and processing, and higher cost on storage space. 200 image pairs were obtained from the Dantec Dynamics system for steady laminar flow setup while 150 image pairs were obtained from the LaVision Davis software. Only a maximum of 150 image pairs could be obtained using LaVision setup.

4.7 Experimental uncertainties

One source of systematic error resulting from instrumentation factor is the misalignment between the plane of investigation and the laser light sheet. This can be minimized by calibration and adjustment of the laser light on the arcylic. Systematic error due to the refractive index of the working fluid (1.445) which is lower than the acrylic valve mounting chambers (1.49) may result in optical distortion of laser beams. As such, the near wall regions were generally excluded from analysis. The leaflet in the simulation model was limited to prescribed rotation only while in experimental setup, the leaflets are free to rotate and translate up and down along the leaflet axis. This may induce some errors on the computational results of the leaflet movement.

CHAPTER 5: RESULTS AND DISCUSSIONS

In this chapter, the results from simulations and experimental validations for the project aims listed in Chapter 2 will be presented. The discussion on the hemodynamic performance of the mechanical heart valves will be presented in the following order:

Project Aim 1:

- Steady Laminar Flow Simulation and Validation Study
- Turbulent Flow Simulation
- Pulsatile Flow Simulation And Validation Study

Project Aim 2a:

- Comparison of Hinge Microflow Fields of Bileaflet Mechanical Heart Valves Implanted in Different Sinus Shape and Downstream Geometry
- Comparison of Different Implantation Angles for Bileaflet Mechanical Heart Valves

Project Aim 2b:

- Comparison of Trileaflet Heart Valve and Bileaflet Mechanical Heart Valve, and Different Implantation Angles of Trileaflet Heart Valves

Project Aim 3:

- Fluid-Structure Interaction Study of Bileaflet Mechanical Heart Valve using the six degree of freedom (DOF) solid body motion approach in OpenFOAM

5.1 Steady Laminar Flow Simulation and Validation

The results in this section have been published in an earlier work by Nguyen *et al.,* (2012) and is for Project Aim 1.

5.1.1 3-dimensional *Valve Model and Flow Domain*

The valve geometry used in the steady laminar flow study for Re=350, 750, and 1000, was a valve based on the design of a 29mm ATS Open Pivot Valve placed in a simplified model of aortic chamber. This chamber consisted of a single axisymmetric sinus in a straight pipe. The BMHV model used in the simulation was simplified by omitting the hinge mechanism of the valve leaflets. The computational domain was subdivided into an unstructured

mesh of approximately 2.2 million tetrahedral elements. Mesh independence study was performed at steady laminar flow condition. Mesh refinement was performed by changing the size function and mesh growth rate at the edges of the leaflets. Further refinement of the grid did give much change to the simulation results with a percentage difference of 5%. Figure 5-1 shows the cross-section view of the model with the simplified hinge mechanism.

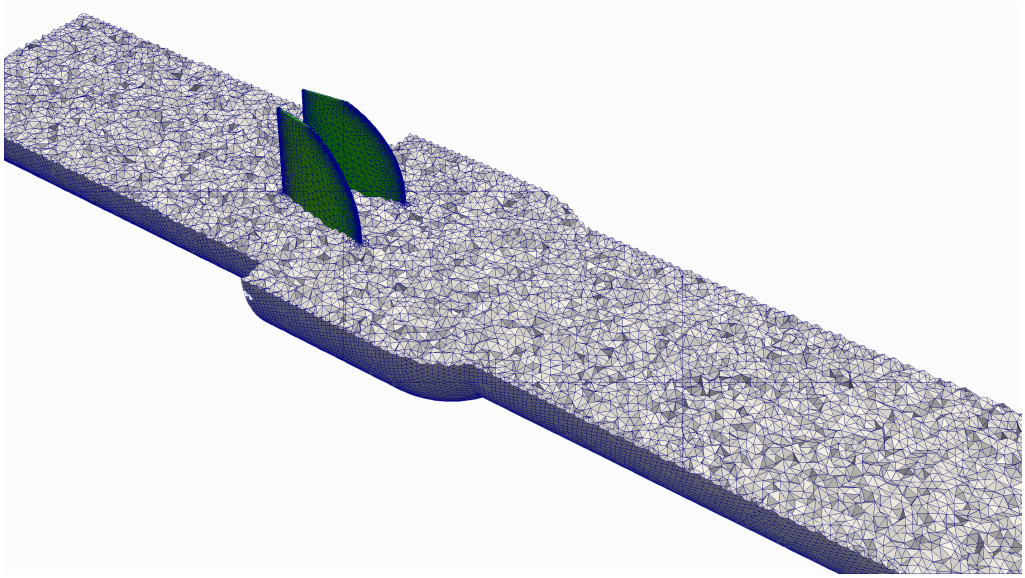

Figure 5-1: Cross section view of the simulation model of BMHV placed in an axis-symmetric simplified sinus chamber

5.1.2 Boundary Conditions

For the fully developed flow simulation, parabolic velocity profile was imposed at the inlet. The maximum velocity was 0.0953ms^{-1}, 0.204ms^{-1} and 0.272ms^{-1} for steady inflow conditions corresponding to Reynolds numbers Re=350, 750 and 1000 respectively. The inflow velocity was compared with experimental data as shown in Figure 5-2 using the Minilase-III PIV system (New Wave Research, USA) at the upstream of the mechanical valve to find out the incoming flow profile. The experimentally obtained flow profiles were similar to the fully developed flow in the simulations for all the simulated Reynolds numbers. The shape and magnitude of the time-averaged flow profiles were similar for both the simulation and experiment for all the three Reynolds numbers.

(A)

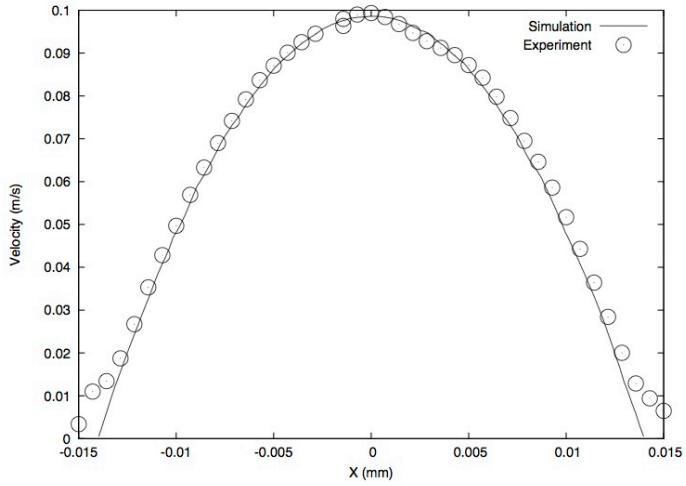

(B)

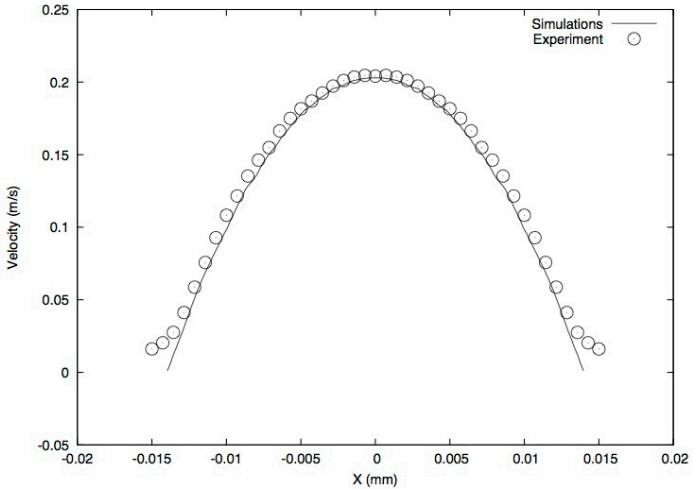

(C)

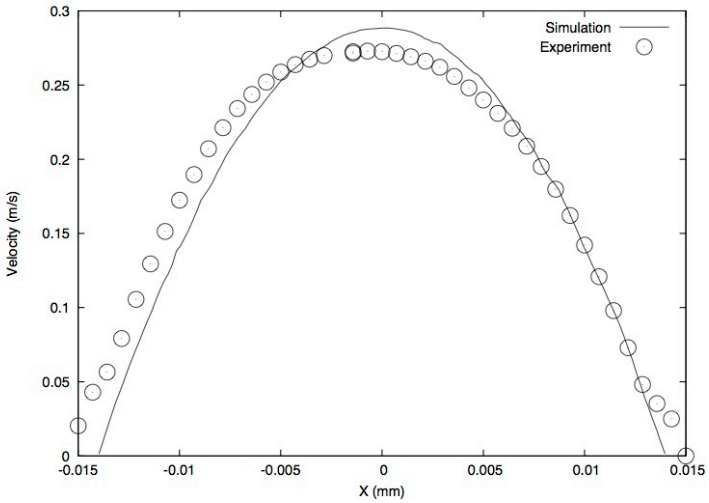

Figure 5-2: Fully developed inlet flow profile validated using PIV system
(A) Re=350, (B) Re=750 and (C) Re=1000

5.1.3 Results and Discussion

The laminar flow was studied at the maximum opening of the valves at 85^{o} and comparisons with experimental data were made to validate the simulations. Experimental validations under laminar conditions were

conducted for the valve fixed at the fully opened condition for Reynolds numbers ranging from 350 to 1000. The velocity flow fields were averaged from 200 image pairs which were analyzed using the DynamicStudio software (Dantec Dynamics, Denmark). The investigation area was a 99x74 vector field and the velocity range observed in the experiment was 0 to 0.3ms^{-1}. In order to reduce the near wall bias, the boundary of the interrogation areas was matched with that of the model.

The origin of X and Y-axes is at the center of the flow channel with the Z=0 plane located at the trailing edge of the leaflets with the corresponding velocity components *u, v* and *w* respectively. Comparisons for the streamwise velocity profiles were made at three different locations as follows: Z=1D, 2D and 4D, as shown in Figure 5-3.

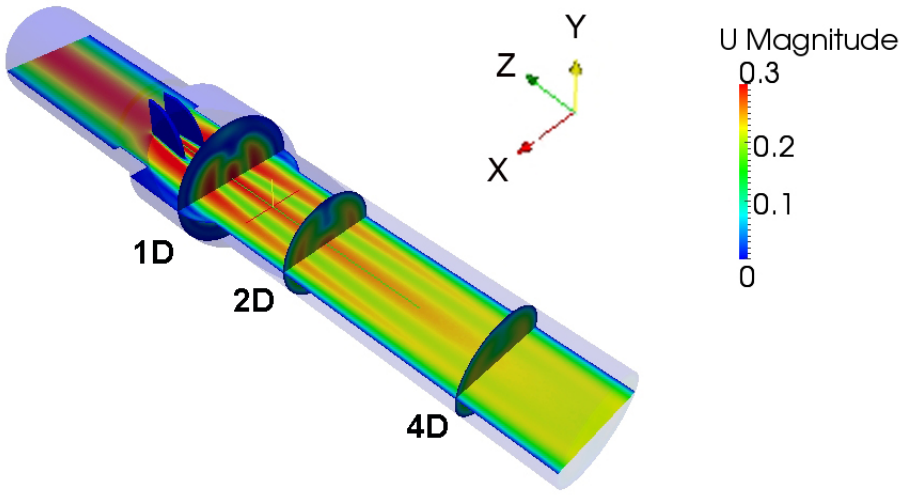

Figure 5-3: Plan view of streamwise velocity contours (Re=1000) at three cross section planes Z=1D, 2D and 4D

In Figure 5-4, the predictive capabilities of the numerical model re demonstrated by comparing the numerical results with the experimental time-averaged, streamwise velocity profiles for laminar flow at Re=350 at the three locations downstream of flow. At position 1D, the triple-jet structure of the flow can be seen clearly, just as predicted by the simulation. However, the center jet measured in the experimental result showed lower values of velocity at 0.0855ms^{-1} compared to 0.0893ms^{-1} obtained from the simulation (Nguyen *et al.,* 2012). On the other hand, two lateral jet profiles were evidently shown and accurately predicted from both numerical simulation and experiment. At

position 2D, the velocity profile was near the transition phase from a triple-jet structure merging into two lateral jets downstream, as can be seen with a flatter center jet velocity profile. The simulation was able to provide an accurate prediction as compared to the experimental results in terms of magnitude and velocity profile. Further downstream at position 4D, two flatter lateral jets were visibly taking shape. At this location, the simulation results at the center profile had a nearly identical velocity magnitude to the experimental results.

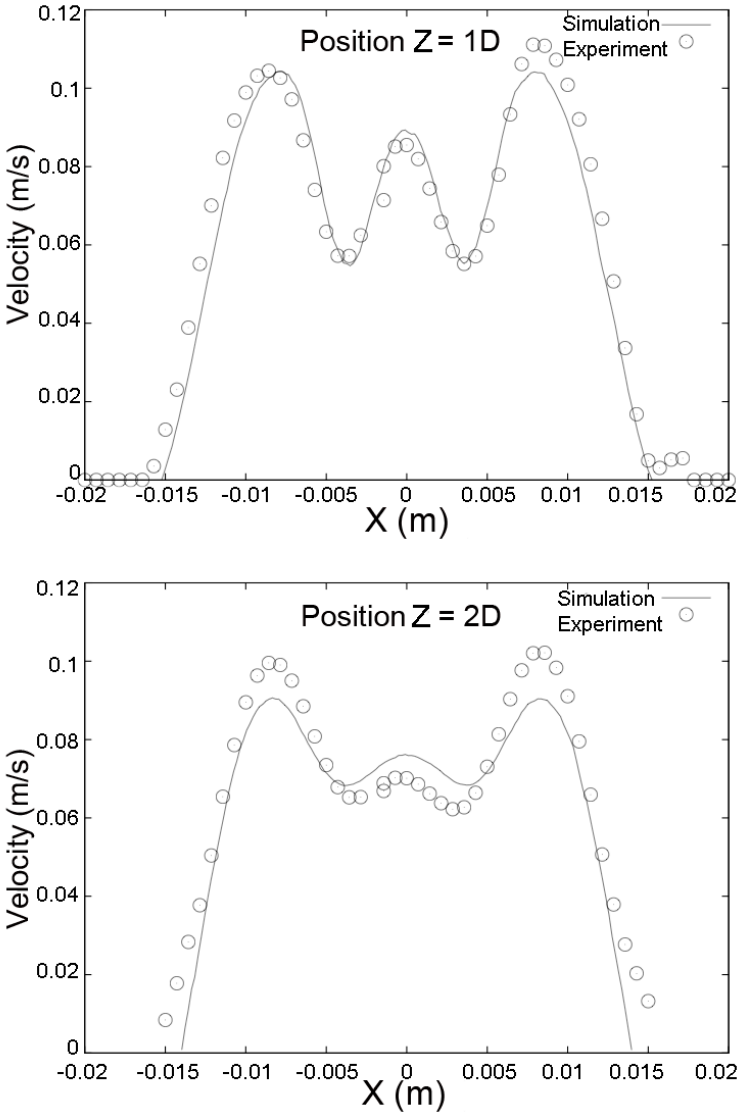

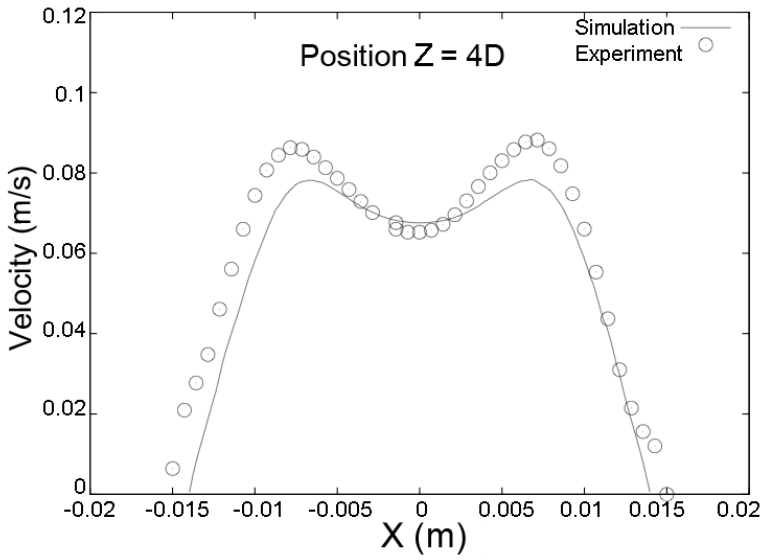

Figure 5-4: Velocity profile comparisons between experimental (o) and numerical simulation (–) for Re=350 at position Z=1D, 2D and 4D

The two lateral jet profiles in the experiment were within 10% of the simulation results. Hence, it is shown that the numerical simulations are able to capture essential features as observed in the experiments with good accuracy in terms of the magnitude and general velocity profile. It can be observed that the complex transverse velocity distribution across the Y-axis and the fluid velocity of the flow profiles in Figure 5-4. The well-known triple-jet structure of the flow in the wake of the leaflets can be seen clearly at position 1D before it merged into two lateral jets further downstream at position 4D.

In Figure 5-5, similar comparison can be seen for Re=750 and Re=1000 at position 1D. The flow profile and velocity magnitude obtained in the simulation showed good agreement with the experimental results. A significant feature captured by the simulation, which was also verified experimentally, was the formation of vortices near the edge of the wall. The magnitude of the vortices obtained from the simulation was almost identical to the experimental results. The triple-jet structure was also visible at position 1D for Re=750 and Re=1000.

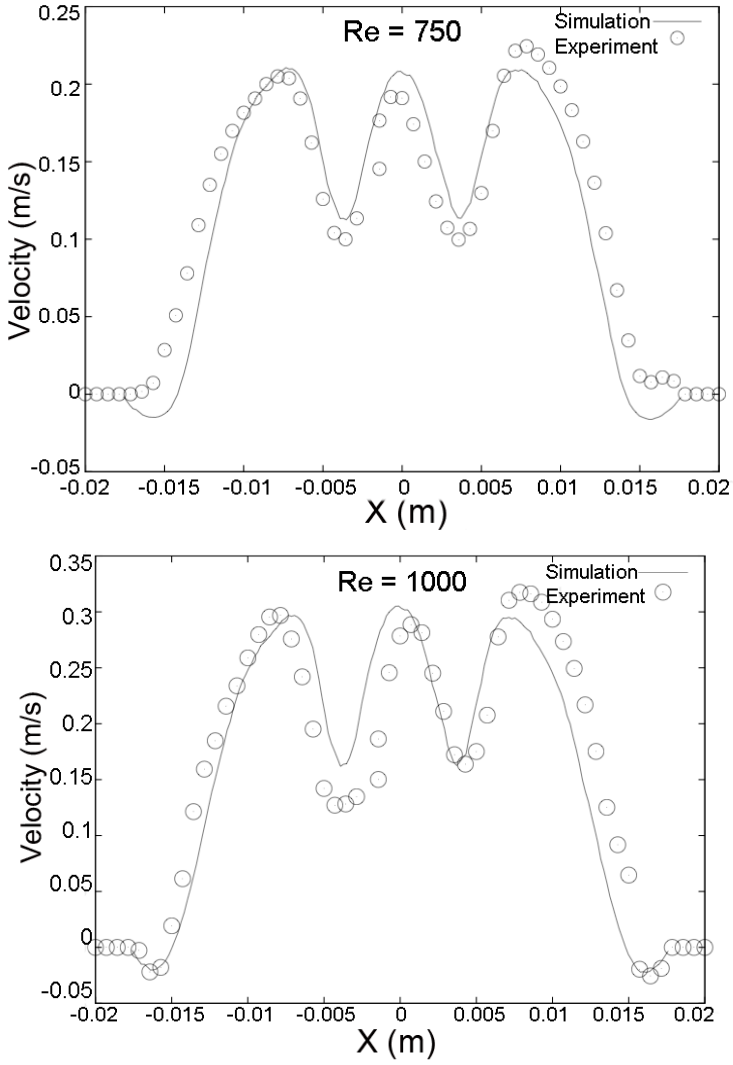

Figure 5-5: Velocity profile comparisons between experimental (o) and numerical simulation (–) for Re=750 and Re=1000 at position Z=1D

However, there were asymmetries in the experimental results obtained where the velocity profile was slightly shifted to the right-hand side (higher X values). The likely reason is the breakdown of the steady flow assumptions in the flow domain. It could also be due the valve not being at fully open position at the time of experiment. The experiments and the simulations in terms of the velocity profiles and velocity magnitudes were quite instructive. The simulations were able to capture the essential features of the mean flow in the experiment, notably the vortices near the walls of the sinus chamber. As mentioned earlier, the triple-jet structure which resulted from the blockage of the flow by the two valve leaflets and the vortex formation can be observed in the simulations at both Reynolds numbers, which was also reported by (Ge *et al.,* 2005).

5.1.4 Limitations

The BMHV model used in the simulation was simplified by neglecting the hinge mechanism of the valve leaflets. The lack of hinges may play a role in the upstream region during regurgitation. In reality, the hinge may vary from one side to another due to manufacturing tolerances. As shown by Simon *et al.,* (2010), the design of the hinge might play a role in the thromboembolic complications of the valve due to the unsteadiness of the hinge flow fields. The presence of hinge geometry should be accessed for a more accurate simulation.

5.1.5 Summary

The study has developed and validated the laminar using a 29mm ATS Open Pivot Valve with simplified hinge design. The flow profiles for different planes downstream of the valves were compared and showed close accuracy with the simulated results. The 3-dimensional model used in the numerical study was successfully validated using the experimental model.

5.2 Turbulent Flow Simulation

The results in this section were continuation from an earlier work published by Nguyen *et al.,* (2012) to achieve Project Aim 1.

5.2.1 3-dimensional *Turbulent Flow Simulations*

A CFD simulation of flow at near peak systolic condition was considered in this study. As the flow approached this condition, Reynolds number was estimated at about Re=5000 to 6000 in which full turbulent regimes were expected to be observed in the flows. Similar to the laminar flow study, the valve geometry used in the turbulent flow study for Re=5000, was a valve based on the design of a 29mm ATS Open Pivot Valve placed in a single axisymmetric sinus in a straight pipe. The hinge mechanism of the valve leaflets was omitted in the BMHV model. Simulations were performed for three different turbulent models. For k-epsilon and SA turbulent models, the same geometry as the laminar flow study was used, which were subdivided each into an unstructured mesh of approximately 2.2 million tetrahedral elements. For the LES simulation, the surface boundary layers on the leaflets were included, and the size of the unstructured mesh was approximately 3.4 million tetrahedral elements. The close up view of the surface boundary layer on one of the leaflets is shown in Figure 5-6.

Figure 5-6: Close up view of the surface boundary layer at the leaflets for LES modeling

5.2.2 Boundary Conditions

For the fully developed turbulent flow simulation, the power law inlet velocity was used for Reynolds number Re=5000. Figure 5-7 shows the inlet boundary condition for turbulent flow for all the k-epsilon, SA and LES simulations.

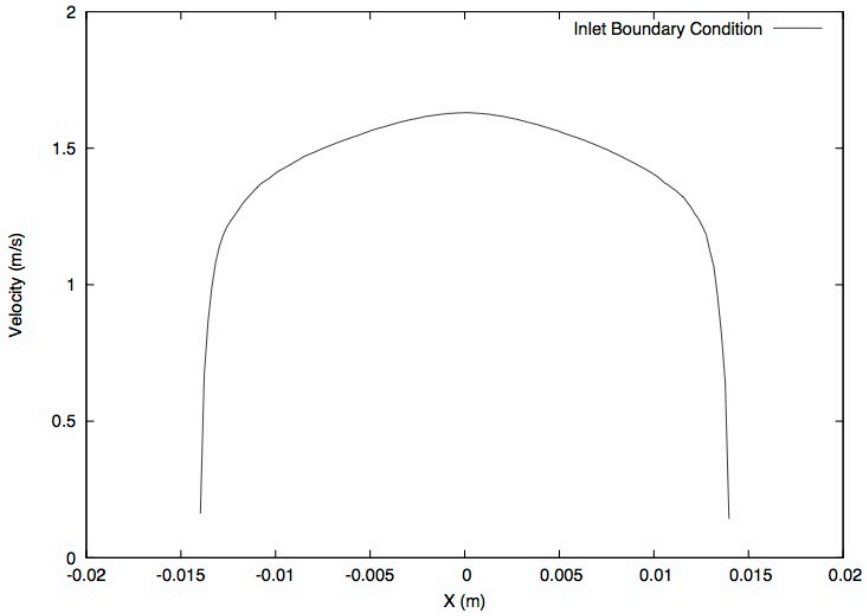

Figure 5-7: Inlet boundary condition for turbulent flow

5.2.3 Results and Discussion

The URANS approach was used to simulate turbulent flow. Figure 5-8 shows time-averaged velocity contour of flow at Reynolds number Re=5000 using SA turbulence model. The current model was able to capture flow features at high Reynolds number in which the three-jet structure was present and the rotation of flow axis at downstream was observed through velocity vector profile at four X-Y planes at Z=0D, 1D, 2D and 4D downstream.

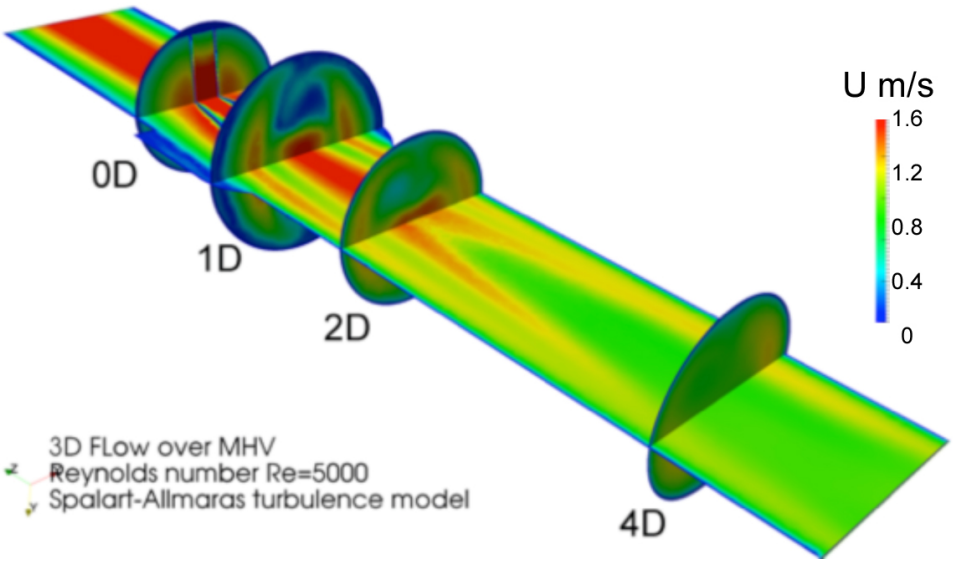

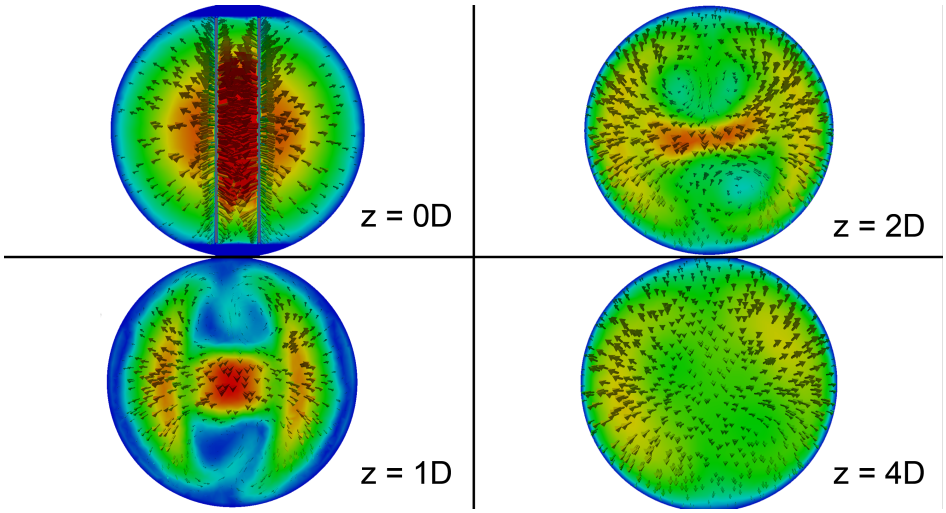

Figure 5-8: Flow at Re=5000 using Spalart-Allmaras turbulence model plan view and 4 cut planes of Z=0D, 1D, 2D and 4D

The flow solutions of k-epsilon and SA models could only predict the time-averaged quantities and it required a more detailed turbulent flow model, such as LES or DES to be able to probe more turbulent flow statistics. The three turbulent flow models, k–epsilon, SA and LES were compared as shown in Figure 5-9. The velocity profiles at three different cut-planes for all the three models showed difference in the time-averaged velocity. The k–epsilon and SA results showed more symmetric profiles than LES. The general shape and velocity magnitude between the three turbulent flow models were similar. LES showed a more detailed representation of the turbulent flow although this simulation model consumes much more computational resources, about three times as much as the k-epsilon and SA models. Comparing k-epsilon and SA model, it was shown that the SA model could be used as a simplified version of the LES model for optimal consideration between the computational costs and closely resembling shape and flow magnitude, as compared to the k-epsilon model. In the subsequent simulations, SA model was used for the studies.

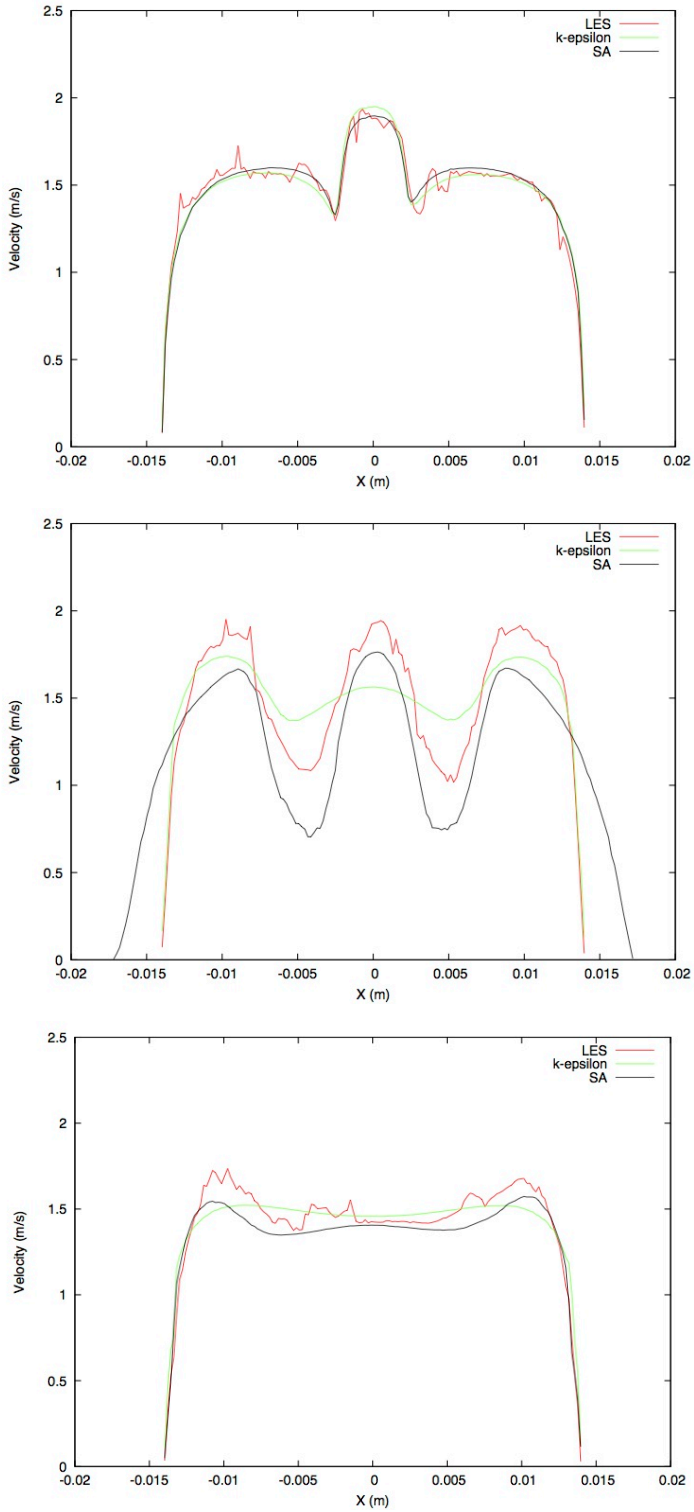

Figure 5-9: Comparison of velocity profiles at different cut-planes for k-epsilon and SA model at position Z=1D, 2D and 4D

Similar vorticity contours can be observed in Figure 5-10 where the two turbulent flow models, k-epsilon and SA are shown.

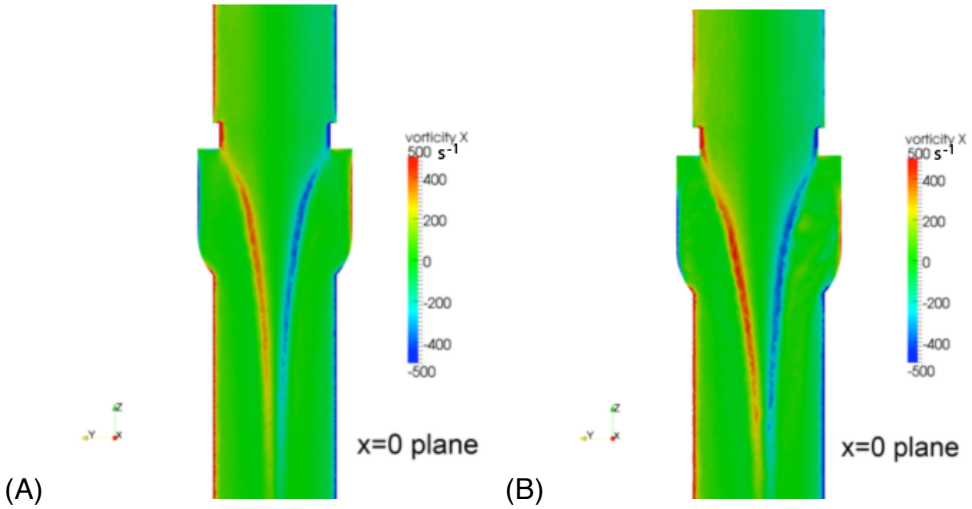

Figure 5-10: Comparison of vorticity profiles at Re =5000 (A) k-epsilon, (B) Spalart-Allmaras

5.2.4 Summary

The study investigated the turbulence modeling using SA, k-epsilon and LES models. Comparing all these three models, the study has shown that the SA model could be used as a simplified version of the LES model for optimal consideration between the computational costs and closely resembling shape and flow magnitude, as compared to the k-epsilon model.

5.3 Pulsatile Flow Simulation and Validation Study

To investigate the flow through BMHV under physiological condition for Project Aim 1, the numerical model is required to be capable of simulating the moving boundaries of the valve leaflets. One of the most important flow features of cardiovascular flow is its pulsatile nature. The CO in the aorta changes in time and peaks at a flow rate of about 25Lmin^{-1}. The blood flow through the BMHV undergoes periodic transition to turbulent flow as the peak systolic flow rate approaches.

5.3.1 3-dimensional *Model of Straight Pipe*

The valve simulation model used for pulsatile flow was similar to the earlier studies, which was a simplified axisymmetric sinus in a straight downstream aorta as shown in Figure 5-11. The valve was based on the design of a 29mm SJM Masters Series Bileaflet Mechanical Heart Valve with the hinge mechanism. The geometry was subdivided into an unstructured mesh of approximately 3.6 million tetrahedral elements to accommodate the mesh in the hinge regions. The simulation was performed using ALE moving mesh technique with turbMMeshTrackFoam solver in OpenFOAM.

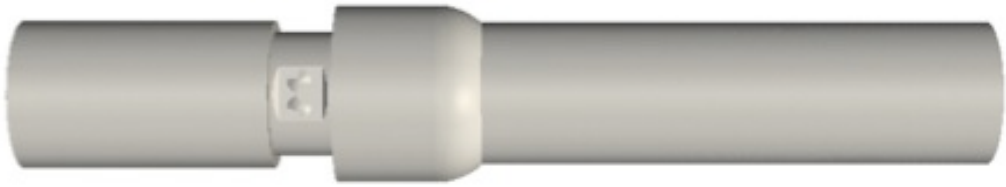

Figure 5-11: 3-dimensional model of a SJM valve placed in a straight pipe with an axis-symmetric sinus

The pulsatile flow was studied for the entire cardiac cycle and comparisons with experimental data were made to validate the simulations. Experimental validations were performed using the pulsatile flow setup with piston pump (Vivitro SuperPump). In this study, the simulation of a pulsatile flow for the cardiac cycle has successfully been validated using PIV. The origin of X and Y-axes is at the center of the flow channel with the Z=0 plane located at the trailing edge of the leaflets with the corresponding velocity components *u*, *v* and *w*, respectively. Comparisons for the streamwise velocity profiles were made at Z=1D, as well as the upstream of the flow at four different time points. The velocity flow fields were averaged from 150 image pairs which were analyzed using the LaVision PIV software (Davis 8.0.5, LaVision,

Germany). The pulse trigger was activated to synchronize the laser and the piston pump at the four time points. The velocity range observed in the experiment was between -0.4 to 1.3ms^{-1}.

5.3.2 Boundary Conditions

As one of the project aims in this study, a 3-dimensional flow was simulated over a typical human cardiac cycle in which the SJM valve was placed at the aortic position. The valve was operated under a prescribed motion using given inlet and outlet waveforms. Typically, a cardiac cycle was divided into systolic and diastolic time intervals where the heart's atria and ventricles were working synchronously to pump the blood through the circulatory system. The prescribed periodic condition started at fully open position of the valve where ejecting velocity kept increasing until it reached a peak flow rate of 25Lmin^{-1}. The whole cardiac cycle was about 0.86s, which was derived from a heart beat condition of a healthy person at 70bpm. The motion of the leaflets was prescribed to rotate from fully open position (85°) to fully closed position (35°). The simulation was driven by the inlet pressure and outlet velocity boundary conditions. Figure 5-12 shows the flow rate of the complete cardiac cycle obtained experimentally with the peak flow rate at 24.1Lmin^{-1}, which is close to peak systolic flow rate of 25Lmin^{-1} (Ge *et al.,* 2005). Four different time points for the simulations and experimental studies were compared. The experimental results were repeatable.

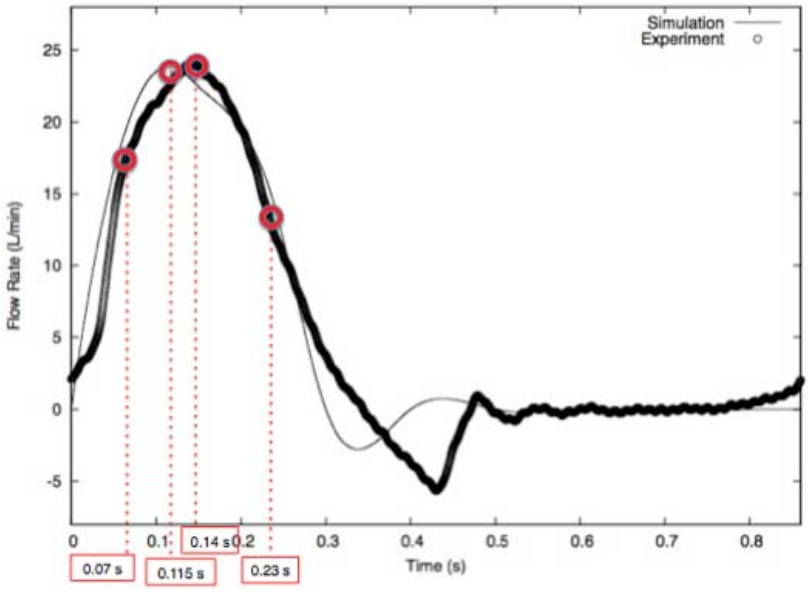

Figure 5-12: Comparison of simulation and experimental flow rate of the cardiac cycle. Four velocity time points were compared at t=0.07s, 0.115s, 0.14s and 0.23s

5.3.3 Results and Discussion

The flow rate profile between simulation and experiment was similar generally in terms of the shape and flow rate magnitude. In the time frame between 0.275s and 0.475s, slight deviation was observed between the simulation and experiment model, partially due to the compliance chamber and the pipe length in the experimental setup. It was tried to mimic the physiological flow as close as possible. There was also a slight difference in the exact time frame of the peak velocity between the simulation and experiment. In simulation, the peak velocity was at time 0.115s while in the experiment, the peak velocity was at time 0.14s. The difference in these two time frames was also due to the difficulty in mimicking exactly the peak systole flow experimentally. Five different time points captured experimentally were chosen to capture the systolic flow. Out of these five points, two time points were chosen near the peak velocity. The flow data captured experimentally was averaged out from 150 image pairs.

The numerical method was applied for simulations of pulsatile flows over BMHV with prescribed motions in a typical human cardiac cycle. The motion of the leaflets as well as boundary conditions is described in the earlier section. In order to investigate the errors of the initial configuration over multiple cardiac cycles, the BMHV was simulated over two cardiac cycles. The results from the first and second cycles were compared and there were no significant differences. As such, the results presented for the second cycle and single cardiac cycle simulation was found to be sufficient to represent the dynamic operation of BMHV. During diastole, there was no flow from left ventricle to aorta while the aortic valve was fully closed. However in this study, the BMHV was not fully closed, with a small gap which was necessary for the simulation to converge. Figure 5-13 shows the velocity contour obtained experimentally for position Z=1D at time t=0.115s.

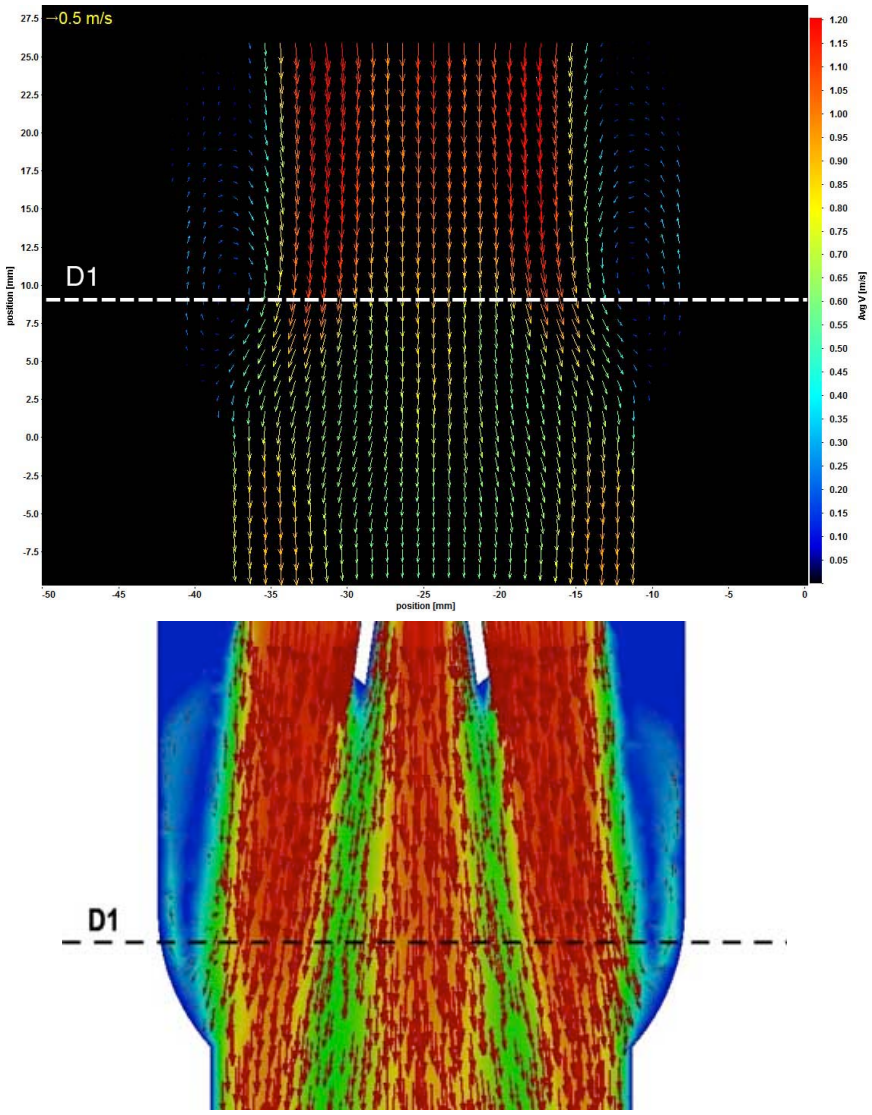

Figure 5-13: Velocity contour of the experimental study and simulation which show the plane at position Z=1D at time t=0.115s

In this study, using prescribed inlet velocity boundary condition, the peak systole was set at time 0.115s at the second cycle. Figure 5-14 shows the velocity variation comparison between simulation and experiment along the radial distance at position upstream, Z=1D downstream of the valve. First, the inlet velocity at the upstream position was compared and found to be similar in terms of the velocity profile and magnitude. The flat inlet velocity profile is consistent with the turbulent flow profile, which was expected at peak systole.

At position 1D, the results showed that the central jet was slightly higher in the simulation ($1.07ms^{-1}$) than the to experiment ($0.9ms^{-1}$). The triple-jet structure of the flow can be seen clearly even though the structure in the experiment appeared to be squashed to the center flow. The achieved

velocity distribution along X-axis in the simulation study had a triple-jet structure with central jet (1.07ms^{-1}) having roughly equal magnitude with the lateral jets (1.13ms^{-1}). In the experiment, the central jet appeared to be lower in magnitude (0.9ms^{-1}) as compared to the lateral jets (1.05ms^{-1}). Negative velocity was seen near the left and right boundaries, arisen from recirculation in the aortic sinus, can be clearly observed in both the simulation and experimental results, both having comparable magnitude at (0.3ms^{-1}). The simulation was able to provide quite an accurate prediction in terms of the magnitude and some velocity contours. The well-known triple-jet structure can be seen in both simulation and experiment.

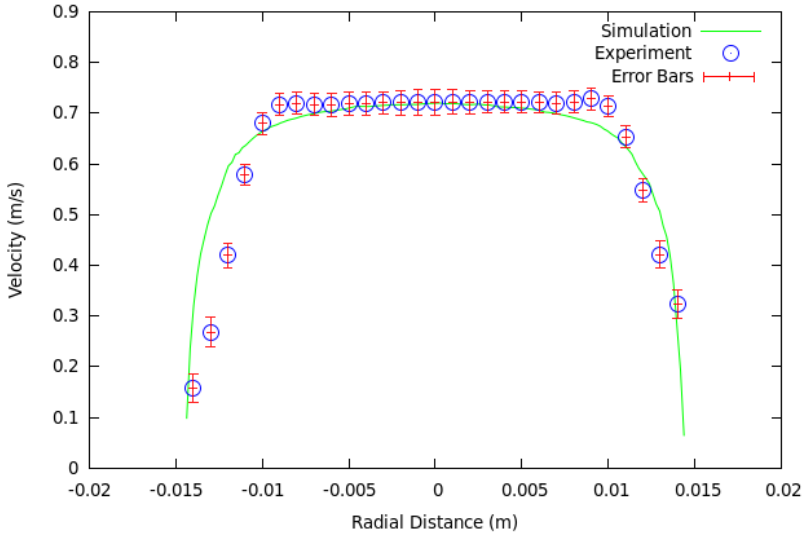

(A)

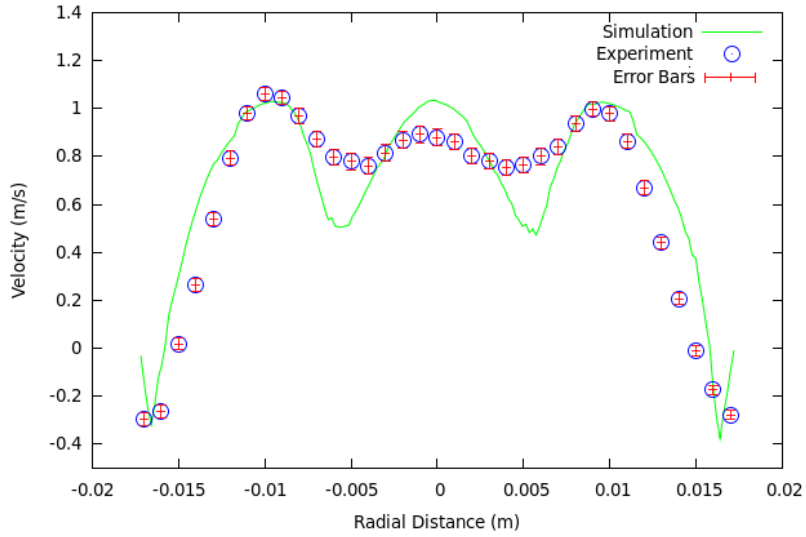

(B)

Figure 5-14: Velocity profile comparisons between experimental (o) and numerical simulation (–) at peak systole time t=0.115s for positions (A) Upstream, (B) Z=1D

Comparisons were also made at the other near peak systole time point at t=0.14s. Figure 5-15 shows the velocity contour obtained experimentally for

position Z=1D at time t=0.14s. The triple-jet structure merges downstream of the valve. In Figure 5-16 at position Z=1D, the triple-jet structure was visible although the velocity magnitude in the experiment was lower by about 10% compared to the simulation.

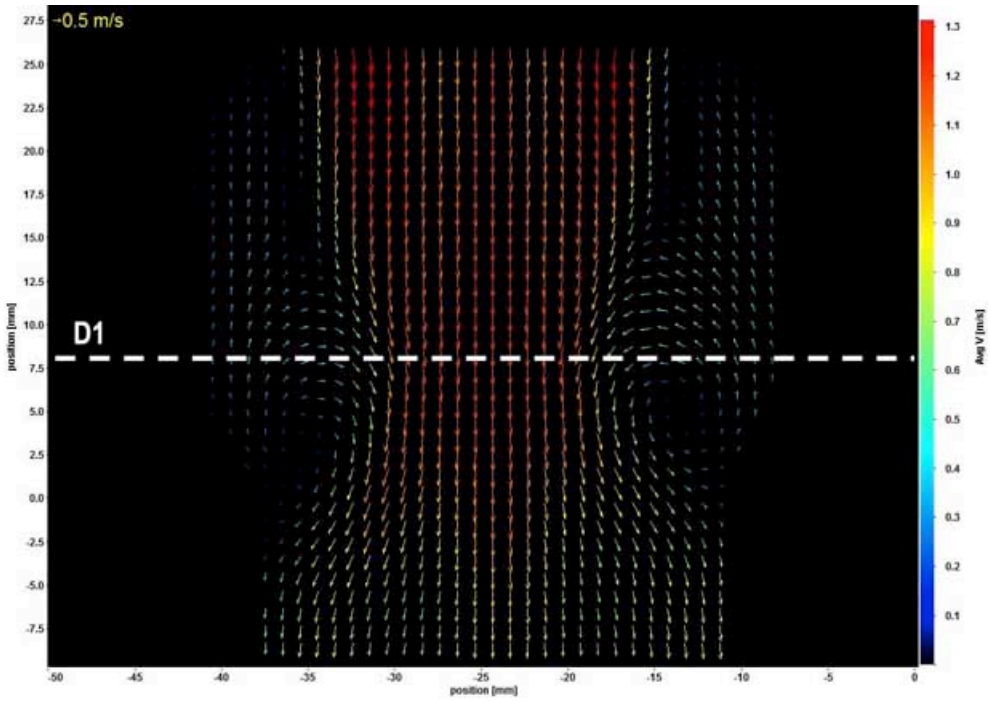

Figure 5-15: Velocity contour of the experimental study which shows the plane at position Z=1D at time t=0.14s

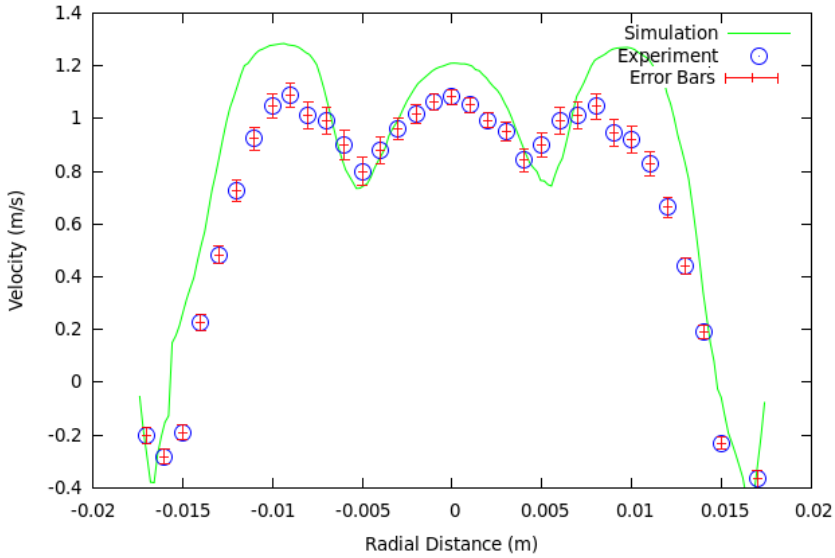

(A)

Figure 5-16: Velocity profile comparisons between experimental (o) and numerical simulation (–) at time t=0.14s for positions Z=1D

Similar comparison can be seen for the velocity profile at two other time points (t=0.07s and t=0.23s) as shown in Figure 5-17 at position Z=1D. The flow profile and velocity magnitude obtained in the simulation showed good

agreement with the experimental results, where the triple-jet structures have merged.

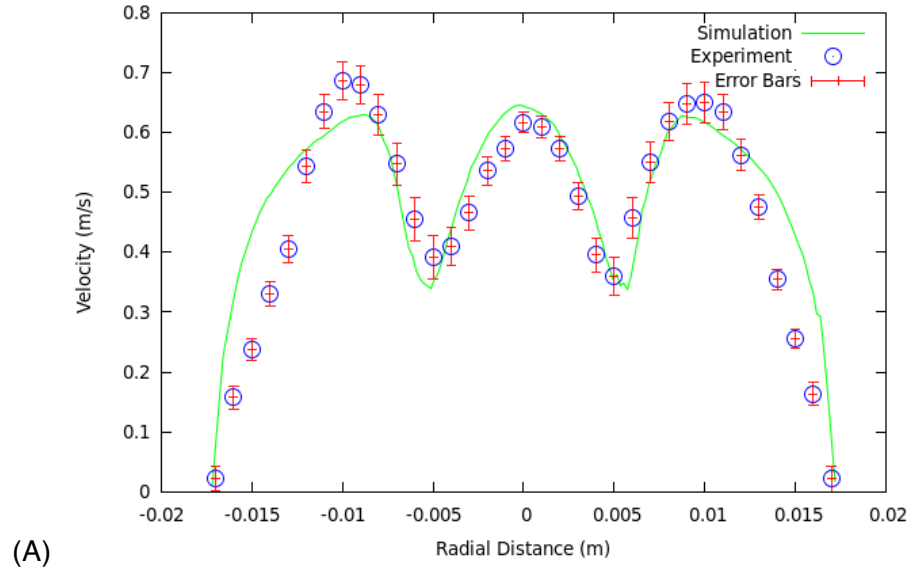

(A)

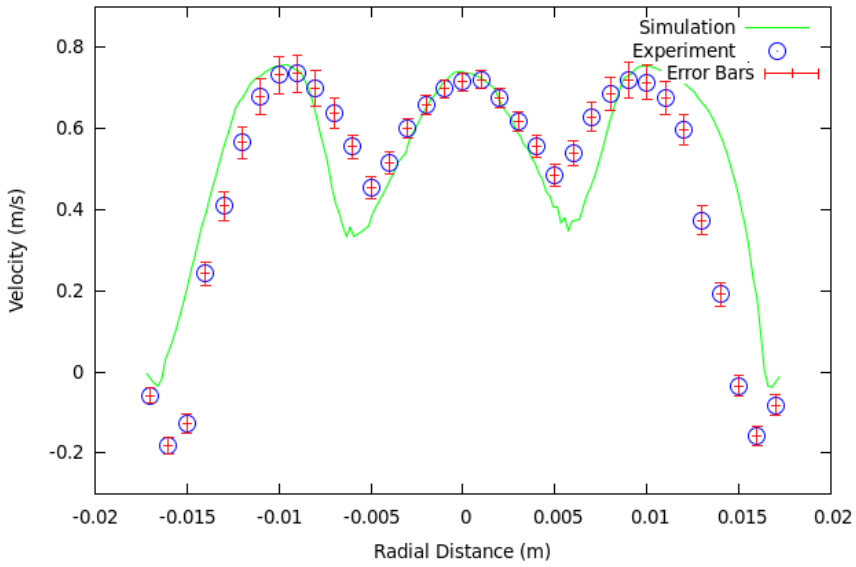

(B)

Figure 5-17: Velocity profile comparisons between experimental (o) and numerical simulation (–) for position 1D at (A) time t=0.07s, and (B) t=0.23s

The simulations were able to capture essential features of the pulsatile flow in the experiments. The recirculations near the walls of the sinus chamber at peak systole were captured in both experiment and simulation and showed comparable results. The triple-jet structure which was resulted from the obstruction of the flow by the two valve leaflets could be observed accurately, with the flow merging into two lateral flow downstream. Interesting flow features were often observed at the peak systole where the high velocity flow may cause blood shear and result in thrombogenicity. The diastole time

points were not captured because the flow rate was minimal. The interesting flow features to be observed during diastole would be the flow leakage through the hinges. However, this data was not able to be captured experimentally due to the opacity of the valve which obstructed the laser sheet.

Wall shear stress is another important parameter in BMHV simulations. Research has shown the association of wall shear stress with platelet activation, hemolysis and thrombus initiation on top of material properties and contact activation (King *et al.,* 1997, Cheng *et al.,* 2004). As the valve leaflets open, the blood is being forced through the valve leaflets, resulting in high velocity jets. These velocity jets will in turn cause high velocity gradients and induce high shear stress. The shear stress may then cause hemolysis or platelet activation. Figures 5-18 shows the wall shear stress distribution on the valve leaflet during the leaflet motion. It was seen from the contour plot that the shear stress was highest at the valve leaflet edge especially at the edge close to the inlet. This agreed with CFD simulation results by (Dumont et al., 2007). It was also observed that the wall shear stress was higher on the side of the lateral orifice than the central orifice, which could be due to the tilting direction of the valve leaflet when the valve was fully opened. When it was fully opened, the leaflet was at 85° from the transverse plane tilting toward lateral side. Therefore, the leaflet surface at the lateral side would be exposed more to the fluid flow, which caused elevated wall shear stress at the lateral surface.

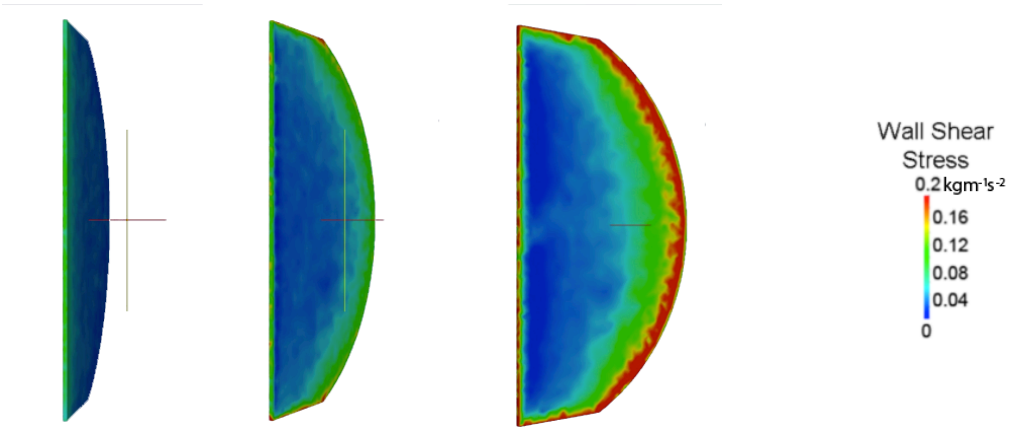

Figure 5-18: Wall shear stress distributions on valve leaflets from fully open to close

5.3.4 Limitations

The PIV laboratory experiments and time-accurate simulations were carried out for a flow through SJM Masters Series BMHV mounted in an axisymmetric sinus chamber. The simulation was started with the leaflets in the fully open position even though in reality, the valve moves from the closed position to the fully open position during diastole as the ventricular chamber is filled. The simulation was conducted in such a way because of the problem faced in mesh regeneration at the start of the simulation if the valve moves from the closed to fully open position; a very high velocity jet was observed in the small clearance region between the leaflets. However, such problem was not encountered when the valve moved from fully open to closed position. Nevertheless, it is important to study the solver to include the motion of the leaflet according to the actual cardiac cycle for a more realistic simulation. The experimental data was captured only during the valve opening and closure as each time point of the valve closure varied slightly during the experiment. As the PIV only averages out the 150 image pairs (which was 150 heart beats), it was not possible to obtain the correct position of the valve movement during opening and closing. The valve only has a window of about 0.04s for each of the opening and closing rotation of the leaflets in one cardiac cycle. Also the laser pulse was synchronized with the movement of the piston pump. The valve might have been closed at a slightly varied time due to several factors such as the pressure difference in the compliance and the pulsatile nature of the flow.

5.3.5 Summary

The study has developed and validated the pulsatile flow with prescribed leaflet motion for a 29mm SJM Masters Series BMHV. The flow profiles for different planes downstream of the valves were compared and showed close accuracy with the simulated results. The 3-dimensional model used in the numerical study was successfully validated using the experimental model.

5.4 Comparison of Hinge Microflow Fields of BMHVs implanted in different sinus shapes and downstream geometries

The objective of this study is to provide a detailed 3-dimensional flow simulation study in the hinge region of a SJM Masters Series bileaflet mechanical heart valve with two different aortic sinus shapes and downstream geometries. This study fulfilled Project Aim 2a by attempting to evaluate the flow fields of all four hinges in a single BMHV (α, β, γ and δ), as shown in Figure 5-21(A). The simulation results showed asymmetrical triple-jet structures in anatomical-straight and anatomical-arch cases, with velocity magnitude of 2ms^{-1} observed in the hinge recess during systolic phase. During early diastolic phase, high-speed leakage jets through the hinge gap regions for all four cases were observed with a maximum velocity of 4.7ms^{-1}. This also corresponded with high wall shear stresses in all four cases. The results of this work provided insights into impact of different aortic sinus shape, the aortic arch geometry and the location of the hinge recess on hinge microflow fields during systolic and diastolic phase.

In the simulation, a second-order Crank Nicholson implicit time discretization with adjustable time-step throughout the simulation with the average time-step in the magnitude of 10^{-5}s, The time-step was dependent on the maximum CFL number = 1. The Courant Number mean was about 0.08. In the unsteady, time-accurate, moving boundary simulation, the turbulent model used was SA model and implemented using the OpenFOAM package. Various forms of SA models can be found in Spalart (2000). The ALE formulation was used to discretize the system with prescribed leaflet motions over two cardiac cycles. The details of the finite volume method used in this study as discussed in the previous work (Nguyen *et al.*, 2012).

5.4.1 Hinge Model and Flow Domain

The valve geometry in this study was based on the design of a 29mm SJM Masters Series BMHV. In order to investigate the effects of sinus and aortic geometries on the flow fields, four different cases were modeled in this study, as follows: (i) a simplified axisymmetric sinus in a straight downstream pipe (simple-straight), (ii) a simplified axisymmetric sinus in a downstream curved

aortic arch (simple-arch), (iii) a three-sinus aortic root model in a straight downstream pipe (three-sinus straight) and (iv) a three-sinus aortic root model in a simplified downstream curved aortic arch (three-sinus arch), as shown in Figure 5-19(B). In this study, all the four hinges were modeled together with the entire valve geometry. The hinge gap width was the distance between the tip of the leaflet ear and the bottom of the hinge recess, defined as (y - x), as shown in Figure 5-19(C). In the model, the leaflet ear was placed within the butterfly-shaped depression (hinge recess) with a hinge gap width of 150 μ m, as observed in clinical valves (Simon *et al.,* 2010). In the first case, the BMHV was inserted into a simplified aorta model consist of a straight pipe with axisymmetric sinus and three-sinus aortic root. In the second case, the BMHV was inserted into a simplified curved aortic arch with the axisymmetric sinus and three-sinus aortic root in an anatomical position.

The centerline of the aorta followed the curvature of the normal diameters for the thoracic aorta of adults obtained by helical computed tomography (Hager *et al.,* 2002). However the three branches on the top were excluded to minimize the complexity of the flow simulation. The computational fluid domain of each of the four cases; namely simple-straight, three-sinus straight, simple-arch and three-sinus arch was subdivided into an unstructured mesh of approximately 3.6 million tetrahedral elements. The grid contained approximately 100,000 nodes with resolution of 7-8 μ m in the 150 μ m gap. During systolic phase, the valve was fully opened at an angle of 85° between the leaflet and the X-Y plane. After valve closure, the fully closed SJM leaflets formed a 35° angle.

(A) Inlet View

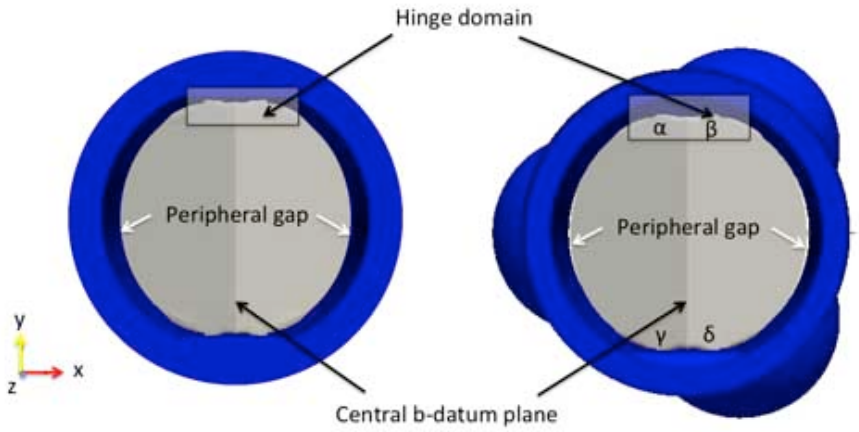

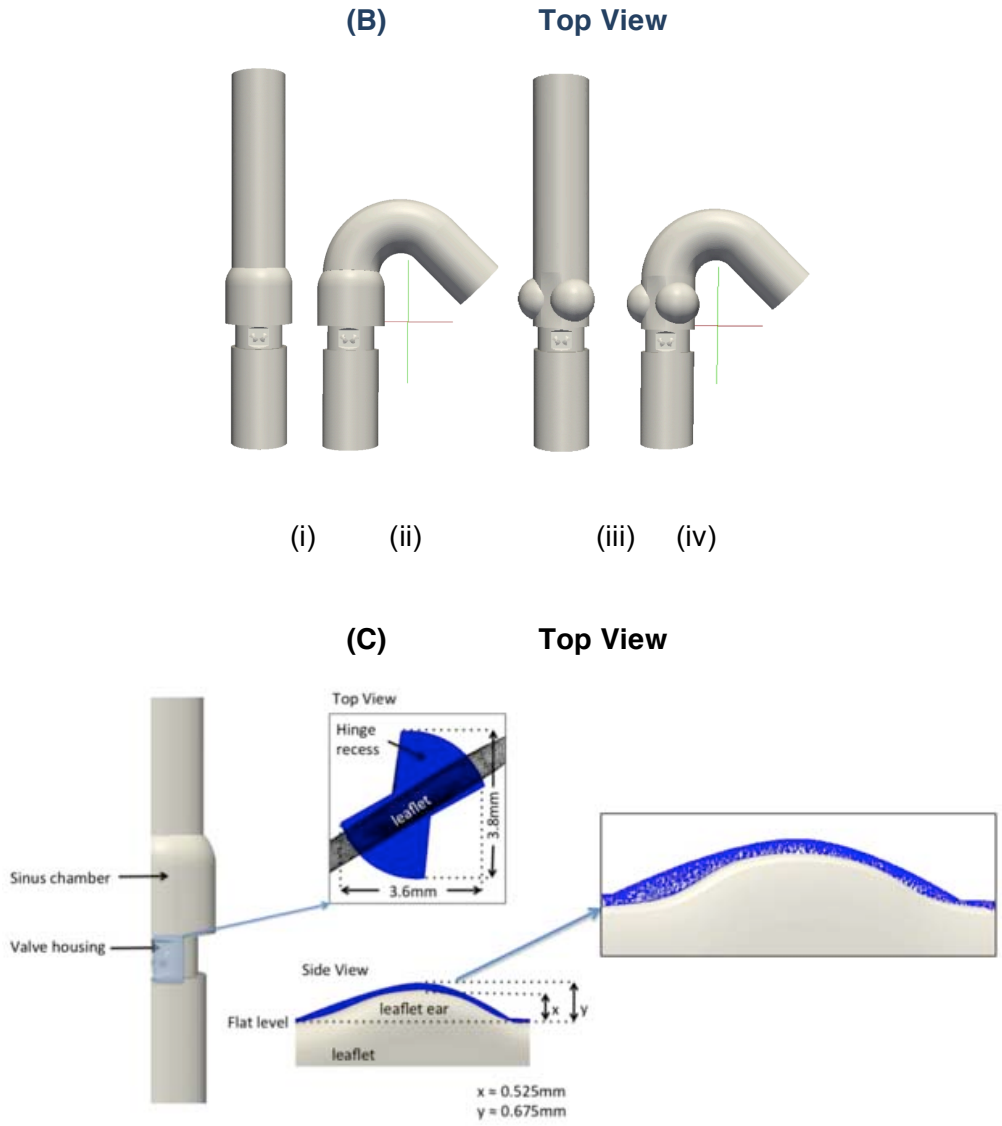

Figure 5-19: (A) the inlet view of the valve leaflet in the two sinus chambers, (B) Four simulation models with two different sinus chambers and two downstream geometries where a SJM valve model is inserted, (C) Hinge model with the butterfly shape hinge recess of SJM valve visible. The gap between the leaflet and the housing is about 0.15mm

5.4.2 Boundary Conditions

The BMHV was subjected to physiologic conditions and the velocity profile was obtained from the experimental data of the left ventricle study published by Lim *et al.,* (2001). The prescribed periodic condition started at fully open position where the ejecting velocity increased from zero to a peak velocity of 1.35ms^{-1}. The data points for aorta outlet pressure-time profile corresponded to the aorta blood pressure (Nichols and O'Rourke, 2005) and the peak flow rate was set at approximately 25Lmin^{-1}. The full cardiac cycle was 0.86s,

which corresponded to a heart rate of about 70bpm. At the inlet and outlet of the simulation cases, the velocity and pressure were prescribed using the given waveforms, shown in Figure 5-20. No-slip boundary condition was imposed at the channel walls, the leaflet walls and all body surfaces. The cardiac cycle condition used in this simulation was described earlier in section 3.4.4. In total, four time points were investigated for each model at peak systole (t=0.115s), early diastole (t=0.340s), mid-diastole (t=0.58s) and end diastole (t=0.82s). The leaflets rotated from 85° in their fully opened position to 35° at fully closed position.

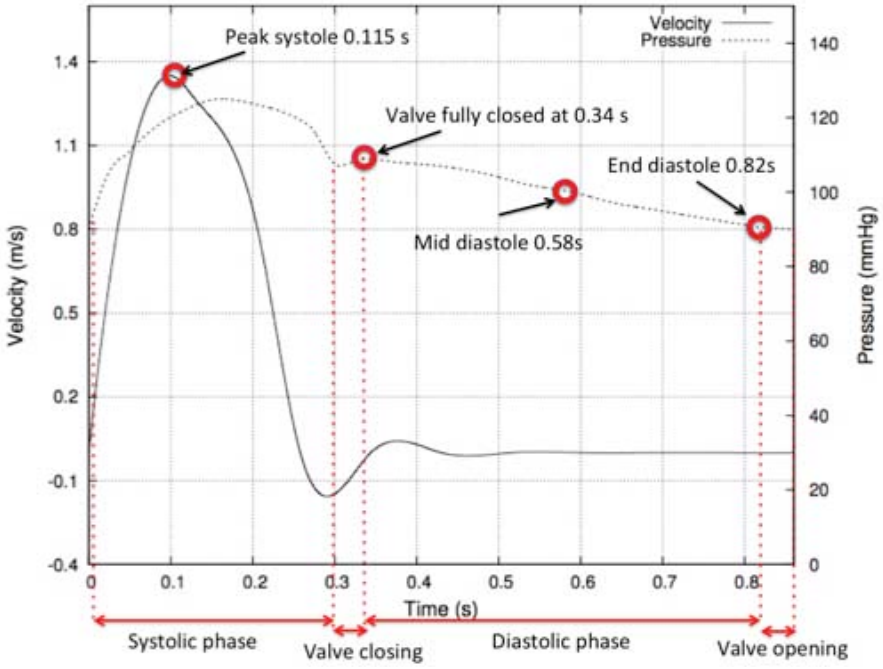

Figure 5-20: Velocity and pressure wave profile. Four time points were analyzed at peak systole 0.115 s, early-diastole 0.34 s, mid-diastole 0.58s and late-diastole 0.82s

5.4.3 Results

The terminologies used to describe the hinge recess geometry and flow patterns were shown in Figure 5-19. The flat level of the leaflet was used as the plane of reference. The vertical direction was the direction perpendicular to the flat level and parallel to the leaflet axis. The direction parallel to the main flow was the axial direction while the direction from the b-datum plane to the valve housing was the transverse direction.

5.4.3.1 Downstream flow fields of BMHV

During the systolic phase, the general flow fields were observed to be highly 3-dimensional with strong forward flow. The downstream flow profiles for both

the straight and the curved aortic arch were compared. The origin of X and Y-axes was at the center of the flow channel with the Z=0 plane located at the trailing edge of the leaflets with corresponding velocity components *u, v* and *w* respectively. The streamwise velocity profiles were compared at position Z=1D (D = inlet diameter).

Figure 5-21 showed the velocity contour plot in the mid-plane at peak systole for all the simulation cases. At peak systole, the triple-jet structures of the flow were observed in all simulation cases. The flow features were the result of the presence of the two valve leaflets and have been reported in previous BMHV studies and were considered a typical flow pattern observed in BMHV placed in a straight pipe (Leo 2005, Ge *et al.,* 2005, Nguyen *et al,.* 2012).

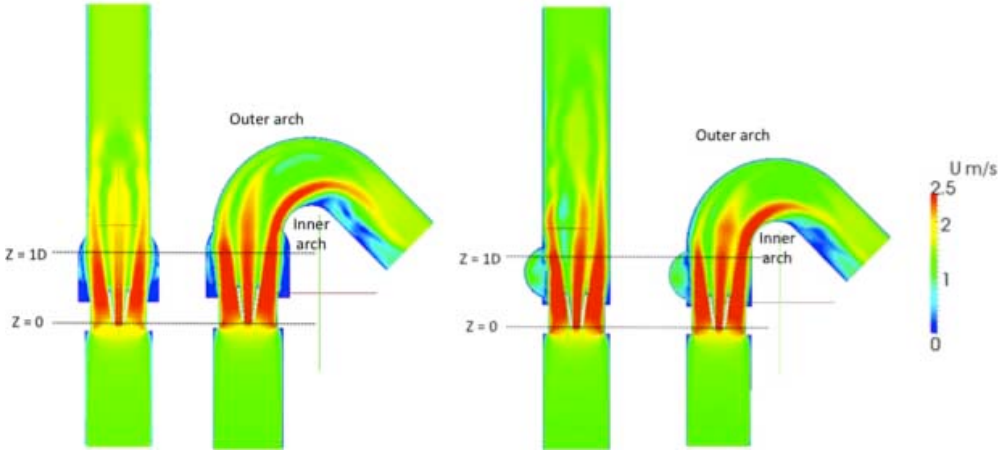

Figure 5-21: Plan view of streamwise velocity contours for all four simulation models at cross sectional plane, Z=1D at peak systole 0.115s

For the simple-straight model, the triple-jet structure appeared to be symmetrical at position Z=1D, as shown in Figure 5-22 (i). However, for the simple-arch model in Figure 5-22 (ii), the downstream flow profile was not symmetrical and deviated towards the inner arch of the aorta. Similarly, in the three-sinus straight and three-sinus arch models, the triple-jet structure was not symmetrical, as shown in Figure 5-22 (iii) and (iv). The simulation of BMHV placed in a curved aorta downstream has not been studied before. In both the latter cases, the central jet shifted away from the sinus chamber on the right towards the inner arch, as viewed from the inlet position for the three-sinus aortic root.

Another key feature observed in the simulations was the formation of vortices near the wall edge in the sinus chambers. The flow recirculation in the sinus chambers was observed in both simple-arch and three-sinus arch cases. Interestingly, regions of recirculation were also observed downstream in both the simple-arch and three-sinus arch cases, as highlighted in Figure 5-23. These flow features have not been discussed in earlier studies and could be the cause for flow stagnation in the downstream regions. The formation of vortices in the aortic sinus was also observed at the downstream of the hinge regions. In general, the downstream flow velocity during diastolic phase was low and decreased to almost stagnat in all four simulated cases.

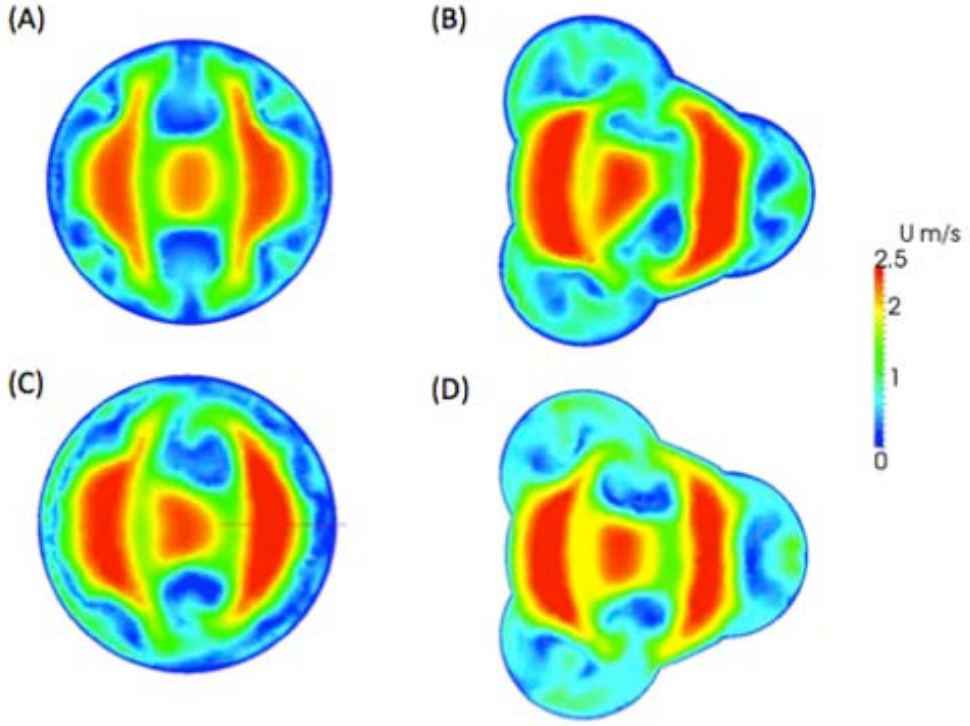

Figure 5-22: Cross sectional planes at Z=1D which show the triple-jet structures at peak systole 0.115s for (A) simple-straight, (B) simple-arch, (C) three-sinus straight, and (D) three-sinus arch

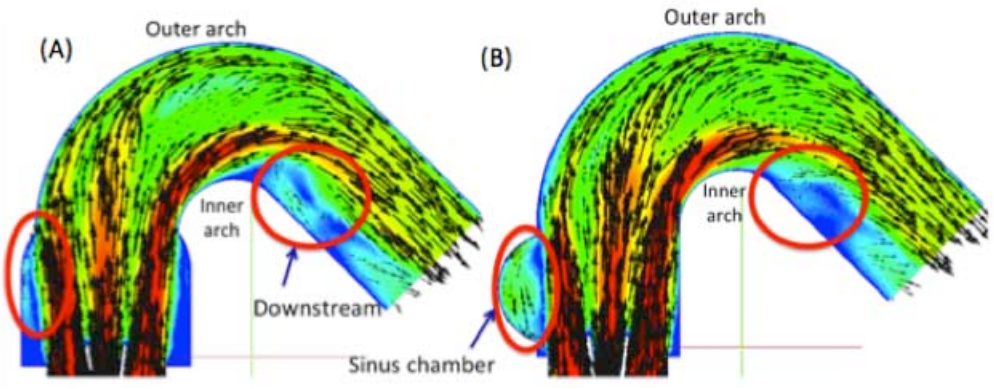

Figure 5-23: Recirculation regions observed in the circled regions at peak systole 0.115s in (A) simple-arch and (B) three-sinus arch

5.4.3.2 Hinge Microflow Fields during Systole

The velocity contour plot for the two hinges, α and β, for each model were shown in Figure 5-24 (A). Generally, the flow velocity was higher at the outer face of the leaflet ears from the center plane than that at the inner face of the leaflet ears. The flow velocity throughout the hinge recess followed closely the magnitude of the valvular flow rate in all the four-simulation cases with the maximum velocity magnitude within the hinge recess reaching approximately 2ms^{-1} during peak systole. No significant differences in velocity magnitude were observed at the hinge region when comparing between the straight pipe models (Figure 5-24 (A)(i) and 5-24 (A)(iii)), and between the simplified aortic arch models (Figure 5-24 (A)(ii) and Figure 5-24 (A)(iv)). However, velocity differences were observed in the inner flow circled region between the straight pipe and aortic arch models. The flow velocities in hinge β of aortic arch models were lower compared to those in the straight pipe models. The flow fields between the two hinges (α and β) were not symmetrical in the aortic arch models. To investigate further, the hinge flow fields for all four hinges (α, β, γ and δ) in the three-sinus arch model were compared. Figure 5-24 (B) compared the velocity contours in all of the four hinges in the three-sinus arch model at peak systole. The flow patterns were different among the four hinges and they were not identical. The flow fields for the other three cases exhibited similar asymmetric flow patterns during peak systole (not shown here). The velocity values at the inner face region of the four hinges were different from each other especially at the outer face and the trailing edge regions. The flow velocity in hinge α at the inner face region was higher than the other three hinges. At the leading edge of the leaflet

regions, hinges γ and δ appeared to have smaller regions of high velocity flow compared to α and β. These flow pattern differences affect the shear stress distribution in the hinge regions.

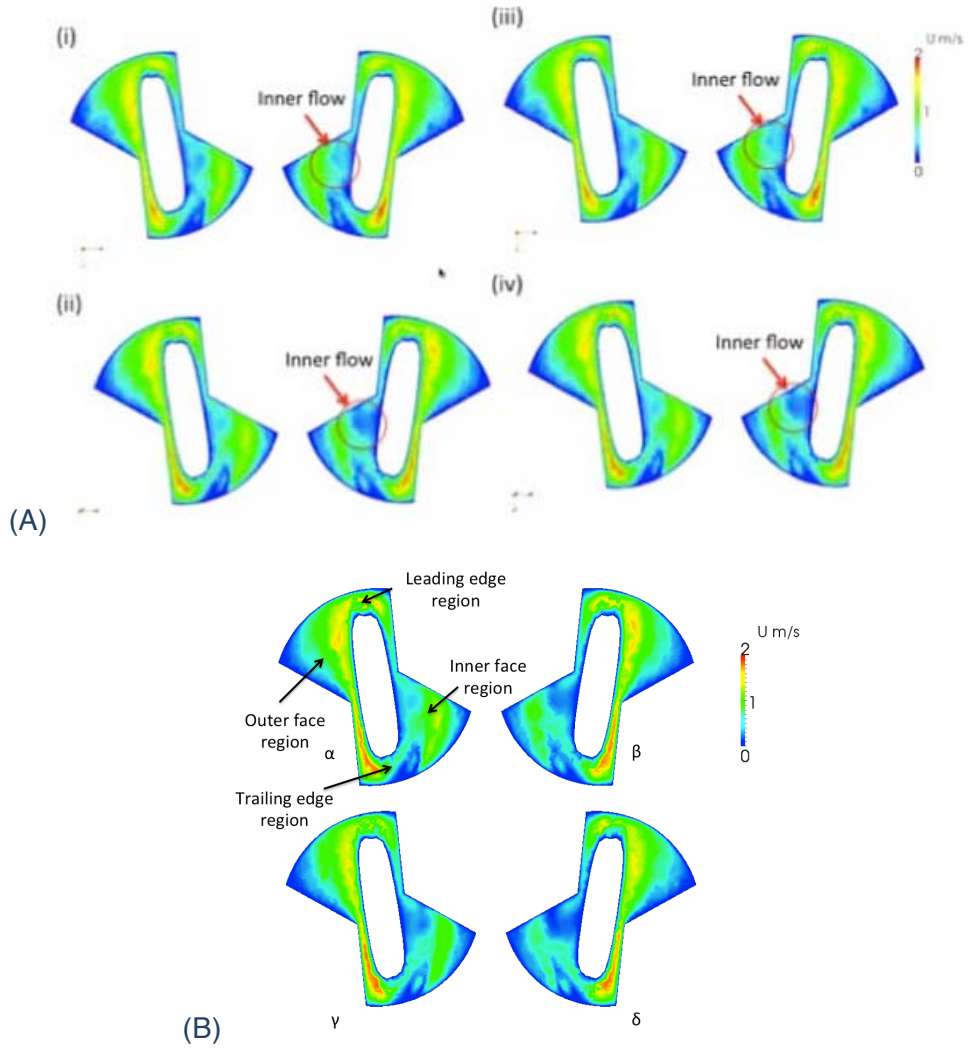

Figure 5-24: (A) Flow fields at hinge α and β for (i) simple-straight, (ii) simple-arch, (iii) three-sinus straight, and (iv) three-sinus arch at peak systole, (B) Hinge flow fields for all four hinges α, β, γ and δ for three-sinus arch at peak systole

5.4.3.3 Hinge Microflow Fields during Diastole

Figure 5-25 (A) compared the velocity fields at early diastolic phase for hinges α and β, for all the four cases. The general trend of the flow within the hinge recess was similar across all four cases at the near wall regions, except with higher velocity observed at the trailing edge region when compared to the leading edge region of the hinge recess. Unlike at peak systole, no significant differences in velocity magnitude were observed in the hinge regions between the straight pipe and aortic arch models during early diastole. Figure 5-25 (B) compared the flow field among the four hinges in the

three-sinus arch model. In the circled region of the outer face of the leaflets for hinge α, the velocity appeared to be slightly lower than the other three hinges β, γ and δ.

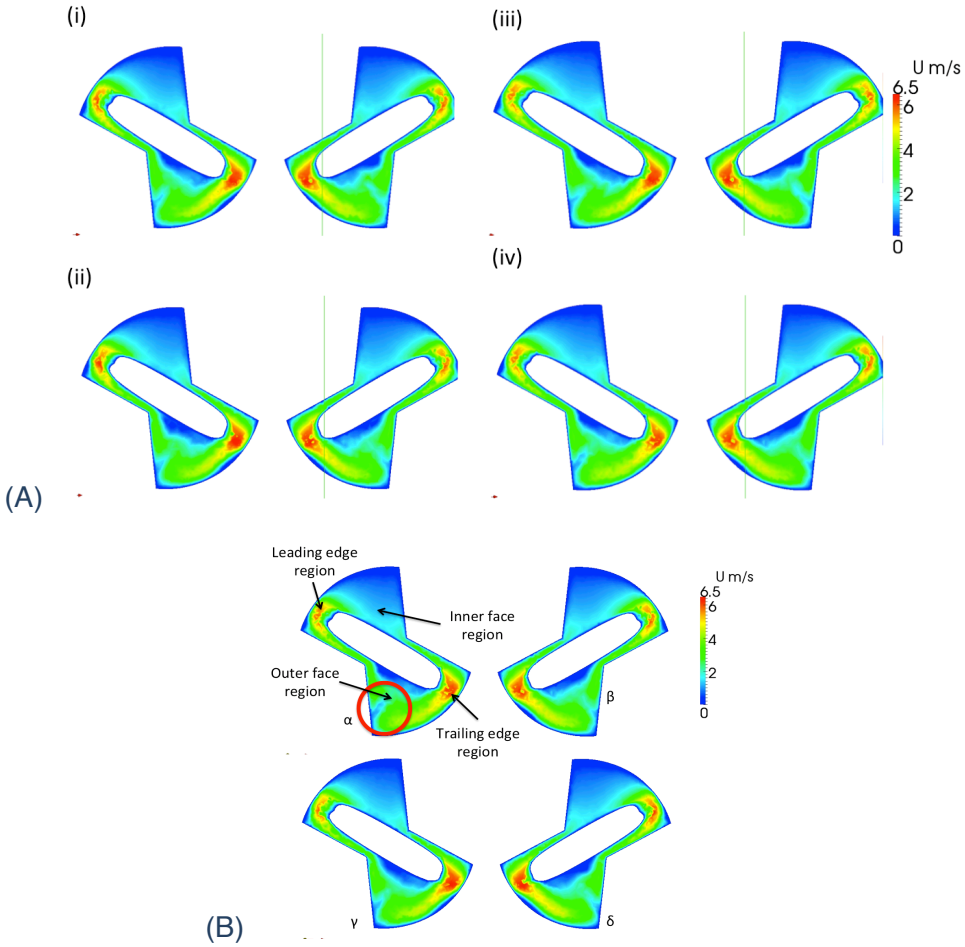

Figure 5-25: (A) Flow fields at hinge α and β for (i) simple-straight, (ii) simple-arch, (iii) three-sinus straight, and (iv) three-sinus arch at early diastole, (B) Hinge flow fields for all four hinges α, β, γ and δ for three-sinus arch at early diastole

The leakage flow rates observed in the 29mm SJM BMHV at early diastole were shown in Table 5-1. The average leakage flow rate for the four models was found to be 0.457 ± 0.001Lmin^{-1}. This leakage rate was observed to be between that of the high leakage prototype (0.490 ± 0.021Lmin^{-1}) and low leakage prototype valves (0.049 ± 0.001Lmin^{-1}) reported by Leo *et al.,* (2006). Comparing the leakage rates through each individual hinge, the difference between the highest and lowest flow rate for the cases were 2.80% (simple-straight), 2.62% (simple-arch), 2.35% (three-sinus straight), and 3.06% (three-sinus arch). The indifference in the leakage rates showed that they ere independent of the different sinus shapes and downstream geometries. Nevertheless, the leakage rates were not able to account for the shear stress

distribution within the hinge recess. The shear stress distribution was based on the flow profiles in the hinges.

Table 5-1: Leakage flow rate through the hinge regions

	Hinge α $Lmin^{-1}$	Hinge β $Lmin^{-1}$	Hinge γ $Lmin^{-1}$	Hinge δ $Lmin^{-1}$	Total Flow Rate $Lmin^{-1}$
Simple-straight	0.1134	0.1166	0.1139	0.1145	0.4584
Simple-arch	0.1155	0.1135	0.1125	0.1149	0.4564
Three-sinus straight	0.1122	0.1149	0.1138	0.1147	0.4556
Three-sinus arch	0.1161	0.1139	0.1126	0.1146	0.4572

5.4.3.4 Hinge Flow Fields In Anatomical-Arch Model

Figure 5-26 showed the flow fields within hinges β during diastole phase. High-velocity jets were observed at the position *c* and *d* at early diastole. These high-velocity leakage jets had large out-of-plane velocity components with a maximum velocity of $4.7ms^{-1}$. Figure 5-26 (A) showed the six planes, which were 100 μm apart from each other starting from the flat level. High reverse velocities were observed in all planes within the hinge recess. The leakage flow between the leaflets at the hinge housing was observed at the side view. The strong and highly 3-dimensional flow structures showed the complexity of the flow in the hinge regions during early diastole. There were not much flow variations among the four simulation cases during early diastole. At mid-diastole in Figure 5-26 (B), high-velocity jets were also observed at the position *c* and *d* but at comparatively lower velocity magnitudes of $0.46ms^{-1}$. The highest leakage flow velocity was also observed at the area between of the tip of the leaflet ears and the hinge recess at 100 μm from the flat level (point *e*). The flow leakage was also observed between the hinge and the leaflet ear. The highest leakage velocity was $0.076ms^{-1}$ in the backflow direction through the gap between the leaflet ear and the hinge recess. Figure 5-26 (C) showed the flow field at late diastole when the flow was almost zero.

(A) Top View Side View

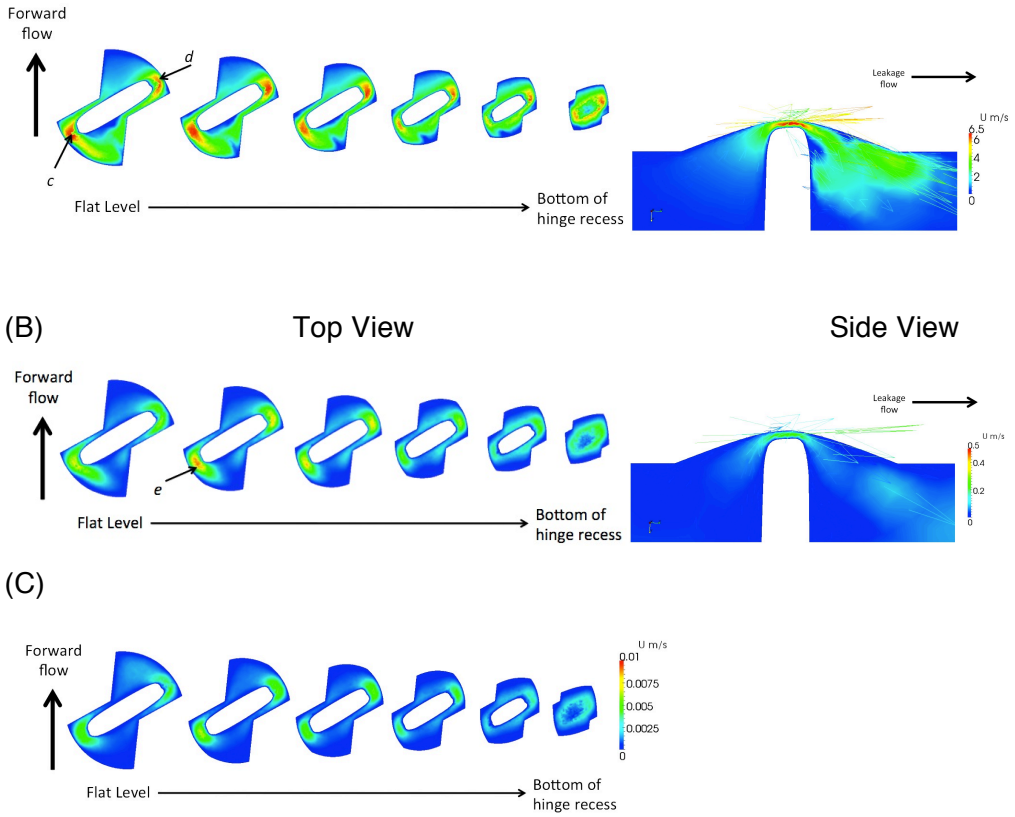

Figure 5-26: Hinge flow fields along six different planes within the hinge recess at (A) early diastole, (B) mid-diastole and (C) late-diastole for three-sinus arch. The six planes shown here are 100μm apart from each plane starting from the flat level. Leakage flow can be observed at the side view

5.4.3.5 Wall Shear Stress Distribution

At peak systole, the wall shear stress magnitude at the hinge recess for all four cases was approximately 270Pa. High wall shear stress magnitude was typically observed during early diastole phase (with the maximum level at 1.6kPa in hinge β). There were slight variations in the wall shear stress distribution among the four cases largely because the velocity profile near the wall of the leaflets were largely similar. However, only the three-sinus arch results for hinge β at peak systolic and early diastolic phase will be presented (Figure 5-27). In general, the wall shear stress levels within the hinge recess during peak systole were lower compared to those during the early diastole (Figure 5-27 (A)). At early diastole, the high-wall shear stress region was coincident with the region of high-velocity leakage jets, as shown at positions *f* and *g* in Figure 5-27 (B). The wall shear stress in the hinge recess cavity at peak systole was about the same magnitude at 270Pa as seen in Figure 5-27 (C). On the other hand, the hinge recess cavity demonstrated a slightly higher wall shear stress magnitude of approximately

1.65kPa when compared to the hinge area during early diastole. Elevated wall shear stress was also observed in regions *h* and *j* at the upstream of the flow, during early diastolic phase in Figure 5-27 (D). In mid-diastole and late diastole, the wall shear stress was observed in the same location but with smaller magnitude.

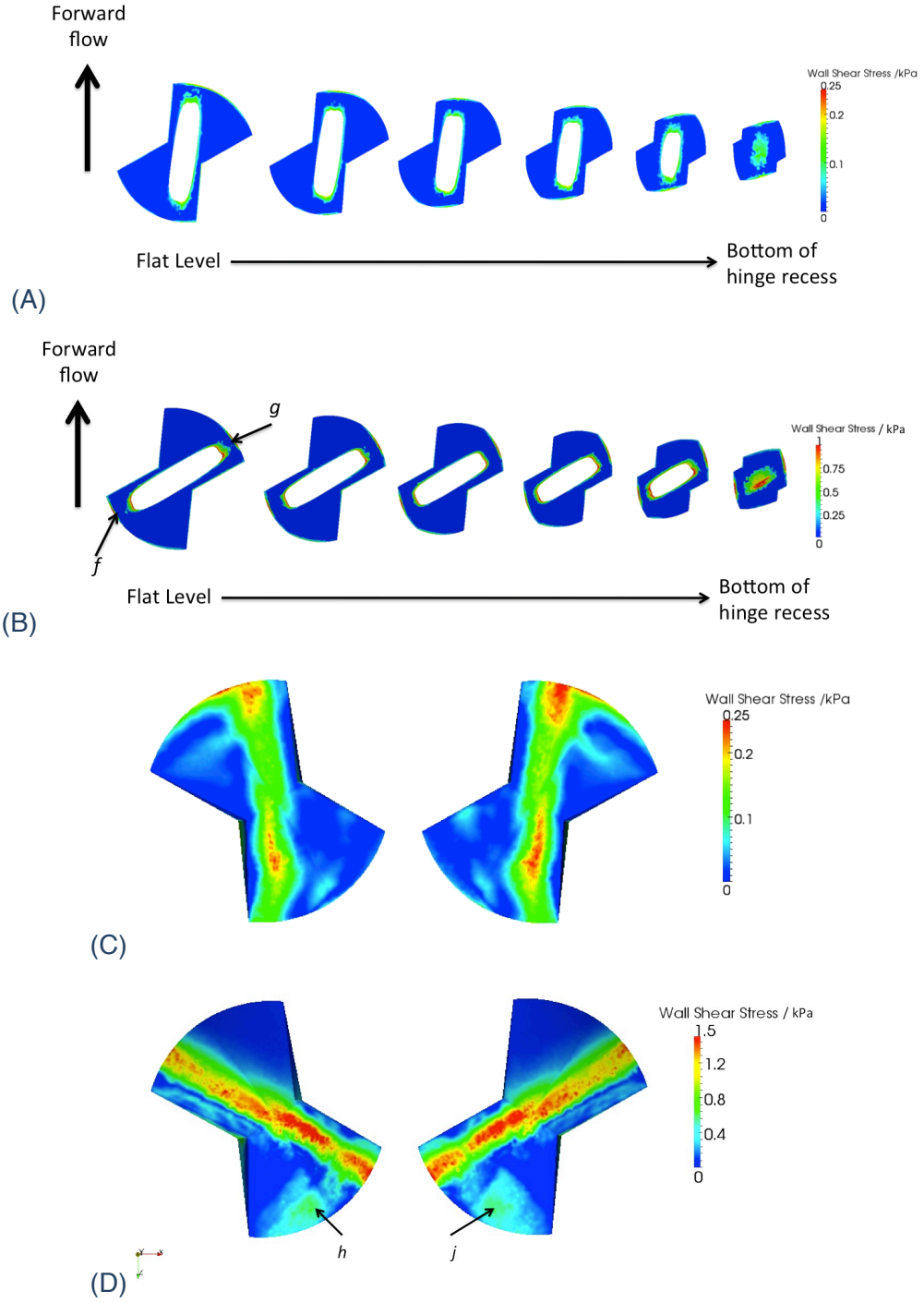

Figure 5-27: Wall shear stress along six different planes within the flow domain in hinge recess for three-sinus arch. The six planes shown here are 100µm apart from each plane starting from the flat level at (A) peak systole, (B) early diastole, Wall shear stress of the hinge recess surface for three-sinus arch at (C) peak systole, (D) early diastole

5.4.4 Discussion

In this study, a 3-dimensional, time-accurate flow simulation of a SJM valve was performed under physiological flow conditions. All the four hinges were modeled in order to identify the flow differences within these pivot recess regions. Four types of geometries were performed to understand the effects of the sinus shape on the hinge recess flow. Simulations based on a section of the cardiac cycle; such as the forward flow phase (Kelly *et al.,* 1999) or limited to just steady flow conditions (Wang *et al.,* 2001) are not able to capture the flow unsteadiness accurately. As such, physiological flow conditions were imposed so as to observe these flow characteristics in the hinge flow fields, as recommended by Simon *et al.,* (2010) too. It is important to model the flow based on physiological boundary conditions in order to access the performance of the hinge design. The prescribed motion of the leaflets was performed with a constant angular velocity and a closing time equal to that of the opening time

The current model uses the ALE method so that the mesh is deforming with time as leaflet is rotating from its full open position (85°) to valve closure (35°). The use of ALE method has many advantages although it relies on the continuous regeneration of mesh while maintaining good mesh quality. By performing a constant angular velocity, the flow field during the hinge movement may not be captured accurately. However, during the four time points that was observed in the simulation (peak systole, early diastole, mid diastole and late diastole), the time varying nature of the angular velocity of the leaflets are not as critical. As such, imposing a constant velocity movement was conducted. The flow field was analyzed during peak systole, when the leaflets are fully open with majority of the bulk flow through the open valve, and the early, mid and late diastole when the leaflets are fully closed.

The rotation angle was determined based on the pressure and the velocity flow at both the inlet and outlet. The resistance offered to the flow by the hinges and the peripheral gap was also dependent on the dimensions and geometry of these gaps. To achieve optimal spatial resolution while managing

the computational resources, each element was about 7-8 μ m in size in the 150 μ m gap, as observed in clinical valves.

5.4.4.1 Downstream Flow Fields of the BMHV

In this simulation, a 3-dimensional, time-accurate flow simulation of a SJM valve was performed under physiological flow conditions. Each of the four valve geometry was modeled with all four hinges. The results showed that the hinge microflow fields are highly 3-dimensional and complex. The downstream geometry between straight pipe and aortic arch were shown to have affected the hinge flow fields during peak systole although such differences were not observed during diastole. Triple-jet structures were observed among the four cases during peak systole but with non-symmetrical downstream flow profiles observed in both the three-sinus aortic root cases. With the simplified aortic arch geometry, the triple-jet structures shifted towards the inner arch wall with the formation of flow recirculation regions observed between position 2D and 4D downstream from the valve. Such flow structures were not evident in the straight pipe cases. The difference was due to the shape of the arch which forced the flow to be directed towards the inner arch direction. The significance of such observation helped to highlight the potential area where thrombosis may occur and this can affect the angle of implantations in a clinical setting.

5.4.4.2 Sensitivity of Hinge Flow Fields

Flow unsteadiness in the lateral and ventricular corners of the hinge region was observed at peak systole and early diastole. By investigating the four-hinge geometries in this study, the results showed that the four hinges generally exhibit slightly different flow fields. During systolic phase, the shape of the sinus chambers appeared to have minimal effect on the bulk flow through the fully open valve and the hinge flow regions. However, the downstream shape affected the flow in the hinge regions where lower velocities were observed in the aortic arch downstream models at peak systole. One possible explanation would be due to the asymmetrical downstream flow profile in the aortic arch downstream models. The triple jet structures were pushed towards the inner walls and affected the hinge flow profiles.

Highly complex 3-dimensional flow fields were observed throughout the diastolic phase with decreasing leakage flow rate from early diastole to late diastole. The backflow velocity through the hinge regions was much higher at 4.7ms^{-1} compared to the rest of the flow domain with average velocities ranging from 0.042ms^{-1} to 0.156ms^{-1}. The high-speed leakage jets could impact the level of hemolysis and platelet activation at the ventricular corner, which may potentially affect the performance of the valves. The backflow in the simulations conducted in an earlier paper was 4.75ms^{-1} (Simon *et al.,* 2010).

5.4.4.3 The Relative Position Of The Hinge Does Not Affect Hinge Flow Leakage Rate

The reported leakage rate between the various cases differs by 2-3%. These results suggest that the difference between the four cases may not be significant. Nevertheless, there is still merit to study the difference in the various velocity contours in each of the four hinges as shown earlier for three-sinus arch. The velocity contours of the hinges were subtlety different from each other, especially when a non-symmetric sinus chamber was modeled. A human native aorta bulges outwards to form the three-sinuses (Ho 2009). The three-sinus model was used in the simulation to mimic the human native aortic sinus. The study demonstrated subtly differences in the hinge flow fields contour between straight pipe and downstream aortic arch at peak systole. Hinge flow patterns differences were observed when the flow fields in all four hinges were analyzed within the aortic arch model although the leakage rate suggested similar rate. Using a model which closely resembled geometry to the native aortic sinus would be a better choice, hence a more accurate representation of the hinge micro flow fields. As such, the hinges in conjunction with a three-sinus aortic root geometry and curved downstream aortic arch that closely resembled that of native human model should be included in future hinge flow contours study. It is not necessary to simulate all four hinges if the research focuses on the leakage rate through the valves and not the flow contours.

5.4.4.4 Elevated Wall Shear Stress May Lead To Hemolysis And Platelet Activation

The threshold level responsible for red blood cell hemolysis to occur was found to be approximately 400Pa, below which a sublethal region of zero hemolysis was observed (Sallam and Hwang, 1984). Earlier studies also reported that platelet activation and aggregation could occur at shear stress as low as 5Pa, and irreversible platelet aggregation occurs at shear stress of 10Pa (Hung *et al.,* 1976, Ramstack *et al.,* 1979, Slack *et al.,* 1993). The blood elements experienced higher rate of collision with the valve wall due to the recirculation flow formed near the wall as a result of turbulent flow. Such platelet activation by high wall shear stresses may lead to thromboembolic complications (King *et al.,* 1997 and Cheng *et al.,* 2004). These regions were associated with high wall shear stress, and may lead to hemolysis and platelet activation. The large wall shear stress during diastolic phase may be more detrimental to blood elements compared to the systolic phase. This observation is consistent with earlier studies (Ellis *et al.,* 1996, Lamson *et al.,* 1993, Maymir *et al.,* 1997, Steegers *et al.,* 1999, Simon *et al.,* 2010). As a result, the design of the leaflet ear, the wall curvature of the hinge recess and the upstream of the leaflet edge may contribute significantly to the thromboembolic risk in the BMHV. Higher wall shear stress was observed during diastole phase compared to peak systole, which suggest that diastole played a bigger role in causing detrimental damage to the blood elements. Nevertheless, through this numerical simulation, it can be postulated that the hinge design is important to minimize any unfavorable flow features during the cardiac cycle. It can also be used as an important tool to characterize potential thromboembolic complications in regions which cannot be measured experimentally due to the design and opacity of the hinge.

During the forward flow phase at peak systole, the highest shear stress regions are located at the upstream and downstream of the hinge and along the surface of the leaflets. The shear rate recorded here is about 0.25kPa, which potentially lead to thrombosis due to platelet activation. On the other hand, the simulations showed the maximum elevated wall shear stress at the hinge recess during early diastole recorded at 1.65kPa at near wall regions, which include the peripheral gap formed by the closed leaflet and the valve

housing, the tip of the leaflet ear and the hinge recess, and the wall of the ventricular side of the hinge. This suggests that during this phase, the blood elements flowing through the hinge regions can lead to hemolysis as a result of the high shear rates they experience.

5.4.5 Limitations

The leaflet in the simulation model was limited to prescribed rotation only while in actual scenario, the leaflets are free to rotate and translate up and down along the leaflet axis. The blood was modeled as an incompressible single-phase Newtonian fluid (Yun *et al.,* 2012, Leo *et al.,* 2006, Simon *et al.,* 2004, Ellis *et al.,* 2000a). The blood exhibits non-Newtonian properties at low shear rates in reality. The downstream aorta was simplified to omit the head vessels in the arch region and coronary outlets due to the computational difficulties to set multiple outlet boundary conditions with physiological pressure waveforms.

5.4.6 Summary

The study has highlighted the regions of high wall shear stress in the hinge regions which may cause platelet activation leading to thromboembolic complications. There were differences noted within the flow field profile of the four hinges during peak systole of the three-sinus arch model. Nevertheless each individual hinge did not vary much in terms of the leakage flow rate through the valves. As such, it is not necessary to simulate all four hinges together but the hinge should be simulated with a three-sinus aortic root geometry and curved downstream aortic arch since this geometry resembled that of native human model.

5.5 Comparison of Different Implantation Angles for Bileaflet Mechanical Heart Valves

The current study quantifies the flow through the valve placed in different sinus and aortic arch models in order to accurately capture the impact of valve's orientation on its downstream flow. This study compared the downstream flow fields of two different sinus geometries and two different downstream aortic arch geometries due to the different valve orientations (0°, 30°, 60° and 90°) during peak systole. The flow in valves implanted at 0° with respect to the anatomical position showed lower velocity magnitude and more evenly distributed flow profiles while flow in valves implanted at 90° (anti-anatomical position) displayed larger velocity gradients. The result of this work provided insights into the impact of different valve orientation on the flow fields of aortic sinus and aortic arch. This results of this section has been accepted for publication in Journal of Heart Valve Disease.

5.5.1 Geometry of BMHV and Aortic Sinuses

The valve geometry used in this study was based on the SJM 29mm BMHV design. The native aortic valve consists of three leaflets and three aortic sinuses (Valsalva sinuses), with approximately 120° rotational symmetry. To investigate the effects of sinus shape and downstream geometry of aortic arch on the flow field, the flow through four different geometric models were analyzed and compared with each other. The four models are (i) a simplified axisymmetric sinus in a straight downstream pipe (simple-straight), (ii) a simplified axisymmetric sinus in a downstream curved aortic arch (simple-arch), (iii) the three-sinus aortic root in a straight downstream pipe (three-sinus straight) and (iv) the three-sinus aortic root in a downstream curved aortic arch (three-sinus arch), as shown in Figure 5-28(A). In the models with downstream curved aortic arch, the geometry was simplified without the main aorta branches on the aortic arch. The computational models and boundary conditions were similar to those used in Section 5.4, including, the aorta geometry, sinus geometry (both simplified and three-sinus shape), BMHV design and flow waveform. In each model, BMHVs were positioned at different angles (0°, 30°, 60° and 90°), as shown in Figure 5-28 (B and C). The reference 0° is the preferable orientation of aortic valve, known as

anatomic position, is shown in Figure 5-29 (Kheradvar and Pedrizzetti, 2012). The valve leaflets were fully opened at an angle of 85° between the leaflet and the X-Y plane during systolic phase. The computational fluid domain of each case was subdivided into an unstructured mesh of approximately 3.5 million tetrahedral elements.

(A) Top View

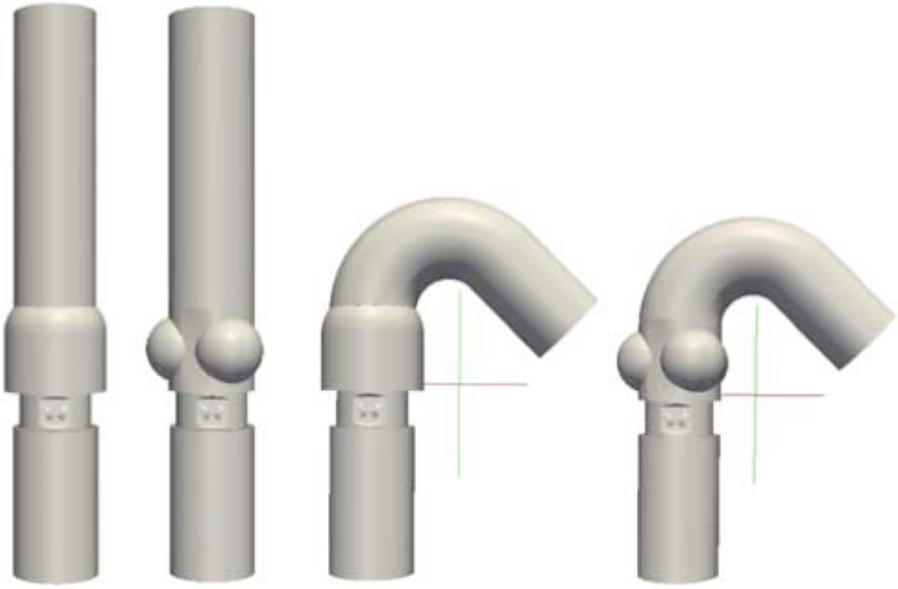

(B) Inlet View

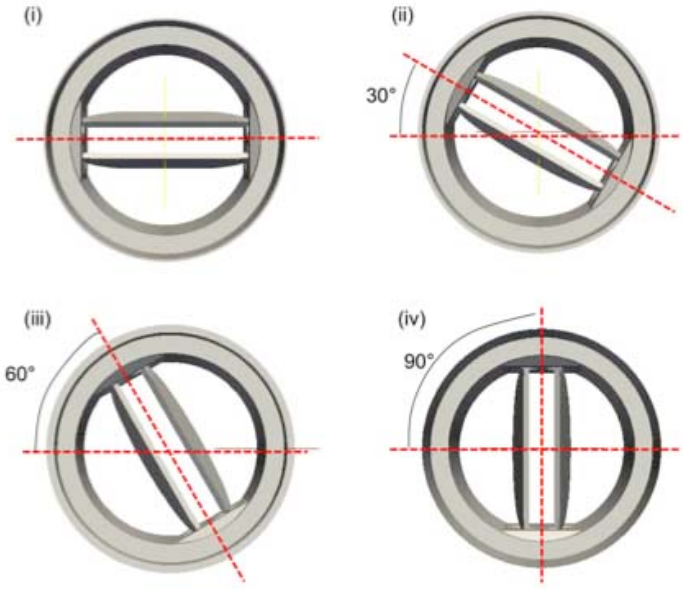

(C) Inlet View

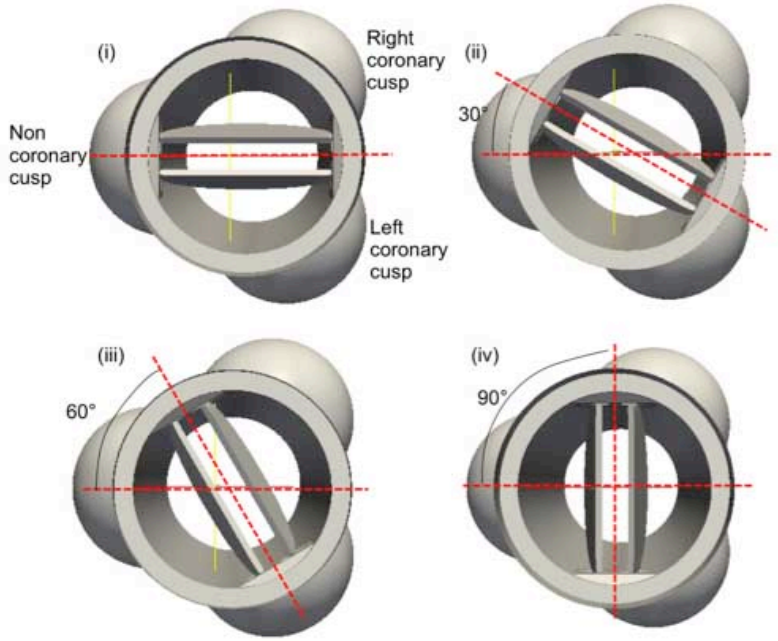

Figure 5-28: (A) Four geometric models with two different sinus chambers and two downstream geometries where a SJM valve model is inserted; four different valve orientations for (B) simplified axisymmetric sinus and (C) three-sinus aortic root geometry

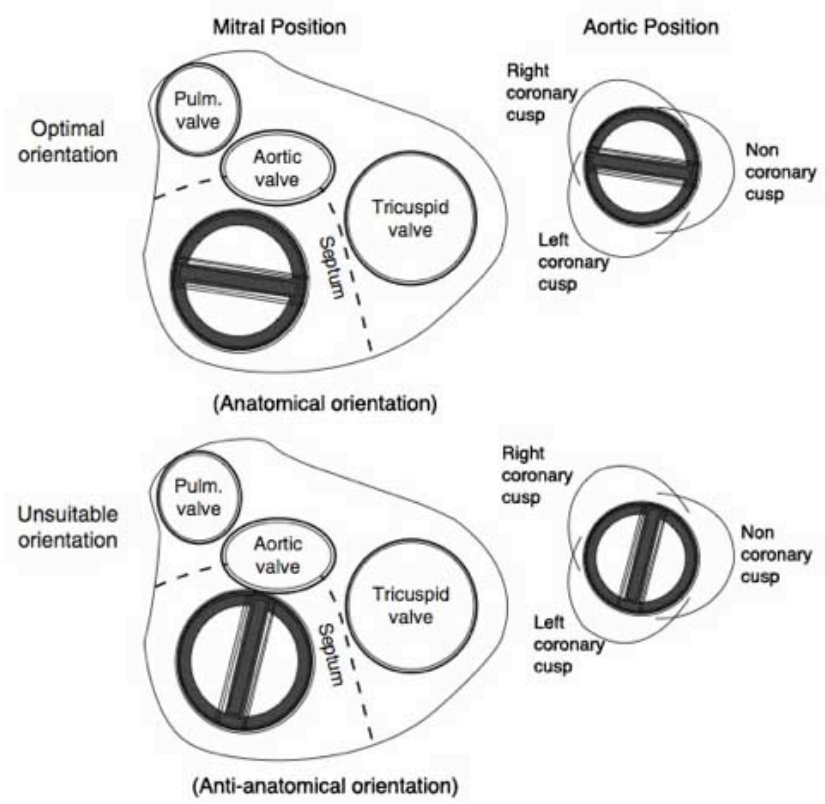

Figure 5-29: Anatomical and anti-anatomical orientation of a BMHV at the aortic positions (outlet view)

5.5.2 Numerical Methodology and Boundary Conditions

Only a brief description of the numerical method was presented as the details of this methodology have been discussed in the previous work (Nguyen et al., 2012). The blood was modeled as an incompressible viscous Newtonian fluid, with properties representative for healthy adult; density of ρ=1050kgm^{-3} and kinematic viscosity of v=3.81×10^{-6}m^{2}s^{-1}. The flow was governed by NS equations and was discretized in space using a FV method. The second-order Crank Nicholson implicit time discretization with adjustable time-step, dependent on the CFL number = 1, was used. In the simulations, SA turbulence modeling was used and implemented using the OpenFOAM package. The ALE formulation was used to discretize the system with prescribed leaflet motions over two cardiac cycles. The cardiac cycle condition used in this simulation was described earlier in section 3.4.4, with the peak flow rate was set at approximately 25Lmin^{-1}. Figure 5-30 shows the prescribed velocity and pressure at the outlet and inlet of the simulation cases. No-slip boundary condition was assigned at the channel walls, the leaflet walls and all body surfaces. The flow field at peak systole (time t=0.115 s) for each case was investigated.

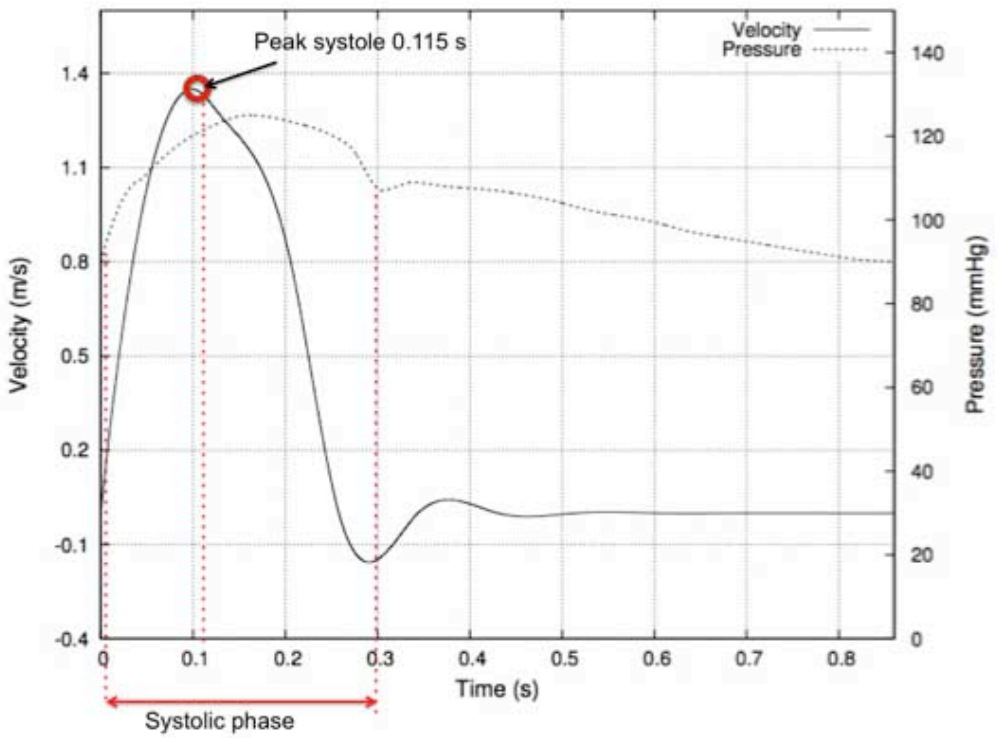

Figure 5-30: Inlet velocity and outlet pressure wave profiles; the flows were analyzed at peak systole (t=0.115 s)

5.5.3 Results

5.5.3.1 Hemodynamic Performances

The origin of X and Y-axes was at the center of the flow channel with Z=0 plane located at the trailing edge of the leaflets with the corresponding velocity components *u, v* and *w* respectively. The streamwise velocity profiles of different valve sinus geometries and downstream anatomy between curved and straight pipe were compared at three different locations, Z=1D, 2D, and 4D (D = inlet diameter) along the center line of the models at all four implantation angles. Figure 5-31 showed one of the implantation angles at 90°. The general flow fields were found to be highly 3-dimensional with strong forward flow during the systolic phase at all implantation angles. The triple-jet structures of the flow were visible in all simulation cases at peak systole which were consistent with earlier research studies (Nguyen *et al.,* 2012, Ge *et al.,* 2005, Leo 2005). The triple-jet structures were formed due to the flow disruption by the two valve leaflets and were observed all other studies of BMHV placed in a straight pipe. The velocity magnitudes were similar for all four models with four different implantation angles. Recirculation regions were observed in the sinuses as well as near the inner wall of the aortic arch curvature between Z=2D and 4D.

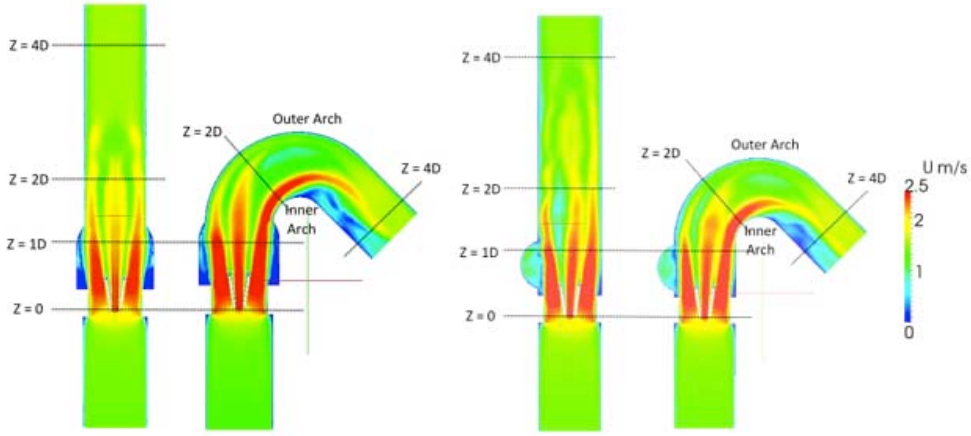

Figure 5-31: Plan view of streamwise velocity contours for all simulation models with the valve implanted at 90°. Cross sectional positions Z=1D, 2D and 4D downstream along the center line were shown for different geometric models

Simple-straight model

For the simple-straight model, the triple-jet structures appeared to be symmetrical at position Z=1D, as shown in Figure 5-32 for all four implantation angles. The triple-jets were observed to be oriented according to the implantation angle of the BMHV. At position Z=2D, the flow profile was not symmetrical but similar observations can be seen with regards to the

effect of implantation angles on the downstream flow. When the valve was rotated, the flow downstream shifted as well at similar angles. At this position, the velocity profile was near the transition phase from a triple-jet structure merging into two lateral jets downstream, as could be seen with a more evenly distributed velocity contour. Further downstream at position Z=4D, two symmetrical lateral jets were visible. This symmetrical flow was observed in all four cases, regardless of the valve implantation angle.

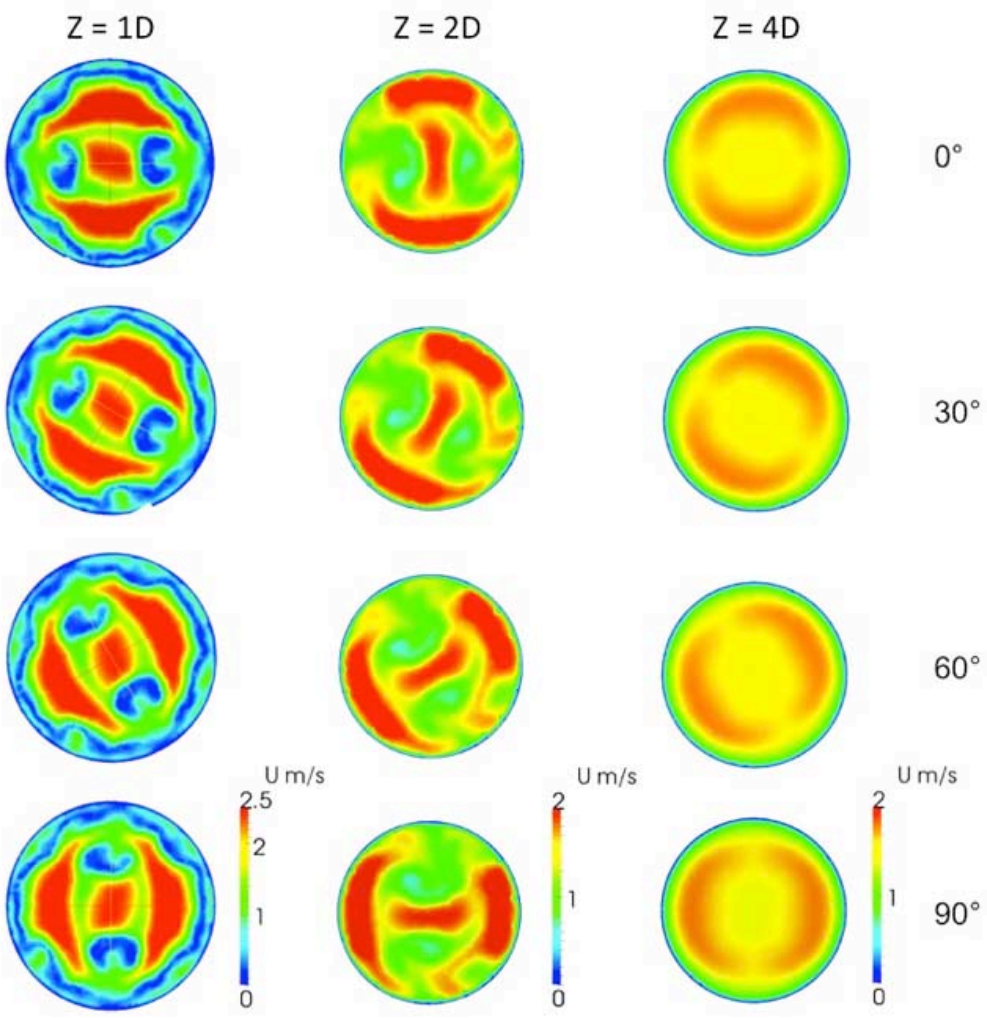

Figure 5-32: Velocity contours of simple-straight model with implantation angle of 0°, 30°, 60° and 90° at positions Z=1D, 2D and 4D at peak systole (inlet view)

Simple-arch model

The triple-jet structures were visible in the simple-arch model at all four implantation angles. Again, these flow features appeared to be symmetrical at position Z=1D, as shown in Figure 5-33. The peak velocity at this position was approximately 2.6ms^{-1}. At position Z=2D, the flow profiles were highly irregular in all four angles of implantations. At position 0°, the triple-jet

structures appeared to shift away from the center of the sinus chamber towards the inner arch, as viewed from the inlet position. Lower velocity regions were observed in the region near the outer wall of the arch's curvature, at position *a*. At 30°, this low velocity region faded and higher velocity flow was observed near the inner wall of the arch's curvature. As the valve rotated further, the tilted triple-jet structures were visible, with more defined high velocity flow at the inner wall of the arch's curvature compared to the outer wall. At 90°, it was observed that the center jet shifted towards the outer wall of the arch with the bulk of the high velocity at the inner wall of the arch's curvature. Further downstream at position Z=4D, lower velocity regions were observed at the inner wall. The flow profile was more evenly distributed at angle 0°. Lateral jets were not seen in this region of the aortic downstream compared to the straight pipe downstream. At implantation angle 90°, the change in the flow profile was steeper. Recirculation regions were also more apparent at this implantation angle.

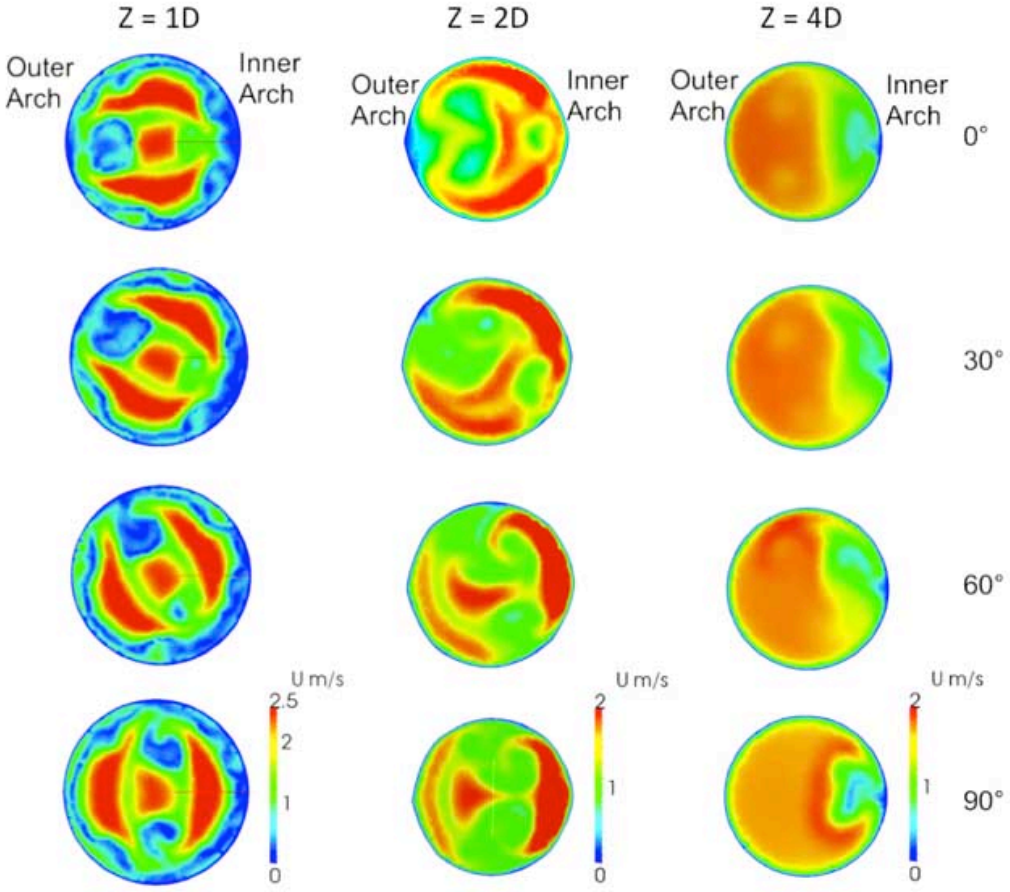

Figure 5-33: Velocity contours of simple-arch model with implantation angle of 0°, 30°, 60° and 90°at positions Z=1D, 2D and 4D at peak systole (inlet view)

Three-sinus straight model

For the anatomical-straight model at position Z=1D, as shown in Figure 5-34, the triple-jet structures were generally symmetrical at implantation angles 0° and 60°. The center jet shifted away from the right coronary cusp at 30° and away from the non-coronary cusp at 90°. At position Z=2D, symmetrical profiles were found at implantation angles 0° and 60°. As for the other two-implantation angles, the center jet profile continued to shift away from the right coronary cusp and non-coronary cusp. The jet profiles nearer to these two cusps began to show signs of flow division into two smaller jets. Further downstream at position Z=4D, the triple-jet structures were merged into two lateral jets. At implantation angles 30° and 90°, the jet profiles nearer to the two cusps continued to be divided into two smaller jets although not completely separated yet.

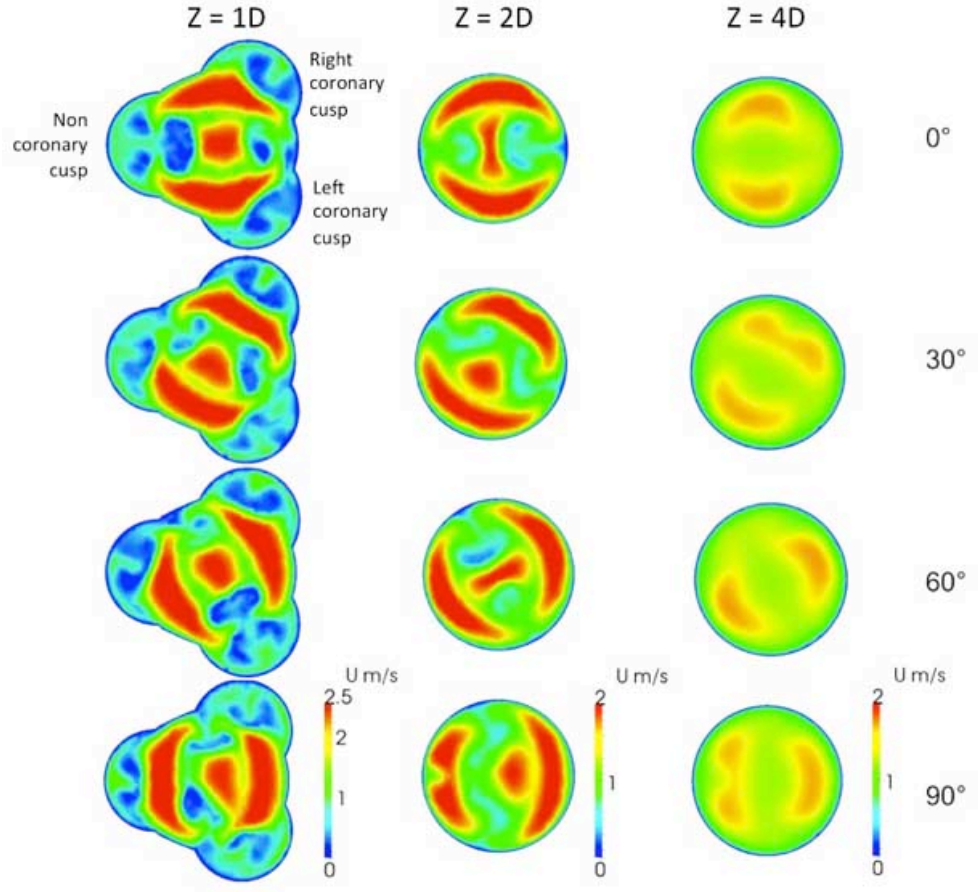

Figure 5-34: Velocity contours of three-sinus straight model with implantation angle of 0°, 30°, 60° and 90° at positions Z=1D, 2D and 4D at peak systole (inlet view)

Three-sinus arch model

Figure 5-35 shows the downstream profiles for three-sinus arch model at different implantation angles. At position Z=1D, the flow profiles were similar to the three-sinus straight model for all four implantation angels. Further

downstream at position Z=2D, the triple-jet structures were shifted away from the center of the sinus chamber towards the inner wall of the arch's curvature, as viewed from the inlet position. Two low velocity regions were observed near the center, while most of the high velocity flow was at the regions near the inner wall of the arch's curvature. Unlike the axisymmetric sinus, the flow profile at this position for three-sinus arch model had regions of low velocity magnitude. At position 30°, the flow velocity near to the inner wall of the arch's curvature increased in magnitude while the flow velocity towards the outer arch decreased in magnitude. At the valve implantation angle 60°, the high velocity regions near the inner wall of the arch's curvature increased in size. At implantation angle 90°, the center jet was faintly visible but deviated slightly towards the inner wall as compared to the simple-straight model. At position Z=4D, low velocity regions were observed at the inner wall, similar to that in the simple-straight model for all four implantation angles. At angle 0°, the flow profile appeared to be more evenly distributed, similar to that in the simple-arch model. Higher velocity magnitudes and larger regions of recirculation were observed at 90°.

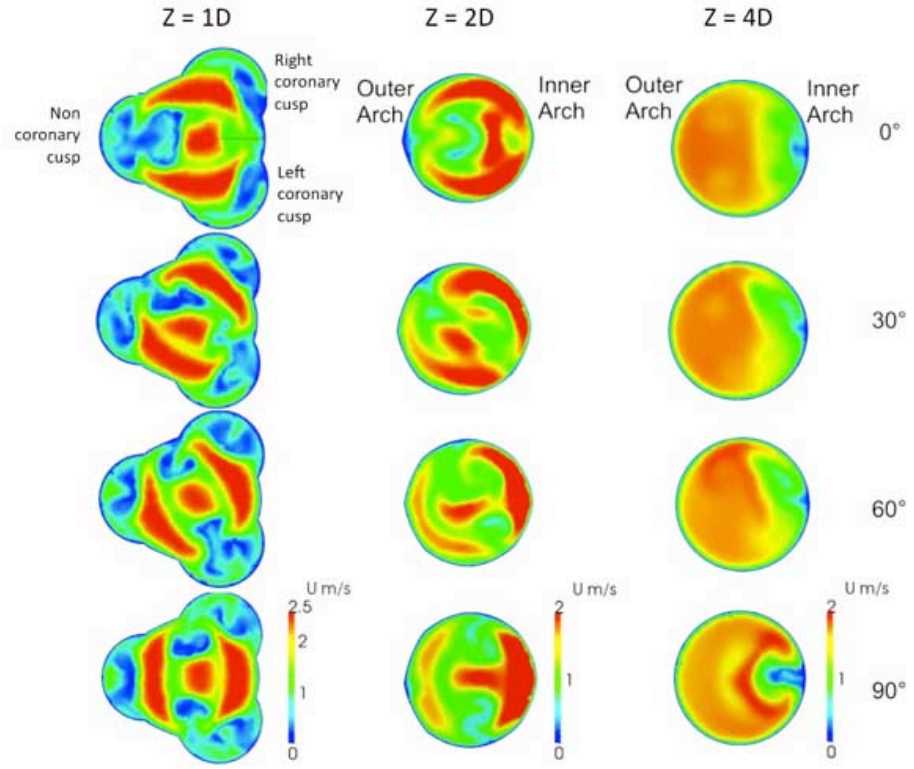

Figure 5-35: Velocity contours of three-sinus arch model with implantation angle 0°, 30°, 60° and 90° at positions Z=1D, 2D and 4D at peak systole (inlet view)

5.5.3.2 Wall Shear Stress

The wall shear stress magnitude in the downstream aortic arch between positions 2D and 4D was found to be minimal, as shown in Figure 5-36. In all four implantation angles for both simple-arch and three-sinus arch models, the wall shear stress at the inner wall of the arch's curvature had a magnitude of about 0.2kPa. There was no significant difference in the wall shear stress distribution among the models with various implantation angles.

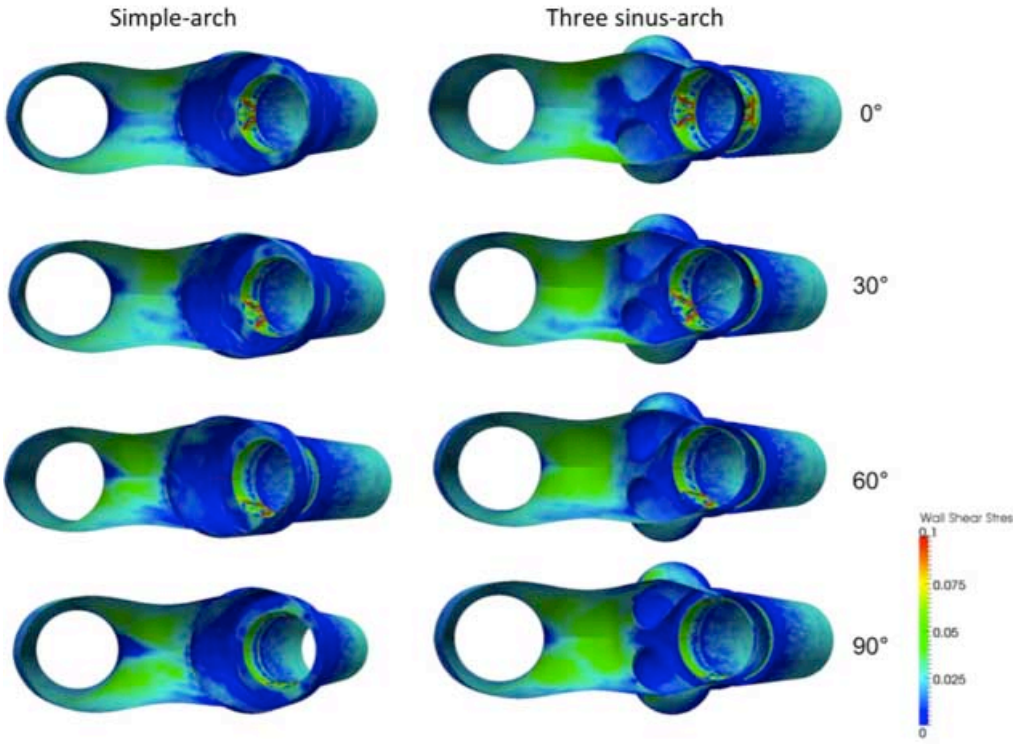

Figure 5-36: Wall Shear Stress distribution for simple-arch and three-sinus arch of the inner wall of the arch's curvature between cross section Z=2D and Z=4D

5.5.4 Discussion

In this study, 3-dimensional time-accurate flow simulations of SJM valve at different implantation angles were performed under physiological flow conditions. Triple-jet structures were visible in the four geometric cases and at four different implantation angles during peak systole. However, non-symmetrical downstream flow profiles were observed in all the three-sinus aortic root cases. Another key feature observed in the simulations was the formation of vortices near the wall edge in the sinus chambers. The flow recirculation was stronger in the three-sinus chamber than in the simplified sinus geometry. Regions of recirculation were also observed downstream in both the simple-arch and three-sinus arch cases for all angles of

implantations, as highlighted in Figure 5-33. In the simplified aortic arch geometry, the triple-jet structures were shifted towards the inner wall of the arch's curvature with the formation of flow recirculation regions between positions 2D and 4D downstream the valve. These flow features have not been discussed and may be the cause for flow stagnation in the downstream regions. Such flow structures were not evident in the straight pipe cases.

The simulation results showed that the position and orientation of BMHVs could affect the downstream flow field. An asymmetric and complex 3-dimensional flow field is dependent on the valve orientation with respect to the three-sinuses of Valsalva in the aortic root and the anatomic geometry of the aortic arch (Borazjani and Sotiropoulos, 2010, Nobili *et al.,* 2008). The placement of BMHVs with optimal orientation at aortic root has to consider the eccentric blood flow pattern in the anatomical aortic sinus. It has been found that hemodynamic conditions similar to normal physiological flow can be obtained in optimal orientation where the large orifice is directed toward the right coronary cusp, equivalent to the implantation angle of 0° (Laas *et al.,* 1999). Kleine *et al.,* (2002) found that such implantation results in less turbulence and higher coronary perfusion. This observation was confirmed by the simulation results performed in this study. The observations for valves implanted at 0° with respect to the anatomical position showed lower velocity magnitude and more evenly distributed flow profiles. In contrast, BMHVs implanted at anti-anatomical position displayed larger velocity gradients.

The sinus shape and downstream geometry were shown to have an effect on the flow field at the immediate downstream of the valve leaflets. The formation of flow recirculation in the sinus regions was more noticeable in the three-sinus aortic root than in the simplified axisymmetric sinus. The simplified three-sinus aortic arch model was used in this simulation to follow closely the natural anatomy of the aortic sinus. The vortical structure was expanded towards the modified sinus cavity and stayed there during most of the acceleration phase. The anatomic curvature of the downstream aorta resulted in a more significantly asymmetric flow condition. Unlike typical symmetrical straight downstream pipe, the forward jets flowing through the leaflets were suppressed and defused rapidly downstream of the aortic sinus.

As a result, local turbulence and recirculation downstream of the leaflets were formed (Kheradvar and Pedrizzetti 2012).

The orientation of the BMHVs did not have significant effects on the wall shear stresses experienced by blood elements. An earlier work has reported that Reynolds stresses downstream of similar bileaflet valves were less sensitive to orientation (Borazjani and Sotiropoulos, 2010).

5.5.5 Limitations

The leaflets in the present simulations were prescribed during the cardiac cycle. The simulations for the models were only performed during a single cycle of the physiological flow, as the simulation of the moving heart valves for the four valve orientations in four different models would exceed the currently available computational resources. The blood exhibits non-Newtonian properties at low shear rates in reality. Nevertheless in most blood flow in large arteries and heart valves, blood is usually modeled as an incompressible single-phase Newtonian fluid with constant viscosity value and high shear rate limit viscosity of blood ($\mu = \mu_\infty$) which is the case in the earlier simulations (Nguyen *et al.,* 2012, Yun *et al.,* 2012, Ge *et al.,* 2005, Leo *et al.,* 2006, Simon *et al.,* 2004, Ellis *et al.,* 2000b, De Hart *et al.,* 2003).

5.5.6 Summary

The different implantation angles of the valves, as well as the sinus and downstream geometries in the simulation model, affects the flow hemodynamics as shown in this study. Implantation of valves often depend on the surgeon's skillset in a surgical operation. The simulation results showed that the flow profile through valve implanted at anatomical correct position (at angle 0°) has more uniform flow and lower velocity gradient compared to the rest. The implantation angles different from the anatomical correct position may have dire consequences on the flow in the sinus chamber and downstream.

5.6 Comparison of Trileaflet Heart Mechanical Valve and Bileaflet Mechanical Heart Valve, and Different Implantation Angles of Trileaflet Mechanical Heart Valves

For Project Aim 2b, the understanding of the hemodynamics of a trileaflet mechanical heart valve design placed in a downstream curved aorta will be investigated. This study is to provide a detailed 3-dimensional flow simulation results of a trileaflet mechanical heart valve (TMHV) and to compare it to the existing BMHV implanted at anatomical position. Following that, the study compares the downstream flow fields of the TMHV implanted at different valve orientations (0°, 30°, 60° and 90°) during peak systole.

5.6.1 Heart Valve Model

The BMHV geometry used in this study was based on the SJM 29mm BMHV design placed in a downstream curved aorta at the anatomic position at 0°, which is the preferable orientation of the aortic valve (Kheradvar and Pedrizzetti, 2012). The 29mm new TMHV design was also placed in another downstream curved aorta at similar anatomic position at 0°. The TMHV design was designed in-house, as shown in Figure 5-37.

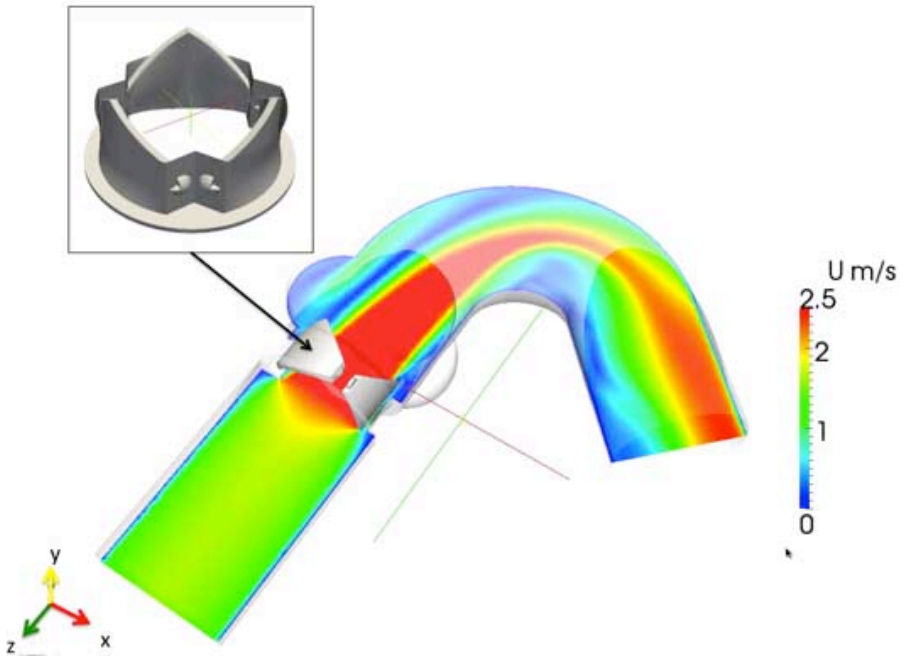

Figure 5-37: Velocity contour of the TMHV placed in the downstream curved aorta

The geometry of the curved aortic arch model was simplified without the three branches on the aortic arch to minimize the complexity of the flow simulation.

The centerline of the aorta model followed the curvature and dimension of the normal diameters for the thoracic aorta of adults obtained by helical computed tomography (Hager et al. 2002) with a 5D upstream. The sinus design was based on Pisani et al. (2013) which was similar to the native aortic valve. The native valve consists of three aortic Valsalva sinuses, with approximately 120° rotational symmetry. The orientation of the valve in relation to the sinus is important in modulating the obstruction of the flow present during the cardiac output. Figure 5-38 shows the orientation of the SJM BMHV and trileaflet mechanical heart valve as viewed from the inlet position at 0°.

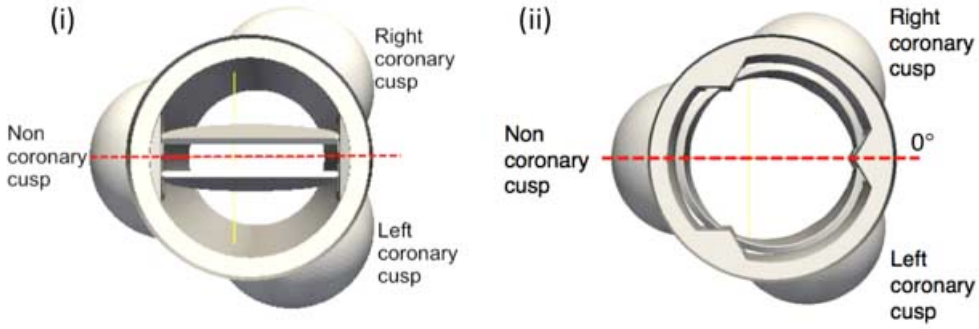

Figure 5-38: Orientation of BMHV and TMHV in anatomic position at 0°

5.6.2 Boundary Conditions

The numerical method has been described in earlier work (Nguyen et al.,, 2012) similar to earlier sections. The flow was governed by NS equations and was discretized in space using finite volume method. The blood was modeled as an incompressible viscous Newtonian fluid, with density of ρ=1050kgm^{-3} and kinematic viscosity of v=3.81×10^{-6}m^{2}s^{-1}. The SA turbulence modeling was used and implemented using the OpenFOAM package. Figure 5-39 shows the prescribed velocity and pressure. No-slip boundary condition was assigned at the walls, the leaflets and all body surfaces. The cardiac cycle condition used in this simulation was described earlier in section 3.4.4. The flow field at peak systole (t=0.115s) for each case was investigated. The computational domain for the SJM 29mm BMHV was subdivided into an unstructured mesh of approximately 3.6 million tetrahedral elements while the TMHV was subdivided into an unstructured mesh of approximately 3.5 million tetrahedral elements. During the systolic phase, the BMHV was fully opened

at an angle of 85° between the leaflet and the X-Y plane. For the TMHV, the leaflets were fully opened at 90°.

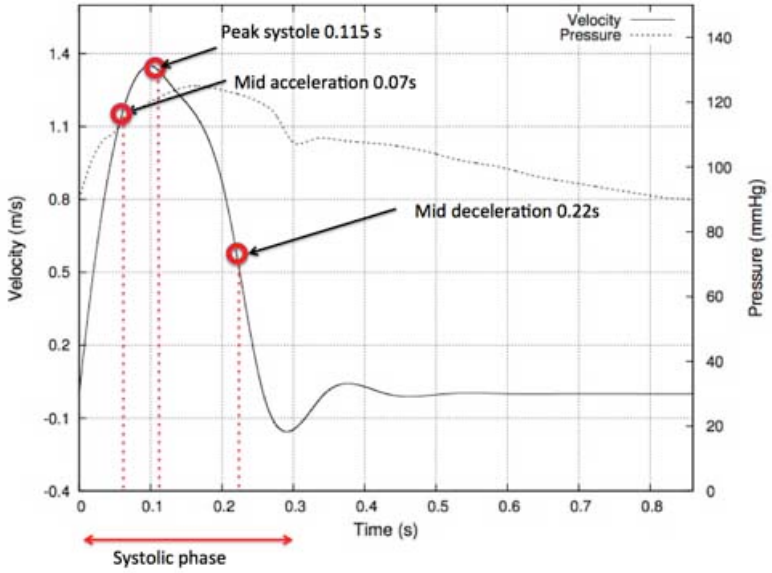

Figure 5-39: Velocity and Pressure wave profiles with three different time points during the systolic phase (mid-acceleration t=0.07s, peak systole t=0.115s, and mid-deceleration t=0.22s) at which the results were analyzed

The centerline of the aorta followed the curvature of the normal diameters for the thoracic aorta of adults obtained by helical computed tomography (Hager *et al.,* 2002) without the three aortic branches on the top to minimize the complexity of the flow simulation. The origin of X and Y-axes is at the center of the flow channel with the Z=0 plane located at the leading edge of the leaflets. The streamwise velocity profiles for the BMHV and TMHV were compared at three different locations, Z=1D, 2D and 4D (D = inlet diameter) along the centerline of the models, as indicated in Figure 5-40.

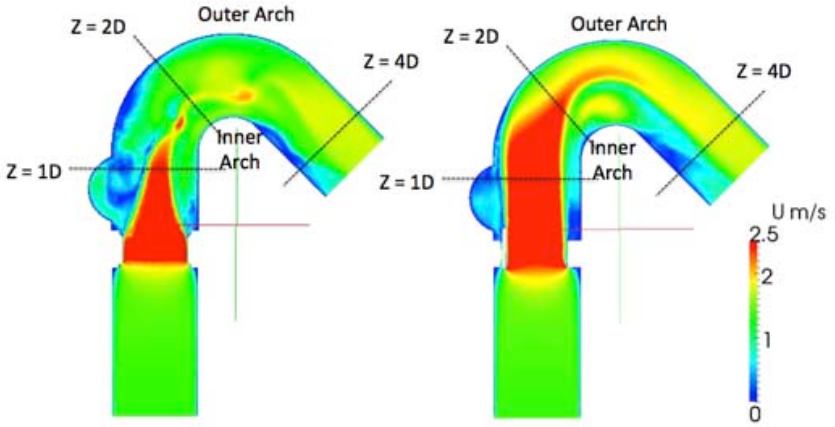

Figure 5-40: Plan view of streamwise velocity contours for BMHV and TMHV with valve implanted at 0°. Cross sectional positions Z=1D, 2D and 4D downstream along the center line were shown with different geometric models

5.6.3 Results

In this section, the results from the simulations of the BMHV and TMHV will be presented and discussed in the following order. The velocity plots of BMHV and TMHV at position Z=1D, 2D and 4D at three different timepoints mid-acceleration t=0.07s, peak systole t=0.115s and mid-deceleration t=0.22s. The velocity profiles at each cross-sectional plane for the BMHV and TMHV were compared at the three locations Z=1D, 2D and 4D for the respective timepoints. Finally, the wall shear stress at the valve leaflets, hinge regions, sinus and aorta between the BMHV and TMHV were analyzed and compared.

5.6.3.1 Hemodynamic performances

The velocity plots at cross sectional view of Z=1D, 2D and 4D for both BMHV and TMHV during mid-acceleration, peak systole and mid-deceleration as viewed from the outlet are shown in Figure 5-41. During mid-acceleration (t=0.07s), the flow through the BMHV showed a triple-jet structure visibly taking shape. Similarly, the central orifice flow of the TMHV can be seen at position Z=1D. There was no obstruction in the TMHV in the central region unlike the leaflets of the BMHV which gave rise to the triple-jet structures. The shape of the central orifice flow was a hexagon and it followed the position of the leaflets. At peak systole (t=0.115s), the profile of the triple-jet structure of the flow was fully visible in the BMHV model while central orifice jet flow was visible in the TMHV at position Z=1D. During mid-deceleration (t=0.22s), triple-jet structure of the flow in the BMHV model has decreased in strength while central orifice jet flow was higher in the TMHV at position Z=1D. The velocity plots showed higher vorticity forming along the curvature of the sinus in the BMHV compared to TMHV. This feature appeared strongly in all three timepoints in BMHV whereas in the BMHV, the vorticity was less visible at mid-acceleration and peak systole. At position Z=2D, the higher velocity flow was observed nearer to the inner arch at mid-acceleration for both BMHV and TMHV although higher velocity plots were found in the BMHV model. At peak systole, the velocity plots and profiles in the BMHV and TMHV were completely different. There are several regions of high velocity gradients in the BMHV, with the majority of the high velocity flow around the wall of the aorta nearer to the inner arch. Meanwhile, the central orifice flow was more

evenly distributed in the TMHV. The vortices at the BMHV were located nearer to the center-line away towards the outer arch while the vortices in the TMHV were located near the wall towards the inner arch. At mid-deceleration, two vortices in the BMHV were still visible in the same region. Meanwhile, the vorticity in the TMHV was no longer visible with a more evenly distributed velocity plot along the center-line. At position Z=4D, the velocity plots and profiles during mid-acceleration were similar for both BMHV and TMHV. During peak systole, the vortices in the BMHV were still visible at this position. At mid-deceleration, the two vortices in the BMHV combined into one with a more complex flow profile compared to the TMHV.

(i) Bileaflet mechanical heart valve

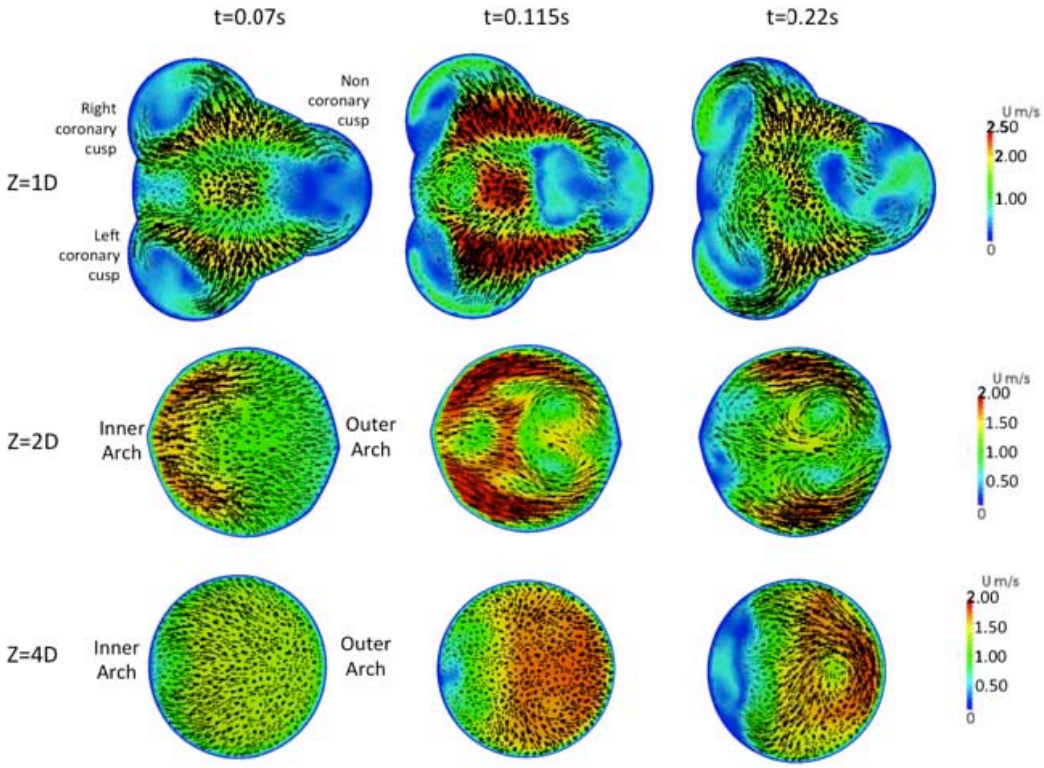

(ii) Trileaflet mechanical heart valve

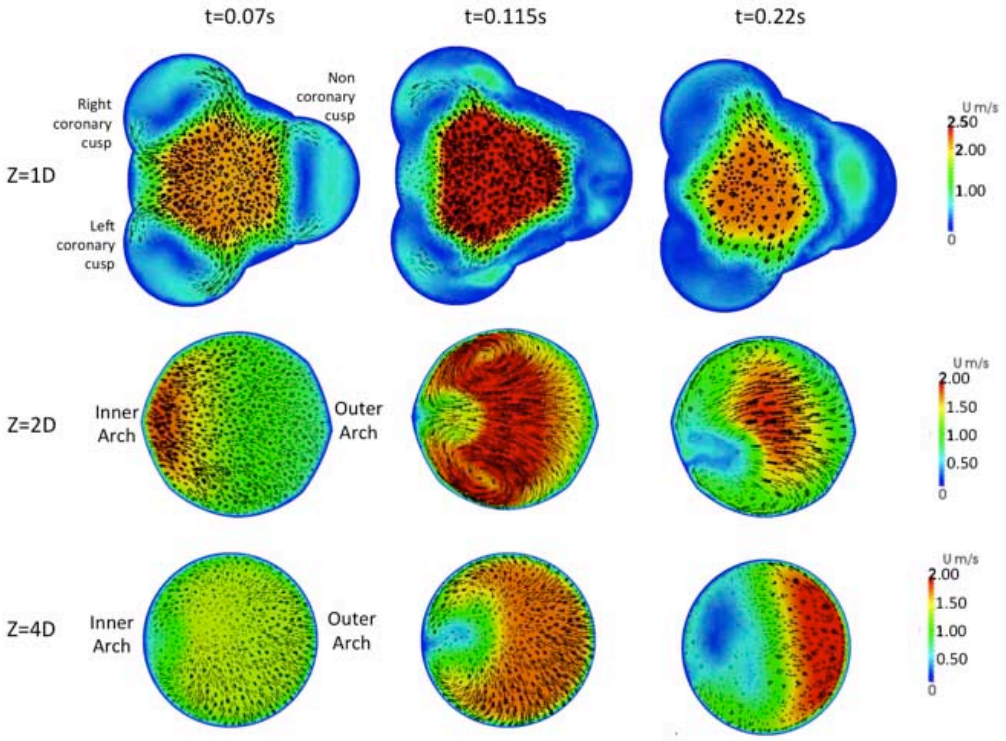

Figure 5-41: Velocity plots at cross sectional view of Z=1D, 2D and 4D for both (i) BMHV and (ii) TMHV during mid-acceleration t=0.07s, peak systole t=0.115s and mid-deceleration t=0.22s as viewed from the outlet

Figure 5-42 shows the velocity profiles at each cross-sectional plane at the three locations Z=1D, 2D and 4D for both the BMHV and TMHV at mid-acceleration t=0.07s. At this time point, the peak velocity for BMHV was 1.84ms^{-1} while for TMHV, it was 2.13ms^{-1}. A flat velocity profile was visible in majority of the plane for TMHV while only a small portion of the velocity profile was flat in BMHV. The backflow at the sinus region was of a higher velocity magnitude for TMHV at 0.64ms^{-1} compared to BMHV at 0.33ms^{-1} as observed at the non-coronary cusp in the cross sectional view Z=1D. At position Z=2D, the flow shifted towards the inner arch. The peak velocity for BMHV was 1.47ms^{-1} which was almost 16% lower than the peak velocity of TMHV at 1.75ms^{-1}. Further down at position z=4D, the flow profiles for both BMHV and TMHV were identical.

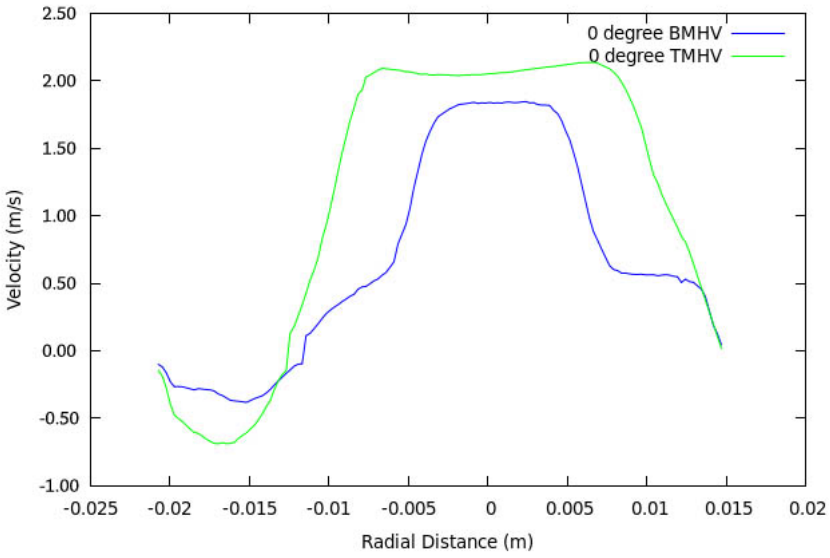

)

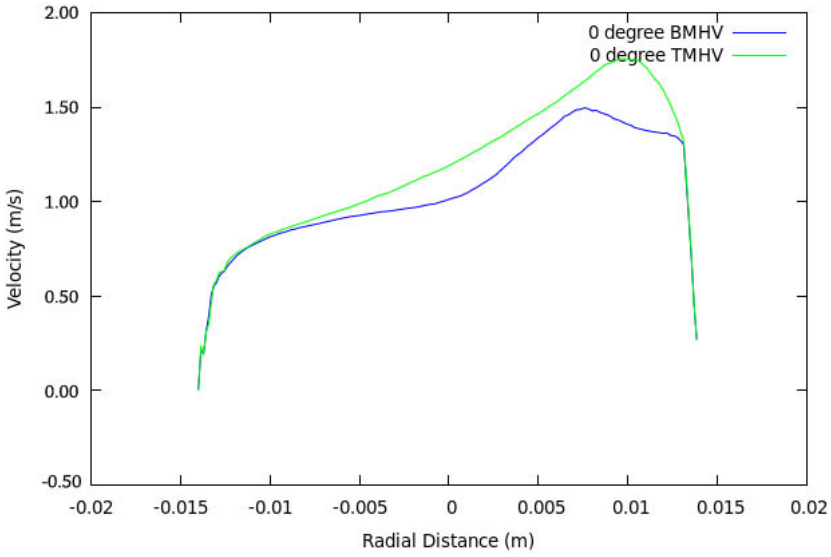

(ii)

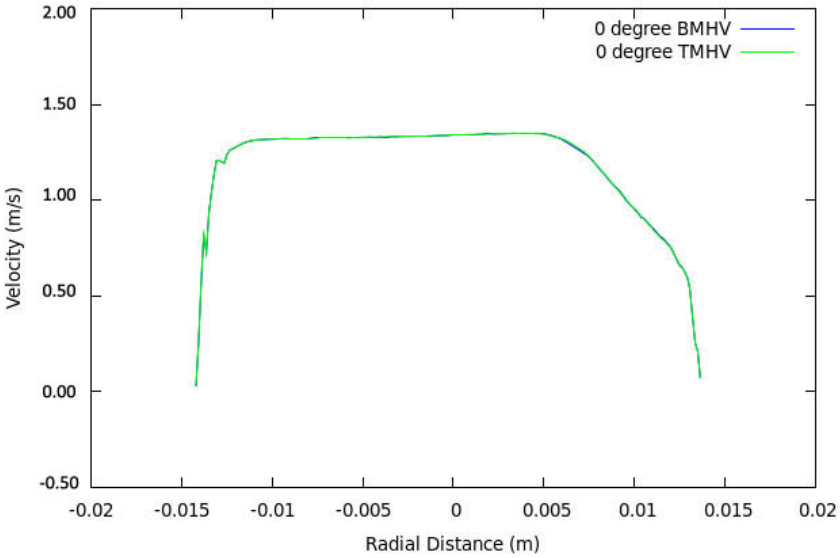

(iii)

Figure 5-42: Comparison of the velocity profiles of BMHV and TMHV at positions (i) Z=1D, (ii) 2D and (iii) 4D at mid-acceleration t=0.07s

Figure 5-43 shows the velocity profiles at each cross-sectional plane at the three locations Z=1D, 2D and 4D for both the BMHV and TMHV at peak systole t=0.115s. At this point, the peak velocity of BMHV was 2.5ms^{-1} while the peak velocity for TMHV was 2.75ms^{-1}. Two regions of recirculation in the BMHV were observed with velocity of about 0.87ms^{-1}. On the other hand, the TMHV displayed minimal recirculation flows as confirmed, with lower velocity values recorded at 0.36ms^{-1}. This was quite different compared to the mid-acceleration phase and could be attributed to the majority of the flow through the central orifice for the TMHV compared to BMHV, At position Z=2D, the triple-jet structure and lateral jets of the BMHV shifted towards the inner arch. For the TMHV, the central orifice jet was still prominent at this location. The hexagonal shape disappeared at this stage. The difference between the BMHV and TMHV was obvious with three different peaks observed in the BMHV while only one peak observed in the TMHV. The peak velocity values were 2.42ms^{-1} and 2.65ms^{-1} in the BMHV and TMHV, respectively. At position Z=4D, the flow velocity has reduced to a magnitude of 1.73ms^{-1}. The velocity shape and profile observed for the two models were generally similar except the region from the centerline towards the inner arch. At this position, both the BMHV and TMHV displayed a central orifice jet shifted more towards the outer wall of the arch's curvature, with regions of low velocity and recirculation at the inner wall. The centrifugal force is prevailing due to the curvature of the aortic arch.

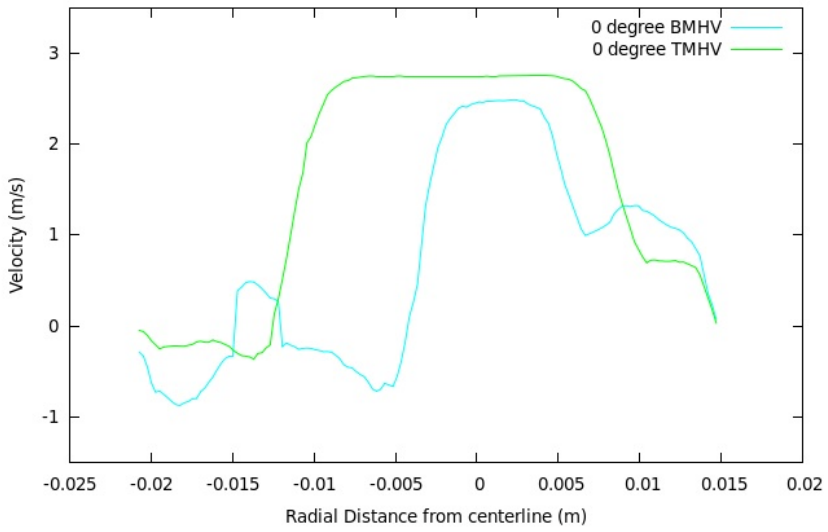

(i)

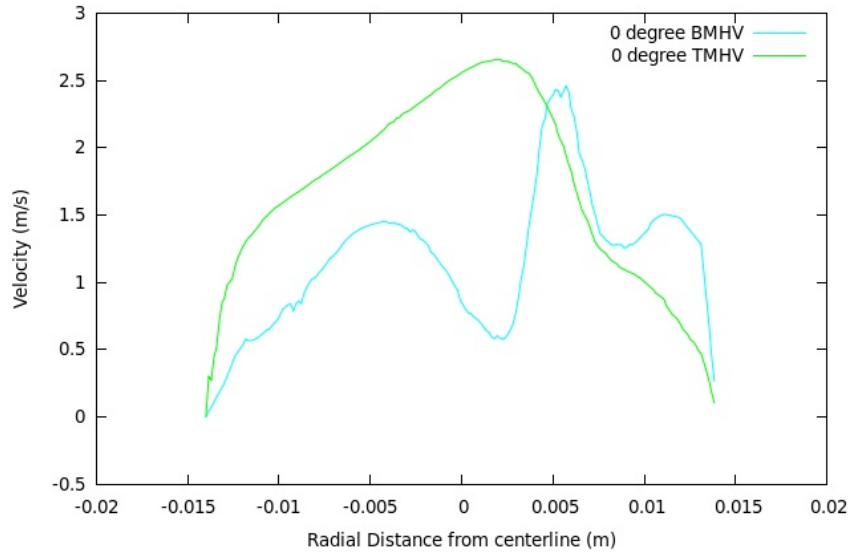

(ii)

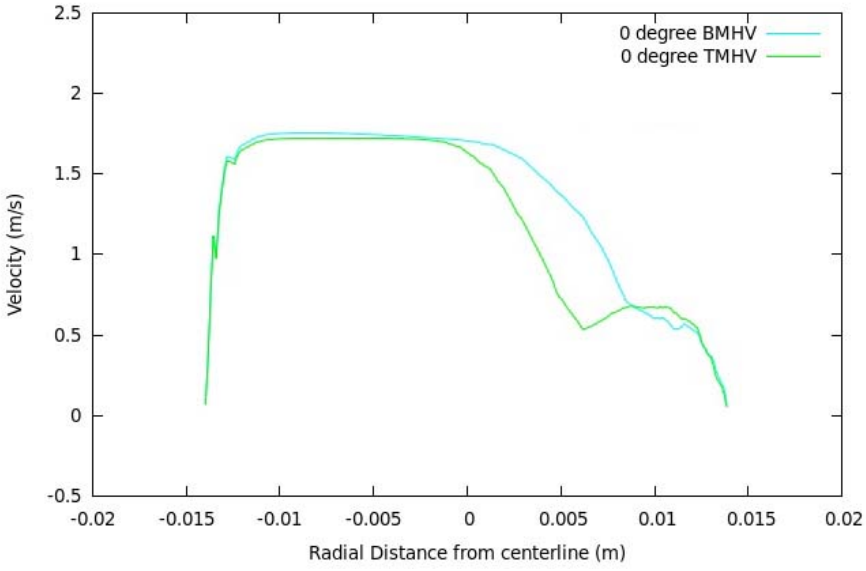

(iii)

Figure 5-43: Comparison of velocity profiles between BMHV and TMHV at positions (i) Z=1D, (ii) 2D and (iii) 4D at peak systole t=0.115s

Figure 5-44 shows the velocity profiles at each cross-sectional plane at the three locations Z=1D, 2D and 4D for both the BMHV and TMHV at mid-deceleration t=0.22s. The peak velocity of BMHV at the mid-deceleration was 1.9ms^{-1} while the peak velocity for TMHV was 2.2ms^{-1}. The BMHV model has a bigger region of recirculation flow at the non-coronary cusp compared to the TMHV model even though the velocity magnitude was about 1ms^{-1} for both the models. Further downstream, the strength of the central orifice flow for TMHV decreased minimally with the peak velocity at about 2ms^{-1}. On the other hand, the highest velocity recorded for BMHV was 1.4ms^{-1} with regions of back flow near the inner arch of the model. This was not visible in TMHV and could be due to the merging of the triple jet structure into two lateral jets

for the BMHV model. At position Z=4D, two peaks were observed in the BMHV while only one peak observed for TMHV.

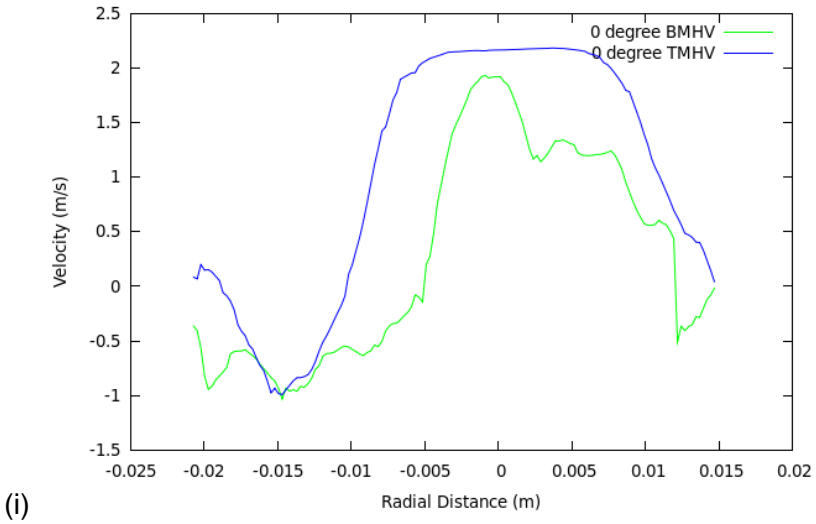

(i)

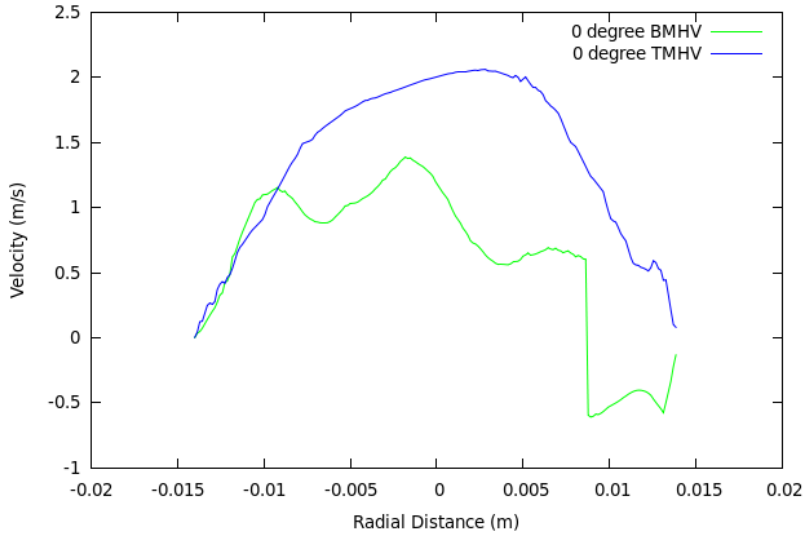

(ii)

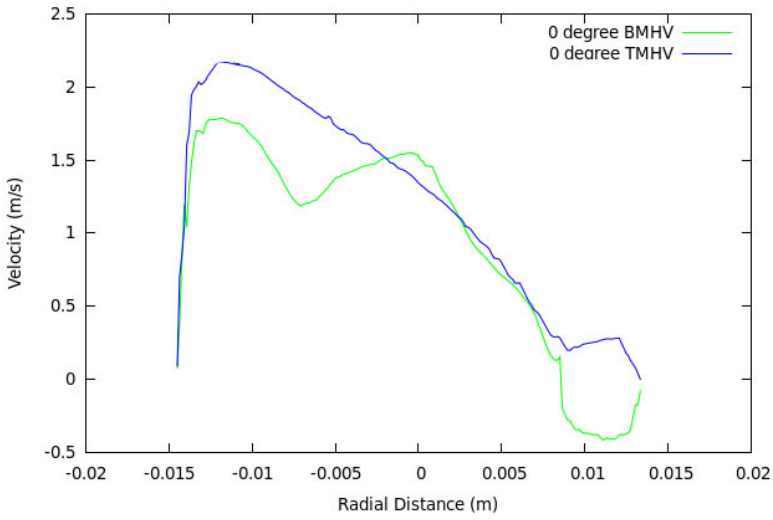

(iii)

Figure 5-44: Comparison of velocity profiles of BMHV and TMHV at positions (i) Z=1D, (ii) 2D and (iii) 4D at mid-deceleration t=0.22s

Figure 5-45 shows the velocity vector of the flow through the BMHV and TMHV with regions of recirculation at the aortic sinus. Higher recirculation flows were observed in the BMHV model, especially near the sinus region at the non-coronary cusp compared to TMHV. The flow through the BMHV was not in a streamline pattern as a result of blood hitting and reflecting through the aortic wall, as can be seen in the figure. Comparatively, the TMHV has a streamline flow with the majority of flow along the central orifice.

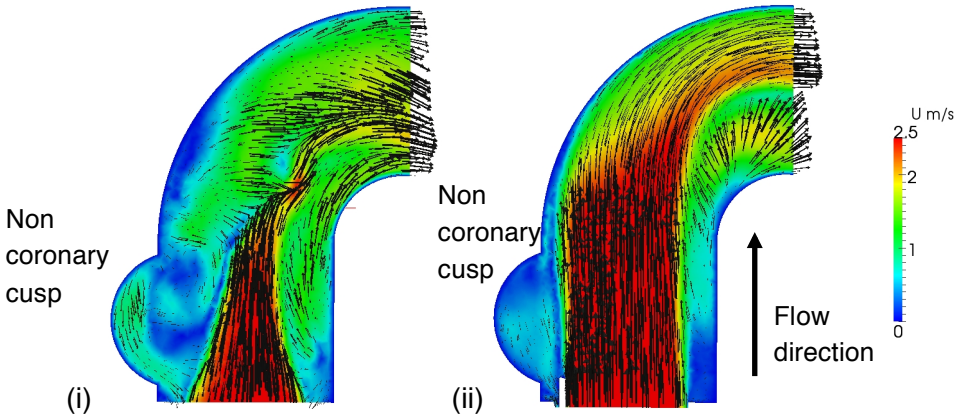

Figure 5-45: Velocity vectors of the flow through (i) BMHV and (ii) TMHV at Y=0 at peak systole t=0.115s

5.6.3.2 Wall Shear Stress

Figure 5-46A shows the wall shear stress at the hinge region of the BMHV and TMHV at peak systole t=0.115s. The regions of high wall shear stress in the BMHV were mainly on the leading and trailing hinges at 0.255kPa. On the other hand, the concentration of high wall shear stress for the TMHV was within 10% of the BMHV at 0.27kPa. The distribution of the wall shear stress regions were mainly on the leading hinges nearer to the inlet and appeared to be in a bigger region compared to BMHV. The TMHV also has an evenly distributed wall shear stress on the peripheral gap between the leaflets and the valve holder. Figure 5-46B shows the wall shear stress distribution at the sinus region and the downstream aorta wall. The sinus region in the BMHV has a higher wall shear stress compared to the TMHV. Meanwhile, the wall shear stress also appeared to be distributed more evenly in the TMHV compared to BMHV although the area seemed to have higher wall shear stress. The wall shear stress of the valve leaflets are shown in Figure 5-46C. The side profile showed the wall shear stress distributed across the external surface of the BMHV. For the TMHV, the wall shear stress was observed at

the region where leaflets were contained within the valve holder. From the inlet view, it was shown that the higher wall shear stress distributions were observed at the inner edge of the leaflets. High wall shear stress also occurred at the hinge of the leaflets for both BMHV and TMHV although it was observed that the stress concentration on the hinges was lesser in the TMHV model.

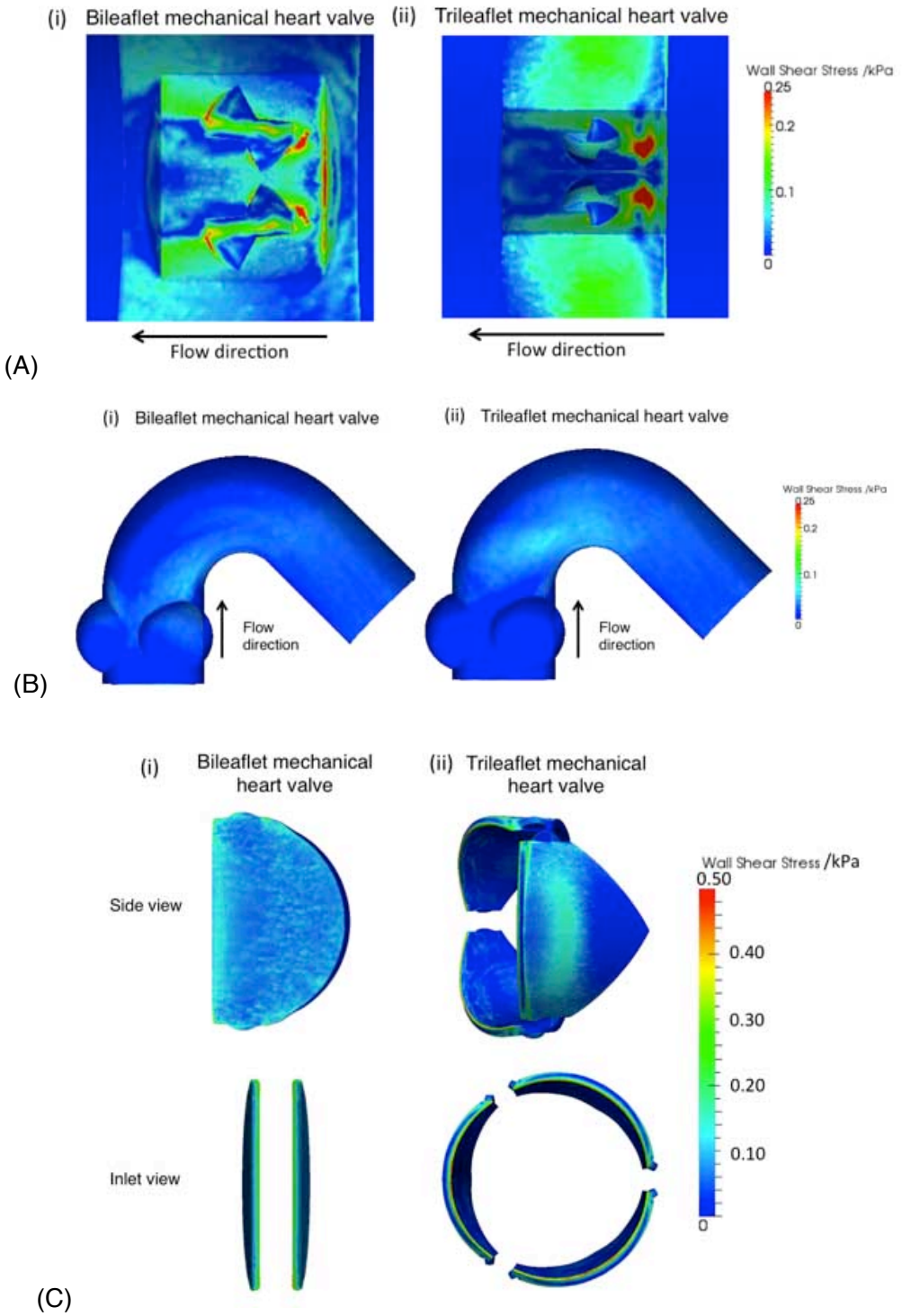

Figure 5-46: Wall shear stress at the (A) hinge region, (B) aorta wall and sinus region, and (C) valve leaflets of the BMHV and TMHV at peak systole t=0.115s

5.6.4 Discussion

5.6.4.1 Hemodynamic Performances

The bileaflet divides the area available for the flow into three regions which consist of the central orifice and two lateral orifices, as reported by Dasi et al. (2009). This flow feature is also commonly known as the triple jet structure. The flow in the BMHV becomes more disturbed as it travels further downstream of the valve compared to the TMHV which has a central orifice flow. The upstream flow profiles through the mechanical heart valves played an important role in the shape of the downstream flow profile from the peak systole onwards as observed.

According to Li et al. (2011), the closure mechanisms were different between the TMHV and the BMHV, and the TMHV only required very little reversed flow to seal it. The vortices that formed in the sinus regions counter-act the closure mechanism of the BMHV leaflets and is not physiological desired. On the other hand, these vortices would benefit the closure of the TMHV leaflets as the vortices push the leaflets inwards during closure, which is similar to how the native aortic valve functions. The higher velocity plots near the sinus wall in the BMHV during the mid-acceleration phase may lead to higher wall shear stress. At the locations with high-velocity gradients especially in the BMHV, high turbulent shear stresses are present which may lead to hemolysis and platelet activation. The wake flow regions downstream of the valve leaflets generally correspond to the large regions of vorticity. As such, the flow may slow down or even stay in these regions with longer residue time. This can be dangerous as it may cause formation of thrombus, and eventually leading to thromboembolic complications. Compared to BMHV, it appeared that the flow velocity through the TMHV was larger with lower distribution of vorticity along the central orifice.

Placement of the BMHV with optimal orientation at the aortic root has to be considered to ensure eccentric blood flow pattern in the anatomical aortic sinus. The flow at downstream position Z=4D showed desirable hemodynamic velocity profile due to lower velocity gradients. Despite the hemodynamic superiority of the BMHV implanted in the optimal position which was equivalent to the implantation angle of 0° (Laas *et al.,* 1999), the

flow profiles for BMHV at position Z=1D and 2D showed higher velocity gradient and larger recirculation regions. When the flow profile through a TMHV was compared with that of a BMHV, less turbulence were observed. The observations for the TMHV implanted at 0° with respect to the anatomical position showed even more evenly distributed flow profiles.

The triple-jet structures and lateral jets observed in a BMHV are not physiological and the long-term effect of such flow structures in human circulatory system has yet to be understood. Such flow profiles are potentially more damaging to the aorta compared to the streamline central orifice flow of the TMHV. The regions with higher blood hit along the aorta wall correlates with an increased in wall shear stress.

5.6.4.2 Wall Shear Stress

For the BMHV, non-uniform distributions of high wall shear stress regions were observed at the hinge regions. The difference in the wall shear stress distribution was largely due to the design of the two valves. When the TMHV was fully open, there were gaps between the leaflets and the valve holder. The flow through the gap caused a slightly elevated wall shear stress compared to the BMHV. The regions of high wall shear stress were found at the frontal side of the leaflets.

It was observed that the wall shear stress was the highest at the inner edge of the valve leaflet. At fully open position, the BMHV leaflets were at 85° from the transverse plane tilting toward lateral side, while the TMHV leaflets were at 90° from the transverse plane. Therefore, the leaflet surface at the lateral side would be exposed more to the fluid flow, which caused elevated wall shear stress at the lateral surface.

The associated increase in wall shear stress often correlates to higher risk of hemolysis and platelet activation. One of the common congenital conditions of the aortic valve is the bicuspid aortic valve, where the aortic valvular leaflets fused during the development. As a result, instead of a normal tricuspid configuration, a bicuspid valve appeared. Bicuspid aortic valve often lead to non-physiological flow hemodynamics as well as the tendency to

develop ascending aortic aneurysm due to the higher wall shear stress along the surface of aorta arch. Similarly, it was observed that higher wall shear stress in the sinus regions of the BMHV are susceptible to increased risk of aortic aneurysm compared to TMHV. The hemolysis red blood cell occurs at approximately 400Pa, below which a sublethal region of zero hemolysis was observed (Sallam and Hwang, 1984). Meanwhile, irreversible platelet aggregation can occur as low as at shear stress of 10Pa (Hung *et al.,* 1976, Ramstack *et al.,* 1979, Slack *et al.,* 1993).

The blood elements experienced higher rate of collision with the valve wall due to the vorticity formed near the wall as a result of turbulent flow. The platelet activation by high wall shear stresses may lead to thromboembolic complications (King *et al.,* 1997 and Cheng *et al.,* 2004). These regions were often associated with high wall shear stress, and may lead to hemolysis and platelet activation

The high wall shear stress at the hinge regions for both BMHV and TMHV showed that the hinge joints are critical to the design of an artificial heart valve. The concentrated area of wall shear stress in this study was consistent with earlier findings (Kiang-ia and Chatpun 2013, Yuan et al. 2003, Dumont et al. 2007). The design of the hinge in mechanical heart valve is important to minimize any undesirable flow features and wall shear stress during the cardiac cycle. It can also be used as an important tool to characterize potential thromboembolic complications in regions which cannot be measured experimentally due to the design and opacity of the hinge.

Generally, the major drawback associated with the implantation of mechanical heart valves is the need for chronic daily anti-coagulation therapy to reduce the risk of thrombosis and thromboembolic complications. Patients with such therapies are exposed to an increased risk of bleeding, infection, and/or autoimmune response (Walker and Yoganathan, 1992). The present numerical study has shown that the TMHV provided a flow condition which is more similar to the natural valve due to its large central free region compared to the triple jet structures of BMHV. The central orifice flow in TMHV presented a configuration with smaller resistance for blood flow. The velocity

gradient in any radial direction in the TMHV is also smaller compared to the BMHV. Clinically, this will reduce the wall shear stress level in TMHV since the incidence of blood hits on the wall decreases due to the more concentric streamlined flow of the TMHV.

Blood flow through mechanical prostheses can lead to high turbulent stresses that may damage and/or activate blood elements and initiate platelet aggregation. Platelet aggregation can lead to thrombus formation with disastrous consequences for the patient. Thrombi may even detach from the valve and lodge in a downstream blood vessel, thus reducing or even cutting off the blood supply to vital tissues. The hemodynamics of a BMHV differs significantly from that of natural healthy heart valve. As such the use of a TMHV valve may yield a more physiological hemodynamics due to the central orifice flow similar to that of native human valve.

To understand the flow through the TMHV further, the impact of the valve implantation angle on the downstream flow was investigated. The trileaflet valve was positioned at different angles (0°, 30°, 60° and 90°), as shown in Figure 5-43, in a curved downstream aortic arch model. The reference 0° is the preferable orientation of aortic valve, known as anatomic position as described earlier.

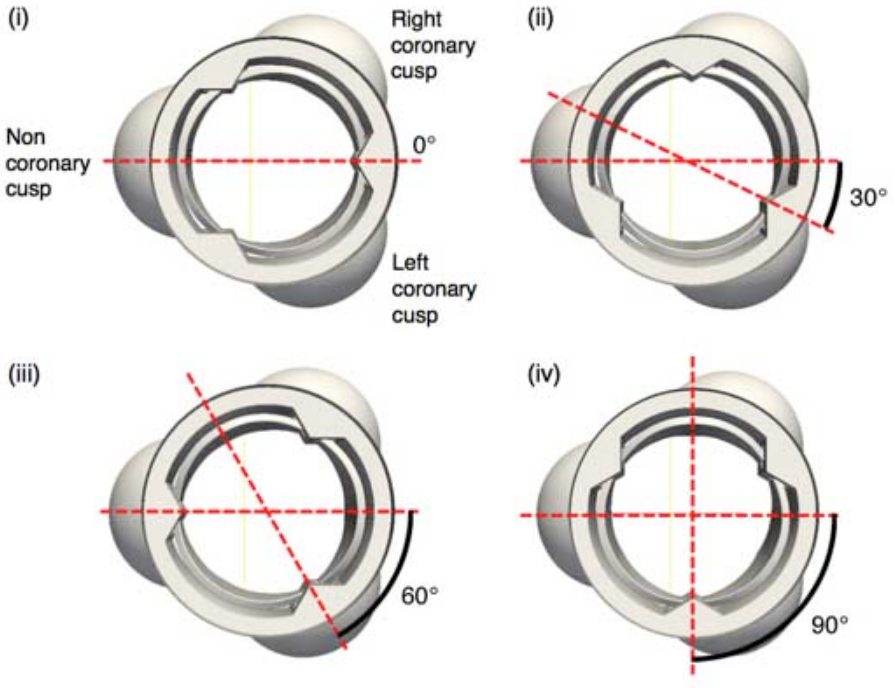

Figure 5-47: Four different valve orientations for TMHV model

The flow field at peak systole (t=0.115s) was investigated for each case at the three different positions Z=1D, 2D and 4D downstream along the centerline of the geometric model. Comparisons of the flow field velocity contours are presented in Figure 5-44.

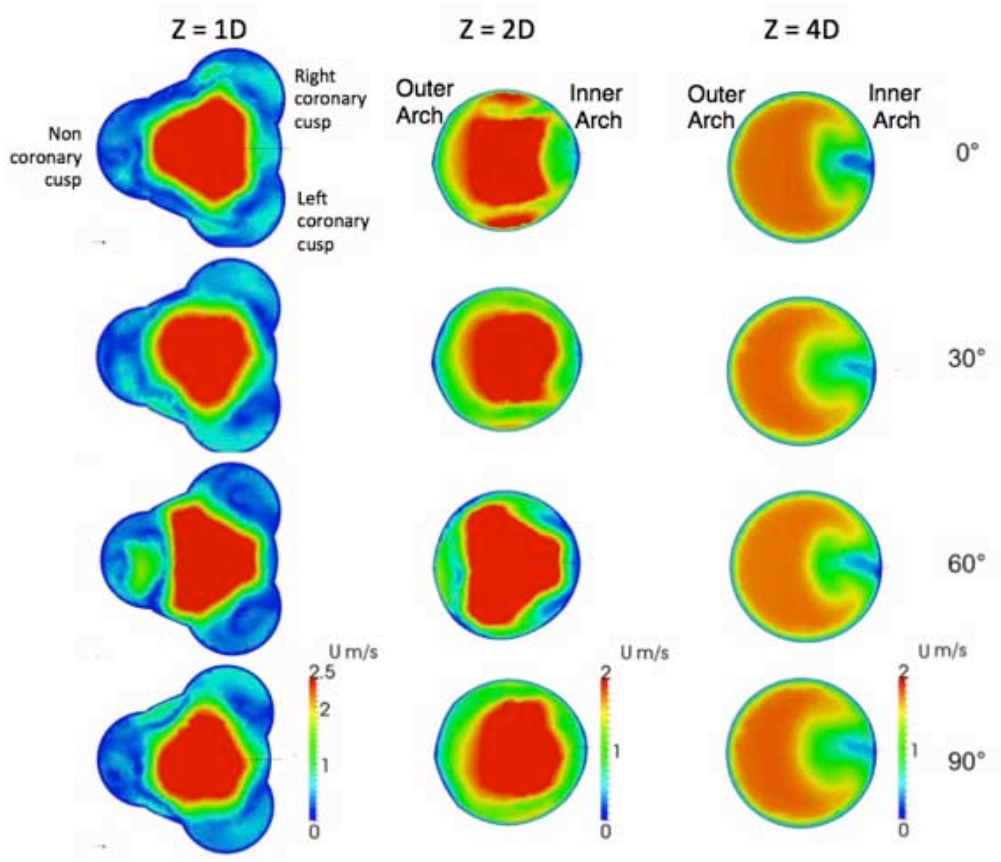

Figure 5-48: Velocity contours of four implantation angles of 0°, 30°, 60° and 90° at positions Z=1D, 2D and 4D at peak systole (inlet view)

As described earlier for implantation angle 0°, the flow profile through the TMHV at position Z=1D was a bulk flat profile. For the other two implantation angles (30° and 90°), similar flat profiles were observed. The recirculation regions were also similar with comparable velocity magnitude as shown in Figure 5-45. On the other hand, the velocity profile for 60° had a shorter flat profile and a bigger velocity magnitude for recirculation region at 1.7ms^{-1}. This unusual big recirculation region could be due to the position of the leaflets where the hinges were located along the centerline of the sinus chamber at the non-coronary cusp. Meanwhile, at the downstream positions Z=2D and 4D, similar flow profiles were observed for all the valves implanted at the different angles.

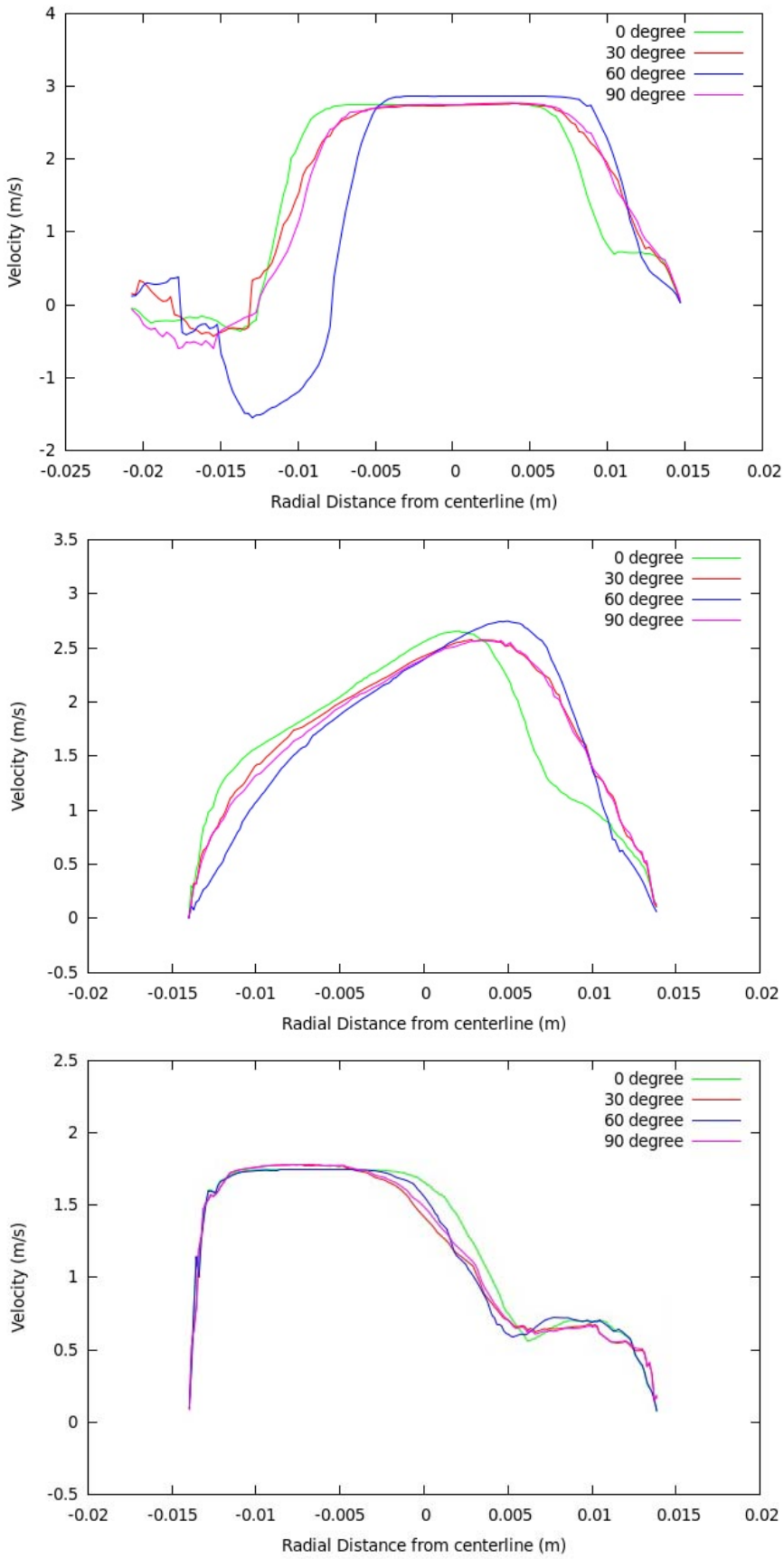

Figure 5-49: Velocity profile comparison between the different implantation angles of TMHV (0°, 30°, 60° and 90°) at position Z=1D, 2D and 4D at peak systole t=0.115s

The implantation angles of the TMHV have a limited effect on the downstream flow profile, especially at the immediate downstream as seen at position Z=1D. The difference further downstream at positions Z=2D and 4D was not noticeable. The simplified three-sinus aortic root model used in the simulation followed closely the natural anatomy of the aortic sinus without the three aortic branches. The anatomic curvature of the downstream aorta resulted in an asymmetric flow condition, and the flow feature was consistent among all the models in general despite the different valve implantation with more distributed flow profile.

The wall shear stress distributions of the valves in all implantation angles were similar. Figure 5-46 shows the wall shear stress distribution on the valve leaflets at orientation 0°. As the valve leaflets opened, the blood was being forced through the valve leaflets, resulting in high velocity jets. These velocity jets will in turn cause high velocity gradients and induce high shear stress. The shear stress may then cause hemolysis or platelet activation. It was seen from the contour plot that the shear stress was highest at valve leaflet edge especially at the edge close to the inlet. This agreed with the CFD simulation results of the earlier study by Dumont *et al.,* (2007). It was also observed that the wall shear stress was higher on the side of the lateral orifice than the central orifice, which could be due to the tilting direction of the valve leaflet when the valve was fully opened. When the valves were fully opened, the external surfaces of the trileaflet valves had elevated wall shear stress values as compared to the inner surfaces. However, the trailing edges of the valves exhibited higher wall shear stresses at the inner edges than at the outer edges.

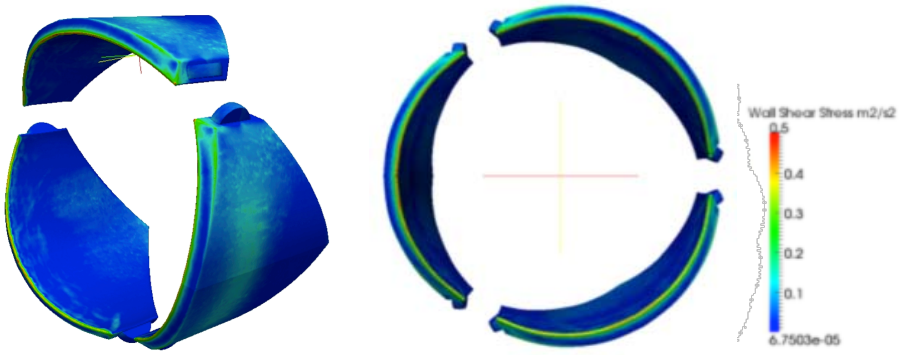

Figure 5-50: Wall Shear Stress distribution on the leaflet found to be higher at the inner edges of the valves

5.6.5 Limitations

The leaflets' motion in the present simulations was prescribed during the cardiac cycle. Blood was modeled as Newtonian fluid even though in reality, blood exhibits non-Newtonian properties at low shear rates. The curved aorta model was simplified by omitting the three aortic branches, but in reality, the anatomy of the human aorta is more complex.

5.6.6 Summary

The simulation results showed different flow fields at the downstream positions at Z=1D and 2D for BMHV and TMHV. At further downstream at Z=4D, it was found that the flow field shared similarities in terms of the flow profile and the velocity magnitude. The study also showed implantation of the TMHVs in different angles did not affect the downstream flow field as much compared to the BMHVs. In the simulations, it was observed that the flow profile through the valve implanted at all the four locations shared similar flow structures, except for the valve implanted at 60° as compared at position Z=1D. Wall shear stress distribution on the leaflets was similar in all four cases.

5.7 Fluid-Structure Interaction Study of Bileaflet Mechanical Heart Valve Using the Dynamic Mesh Method in OpenFOAM

5.7.1 Heart Valve Model

For Project Aim 3, the 2-dimensional model of the BMHV consists of an inlet flow, a simplified sinus and the leaflets at the center plane Y=0. The computational mesh is shown in Figure 5-47. The mesh contains about 150,000 unstructured tetrahedral elements. Due to the limitations of the dynamic mesh model using ALE method, a minimum of one cell is required to cover the gap between the valve leaflet and the wall and the gap between the two leaflets. This one cell is required to ensure the continuity and preservation of the fluid domain as one entity. To increase the accuracy of the flow calculations, the mesh at the gap is increased. The valve model for the prescribed leaflet movement was based on Section 5-3.

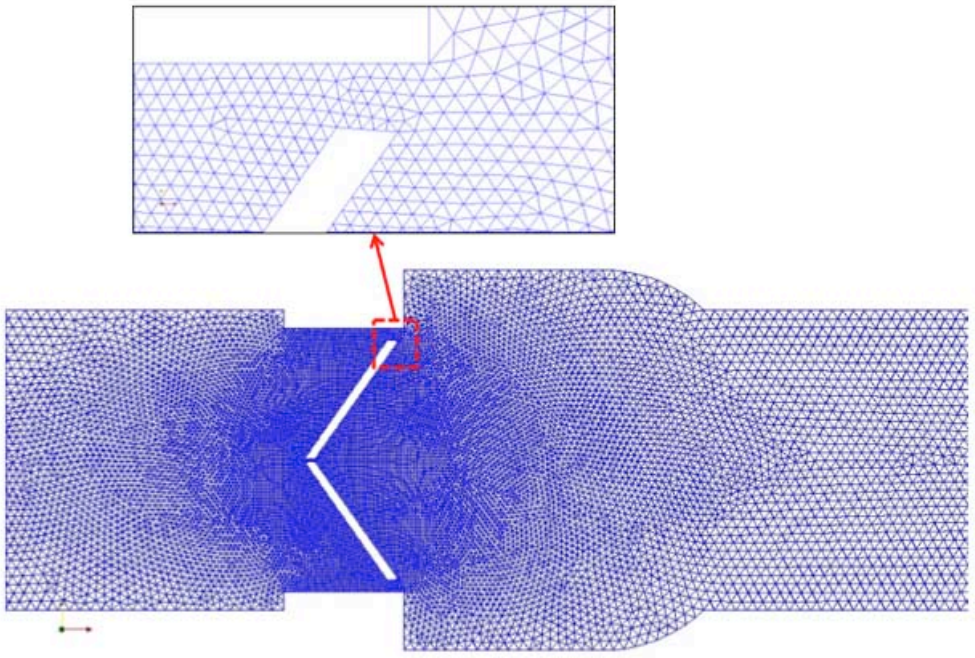

Figure 5-51: Geometry and mesh of the 2-dimensional BMHV model

5.7.2 Boundary Conditions

The boundary condition used for the inlet and outlet followed the earlier sub sections. Variable time-step was used in the simulations with maximum Courant number = 1. The fluid was assumed to be incompressible Newtonian fluid with a density of ρ=1050kgm^{-3} and kinematic viscosity of v=3.81×10^{-6} m^{2}s^{-1}. The flow was governed by NS equations and the domain was

discretized in space using finite volume method. Figure 5-48 shows the boundary conditions velocity and pressure. No-slip boundary condition was assigned at the walls, the leaflets and all body surfaces. The flow field at four different time points, namely early systole (t=0.01s), mid systole (t=0.07s), peak systole (t=0.115s) and late systole (t=0.23s) were investigated and compared with the prescribed leaflet motions at position Z=1D. The FSI technique was implemented in OpenFOAM by the functions described in Chapter 3. The code runs a sub-iteration loop for every time-step in order to solve the blood-leaflet interaction to calculate the numerical derivative of the moment of the leaflets. Once converged, a new flow solution is computed starting from the results of the previous time-step. Unless the equation of motion is satisfied, the process continues. For every new time-step, a new valve leaflet position is computed. In every time-step, at least two sub-iterations are required. The FSI problem converged in four to six sub-iteration steps. The simulation of the prescribed leaflet movement was conducted using a 3-dimensional model and presented in Section 5-3. Validation study for the streamwise velocity profiles were conducted at Z=1D at three different time points (t=0.07s, 0.115s and 0.23s). Experimental validations were performed with the pulsatile flow setup using the piston pump (Vivitro SuperPump). The velocity flow fields were averaged from 150 image pairs which were analyzed using the LaVision PIV software (Davis 8.0.5, LaVision, Germany). The pulse trigger was activated to synchronize the laser and the piston pump at the three time points. The velocity range observed in the experiment was between -0.4 to 1.3ms^{-1}. In this study, the simulation of a FSI and prescribed leaflet movement flow for the cardiac cycle has successfully been validated using PIV.

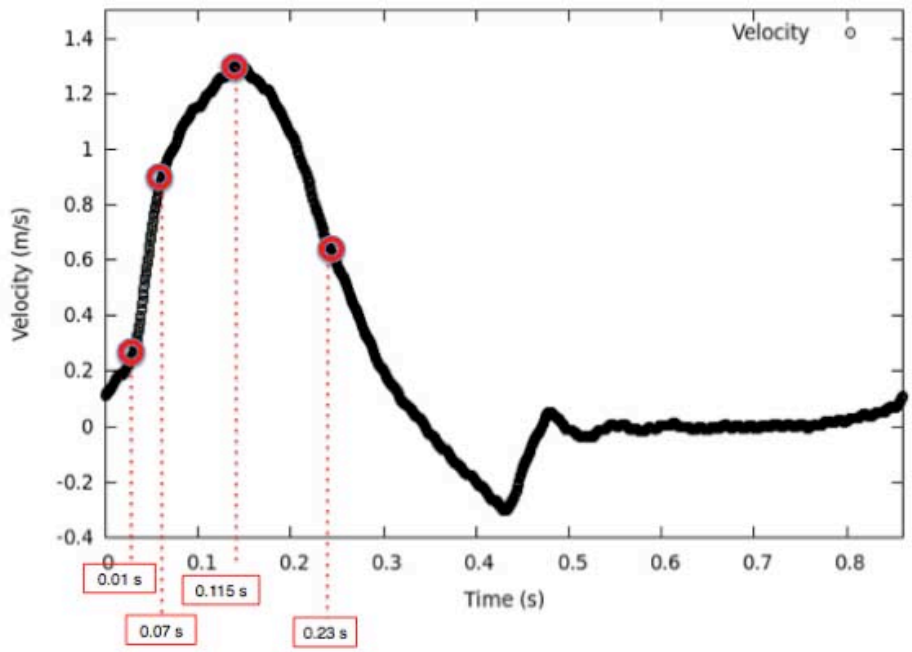

Figure 5-52: Velocity profile with four time points investigated at early systole (t=0.01s), mid systole (t=0.07s), peak systole (t=0.11s) and late systole (t=0.23s)

5.7.3 Results and Discussion

Figure 5-49 compares the velocity contours for FSI and prescribed leaflet movements at position Z=1D at time point t=0.01s. The flow velocity contour for prescribed leaflet movement was obtained at the center plane Y=0. In early systole at t=0.01s, the valve leaflets were pushed away from the wall towards the center. During this phase in the FSI simulation, it was shown that the three small velocity jets were visible moving through the gap in the leaflets. The two lateral jets appeared to be of higher velocity magnitude at $0.26ms^{-1}$ compared to the center jet at $0.04ms^{-1}$. In the prescribed leaflet movement, the leaflets were rotated based on a constant angular velocity. At this point, the velocity jets were not visible at all in the prescribed leaflet movement. At position D1, there was a significant difference between the FSI and prescribed movements in the lateral leakage jets. The velocity recorded for FSI simulation was about $0.26ms^{-1}$ while the velocity in the prescribed movements was only $0.05ms^{-1}$. The difference in the velocity profile was due to the prescribed motion of the leaflets being unable to match that of the flow domain at this time point.

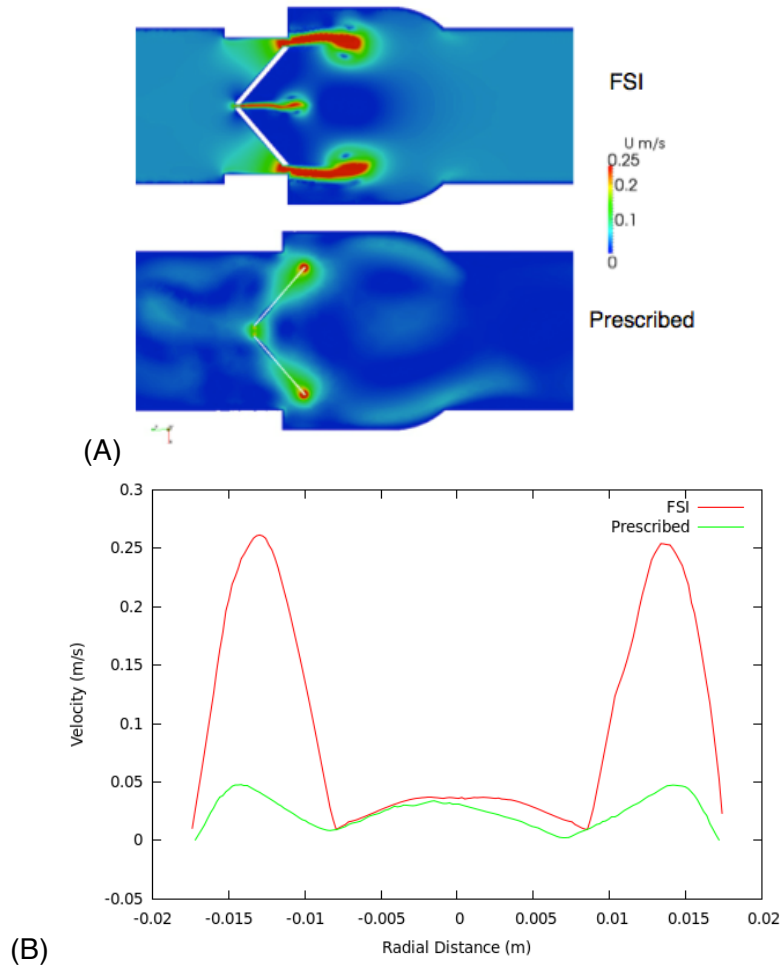

Figure: 5-53: Comparison of (A) velocity contours and (B) velocity profile, for FSI and prescribed leaflet movements at position Z=1D at time t=0.01s

Figure 5-50 shows the comparison of velocity profile for FSI, prescribed leaflet movement and experimental results at three different time points, namely mid systole (t=0.07s), peak systole (t=0.115s), and late systole (t=0.23s). The FSI and prescribed leaflet movement simulations were similar in terms of the velocity magnitude and flow hemodynamics. At mid systole (t=0.07s), the velocity profile for the FSI, prescribed leaflet movement simulations and experimental results showed comparable velocity magnitude and profiles. At this point, the leaflets have rotated from fully closed to fully open at an angle of 85° between the leaflet and the X-Y plane. The difference in the peak velocity was about 10%. The triple-jet structures were visible at mid systole when the flow was still in acceleration phase. At peak systole (t=0.115s), the FSI and prescribed leaflet movements showed comparable results with the experimental data. The triple-jet structures were fully developed at this stage when the flow reached the maximum velocity. It was also observed that both simulations captured the recirculation regions near

the edges with comparable velocity magnitudes, and these flow structures were validated experimentally. At late systole (t=0.23s), the leaflets were still fully open when the flow was in a deceleration phase. The strength of the triple-jet structures decreased to a lower magnitude at 0.75ms^{-1} from 1.1ms^{-1} at peak systole. The FSI simulation was able to capture the flow recirculation regions better than the prescribed leaflet movement simulation at this time.

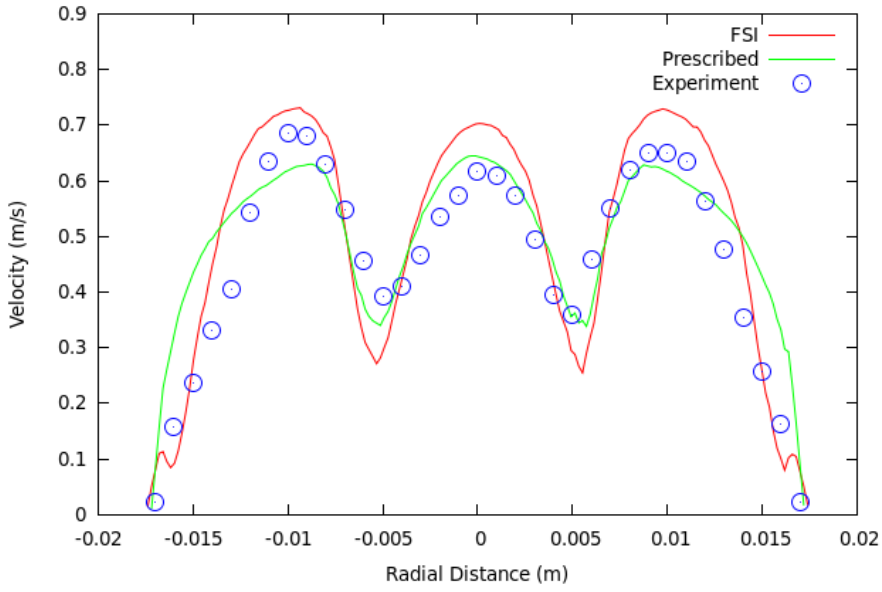

(A)

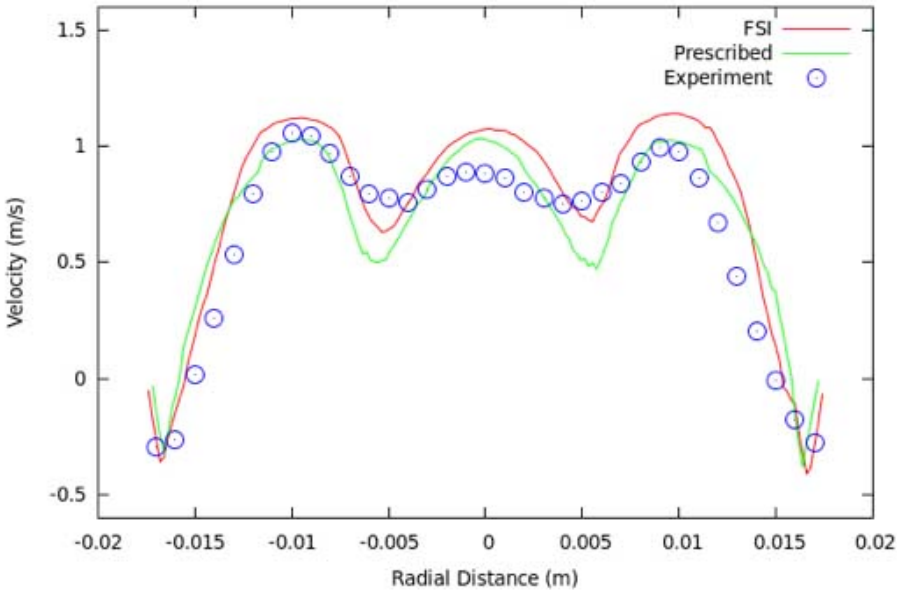

(B)

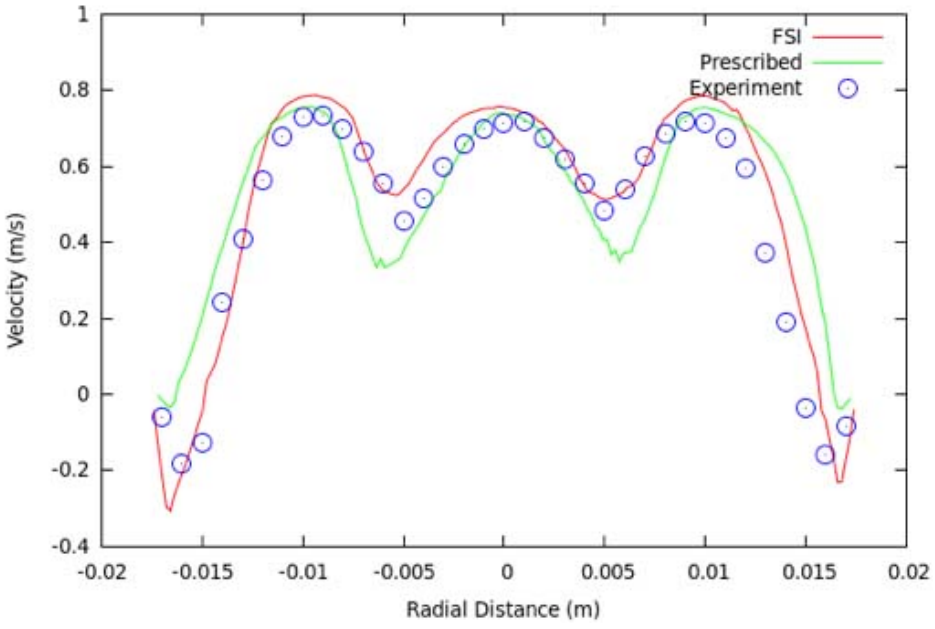

(C)

Figure: 5-54: Comparison of velocity profile for FSI, prescribed leaflet movements and experimental results at position Z=1D at time (A) t=0.07s, (B), t=0.115s, (C) t=0.23s

Comparing the FSI and prescribed leaflet movement simulations, it was observed that there were drastic differences at early systole (t=0.01s) when the leaflets were in motion. The prescribed leaflet movement was not able to capture the flow velocity that pushed the leaflets near the wall edges as well as leakage through the b-datum gap between the two leaflets. On the other hand, the FSI simulation was able to capture the velocity profiles showing the interaction between the fluid and solid domain.

When the leaflets were fully opened at mid diastole (t=0.07s), peak diastole (t=0.115s) and late systole (t=0.23s), it was shown that the simulation results for both FSI and prescribed leaflet movement were quantitatively comparable, and the velocity profiles were similar to that of the experimental results. The key flow velocity structures such as the triple-jet structures and recirculation regions were visible and captured in both simulations. These two simulation results were validated experimentally at all three time points. Nevertheless, the validation study when the leaflets were in motion during the opening and closing phase has not been performed due to the difficulty in capturing the motion of the valve in the short time frame consistently.

5.7.4 Limitations

This study was a preliminary study to investigate the effectiveness of the OpenFOAM to perform FSI in a large deformable domain. The gap in the computational model between the leaflets and the wall may induce some errors in the computational results. The current remeshing technique does not allow simulation of fully closed leaflets, and this is the main limitation of this technique. Only a 2-dimensional FSI model was developed using the open source codes due to the limitations in computational power using the existing infrastructure.

5.7.5 Summary

In this study, the FSI model of the BMHV which was based on the dynamic mesh method of the OpenFOAM software was developed, demonstrated and validated experimentally. The FSI results showed the opening of the valve during the ejection phase of the cardiac cycle at the start of the systole and showed different flow structures compared to prescribed leaflet movement. At other time points of the systolic phase, the FSI simulation was able to highlight the important structures of the flow profile of a BMHV (i.e. the triple-jet structure) as reported by Ge et al., (2005). When the valve was closed at the start of the cardiac cycle, the force exerted by the fluid domain started to push forward the leaflets. As the velocity increased, the leaflets continued to open from 35° to 85° which was the maximum angle that the leaflets could open to. The FSI study provided a platform to further investigate the flow especially the opening and closing stage of the heart valves.

CHAPTER 6: CONCLUSION AND RECOMMENDATION

Artificial heart valves failures and complications arising from the implantation remain a crucial factor in determining the quality of life for patients with heart valve diseases. In the quest to design an improved artificial heart valve in the market, there is a need to look at the fundamentals involving fluid hemodynamics and interaction between the valve leaflets with the flow. Since *in vivo* and *in vitro* experiments are expensive and time consuming to setup, CFD provides a platform to study and identify areas, which cannot be captured experimentally. From CFD perspective, the challenging task ahead would be to model the dynamic interaction of the artificial heart valves with the surrounding blood, and to calculate the local deformations and stresses on the structure, as well as other hemodynamic properties. The potential of this numerical model as a research and development tool to study mechanical heart valves has been demonstrated in this study.

The study has developed and validated both laminar and pulsatile flow with prescribed motion. In the numerical simulations, the turbulence modeling using SA, k-epsilon and LES models was utilized. This was then extended to include the full cardiac cycle modeling. In the process to simulate the movement of leaflets, a solver in OpenFOAM was used to regenerate the mesh using ALE in a prescribed motion. The solver packages allowed the simulation of the valve leaflets rotation. A PIV experimental study for laminar flow using a 29mm ATS Open Pivot Valve was performed. The validation study for pulsatile flow used a 29mm SJM Masters Series BMHV. The flow profiles in the simulation studies for different planes downstream of the valves were compared and showed close similarity with the PIV experimental results. This showed that 3-dimensional model used in the numerical study was successfully validated using the experimental model.

With the validated simulation model, the study proceeded to investigate the importance of hinge microflow simulation so as to understand the complexity of the leakage flow during diastolic phase. The 3-dimensional and unsteady nature of the flow fields have highlighted the regions of high wall shear stress which may cause platelet activation leading to thromboembolic complications.

There were differences noted within the flow field profiles of the four hinges during peak systole in the three-sinus arch model. The hinge microflow fields may yield a dynamically complicated vortical flow structures and could impact the level of hemolysis and platelet activation. However, each individual hinge did not vary much in terms of the leakage flow rate through the valves. As such, it is not necessary to simulate all four hinges together. However, the hinge should be simulated with a three-sinus aortic root geometry and curved downstream aortic arch since this geometry resembled that of native human model. This may potentially determine the clinical performance of the valve. The numerical simulation acted as a tool for thromboembolic potential characterization to observe the physical viscous stresses experienced by the blood elements and the capability to refine the analysis to a level of spatial details that would be hard to achieve experimentally.

The next investigation focused on the implantation position of the BMHVs with respect to the three-sinus aortic root chamber to study its effect on the flow fields and the downstream blood flow characteristics. The study has shown that the implantation orientation angle of the valve, as well as the sinus and downstream geometries in the simulation model, affects the valve performance and flow hemodynamics. The valves could be implanted with various angles depending on the surgeon's performance in a surgical operation. The simulation results showed that the flow profile through valve implanted at anatomically correct position (at angle 0°) has more distributed flow and lower velocity gradient. It is important to note that implantation angles different from the anatomically correct position may have dire consequences on the flow in the sinus chamber and downstream. There were differences in the flow field which could impact the level of hemolysis and platelet activation. The 3-dimensional and unsteady nature of the flow fields downstream of the aortic arch has highlighted the regions of recirculation and high velocity flow. The rotated implantation affected the size of flow recirculation region in the sinus chambers and the downstream flow, which would lead to asymmetrical flow near the BMHVs. This may potentially affect the clinical performance and lifespan of the BMHVs.

Following that, the investigation focused on the comparison of the flow fields through BMHVs and TMHVs implanted at anatomical position. The simulation results showed different flow fields at the downstream positions at Z=1D and 2D. At further downstream at Z=4D, it was found that the flow field shared similarities in terms of the flow profile and the velocity magnitude. Further investigation was performed to study the effect of implantation position of TMHVs in a three-sinus aortic root chamber with a curved downstream aortic arch to look at the downstream flow fields and characteristics. The study showed that the implantation angles of the TMHVs did not affect the downstream flow field much as compared to the BMHVs. Generally, the flow profile through the valve implanted at all the four locations shared similar flow structures, except for the valve implanted at 60° as compared at position Z=1D. It is important to highlight that the implantation angles of the TMHVs have minimal consequences as compared to the BMHVs. Nevertheless, the effect of the implantation angle on the valve closure, which may affect the clinical performance of the TMHVs has not been investigated.

Finally, at this stage, a FSI model of the BMHV hemodynamics using the remeshing technique in OpenFOAM was presented for the acceleration phase of the cardiac cycle. The FSI model was able to capture more accurately the flow structures at early systole when the leaflets were in motion. When the leaflets were fully opened, the FSI model and the prescribed leaflet motion showed comparable results, and were validated experimentally. At this stage, only a 2-dimensional model was being developed using the open source codes. An extension to a full 3-dimensional model using different valve designs can help to uncover important parameters, especially at the opening and closing phase of the leaflets in order to simulate the cardiac cycle with a more accurate physiological flow.

In summary, the research has demonstrated that the moving mesh technique in OpenFOAM has successfully studied detailed and complex heart valve fluid dynamics. The numerical simulation codes have also been validated using the PIV method. With the OpenFOAM code, an accurate *in vitro* computational model was developed to investigate the hemodynamic characteristics of artificial valves especially on the effect of hinges and valve

implantations on downstream flow. The use of anatomical correct aortic arch which was seldom researched into and new trileaflet mechanical heart valve model designed in house were used in the simulations. The results of the simulation allows biomedical engineers to identify regions of high wall shear stress to better understand, develop and improve on new mechanical heart valves. This research sets the foundation to further improve the numerical model to include 3D FSI for mechanical heart valves using OpenFOAM. It is believed that the work done will be useful in developing a more accurate flow simulation in heart valves, such as the FSI for TMHV. Through this research, we are able to capture the essential 3D flow fields and will be able to provide feedback to the biomedical engineers to further improve the design of mechanical heart valves. With the 3D simulation where the maximum shear stress occurs, doctors are able to pin point the high wall shear stress which is the key indicator on potential structural failure. This will enable clinicians and engineers to further improve in understanding and developing better artificial heart valves. New valve design has potential to improve quality of life of MHV recipients by reducing or possibly eliminating need for long-term anti-coagulant therapy

REFERENCES:

1. Akutsu, T., Dreyer, B., and Kolff, W. Polyurethane artificial heart valves in animals. *J Appl Physiol*, 14, pp. 1045-1048. 1959.
2. American Heart Association. Heart, How It Works. Retrieved from http://www.heart.org/HEARTORG/Affiliate/Heart-How-It-Works_UCM_ 428843_Article.jsp [Assessed on 12 Jan 2014] 2012a
3. American Heart Association. Heart Valve Problems and Causes. Retrieved from http://www.heart.org/HEARTORG/Conditions/More/HeartValve ProblemsandDisease/Problem-Aortic-Valve-Regurgitation_UCM_450611_ Article.jsp [Assessed 12 Jan 2014] 2012b.
4. Aluri, S., and Chandran, K. B. Numerical Simulation of Mechanical Mitral Heart Valve Closure. *Ann Biomed Eng*, 29, pp. 665-676. 2001.
5. Annerel, S., Degroote, J., Vierendeels, J., Claessens, T., Ransbeeck, P. V., Dahl, S. K., Skallerud, B., Hellevik, L. R., Segers, P., and Verdonck, P. Application of a strong FSI coupling scheme for the numerical simulation of bileaflet mechanical heart valve dynamics: study of wall shear stress on the valve leaflets. *Progr Comput Fluid Dynam Int J*, 12(2), pp. 68-79, 2012.
6. ATS Medical. ATS Open Pivot Bileaflet Valve: Instructions for Use. p. 1-21. Available from: http://www.accessdata.fda.gov/cdrh_docs/pdf/ P990046c.pdf [Accessed: 08 March 2014] (2014)
7. Bai, Y., Zong, G. J., Wang, H. R., Jiang, H. B., Wang, H., Wu, H., Zhao, X. X., and Qin, Y. W. An integrated pericardial valved stent special for percutaneous tricuspid implantation: an animal feasibility study. *J Surg Res,* 160, pp. 215–221. 2010.
8. Banerjee, R. K., Ashtekar, K. D., Helmy, T. A., Effat, M. A., Back, L. H., and Khoury, S. F. Hemodynamic diagnostics of epicardial coronary stenoses: in-vitro experimental and computational study. *Biomed Eng Online*, 27, pp.7-24. 2008.
9. Baskurt, O. K., and Meiselman, H. J. Blood rheology and hemodynamics. *Semin Thromb Hemost*, 29(5), pp. 435-450. 2003.
10. Bird, R. B., Stewart, W. E., and Lightfoot, E. N. Transport Phenomena. p. 42, New York: NY Wiley. 1960.
11. Blot, W. J., Ibrahim, M. A., Ivey, T.D. Acheson, D. E., Brookmeyer, R., Weyman, A., Defauw, J., Smith, J. K., and Harrison, D. Twenty-five-year experience with the Björk-Shiley convexoconcave heart valve: a continuing clinical concern. *Circulation*, 111(21), pp. 2850-2857. 2005.
12. Bluestein, D. W., Einav, S., and Hwang, N. H. C. A squeeze flow phenomenon at the closing of a bi-leaflet mechanical heart valve prosthesis. *J Biomech*, 27, pp. 1369-1378. 1994.
13. Borazjani, I., Ge, L., and Sotiropoulos, F. Curvilinear immersed boundary method for simulating Fluid-Structure Interaction with complex 3d rigid bodies. *J Comput Phys*, 227(16), pp. 7587–7620. 2008.
14. Borazjani I., and Sotiropoulos F. The Effect of Implantation Orientation of a Bileaflet Mechanical Heart Valve on Kinematics and Hemodynamics in an Anatomic Aorta. *J Biomech Eng*. 132(11), 111005. doi: 10.1115/1.4002491. 2010.
15. Bourguignon, T., Bergöend, E., Mirza, A., Ayegnon, G., Neville, P., Aupart, M. R., and Marchand, M. Risk Factors for valve-related

complications after mechanical heart valve replacement in 505 patients with long term follow up. *J Heart Valve Dis*, 20(6), pp. 673-680. 2011.
16. Boudjemline, Y., Agnoletti, G., Bonnet, D., Behr, L., Borenstein, N., Sidi, N., and Bonhoeffer, P. Steps toward the percutaneous replacement of atrioventricular valves: an experimental study. *J Am Coll Cardiol*, 46(2), pp. 360–365. 2005.
17. Brewer, M., Diachin, L., Leurent, T., and Melander, D. The mesquite mesh quality improvement toolkit. *Proceedings, 12th International Meshing Roundtable*, pp. 239–250. 2003.
18. Brossard, C., Monnier, J-C., Barricau, P., Vandernoot, F-X., Le Sant, P., Champagnat, F., and Besnerais, G. Le. Principles and Applications of Particle Image Velocimetry. *J Aerosp Lab*, 1, pp.1-11. 2009.
19. Carreau, P. Rheological equations from molecular network theories. *Trans Soc Rheol*, 16(1), pp. 99-127. 1972.
20. Carson-DeWitt, R., Aortic Valve Replacement. Available from: http://www.beliefnet.com/healthandhealing/getcontent.aspx?cid=103224. [Accessed on 15 April 2014]. 2014.
21. Cebi, N., and Bozkurt, E. Mid-term results of mitral valve repair for complicated active bacterial endocarditis in high-risk patients. *Heart Vessels*, 19(4), pp. 179-82. 2004.
22. Chandran, K. B., Fatemi, R., Schoephoerster, R., Wurzel, D., Hansen, G., and Pantalos, G. In vitro comparison of velocity profiles and turbulent shear distal to polyurethane trileaflet and pericardial prosthetic valves. *Artif Organs*, 13, pp. 148-154. 1989.
23. Chandran, K. B., Rittgers, S. E., and Yoganathan, A. P. Biofluid Mechanics: The Human Circulation. 2nd Edition, Florida: CRC Press. 2012.
24. Cheeta, G., and Llyod, J. The design, fabrication and evaluation of a trileaflet prosthetic heart valve. *J Biomech Eng*, 102, pp. 34-41. 1980.
25. Cheng, R., Lai, Y., and Chandran, K. B. Two-dimensional Fluid-Structure Interaction simulation of bileaflet mechanical heart valve flow dynamics. *J Heart Valve Dis,* 12(6), pp. 772–780. 2003.
26. Cheng, R., Lai, Y., and Chandran, K. B. Three-dimensional Fluid-Structure Interaction simulation of bileaflet mechanical heart valve flow dynamics. *Ann Biomed Eng,* 32(11), pp. 1471–1483. 2004.
27. Chien, S. Biophysical behavior of red blood cells in suspensions in Red Blood Cell, 2nd Ed, Vol 2. pp. 1031-1133. New York: Academic. 1975.
28. Cho, Y. I., and Kensey, K. R. Effects of the non-Newtonian viscosity of blood on flows in a diseased arterial vessel. Part 1: steady flows. *Biorheology*, 28(3-4), pp. 241-262. 1991.
29. Choi, C. R., Kim, C. N., Kwon, Y. J., and Lee, J. W. Pulsatile blood flows through a bileaflet mechanical heart valve with different approach methods of numerical analysis; pulsatile flows with fixed leaflets and interacted with moving leaflets. *KSME International Journal*, 17(7), pp. 1073-1082. 2003.
30. Corden, J., David, T., and Fisher, J. Determination of the curvatures and bending strains in open trileaflet heart valves. *Proc Inst Mech Eng H,* 209(2), pp. 121-128. 1995.
31. Cribier, A., Eltchaninoff, H., Bash, A., Borenstein, N., Tron, C., Bauer, F., Derumeaux, G., Anselme, F,, Laborde, F., Leon, M. B. Percutaneous Transcatheter Implantation of an Aortic Valve Prosthesis for Calcific

Aortic Stenosis: First Human Case Description. *Circulation*, 106, pp. 3006-3008. 2002.
32. Curtin, R.J., and Griffin, B.P. Mitral Valve Disease: Stenosis and Regurgitation, Disease Management Project, Retrieved from: http://www.clevelandclinicmeded.com/medicalpubs/diseasemanagement/cardiology/mitral-valve-disease/ [Assessed 22 Jan 2014]. 2008.
33. Dasi, L. P., Simon, H. A., Sucosky, P., and Yoganathan, A. P. Fluid Mechanics of Artificial Heart Valves. *Clin Exp Pharmacol Physiol,* 36(2), pp. 225-237. 2009.
34. D'Souza, S. S., Butterfield, M., and Fisher, J. Kinematics of synthetic flexible leaflet heart valves during accelerated testing. *J Heart Valve Dis*, 12(1), 110-9; discussion 119-120. 2003.
35. Daebritz, S. H., Sachweh, J. S., Hermanns, B., Fausten, B., Franke, A., and Groetzner, J. Introduction of a flexible polymeric heart valve prosthesis with special design for mitral position. *Circulation*, 108 Suppl 1, II134-II139. 2003.
36. Daebritz, S. H., Fausten, B., Hermanns, B., Schroeder J., Groetzner, J., Austschbach, R., Messmer, B. J., and Sachweh, J. S. Introduction of a flexible polymeric heart valve prosthesis with special design for aortic position. *Eur J Cardiothorac Surg*, 25, pp. 946-952. 2004.
37. Dai, M., and Schmidt, D. P. Adaptive tetrahedral meshing in free-surface flow. *J Comput Phys,* 208(1), pp. 228-252. 2005.
38. Dantec Dynamics. Particle Image Velocimetry measurement principles. Retrieved from: http://www.dantecdynamics.com/Default.aspx?ID=820 [Assessed on 23 November 2011]. 2011.
39. Dasi, L. P., Ge, L., Simon, H. A., Sotiropoulos, F., and Yoganathan, A. P. Vorticity dynamics of a bileaflet mechanical heart valve in an axisymmetric aorta. *Physics of Fluids*, 19, 067105. 2007.
40. De Hart, J., Peters, G. W. M. , Schreurs, P. J. G., and Baaijens, F. P. T. A three-dimensional computational analysis of fluid–structure interaction in the aortic valve. *J Biomech*, 36(1), pp.103–112. 2003.
41. Dumont, K., Stijnen, J. M. A., Vierendeels, J., Van de Vosse, F. N., and Verdonck, P. R. Validation of a Fluid-Structure Interaction Model of a Heart Valve Using the Dynamic Mesh Method in Fluent. *Comput Methods Biomech Biomed Eng,* 7(3), pp. 139.146. 2004.
42. Dumont, K. Experimental and numerical modeling of heart valve dynamics, Ph.D Thesis, Ghent University. 2005.
43. Dumont, K., Vierendeels, J., Kaminsky, R., Nooten, G. v., Verdonck, P. and Bluestein, D. Comparison of the Hemodynamic and Thrombogenic Performance of Two Bileaflet Mechanical Heart Valves Using a CFD/FSI Model. *J Biomech Eng,* 129(4), pp. 558-565. 2007.
44. Dupire, J., Socol, M., and Viallat, A. Full dynamics of a red blood cell in shear flow. *Proc Natl Acad Sci U S A*, PNAS Early Edition, pp. 1-6. 2012.
45. Ellis, J. T., Healy, T. M., Fontaine, A. A., Saxena R., and Yoganathan, A. P. Velocity measurements and flow patterns within the hinge region of a medtronic parallel bileaflet mechanical heart valve with clear housing. *J Heart Valve Dis,* 5(6), pp. 591-599. 1996.
46. Ellis, J. T., Travis, B. R., and Yoganathan, A. P. An *in vitro* study of the hinge and near-field forward flow dynamics of the St Jude Medical Regent bileaflet mechanical heart valve. *Ann Biomed Eng*, 28(5), pp. 524-532. 2000a.

47. Ellis, J. T., and Yoganathan, A. P. A comparison of the hinge and near-hinge flow fields of the St Jude Medical Hemodynamic Plus and Regent Bileaflet Mechanical Heart Valves, *J Thorac. Cardiovasc. Surg.,* 119(1), pp.83-93. 2000b.
48. Esquivel, C., Rosenberger, M., Gueijman, S., Schvezov, C., and Amerio, O. Design of a fourth generation prosthetic heart valve: tri-leaflet valve. *Third Congress of Cardiology on the Internet, CITEFAC- Bioingenieria UNER,* 2003.
49. Fahraeus, R., and Lindqvist, T. The viscosity of blood in narrow capillary tubes. *American J Physiol*, 96, pp. 562-568. 1931.
50. Ferziger, J. H., and Peric, M. Computational Methods for Fluid Dynamics, 2nd Edition, Berlin Heidelberg: Springer-Verlag. 1999.
51. Fung, Y. C. Biodynamics : Circulation. New York: Springer-Verlag. 1984.
52. Gallegos, R. P., Rivard, A. L., Suwan, P. T., Black, S., Bertog, S., Steinseifer, U., Armien, A., Lahti, M., and Bianco, R. W. In-vivo experience with the Triflo trileaflet mechanical heart valve. *J Heart Valve Dis*, 15(6), pp. 791-799. 2006.
53. Gallocher, S. L. Aguirre, A. F., Kasyanov, V., Pinchuk, L., and Schoephoerster, R. T. A novel polymer for potential use in a trileaflet heart valve. *J Biomed Mater Res B Appl Biomater*, 79, pp. 325-334. 2006.
54. Ghaeb, N. H., Khalaf, T. Y., and Al-Timemy, A. Velocity Analysis of Bileaflet Artificial Heart Valve: from Opening to near Close Position. *J Appl Sci Res*, 5(10), pp. 1455-1462. 2009.
55. Ge, L., Leo, H. L., Sotiropoulos, F., and Yoganathan, A. P. Flow in a mechanical bileaflet heart valve at laminar and near-peak systole flow rates: CFD simulations and experiments. *J Biomech Eng*, 127(5), pp. 782-797. 2005.
56. Ghanbari, H., Viatge, H., Kidane, A. G., Burriesci, G., Tavakoli, M., and Seifalian, A. M. Polymeric heart valves: new materials, emerging hopes, *Trends Biotechnol*, 27(6), pp. 359-367. 2009.
57. Gijsen, F., van de Vosse, F., and Janssen, J. Influence of the non-newtonian properties of blood on the flow in large arteries: steady flow in a carotid bifurcation model. *J Biomech,* 32(6), pp. 601-608. 1999a.
58. Gijsen, F., van de Vosse, F., and Janssen, J. Influence of the non-newtonian properties of blood on the flow in large arteries: unsteady flow in a 90 degree curved tube. *J Biomech,* 32(7), pp. 705-713. 1999b.
59. Gilmanov, A., and Sotiropoulos, F. A hybrid cartesian/immersed boundary method for simulating flows with 3D, geometrically complex, moving bodies. *J Comput Phys,* 207, pp. 457-492. 2005.
60. Goldsmith, I., Turpie, A.G., and Lip, G. Y. Valvular heart disease and prosthetic heart valves. *BMJ*, 325, pp. 1228-1231. 2002.
61. Griffith, B. E. Immersed boundary model of aortic heart valve dynamics with physiological driving and loading conditions. *Int J Numer Meth Biomed Eng,* 28, pp. 317-345. 2013.
62. Hager, A., Kaemmerer, H., Rapp-Bernhardt, U., Blucher, S., Rapp, K., Bernhardt, T.M., Galanski, M., Hess, J. Diameters of the thoracic aorta throughout life as measured with helical computed tomography. *J Thorac Cardiovasc Surg*, 123(6), pp.1060-1066. 2002.
63. Harker, L. A., and Slichter, S. J. Studies of platelet and fibrinogen kinetics in patients with prosthetic heart valves. *New Engl J Med*, 283(24), pp. 1302-1305. 1970.

64. Herold, M., Lo, H. B., Ruel, H., Muckter, H., Taguchi, K., Giersiepen, M., Birkle, G., Hollweg, G., Rau, G., and Messmer, B. J. The Helmholtz-Institute-Tri-Leaflet-Polyurethane-Heart Valve Prosthesis: Design, Manufacturing and First In-Vitro and In-Vivo Results. *Polyurethanes in Biomedical Engineering II*, pp. 231-236. 1987.
65. Ho, S. Y. Structure and anatomy of the aortic root, *Eur J Echocardiogr,* 10(1), pp. i3-i10. 2009.
66. Hong T., and Kim C. N. A Numerical Analysis of the Blood Flow around the Bileaflet Mechanical Heart Valves with Different Rotational Implantation Angles. *J Hydrodynam*. 23(5), pp. 607-614. 2011.
67. Hufnagel, C. A., Gillespie, J. F., Conrad, P. W., Mercier, C., and Evangelist, F. A. Cardiac valve replacement-its current status. *Med Ann Dist Columbia*, 35(9), pp. 457-462. 1966.
68. Hung, T. C., Hochmuth, R. M., Joist, J. H., and Sutera, S. P. Shear-induced aggregation and lysis of platelets. *Trans Am Soc Artif Intern Organs*. 22: p. 285-291. 1976.
69. Hyde, J. A., Chinn, J. A., and Phillips, R. E. Polymer heart valves. *J Heart Valve Dis*, 8, pp. 331-339. 1999.
70. Ito, H., Sakata, K., Haruki, T., and Kobayashi, Y. Structural valve deterioration of a mitral Carpentier-Edwards pericardial bioprosthesis in an 87-year-old woman 16 years after its implantation. *J Cardiothorac Surg*, 6(88), pp. 1-3. 2011.
71. Jansen, J., Willeke, S., Reiners, B., Harbott, P., Reul, H., and Lo, H. B. Advances in design principle and fluid dynamics of a flexible polymeric heart valve. *ASAIO Trans*, 37(3), M451-M453. 1991.
72. Johnston, B. M., Johnson, P. R., Corney, S., and Kilpatrick, D. Non-Newtonian blood flow in human right coronary arteries: steady state simulations. *J Biomech*, 37, pp. 709-720. 2004.
73. Kardon, E. M. FACEP, Prosthetic Heart Valves. Available from: http://emedicine.medscape.com/article/780702-overview [Assessed on 26 September 2010]. 2010.
74. Kassiotis, C. Which strategy to move the mesh in the Computational Fluid Dynamic code OpenFOAM, p.1-14. 2008.
75. Kaufmann, T. A. S., Linde, T., Cuenca-Navalon, E., Schmitz, C., Hormes, M., Schmitz-Rode, T., and Steinseifer, U. Transient, Three-Dimensional Flow Field Simulation through a Mechanical, Trileaflet Heart Valve Prosthesis, *ASAIO J*, 57(4), pp. 278-282. 2011.
76. Kelly, S. G., Verdonck, P. R., Vierendeels, J. A. M., Riemslagh, K., Dick, E., and Van Nooten, G. G. A three-dimensional analysis of flow in the pivot regions of an ATS bileaflet Valve, *Int. J. Artif. Organs*, 22, pp. 754-763. 1999.
77. Kheradvar A., and Pedrizzetti G. Effect of Cardiac Devices and Surgery on Vortex Formation. In: Vortex Formation in the Cardiovascular System. pp. 81–124, London: Springer. 2012.
78. King M. J., David T., and Fisher J. Three-dimensional study of the effect of two leaflet opening angles on the time-dependent flow through a bileaflet mechanical heart valve. *Med Eng Phys*, 19(3), pp. 235- 241. 1997.
79. Kitware, Inc. ParaView and ParaViewWeb Available from: http://www.kitware.com/opensource/paraview.html [Assessed on 22 January 2014]. 2014.

80. Klabunde, R. E. Cardiac Cycle. Available from: http://www.cvphysiology.com/Heart%20Disease/HD002b.htm [Assessed on 28 October 2011]. 2011.

81. Kleine P, Perthel M, Nygaard H, Hansen SB, Paulsen PK, Riis C, Laas, J. Medtronic Hall versus St. Jude Medical mechanical aortic valve: downstream turbulences with respect to rotation in pigs. *J Heart Valve Dis*. 7(5) pp. 548-555. 1998.
82. Kleine P, Scherer M, Abdel-Rahman U, Klesius AA, Ackermann H, Moritz A. Effect of mechanical aortic valve orientation on coronary artery flow: comparison of tilting disc versus bileaflet prostheses in pigs. *J Thorac Cardiovasc Surg*. 124(5) pp. 925-932. 2002.
83. Korossis, S. A., Fisher, J., and Ingham, E. Cardiac valve replacement: a bioengineering approach. *Biomed Mater Eng*, 10(2), pp. 83-124. 2000.
84. Kroll, M. H., Hellums, J. D., McIntire, L. V., Schafer, A. I., and Moake, J. L. Platelet and Shear Stress. *Blood,* 88(5), pp. 1525-1541. 1996.
85. Kuan, Y. H., Lakshmi, P. D., Yoganathan, A. P., and Leo, H. L. Recent Advances in Polymeric Heart Valves Research. *Int J Biomater Res Eng,* 1(1), pp. 1-17. 2011.
86. Laas J., Kleine P., Hasenkam M. J., and Nygaard H. Orientation of Tilting Disc and Bileaflet Aortic Valve Substitutes for Optimal Hemodynamics. *Ann Thorac Surg*, 68, pp. 1096-1099. 1999.
87. Laberge, M. Cardiac Cycle. Available from: http://www.healthline.com/galecontent/cardiac-cycle [Assessed on 30 October 2011]. 2002.
88. Lai, Y., Chandran, K., and Lemmon, J. A numerical simulation of mechanical heart valve closure fluid dynamics. *J Biomech*, 35(7), pp. 881–892. 2002.
89. Lamson, T.C., Rosenberg, G., Geselowitz, D.B., Deutsch, S., Stinebring, D.R., Frangos, J.A., and Tarbell, J.M. Relative blood damage in the three phases of a prosthetic heart valve flow cycle. *ASAIO J,* 39:M626-M633. 1993.
90. Leat, M. E., and Fisher, J. The influence of manufacturing methods on the function and performance of a synthetic leaflet heart valve. *Proc Inst Mech Eng H*, 209, pp. 65-69. 1995.
91. Lee, C., and Chandran, K. Numerical simulation of instantaneous backflow through central clearance of bi-leaflet mechanical heart valve at closure: shear stresses and pressure fields. *Med Biol Eng Comput*, 33(3), pp. 257–263. 1995.
92. Lee, W. Y., Hong, J. M., and Bae, J. W. A Case of Fatal Mechanical Mitral Valve Leaflet Fracture Embolization. *Korean J Crit Care Med*, 26(2), pp. 101-104. 2011.
93. Leo, H. L., He, Z., Ellis, J. T., and Yoganathan, A. P. Microflow fields in the hinge region of the Carbomedics bileaflet mechanical heart valve design, *J Thorac Cardiovasc Surg,* 124, pp. 561-574. 2002.
94. Leo, H. L. An *In Vitro* Investigation of the Flow Fields Through Bileaflet and Polymeric Prosthetic Heart Valves, Ph.D Thesis, Georgia Institute of Technology. 2005.
95. Leo, H. L., Simon, H. A., Dasi, L. P., and Yoganathan, A. P. Effect of hinge gap width on the microflow structures in 27mm bileaflet mechanical heart valve. *J Heart Valve Dis*, 15, pp. 800-808. 2006.

96. Li, C-P., and Lu, P-C. Numerical comparison of the closing dynamics of a new trileaflet and a bileaflet mechanical aortic heart valve. *J Artif Organs,* 15, pp. 364-374. 2012.
97. Lim, W. L., Chew, Y. T., Chew, T. C., and Low, H.T. Pulsatile flow studies of a porcine bioprosthetic aortic valve in vitro: PIV measurements and shear-induced blood damage. *J Biomech,* 34(11), pp. 1417-27. 2001.
98. Lohner, R., and Yang, C. Improved ALE mesh velocities for moving bodies. *Commun Numer Methods Eng.* 12, pp. 599-608. 1996.
99. Lomtev, I., Kirby, R. M., and Karniadakis, G. E. A discontinuous Galerkin ALE method for compressible viscous flows in moving domains. *J. Comput Phys,* 155, pp.128-159. 1999.
100. Lu, P. C., Lai, H. C., and Liu, J. S. A reevaluation and discussion on the threshold limit for hemolysis in a turbulent shear flow, *J Biomech,* 34(10) pp. 1361-1364. 2001.
101. Lu, Q., Hofferbert, B. V., Koo, G., and Malinauskas, R. A. In Vitro Shear Stress-Induced Platelet Activation: Sensitivity of Human and Bovine Blood. *Artif Organs,* 37(10), pp. 894-903. 2013.
102. Mackay, T. G., Wheatley, D. J., Bernacca, G. M., Fisher, A. C., and Hindle, C. S. New polyurethane heart valve prosthesis: design, manufacture and evaluation. *Biomaterials*, 17, pp. 1857-1863. 1996.
103. Manji, R. A., Esker, B., Menkis, A. H., and Cooper, D. K. C. Bioprosthetic heart valves of the future. *Xenotransplantation*, 21(1), pp. 1-10. 2014.
104. Manning, K. B., Kini, V., Fontaine, A. A., Deutsch, S., and Tarbell, J. M. Regurgitant flow field characteristics of the St. Jude bileaflet mechanical heart valve under physiologic pulsatile flow using particle image velocimetry. *Artif Organs,* 27(9), pp. 840-846. 2003.
105. Marom, G., Kim, H-S., Rosenfeld, M., Raanani, E, and Haj-Ali, R. Fully coupled Fluid-Structure Interaction model of congenital bicuspid aortic valves: effect of asymmetry on hemodynamics. *Med Biol Eng Comput*, 51, pp. 839-848. 2013.
106. Matthews, R. Cardiology, Available from: http://www.rjmatthewsmd.com/Definitions/pop/107fig.htm [Assessed on 1 Nov 2011]. 2011.
107. Maus, K. J. myIcoFsiFoam and myInterFsiFoam: Constructing solvers for weakly coupled FSI problems using OpenFOAM-1.5-dev, Norwegian University of Life Sciences. 2009.
108. Maymir, J-C., Deutsch,S., Meyer, R.S., Geselowitz, D.B., and Tarbell, J.M. Effects of tilting disk heart valve gap width on regurgitant flow through an artificiial heart valve, *Artif Organs*, 21, pp.1014-1025. 1997.
109. McGraw-Hill, Cardiovascular Heart Parts, Available from http://www.tooloop.com/cardiovascular-heart-parts/ [Assessed on 22 Jan 2014]. 2014.
110. Melling, A. Tracer particles and seeding for particle image velocimetry. *Meas Sci Technol,* 8(12), pp. 1406-1416. 1997.
111. Merrill, E.W. Rheology of blood. *Physiological Reviews*, 49(4), pp.863-888. 1969.
112. Modi, A. Direct Numerical Simulation of Turbulent Flows. 1999.
113. Morbiducci, U., Gallo, D., Massai, D., Ponzini, R., Deriu, M. A., Antiga, L., Redaelli, A., and Montevecchi, F. M. On the importance of blood rheology for bulk flow in hemodynamic models of the carotid bifurcation. *J Biomech*, 44(13), pp. 2427-2438. 2011.

114. Narayan, R. L., and Sharma S. K. Looking to the future of Percutaneous Treatment of Patients with Valvular Heart Disease. *Interv Cardiol Clin*, 1(1), pp. 139-149. 2012
115. Nguyen, V-T., Kuan, Y. H., Chen, P-Y., Ge, L., Sotiropoulos, F., Yoganathan, A. P., and Leo, H. L. Experimentally Validated Hemodynamics Simulations of Mechanical Heart Valves in Three Dimensions. *Cardiovasc Eng Technol*, 3(1), pp. 88-100. 2012.
116. Ngo, C.C. and K. Gramoll. *FLUID MECHANICS - THEORY*. n.d. Available from: http://www.ecourses.ou.edu/cgi-bin/ebook.cgi?doc=&topic=fl&chap_sec=08.3&page=theory [Accessed: 05 October 2010] 2010.
117. Nichols, W. W., and O'Rouke, M. F. McDonald's blood flow in arteries: theoretical, experimental and clinical principles, p. 607. London: Hodder Arnold, 5th edition. 2005.
118. Nobili M., Morbiducci U., Ponzini R., Del Gaudio C., Balducci A., Grigioni M., Maria Montevecchi F., and Redaelli A. Numerical simulation of the dynamics of a bileaflet prosthetic heart valve using a Fluid-Structure Interaction approach, *J Biomech*, 41(11), pp.2539–2550. 2008.
119. Obi, S., Yamamoto, K., Shimizu, N., Kumagaya, S., Masumura, T., Sokabe, T., Asahara, T., and Ando, J. Fluid shear stress induces arterial differentiation of endothelial progenitor cells. *J Appl Physiol,* 106, pp. 203-211. 2009.
120. O'Rourke, D. J., Palac, R. T., Malenka, D. J., Marrin, C. A., Arbuckle, B. E., and Plehn, J. F. Outcome of mild periprosthetic regurgitation detected by intraoperative transesophageal echocardiography. *J Am Coll Cardiol,* 38(1), pp. 163-166. 2001.
121. OpenFOAM The OpenFOAM Foundation. Available from http://www.openfoam.org/ [Accessed: 25 November 2012] 2014.
122. Otto, C. M. Calcification of bicuspid aortic valves. *Heart*, 88(4), pp. 321-322. 2002.
123. Peskin C. S. Flow patterns around heart valves: a numerical method. *J Comput Phys*, 10, pp. 252– 271. 1972.
124. Peskin, C. S. The Fluid Dynamics of Heart Valves - Experimental, Theoretical, and Computational Methods. *Annu Rev Fluid Mech*, 14, pp. 235. 1982.
125. Pick, A. Mechanical Heart Valve Replacement Devices - Pros and Cons, Available from http://www.heart-valve-surgery.com/mechanical-prosthetic-heart-valve.php [Accessed: 20 Jan 2014] 2014.
126. Pisani, G., Scaffa, R., Ieropoli, O., Dell' Amico, E.M., Maselli, D., Morbiducci, U., and De Paulis, R. Role of sinuses of Valsalva on the opening of the aortic valve. *J Thorac Cardiovasc Surg,* 145(4), pp. 999-1003. 2013.
127. Post, F. H., and van Walsum, T. Fluid Flow Visualization. pp. 1-40. *Focus on Scientific Visualization,* Berlin: Springer Verlag. 1993.
128. Price, S. A. and Wilson, L. M. Pathophysiology: Clinical Concepts of Disease Processes (6th ed.), Philadelphia: Mosby- Year Book Inc. 2003.
129. Rallidis, L. S., Moyssakis, I. E., Ikonomidis, I., and Nihoyannopoulos, P. Natural history of early aortic paraprosthetic regurgitation: a five-year follow-up. *Am Heart J*, 138(2 Pt 1), pp. 351-357. 1999.
130. Ramstack, J. M., Zuckerman, L., and Mockros, L. F. Shear-induced activation of platelets, *J Biomech,* 12(2), p. 113-125. 1979.

131. Rand, P. W., Lacombe, E., Hunt, H. E., and Austin, W. H. Viscosity of normal human blood under normothermic and hypothermic conditions. *J Appl Physiol*, 19(1), pp. 117-122. 1964.
132. Reif, T. H. A numerical analysis of back flow between the leaflets of St Jude medical cardiac valve prostheses. *J Biomech*, 24 (8), pp. 733-741. 1991.
133. Rose, A. G. Atlas of Gross Pathology with Histologic Correlation, New York: Cambridge University Press. 2008.
134. Sacks, M. S. Surface strains in the anterior leaflet of the functioning mitral valve. *Ann Biomed Eng*, 30(10), pp. 1281-1290. 2002.
135. Sallam, A. M., and Hwang, N. H. Human red blood cell hemolysis in a turbulent shear flow: contribution of Reynolds shear stresses, *Biorheology,* 21(6), pp. 783-797. 1984.
136. Sato, M., Harasaki, H., Wika, K. E., Soloviev, M. V., and Lee, A. S. Blood compatibility of a newly developed trileaflet mechanical heart valve. *ASAIO J*, 49(1), pp. 117-122. 2003.
137. Saxena R., Lemmon, J., Ellis, J., and Yoganathan, A. P. An in vitro assessment by means of laser doppler velocimetry of the medtronic advantage bileaflet mechanical heart valve hinge flow, *J Thorac Cardiovasc Surg,* 126, pp. 90-98. 2003.
138. Schoen, F. J., Levy, R. J., Hilbert, S. L., and Bianco, R. W. Antimineralization treatments for bioprosthetic heart valves: Assessment of efficacy and safety. *J Thorac Cardiovasc Surg*, 104, pp. 1285-1288. 1992.
139. Sezai, A., Shiono, M., Hata, M., Saito, A., Hattori, T., Wakui, S., Soeda, M., Kasamaki, Y., Tokai, K., Saito, S., Negishi, N., and Sezai, Y. A Case of Transient Bioprosthetic Valve Regurgitation and Hemolysis Developing Early after Surgery Using Carpentier-Edwards Valve. *Ann Thorac Cardiovasc Surg*, 11(6), pp. 413-415. 2005.
140. Shahriari, S., Maleki, H., Hassan, I., and Kadem, L. Evaluation of shear stress accumulation on blood components in normal and dysfunctional bileaflet mechanical heart valves using smoothed particle hydrodynamics. *J Biomech,* 45(15), pp. 2637-2644. 2012.
141. Sheriff, J., Bluestein, D., Girdhar, G., and Jesty, J. High-Shear Stress Sensitizes Platelets to Subsequent Low-Shear Conditions. *Ann Biomed Eng,* 38(4), pp. 1442-1450. 2010.
142. Shih, T. H., Liou, W. W., Shabbir, A., Yang, Z., and Zhu, J. A New k-epsilon Eddy-Viscosity Model for High Reynolds Number Turbulent Flows - Model Development and Validation. NASA Technical Memorandum 106721. 1994.
143. Shu, M. C. S., Gross, J. M., O'Rourke, K. K. and Yoganathan, A. P. An Integrated Macro/Micro Approach to Evaluating Pivot Flow Within the Medtronic ADVANTAGE Bileaflet Mechanical Heart Valve. *J Heart Valve Dis*, 12(4), pp. 503-512. 2003.
144. Siebert, M. W., and Fodor, P. S. Newtonian and Non-Newtonian Blood Flow over a Backward-Facing Step - A Case Study, COMSOL Conference Boston. 2009.
145. Simon, H. A., Leo, H. L., Carberry, J., and Yoganathan, A. P. Comparison of the hinge flow fields of two bileaflet mechanical heart valve under aortic and mitral conditions. *Ann Biomed Eng,* 32, pp. 1607-1617. 2004.

146. Simon, H .A., Ge, L., Sotiropoulos, F., and Yoganathan, A. P. Simulation of the Three-Dimensional Hinge Flow Fields of a Bileaflet Mechanical Heart Valve Under Aortic Conditions. *Ann Biomed Eng,* 38(3), pp. 841-853. 2010.
147. Slack, S. M., Cui, Y., and Turitto, V. T. The effects of flow on blood coagulation and thrombosis. *Thromb Haemost*, 70(1), pp. 129-34. 1993.
148. Smith, R. L., Blick, E. F., Coalson, J., and Stein, P. D. Thrombus production by turbulence. *J Appl Physiol*, 32(2), pp. 261-264. 1972.
149. Sotiropoulos, F., and Borazjani I. A review of state-of-the-art numerical methods for simulating flow through mechanical heart valves. *Med Biol Eng Comput*, 47(3), pp. 245-256. 2009.
150. Spalart, P. R. Trends in Turbulence Treatments. *AIAA J*, pp. 2000-2306. 2000.
151. Stalder, A. F., Frydrychowicz, A., Russe, M. F., Korvink, J. G., Hennig, J., Li, K., and Markl, M. Assessment of flow instabilities in the healthy aorta using flow-sensitive MRI. *J Magn Reson Imaging,* 33(4), pp. 839-846. 2011.
152. Starr, A., Fessler, C. L., Grunkemeier, G., and He, G. W. Heart valve replacement surgery: past, present and future. *Clin Exp Pharmacol Physiol,* 29, pp. 735-738. 2002.
153. Steegers, A., Paul, R., Reul, H., and Rau, G. Leakage flow at mechanical heart valve prostheses: improved washout or increased blood damage? *J. Heart Valve Dis,* 8(3), pp. 312-323. 1999.
154. St Jude Medical. St Jude Medical Masters Series. Available from:
155. https://professional-intl.sjm.com/products/sh/mechanical-valves/aortic-mitral/masters-series#overview [Accessed: 08 March 2014] 2014.
156. Su, B., Zhong, L., Wang, X-K., Zhang, J-M., Tan, R. S., Allen, J. C., Tan, S. K., Kim, S., and Leo, H. L. Numerical simulation of patient-specific left ventricular model with both mitral and aortic valves by FSI approach. *Comput Methods Programs Biomed*, 113(2), pp. 474-482. 2014.
157. Tai, C. H., Liew, K. M. and Zhao, Y. Numerical simulation of 3D fluid–structure interaction flow using an immersed object method with overlapping grids. *Computer and Structures*, 85(11–14), pp. 749–762. 2007.
158. Tokarev, A. A., Butylin, A. A., and Ataullakhanov, F. I. Platelet Adhesion from Shear Blood Flow is Controlled by Near-Wall Rebounding Collisions with Erythrocytes. *Biophys J,* 100(4), pp. 799-808. 2011.
159. Travis, B. R., Leo, H. L., Shah, P. A., Frakes, D. H., and Yoganathan, A. P. An analysis of Turbulent Shear Stresses in Leakage Flow Through a Bileaflet Mechanical Prostheses. *J Biomech Eng*, 124(2), pp. 155-165. 2002.
160. Tu, J., Inthavong, K., and Ahmadi, G. Computational Fluid and Particle Dynamics in the Human Respiratory System. New York: Springer. 2013.
161. Vahanian, A., Alfieri, O., Andreotti, F., Antunes, M. J., Barón-Esquivias, G., Baumgartner, H., Borger, M. A., Carrel, T. P., De Bonis, M., Evangelista, A., Falk ,V., lung, B., Lancellotti, P., Pierard, L., Price, S., Schäfers, H. J., Schuler, G., Stepinska, J., Swedberg, K., Takkenberg, J., Von Oppell, U. O., Windecker, S., Zamorano, J. L., and Zembala, M. Guidelines on the management of valvular heart disease. *Eur Heart J,* 33(19), pp. 2451-2496. 2012.
162. van Loon, R., Anderson P. D., Baaijens, F. P. T., and van de Vosse, F. N. A three-dimensional fluid–structure interaction method for heart

valve modelling. *Comptes rendus-Mécanique*, 333(12), pp. 856–866. 2005.
163. Villiers, E. D. The Potential of Large Eddy Simulation for the Modeling of Wall Bounded Flows, Ph.D Thesis, Imperial College of Science, Technology and Medicine. 2006.
164. Vongpatanasin, W., Hillis, D. L., and Lange, R. A. Prosthetic heart valves. *New Engl J Med,* 335, pp. 407-416. 1996.
165. Walker, P. G., and Yoganathan, A. P. *In vitro* pulsatile flow hemodynamics of five mechanical aortic heart valve prostheses. *Eur J Cardiothorac Surg*, 6 Suppl 1, S113-S123. 1992.
166. WebMD. Normal Function of the Mitral Valve. Available from: http://www.webmd.com/heart/normal-function-of-the-mitral-valve. [Accessed on 16 April 2014]. 2014.
167. Weller, H. G., Tabor, G., Jasak, H., and Fureby, C. A tensorial approach to computational continuum mechanics using object orientated techniques. *Computers in Physics*, 12 (6), p. 620–631. 1998.
168. Wheatley, D. J., Raco, L., Bernacca, G. M., Sim, I., Belcher, P. R., and Boyd, J. S. Polyurethane: material for the next generation of heart valve prostheses? *Eur J Cardiothorac Surg*, 17, pp. 440-448. 2000.
169. Wheatley, D. J., Bernacca, G. M., Tolland, M. M., O'Connor, B., Fisher, J., and Williams, D. F. Hydrodynamic function of a biostable polyurethane flexible heart valve after six months in sheep. *Int J Artif Organs*, 24(2), pp. 95-101. 2001.
170. Whitlock, R. P., Sun, J. C., Fremes, S. E., Rubens, F. D., and Teoh K. H. Antithrombotic and Thrombolytic Therapy for Valvular Disease. *Chest*, 141(2 Suppl), e576S-600S. 2012.
171. Woo, Y. R., Williams, F. P., and Yoganathan, A. P. In-vitro fluid dynamic characteristics of the Abiomed trileaflet heart valve prosthesis. *J Biomech Eng*, 105, pp. 338-345. 1983.
172. Wurzinger, L. J., Opitz, R., Blasberg, P., and Schmid-Schonbein H. Platelet and coagulation parameters following millisecond exposure to laminar shear stress. *Thromb Haemost,* 54, pp. 381–386. 1985.
173. Xia, G. H., Zhao, Y., and Yeo, J. H. Parallel unstructured multigrid simulation of 3D unsteady flows and Fluid-Structure Interaction in mechanical heart valve using immersed membrane method. *Computer & Fluids*, 38, pp. 71-79. 2009.
174. Yakhot, V., and Orszag, S. A. Renormalization Group Analysis of Turbulence: I. Basic Theory. *J Scientif Comput*, 1(1), pp. 1-51. 1986.
175. Yasuda, R., and Cohen, R. Shear-flow properties of concentrated-solutions of linear and star branched polystyrenes. *Rheol Acta*, 20, pp. 163-178. 1981.
176. Yin, W., Alemu,. Y., Affeld, K., Jetsy, J. and Bluestein, D. Flow-induced platelet activation in bileaflet and monoleaflet mechanical heart valves. *Ann Biomed Eng*, 32(8), pp. 1058-1066. 2004.
177. Yoganathan, A. P., Woo, Y. R., Williams, F. P., Stevenson, D. M., Franch, R. H., & Harrison, E. C. In vitro fluid dynamic characteristics of Ionescu-Shiley and Carpentier-Edwards tissue bioprostheses. *Artif Organs*, 7, pp. 459-469. 1983.
178. Yoganathan, A. P., Woo, Y. R., Sung, H. W., Williams, F. P., Franch, R. H., and Jones, M. In vitro hemodynamic characteristics of tissue bioprostheses in the aortic position. *J Thorac Cardiovasc Surg*, 92, pp. 198-209. 1986.

179. Yoganathan, A. P. Cardiac Valve Prostheses. The Biomedical Engineering Handbook Volume 1: Second Edition, CRC Press LLC. 2000.
180. Yoganathan, A. P., Chandran, K. B., and Sotiropoulos, F. Flow in Prosthetic Heart Valves: State-of-the-Art and Future Directions, *Ann Biomed Eng,* 33(12) pp. 1689-1694. 2005.
181. Yun, B. M., Wu, J., Simon, H. A., Arjunon, S., Sotiropoulos, F., Aidun, C. K., and Yoganathan, A. P. A numerical invesigation of blood damage in the hinge area of aortic bileaflet mechanical heart valves during the leakage phase, *Ann Biomed Eng,* 40, pp. 1468-1485. 2012.

APPENDIX A: OpenFOAM Code

myIcoFoam

```
/*---------------------------------------------------------------------------*\
  =========                 |
  \\      /  F ield         | OpenFOAM: The Open Source CFD Toolbox
   \\    /   O peration     |
    \\  /    A nd           | Copyright held by original author
     \\/     M anipulation  |
-------------------------------------------------------------------------------
License
    This file is part of OpenFOAM.
    OpenFOAM is free software; you can redistribute it and/or modify it
    under the terms of the GNU General Public License as published by the
    Free Software Foundation; either version 2 of the License, or (at your
    option) any later version.
    OpenFOAM is distributed in the hope that it will be useful, but WITHOUT
    ANY WARRANTY; without even the implied warranty of MERCHANTABILITY or
    FITNESS FOR A PARTICULAR PURPOSE.  See the GNU General Public License
    for more details.
    You should have received a copy of the GNU General Public License
    along with OpenFOAM; if not, write to the Free Software Foundation,
    Inc., 51 Franklin St, Fifth Floor, Boston, MA 02110-1301 USA
Application
    myIcoFoam
Description
    Transient solver for incompressible, laminar flow of Newtonian fluids.
\*---------------------------------------------------------------------------*/
#include "fvCFD.H"
// * * * * * * * * * * * * * * * * * * * * * * * * * * * * * * * * * * * * * //
int main(int argc, char *argv[])
{
#    include "setRootCase.H"
#    include "createTime.H"
#    include "createMesh.H"
#    include "createFields.H"
#    include "initContinuityErrs.H"
#    include "readTimeControls.H"
// * * * * * * * * * * * * * * * * * * * * * * * * * * * * * * * * * * * * * //
Info<< "\nStarting time loop\n" << endl;
while (runTime.run())
//  for (runTime++; !runTime.end(); runTime++)
 {
        Info<< "Time = " << runTime.timeName() << nl << endl;
    #      include "readPISOControls.H"
    #      include "CourantNo.H"
    #      include "setDeltaT.H" // added
    # set deltaT equivalent for solid
        runTime++; // added

        fvVectorMatrix UEqn
        (
                fvm::ddt(U)
              + fvm::div(phi, U)
               - fvm::laplacian(nu, U)
        );
        solve(UEqn == -fvc::grad(p));
```

```
        // --- PISO loop
        for (int corr=0; corr<nCorr; corr++)
        {
                volScalarField rUA = 1.0/UEqn.A();
                U = rUA*UEqn.H();
                phi = (fvc::interpolate(U) & mesh.Sf())
                    + fvc::ddtPhiCorr(rUA, U, phi);

                adjustPhi(phi, U, p);

                for (int nonOrth=0; nonOrth<=nNonOrthCorr; nonOrth++)
                {
                        fvScalarMatrix pEqn
                        (
                                fvm::laplacian(rUA, p) == fvc::div(phi)
                        );

                        pEqn.setReference(pRefCell, pRefValue);
                        pEqn.solve();

                        if (nonOrth == nNonOrthCorr)
                        {
                                phi -= pEqn.flux();
                        }
                }
        #       include "continuityErrs.H"

                U -= rUA*fvc::grad(p);
                U.correctBoundaryConditions();
        }

  runTime.write();
  Info<< "ExecutionTime = " << runTime.elapsedCpuTime() << " s"
    << "  ClockTime = " << runTime.elapsedClockTime() << " s"
    << nl << endl;
}

Info<< "End\n" << endl;

return(0);
}
// * * * * * * * * * * * * * * * * * * * * * * * * * * * * * * * * * * * * * //
```

myTurbFoam

```
/*---------------------------------------------------------------------------*\
  =========                 |
  \\      /  F ield         | OpenFOAM: The Open Source CFD Toolbox
   \\    /   O peration     |
    \\  /    A nd           | Copyright held by original author
     \\/     M anipulation  |
-------------------------------------------------------------------------------
License
    This file is part of OpenFOAM.
    OpenFOAM is free software; you can redistribute it and/or modify it
    under the terms of the GNU General Public License as published by the
    Free Software Foundation; either version 2 of the License, or (at your
    option) any later version.
    OpenFOAM is distributed in the hope that it will be useful, but WITHOUT
    ANY WARRANTY; without even the implied warranty of MERCHANTABILITY or
    FITNESS FOR A PARTICULAR PURPOSE.  See the GNU General Public License
    for more details.
    You should have received a copy of the GNU General Public License
    along with OpenFOAM; if not, write to the Free Software Foundation,
    Inc., 51 Franklin St, Fifth Floor, Boston, MA 02110-1301 USA
Application
    myTurbFoam
Description
    Transient solver for incompressible, turbulent flow.
\*---------------------------------------------------------------------------*/
#include "fvCFD.H"
#include "incompressible/singlePhaseTransportModel/singlePhaseTransportModel.H"
#include "incompressible/RASModel/RASModel.H"
// * * * * * * * * * * * * * * * * * * * * * * * * * * * * * * * * * * * * * //
int main(int argc, char *argv[])
{
#    include "setRootCase.H"
#    include "createTime.H"
#    include "createMesh.H"
#    include "createFields.H"
#    include "initContinuityErrs.H"
#    include "readTimeControls.H"
// * * * * * * * * * * * * * * * * * * * * * * * * * * * * * * * * * * * * * //
    Info<< "\nStarting time loop\n" << endl;
    while (runTime.run())     //for (runTime++; !runTime.end(); runTime++)
    {
            # include "readPISOControls.H"
            # include "CourantNo.H"
            # include "setDeltaT.H" // added

            runTime++;            // added
            Info<< "Time = " << runTime.timeName() << nl << endl;
            // Pressure-velocity PISO corrector
            {
                    // Momentum predictor
                    fvVectorMatrix UEqn
                    (
                            fvm::ddt(U)
                          + fvm::div(phi, U)
                          + turbulence->divDevReff(U)
```

```
                );

                if (momentumPredictor)
                {
                        solve(UEqn == -fvc::grad(p));
                }

                // --- PISO loop
                for (int corr=0; corr<nCorr; corr++)
                {
                        volScalarField rUA = 1.0/UEqn.A();

                        U = rUA*UEqn.H();
                        phi = (fvc::interpolate(U) & mesh.Sf())
                            + fvc::ddtPhiCorr(rUA, U, phi);

                        adjustPhi(phi, U, p);

                        // Non-orthogonal pressure corrector loop

                        for (int nonOrth=0; nonOrth<=nNonOrthCorr; nonOrth++)
                        {
                                // Pressure corrector

                                fvScalarMatrix pEqn
                                (
                                        fvm::laplacian(rUA, p) == fvc::div(phi)
                                );

                                pEqn.setReference(pRefCell, pRefValue);
                                pEqn.solve();

                                if (nonOrth == nNonOrthCorr)
                                {
                                        phi -= pEqn.flux();
                                }
                        }
                #       include "continuityErrs.H"
                        U -= rUA*fvc::grad(p);
                        U.correctBoundaryConditions();
                }
        }

        turbulence->correct();

        runTime.write();

        Info<< "ExecutionTime = " << runTime.elapsedCpuTime() << " s"
            << "  ClockTime = " << runTime.elapsedClockTime() << " s"
            << nl << endl;
    }
    Info<< "End\n" << endl;

    return(0);
}
// ************************************************************************* //
```

icoMHV3DtrackFoam

```
/*---------------------------------------------------------------------------*\
  =========                 |
  \\      /  F ield         | OpenFOAM: The Open Source CFD Toolbox
   \\    /   O peration     |
    \\  /    A nd           | Copyright held by original author
     \\/     M anipulation  |
-------------------------------------------------------------------------------
License
    This file is part of OpenFOAM.
    OpenFOAM is free software; you can redistribute it and/or modify it
    under the terms of the GNU General Public License as published by the
    Free Software Foundation; either version 2 of the License, or (at your
    option) any later version.
    OpenFOAM is distributed in the hope that it will be useful, but WITHOUT
    ANY WARRANTY; without even the implied warranty of MERCHANTABILITY or
    FITNESS FOR A PARTICULAR PURPOSE.  See the GNU General Public License
    for more details.
    You should have received a copy of the GNU General Public License
    along with OpenFOAM; if not, write to the Free Software Foundation,
    Inc., 51 Franklin St, Fifth Floor, Boston, MA 02110-1301 USA
Application
    cylinderFoam
Description
    Transient solver for incompressible, laminar flow of Newtonian fluids
    with dynamic mesh.
Author
    Sandeep Menon
\*---------------------------------------------------------------------------*/
#include "fvCFD.H"
#include "dynamicTopoFvMesh.H"
// Mesh motion solvers
#include "motionSolver.H"
#include "tetDecompositionMotionSolver.H"
#include "faceTetPolyPatch.H"
#include "tetPolyPatchInterpolation.H"
#include "setMotionBC.H"
#include "rotatePoints.H"
// * * * * * * * * * * * * * * * * * * * * * * * * * * * * * * * * * * * * //
int main(int argc, char *argv[])
{
#    include "setRootCase.H"
#    include "createTime.H"
#    include "createDynamicMesh.H"
#    include "initContinuityErrs.H"
#    include "initTotalVolume.H"
#    include "createFields.H"

    Info<< "Reading transportProperties\n" << endl;

    IOdictionary transportProperties
    (
        IOobject
        (
            "transportProperties",
            runTime.constant(),
            mesh,
```

```
                IOobject::MUST_READ,
                IOobject::NO_WRITE
            )
        );
        dimensionedScalar nu
        (
            transportProperties.lookup("nu")
        );
        // Initialize the motion solver
        autoPtr<motionSolver> mPtr = motionSolver::New(mesh);

        // Define the rotation axis and angle from the dictionary
        IOdictionary rotationParams
            (
                IOobject
                (
                    "flippingFoamDict",
                    runTime.findInstance
                    (
                        "",
                        "flippingFoamDict"
                    ),
                    mesh,
                    IOobject::MUST_READ,
                    IOobject::AUTO_WRITE
                )
            );
//== For first patch ==================================
dictionary patchNames1(rotationParams.subDict("patchNames1"));
wordList patches1 = patchNames1.toc();
vector p11(rotationParams.lookup("axisPointStart1"));
vector p12(rotationParams.lookup("axisPointEnd1"));
vector t1(rotationParams.lookup("translation1"));
doubleScalar angle1 = readScalar(rotationParams.lookup("angle1"));

//== For second patch =================================
dictionary patchNames2(rotationParams.subDict("patchNames2"));
wordList patches2 = patchNames2.toc();
vector p21(rotationParams.lookup("axisPointStart2"));
vector p22(rotationParams.lookup("axisPointEnd2"));
vector t2(rotationParams.lookup("translation2"));
doubleScalar angle2 = readScalar(rotationParams.lookup("angle2"));

bool solveForMotion = readBool(rotationParams.lookup("solveForMotion"));

// Convert angle to radians
angle1 *= (3.14159/180.0);
angle2 *= (3.14159/180.0);
doubleScalar dangle1,dangle2;

Info<< "\nStarting time loop\n" << endl;

while (runTime.run())
{
    # include "readPISOControls.H"
    # include "readTimeControls.H"
    # include "checkTotalVolume.H"
    # include "CourantNo.H"
```

```
 # include "setDeltaT.H"
 runTime++;

 Info<< "Time = " << runTime.timeName() << nl << endl;

 // Translate the axis
 p11 += t1; p12 += t1;
 p21 += t2; p22 += t2;

// Update boundary points and solve for mesh-motion
dangle1 = angle1*runTime.deltaT().value();
 dangle2 = angle2*runTime.deltaT().value();

Info << "Rotating angle: " << dangle1 << "  " << dangle2 << endl << endl;
rotatePoints(mesh, patches1, dangle1, p11, p12, t1);

// Update mesh motion 1
if (solveForMotion)
{
        mesh.movePoints(mPtr->newPoints());
}
    rotatePoints(mesh, patches2, dangle2, p21, p22, t2);

// Update mesh motion 2
if (solveForMotion)
{
         mesh.movePoints(mPtr->newPoints());
}

 #       include "volContinuity.H"
         // Make the fluxes relative to the mesh motion
         fvc::makeRelative(phi, U);

 #        include "UEqn.H"
         volScalarField rUA = 1.0/UEqn.A();

         // --- PISO loop

         for (int corr=0; corr<nCorr; corr++)
         {
                  rUA = 1.0/UEqn.A();
                  U = rUA*UEqn.H();
                  phi = (fvc::interpolate(U) & mesh.Sf());
                   //     + fvc::ddtPhiCorr(rUA, U, phi);
                   // adjustPhi(phi, U, p);

                  for (int nonOrth=0; nonOrth<=nNonOrthCorr; nonOrth++)
                  {
                           fvScalarMatrix pEqn
                           (
                                    fvm::laplacian(rUA, p) == fvc::div(phi)
                            );
                           pEqn.setReference(pRefCell, pRefValue);
                           if (corr == nCorr - 1 && nonOrth == nNonOrthCorr)
                           {
                                    pEqn.solve(mesh.solver(p.name() + "Final"));
                           }
                           else
```

```
                {
                        pEqn.solve(mesh.solver(p.name()));
                }
                if (nonOrth == nNonOrthCorr)
                {
                        phi -= pEqn.flux();
                }
        }
        # include "continuityErrs.H"
        // Some boundary conditions require fluxes to be relative
        fvc::makeRelative(phi, U);
        U -= rUA*fvc::grad(p);
        U.correctBoundaryConditions();
}

Info<< "ExecutionTime = " << runTime.elapsedCpuTime() << " s"
    << "  ClockTime = " << runTime.elapsedClockTime() << " s"
    << nl << endl;

// Make the fluxes absolute before manipulating the mesh.
fvc::makeAbsolute(phi, U);
bool meshChanged = mesh.updateTopology();

if (meshChanged)
{
#       include "checkTotalVolume.H"

        // Update the motion solver
        mPtr->updateMesh(mesh.meshMap());

        // Obtain flux from mapped velocity
        phi = (fvc::interpolate(U) & mesh.Sf());
#       include "correctPhi.H"
#       include "CourantNo.H"
}

// Write out current parameters
rotationParams.instance() = runTime.timeName();
rotationParams.add("patchNames1", patchNames1, true);
rotationParams.add("axisPointStart1", p11, true);
rotationParams.add("axisPointEnd1", p12, true);
rotationParams.add("translation1", t1, true);
rotationParams.add("angle1", angle1*(180/3.14159), true);

rotationParams.add("patchNames2", patchNames2, true);
rotationParams.add("axisPointStart2", p21, true);
rotationParams.add("axisPointEnd2", p22, true);
rotationParams.add("translation2", t2, true);
rotationParams.add("angle2", angle2*(180/3.14159), true);

rotationParams.add("solveForMotion", solveForMotion, true);

runTime.write();

if (runTime.outputTime())
{
        // Write out mesh quality
        volScalarField meshQuality
```

```
                (
                        IOobject
                        (
                                "meshQuality",
                                runTime.timeName(),
                                mesh,
                                IOobject::NO_READ,
                                IOobject::AUTO_WRITE
                         ),
                        mesh,
                        dimensionedScalar("scalar", dimless, 0.0),
                        "zeroGradient"
                );
                meshQuality.internalField() = mesh.meshQuality(true);
                meshQuality.write();

                // Write out the mesh length scales
                volScalarField lengthScale
                (
                        IOobject
                        (
                                "lengthScale",
                                runTime.timeName(),
                                mesh,
                                IOobject::NO_READ,
                                IOobject::AUTO_WRITE
                        ),
                        mesh,
                        dimensionedScalar("scalar", dimLength, 0.0),
                        "zeroGradient"
                );

                lengthScale.internalField() = mesh.lengthScale();
                lengthScale.write();

                // Write out divergence-free fluxes
                volScalarField divPhi = fvc::div(phi);
                divPhi.write();
        }
}

Info<< "End\n" << endl;

return(0);

}
// ************************************************************************* //
```

icoMHV3DtrackFoam

```
/*---------------------------------------------------------------------------*\
  =========                 |
  \\      /  F ield         | OpenFOAM: The Open Source CFD Toolbox
   \\    /   O peration     |
    \\  /    A nd           | Copyright held by original author
     \\/     M anipulation  |
-------------------------------------------------------------------------------
License
    This file is part of OpenFOAM.
    OpenFOAM is free software; you can redistribute it and/or modify it
    under the terms of the GNU General Public License as published by the
    Free Software Foundation; either version 2 of the License, or (at your
    option) any later version.
    OpenFOAM is distributed in the hope that it will be useful, but WITHOUT
    ANY WARRANTY; without even the implied warranty of MERCHANTABILITY or
    FITNESS FOR A PARTICULAR PURPOSE.  See the GNU General Public License
    for more details.
    You should have received a copy of the GNU General Public License
    along with OpenFOAM; if not, write to the Free Software Foundation,
    Inc., 51 Franklin St, Fifth Floor, Boston, MA 02110-1301 USA
Application
    cylinderFoam
Description
    Transient solver for incompressible, laminar flow of Newtonian fluids
    with dynamic mesh.
Author
    Vinh-Tan Nguyen
\*---------------------------------------------------------------------------*/
#include "fvCFD.H"
/For turbulence models
#include "incompressible/singlePhaseTransportModel/singlePhaseTransportModel.H"
#include "incompressible/RASModel/RASModel.H"
#include "dynamicTopoFvMesh.H"
// Mesh motion solvers
#include "motionSolver.H"
#include "tetDecompositionMotionSolver.H"
#include "faceTetPolyPatch.H"
#include "tetPolyPatchInterpolation.H"
#include "setMotionBC.H"
#include "rotatePoints.H"
// * * * * * * * * * * * * * * * * * * * * * * * * * * * * * * * * * * * * //
int main(int argc, char *argv[])
{
#    include "setRootCase.H"
#    include "createTime.H"
#    include "createDynamicMesh.H"
#    include "initContinuityErrs.H"
#    include "initTotalVolume.H"
#    include "createFields.H"

    Info<< "Reading transportProperties\n" << endl;

    IOdictionary transportProperties
    (
        IOobject
        (
```

```
                "transportProperties",
                runTime.constant(),
                mesh,
                IOobject::MUST_READ,
                IOobject::NO_WRITE
            )
        );
        dimensionedScalar nu
        (
            transportProperties.lookup("nu")
        );
        // Initialize the motion solver
        autoPtr<motionSolver> mPtr = motionSolver::New(mesh);

        // Define the rotation axis and angle from the dictionary
        IOdictionary rotationParams
            (
                IOobject
                (
                    "flippingFoamDict",
                    runTime.findInstance
                    (
                        "",
                        "flippingFoamDict"
                    ),
                    mesh,
                    IOobject::MUST_READ,
                    IOobject::AUTO_WRITE
                )
            );
//== For first patch ==================================
dictionary patchNames1(rotationParams.subDict("patchNames1"));
wordList patches1 = patchNames1.toc();
vector p11(rotationParams.lookup("axisPointStart1"));
vector p12(rotationParams.lookup("axisPointEnd1"));
vector t1(rotationParams.lookup("translation1"));
doubleScalar angle1 = readScalar(rotationParams.lookup("angle1"));

//== For second patch ==================================
dictionary patchNames2(rotationParams.subDict("patchNames2"));
wordList patches2 = patchNames2.toc();
vector p21(rotationParams.lookup("axisPointStart2"));
vector p22(rotationParams.lookup("axisPointEnd2"));
vector t2(rotationParams.lookup("translation2"));
doubleScalar angle2 = readScalar(rotationParams.lookup("angle2"));

bool solveForMotion = readBool(rotationParams.lookup("solveForMotion"));

// Convert angle to radians
angle1 *= (3.14159/180.0);
angle2 *= (3.14159/180.0);
Info<< "\nAngles: "<<angle1<<" "<< angle2<<"\n" << endl;

doubleScalar dangle1,dangle2;

Info<< "\nStarting time loop\n" << endl;

while (runTime.run())
```

```
{
    # include "readPISOControls.H"
    # include "readTimeControls.H"
    # include "checkTotalVolume.H"
    # include "CourantNo.H"
    # include "setDeltaT.H"
    runTime++;

    Info<< "Time = " << runTime.timeName() << nl << endl;

    // Translate the axis
    p11 += t1; p12 += t1;
    p21 += t2; p22 += t2;

   // Update boundary points and solve for mesh-motion
   dangle1 = angle1*runTime.deltaT().value();
    dangle2 = angle2*runTime.deltaT().value();

   Info << "Rotating angle: " << dangle1 << "  " << dangle2 << endl << endl;
   rotatePoints(mesh, patches1, dangle1, p11, p12, t1);

   // Update mesh motion 1
   if (solveForMotion)
   {
          mesh.movePoints(mPtr->newPoints());
   }
       rotatePoints(mesh, patches2, dangle2, p21, p22, t2);

   // Update mesh motion 2
   if (solveForMotion)
   {
            mesh.movePoints(mPtr->newPoints());
   }

    #       include "volContinuity.H"
           // Make the fluxes relative to the mesh motion
           fvc::makeRelative(phi, U);

    #       include "UEqn.H"
           volScalarField rUA = 1.0/UEqn.A();

           // --- PISO loop

           for (int corr=0; corr<nCorr; corr++)
           {
                    rUA = 1.0/UEqn.A();
                    U = rUA*UEqn.H();
                    phi = (fvc::interpolate(U) & mesh.Sf());
                     //     + fvc::ddtPhiCorr(rUA, U, phi);
                     // adjustPhi(phi, U, p);

                    for (int nonOrth=0; nonOrth<=nNonOrthCorr; nonOrth++)
                    {
                             fvScalarMatrix pEqn
                             (
                                      fvm::laplacian(rUA, p) == fvc::div(phi)
                              );
                             pEqn.setReference(pRefCell, pRefValue);
```

```
                if (corr == nCorr - 1 && nonOrth == nNonOrthCorr)
                {
                        pEqn.solve(mesh.solver(p.name() + "Final"));
                }
                else
                {
                        pEqn.solve(mesh.solver(p.name()));
                }
                if (nonOrth == nNonOrthCorr)
                {
                        phi -= pEqn.flux();
                }
        }
        # include "continuityErrs.H"
        // Some boundary conditions require fluxes to be relative
        fvc::makeRelative(phi, U);
        U -= rUA*fvc::grad(p);
        U.correctBoundaryConditions();
}

Info<< "ExecutionTime = " << runTime.elapsedCpuTime() << " s"
    << "  ClockTime = " << runTime.elapsedClockTime() << " s"
    << nl << endl;

// Make the fluxes absolute before manipulating the mesh.
fvc::makeAbsolute(phi, U);
bool meshChanged = mesh.updateTopology();

if (meshChanged)
{
#       include "checkTotalVolume.H"

        // Update the motion solver
        mPtr->updateMesh(mesh.meshMap());

        // Obtain flux from mapped velocity
        phi = (fvc::interpolate(U) & mesh.Sf());
#       include "correctPhi.H"
#       include "CourantNo.H"
}

// Write out current parameters
rotationParams.instance() = runTime.timeName();
rotationParams.add("patchNames1", patchNames1, true);
rotationParams.add("axisPointStart1", p11, true);
rotationParams.add("axisPointEnd1", p12, true);
rotationParams.add("translation1", t1, true);
rotationParams.add("angle1", angle1*(180/3.14159), true);

rotationParams.add("patchNames2", patchNames2, true);
rotationParams.add("axisPointStart2", p21, true);
rotationParams.add("axisPointEnd2", p22, true);
rotationParams.add("translation2", t2, true);
rotationParams.add("angle2", angle2*(180/3.14159), true);

rotationParams.add("solveForMotion", solveForMotion, true);

runTime.write();
```

```
        if (runTime.outputTime())
        {
            // Write out mesh quality
            volScalarField meshQuality
            (
                IOobject
                (
                    "meshQuality",
                    runTime.timeName(),
                    mesh,
                    IOobject::NO_READ,
                    IOobject::AUTO_WRITE
                ),
                mesh,
                dimensionedScalar("scalar", dimless, 0.0),
                "zeroGradient"
            );
            meshQuality.internalField() = mesh.meshQuality(true);
            meshQuality.write();

            // Write out the mesh length scales
            volScalarField lengthScale
            (
                IOobject
                (
                    "lengthScale",
                    runTime.timeName(),
                    mesh,
                    IOobject::NO_READ,
                    IOobject::AUTO_WRITE
                ),
                mesh,
                dimensionedScalar("scalar", dimLength, 0.0),
                "zeroGradient"
            );

            lengthScale.internalField() = mesh.lengthScale();
            lengthScale.write();

            // Write out divergence-free fluxes
            volScalarField divPhi = fvc::div(phi);
            divPhi.write();
        }
    }

    Info<< "End\n" << endl;

    return(0);

    }
    // ************************************************************************* //
```

myPimpleDyMFoam

```
/*---------------------------------------------------------------------------*\
  =========                 |
  \\      /  F ield         | OpenFOAM: The Open Source CFD Toolbox
   \\    /   O peration     |
    \\  /    A nd           | Copyright held by original author
     \\/     M anipulation  |
-------------------------------------------------------------------------------
License
    This file is part of OpenFOAM.
    OpenFOAM is free software; you can redistribute it and/or modify it
    under the terms of the GNU General Public License as published by the
    Free Software Foundation; either version 2 of the License, or (at your
    option) any later version.
    OpenFOAM is distributed in the hope that it will be useful, but WITHOUT
    ANY WARRANTY; without even the implied warranty of MERCHANTABILITY or
    FITNESS FOR A PARTICULAR PURPOSE.  See the GNU General Public License
    for more details.
    You should have received a copy of the GNU General Public License
    along with OpenFOAM; if not, write to the Free Software Foundation,
    Inc., 51 Franklin St, Fifth Floor, Boston, MA 02110-1301 USA
Application
    myPimpleDyMFoam.C
Description
    Transient solver for incompressible, flow of Newtonian fluids
    on a moving mesh using the PIMPLE (merged PISO-SIMPLE) algorithm.
    Turbulence modelling is generic, i.e. laminar, RAS or LES may be selected.
\*---------------------------------------------------------------------------*/
#include "fvCFD.H"
#include "singlePhaseTransportModel.H"
#include "turbulenceModel.H"
#include "dynamicFvMesh.H"
// * * * * * * * * * * * * * * * * * * * * * * * * * * * * * * * * * * * * * //
int main(int argc, char *argv[])
{
#    include "setRootCase.H"
#    include "createTime.H"
#    include "createDynamicFvMesh.H"
#    include "readPIMPLEControls.H"
#    include "initContinuityErrs.H"
#    include "createFields.H"
#    include "readTimeControls.H"
// * * * * * * * * * * * * * * * * * * * * * * * * * * * * * * * * * * * * * //
    Info<< "\nStarting time loop\n" << endl;

    while (runTime.run())
    {
        # include "readControls.H"
        # include "CourantNo.H"

        // Make the fluxes absolute
        fvc::makeAbsolute(phi, U);

        # include "setDeltaT.H"

        runTime++;
```

```
        Info<< "Time = " << runTime.timeName() << nl << endl;

        bool meshChanged = mesh.update();
        //mesh.update();

        if (correctPhi && (mesh.moving() || meshChanged))
        {
            # include "correctPhi.H"
        }

        // Make the fluxes relative to the mesh motion

        fvc::makeRelative(phi, U);

        if (mesh.moving() && checkMeshCourantNo)
        {
            # include "meshCourantNo.H"
        }

        runTime.write();

        Info<< "ExecutionTime = " << runTime.elapsedCpuTime() << " s"
            << "  ClockTime = " << runTime.elapsedClockTime() << " s"
            << nl << endl;
    }

    Info<< "End\n" << endl;

    return 0;
}
// ************************************************************************* //
```

Groovy Boundary Condition

inlet

```
{
        type            groovyBC;
        refValue        uniform (0 0 0);
        refGradient     uniform (0 0 0);
        valueFraction   uniform 1;
        value           uniform (0 0 0);
        valueExpression "vector(0,0,velo)";
        gradientExpression "vector(0,0,0)";
        fractionExpression "1";

        //parabolic
        variables
        "amax=1.350;R2=(0.014*0.014);xp=pos().x;yp=pos().y;para=(xp*xp+yp*yp);
        velo=(amax)*(para/R2-1);";

        //power law
        //variables
        //"vmean=-1.350;amax=vmean/0.817;R=0.014;xp=pos().x;yp=pos().y;
        //d=1.0-sqrt(xp*xp+yp*yp)/R;n=1.0/7.0;velo=amax*pow(d,0.14286);";
        //timelines       ();

        //variables
        //"amax=1.8;R2=(0.014*0.014);xp=pos().x;yp=pos().y;para=(xp*xp+yp*yp);
        //velo=(amax)*(para/R2-1);";
        //valueExpression       "vector(0,0,velo)";
  }
```

wallShearStress

```
/*---------------------------------------------------------------------------*\
  =========                 |
  \\      /  F ield         | OpenFOAM: The Open Source CFD Toolbox
   \\    /   O peration     |
    \\  /    A nd           | Copyright held by original author
     \\/     M anipulation  |
-------------------------------------------------------------------------------
License
    This file is part of OpenFOAM.
    OpenFOAM is free software; you can redistribute it and/or modify it
    under the terms of the GNU General Public License as published by the
    Free Software Foundation; either version 2 of the License, or (at your
    option) any later version.
    OpenFOAM is distributed in the hope that it will be useful, but WITHOUT
    ANY WARRANTY; without even the implied warranty of MERCHANTABILITY or
    FITNESS FOR A PARTICULAR PURPOSE.  See the GNU General Public License
    for more details.
    You should have received a copy of the GNU General Public License
    along with OpenFOAM; if not, write to the Free Software Foundation,
    Inc., 51 Franklin St, Fifth Floor, Boston, MA 02110-1301 USA
Application
    wallShearStress
Description
    Calculates and writes the wall shear stress, for the specified times.
\*---------------------------------------------------------------------------*/
#include "fvCFD.H"
#include "incompressible/singlePhaseTransportModel/singlePhaseTransportModel.H"
#include "incompressible/RASModel/RASModel.H"
// * * * * * * * * * * * * * * * * * * * * * * * * * * * * * * * * * * * * * //
int main(int argc, char *argv[])
{
        timeSelector::addOptions();
        # include "setRootCase.H"
        # include "createTime.H"
        instantList timeDirs = timeSelector::select0(runTime, args);
        # include "createMesh.H"

        forAll(timeDirs, timeI)
        {
                runTime.setTime(timeDirs[timeI], timeI);
                Info<< "Time = " << runTime.timeName() << endl;
                 mesh.readUpdate();

                # include "createFields.H"

                volSymmTensorField Reff(RASModel->devReff());

                volVectorField wallShearStress
                (
                        IOobject
                        (
                                "wallShearStress",
                                runTime.timeName(),
                                mesh,
                                IOobject::NO_READ,
                                IOobject::AUTO_WRITE
```

```
                    ),
                    mesh,
                    dimensionedVector
                    (
                        "wallShearStress",
                        Reff.dimensions(),
                        vector::zero
                    )
                );
        forAll(wallShearStress.boundaryField(), patchi)
        {
            wallShearStress.boundaryField()[patchi] =
            (
                -mesh.Sf().boundaryField()[patchi]
                /mesh.magSf().boundaryField()[patchi]
            ) & Reff.boundaryField()[patchi];
        }

        wallShearStress.write();
    }

Info<< "End" << endl;

return 0;
}
// ************************************************************************* //
```

APPENDIX B:

PUBLICATIONS

1. **Kuan, Y. H.,** Lakshmi, P. D., Yoganathan, A. P., and Leo, H. L. Recent Advances in Polymeric Heart Valves Research. *Int J Biomater Res Eng,* 1(1), pp. 1-17. 2011.

2. Nguyen, V-T., **Kuan, Y. H.,** Chen, P-Y., Ge, L., Sotiropoulos, F., Yoganathan, A. P., and Leo, H. L. Experimentally Validated Hemodynamics Simulations of Mechanical Heart Valve in Three Dimensions. *Cardiovasc Eng Technol*, 3(1), pp. 88-100. 2012.

3. Anene-Nzelu, C. G., Peh, K. Y., Fraiszudeen, A., **Kuan, Y. H.,** Ng, S. H., Toh, Y. C., Leo, H. L., and Yu, H. Scalable alignment of three-dimensional cellular constructs in a microfluidic chip. *Lab Chip,* 13(20), pp. 4124-4133. 2013.

4. **Kuan, Y. H.,** Nguyen, V-T., Kabinejadian, F., Su, B., Kim, S., Yoganathan, A. P., and Leo, H. L. Numerical analysis of the hemodynamic performance of bileaflet mechanical heart valves at different implantation angles. *J Heart Valve Dis*, (Accepted for publication) 2014.

5. **Kuan, Y. H.,** Kabinejadian, F., Nguyen, V-T., Su, B., Yoganathan, A. P., and Leo, H. L. Impact of hinge positions on the hinge micro flow fields of bileaflet mechancial heart valves. *Comput Methods Biomech Biomed Eng* (Accepted with minor revision). 2014

6. **Kuan, Y. H.,** Kabinejadian, F., Nguyen, V-T., Su, B., and Leo, H. L. Computational Hemodynamic Investigation of bileaflet and trileaflet mechancial heart valves. (Submitted). 2014

CONFERENCES:

1. **Kuan, Y. H.,** Xu, G. X., Nguyen, V-T., Poh, H. J., Lee, A. K. H., Lou, J., Tan, J. K., Zhang, Y. Yoganathan, A. P., and Leo, H. L. 3D Hemodynamic Simulation of Bileaflet Mechanical Heart Valve at Aortic Position. 6th World Congress in Bioengineering. Singapore. 2010.

2. **Kuan, Y. H**., Nguyen, V-T., Chen, P-Y., and Leo, H. L. Hemodynamic of Bileaflet Mechanical Heart Valve Simulation and Validation, 5th WACBE World Congress on Bioengineering. Tainan, Taiwan. 2011.

3. **Kuan, Y. H.,** Nguyen, V-T., and Leo, H. L., Simulation of Bileaflet Mechanical Heart Valve. IASTED International Conference on Biomedical Engineering. Insbruck, Austria. 2012.

4. **Kuan, Y. H.,** Nguyen, V-T., Su, B., and Leo, H.L. Hinge flow fields simulation of bileaflet mechanical heart valves during diastolic phase. The 7th Asian Pacific Conference on Biomechanics. Seoul, Korea. 2013.

5. **Kuan, Y. H.,** Nguyen, V-T., and Leo, H. L., Hinge flow fields study of SJM Bileaflet Mechanical Heart Valves. The 15th International Conference on Biomedical Engineering. Singapore. 2013.